Caractérisation des Matériaux Magnétostrictifs : Cas du Fe49-Co49-V2, Modélisation du Comportement Couplé et Application à la Récolte d'Energie

Franck Borel Toutsop Zangho

Université Claude Bernard Lyon 1

THESE de DOCTORAT DE
L'UNIVERSITE CLAUDE BERNARD LYON 1
En cotutelle avec l'université de Buea-Cameroun

Ecole Doctorale N° ED 160
Electronique, Electrotechnique et Automatique

Discipline : **Génie Electrique**

Soutenue publiquement le 08/12/2023, par :
Franck Borel TOUTSOP ZANGHO

Characterization of Magnetostrictive Materials: Case of Fe_{49}-Co_{49}-V_2, Modeling of its Coupled Behavior and Application to Energy Harvesting

Devant le jury composé de :

Ngwa, Gideon	Professeur	Université de Buea	Président du Jury
Bernard, Laurent	Professeur	Université Fédérale de Santa Catarina (Brésil)	Rapporteur
Fotsin, Hilaire	Professeur	Université de Dschang	Rapporteur
Chamagne, Didier	Professeur des Universités	Université de Franche Comté FEMTO-ST	Examinateur
Raulet, Marie-Ange	Maître de Conférences	Université Lyon 1	Examinatrice
Toko, Denis	Professeur	Université de Buea	Examinateur
Morel, Laurent	Maître de Conférences	Université Lyon 1	Directeur de thèse
Tsafack, Pierre	Professeur Associé	Université de Buea	Directeur de thèse
Ducharne, Benjamin	Maître de Conférences	Université de Tohoku	Invité
Lallart, Mickaël	Professeur des Universités	INSA de Lyon	Invité

DEDICATION

To my late father Mr. Toutsop Gaston

ACKNOWLEDGMENTS

I wish to acknowledge the substantial help provided by Prof. Laurent Morel for being my thesis director and for continuously supporting me throughout my Ph.D. research. He relented no efforts to make sure everything was OK for me to produce my best. His continuous encouragement especially during and after the COVID-19 outbreak and moral support helped me to hold on till the end of the program.

In addition, I would like to extend my gratitude to my supervisor, Prof. Tsafack Pierre, from the Faculty of Engineering and Technology (FET), University of Buea, for his invaluable supervision, guidance, understanding, constructive and fatherly advice during both studying and living times in Buea.

I also want to express my very great appreciation to my thesis co-director Prof Benjamin Ducharne for his valuable and constructive suggestions during the planning and development of my Ph.D. research work. His patience, motivation, enthusiasm, immense knowledge, and willingness to give his time so generously have been very much appreciated.

I am particularly grateful for the precious scientific support from another co-director Prof. Mickaël Lallart. His rigor, dynamism, promptness, experience, and expertise coupled with his consistent approach to deeper analysis of processes and results, have brought me a lot during these three years, scientifically as well as on a personal level on my path of science. Our discussions were very valuable and essential to the completion of this thesis.

I am grateful to Prof. Agbor Dieudonné Agbor, the dean of the Faculty of Engineering and Technology (FET), for all his tireless efforts in the postgraduate program at FET that led to my Ph.D. admission.

This thesis would not have been accomplished without the financial support of the Cooperation and Cultural Action Service (SCAC) of the French Embassy in Cameroon for the various trips and stays in France.

I'm thankful to the LGEF laboratory for the various research facilities and support that permitted me to successfully conduct my experiments, and publish my work in international peer-reviewed journals. I extend my thankfulness towards all the staff and my fellow doctoral mate of the laboratory for their invaluable help and precious pieces of advice.

To Pierre Brosselard for his constant support and encouragement, my acquaintance and adaptation to the new environment of Lyon would not have been easier without his care and support to make me feel at home.

I am infinitely grateful to my family: Mrs. Toutsop Charlotte, Toutsop Georgette, my brothers Herman and Jordan, and sisters Sandra and Laura for their permanent support, and love, when it seemed to be more difficult than me.

To the Tsafack family and Kamdjou Duplex, since my first day in Buea, they adopted me as a son and brother. They kept reminding me that hard work is the key to success.

The completion of this thesis would have not been possible without the financial support of my sister Mrs. Bougne Albertine who has been there for me and made sure I didn't lack anything.

My special thanks are extended to my senior colleagues and friends: Dr Yves Tene, Dr Valery Nkemeni, Dr. Louis Musong, Dr. Sorelle Nguedjang, Husserl Fonou, Esther Simo, and Gaius Djomo for being motivated seniors and enthusiastic with a fun-loving spirit.

To FEIAC (Fédération Évangélique Internationale des Amis du Cameroun) for the various coaching sessions, financial support, and prayers.

Last but not least, an immense thanks to Ornela Nana for being there for me and with me since the beginning of this adventure, for her tolerance, and assistance in the follow-up of my various tasks, engagements, and responsibilities.

And a big apology to anyone I might have forgotten

RÉSUMÉ

La demande croissante de dispositifs autonomes suscite un intérêt considérable des dispositifs de récupération d'énergie. Pour ces dispositifs, les matériaux magnétostrictifs offrent plusieurs avantages en termes de moyen de conversion des vibrations mécaniques en énergie électrique. Le Permendur est très prometteur à cet égard mais présente des coefficients magnétostrictifs importants ayant des effets sur leurs contraintes internes. Afin de contrôler cette magnétostriction, de donner des explications sur le comportement au niveau de la microstructure du matériau et dans l'optique de mieux caractériser le système de récupération, les contraintes internes peuvent être évaluées. Par conséquent, ce travail étudie tout d'abord la perméabilité magnétique directionnelle incrémentale comme solution.

Pour l'estimation des contraintes mécaniques internes, des contraintes externes homogènes ont été utilisées dans le cadre académique de mes travaux. Les cycles d'hystérésis ont été reconstitués à partir de mesures de perméabilité incrémentales par un capteur conçu ; La nature directionnelle de celui-ci ajoute une dimension supplémentaire à l'observation de la réponse magnétique. L'étude révèle qu'un angle de $\pi/2$ entre les contributions d'excitation magnétique DC et AC et une densité de flux de 10 kA/m est la configuration optimale, présentant la corrélation maximale avec une contrainte de traction appliquée uniformément. La perméabilité magnétique incrémentale étant associée au glissement des parois du domaine, cette étude représente une avancée significative dans la compréhension des mécanismes fondamentaux de la magnétisation.

Pour la conversion magnétostrictive d'énergie, nous avons effectué la caractérisation magnétique sur des tôles sous contraintes mécaniques, la modélisation du comportement anhystérétique, ainsi que l'évaluation des capacités de conversion à l'aide des cycles thermodynamiques d'Ericsson basés sur des courbes anhystérétiques modélisées. Sous une contrainte de 480 MPa et une excitation magnétique de 5.5 $kA \cdot m^{-1}$, une densité d'énergie maximale de 10.45 $mJ \cdot cm^{-3}$ est atteinte. En considérant des pertes dues aux cycles hystérétiques une densité d'énergie de 3.52 $mJ \cdot cm^{-3}$ est obtenue

dans les mêmes conditions. Enfin, des cycles expérimentaux Ericsson ont été étudiés pour valider la faisabilité de la conversion et confirmer les prévisions de niveau d'énergie.

Les travaux ont été conclus par la mise sur pieds d’un démonstrateur pour la récupération d’énergie vibrationnelle et un modèle d’estimation de la puissance en sortie du démonstrateur illustrant ainsi la faisabilité du système de récupération. Mais toutes fois des études poussées entre autres le dimensionnement de chacune des composantes du système doit être effectuée afin d’obtenir des résultats optimaux.

Mots clés : Magnétostriction, couplage magnéto-mécanique, conversion d'énergie, cycle d'Ericsson, contrainte mécanique interne.

ABSTRACT

The increasing demand for autonomous devices is driving considerable interest in energy harvesting devices. For such devices, magnetostrictive materials offer several advantages in terms of conversion means of mechanical vibrations into electrical energy. Permendur is very promising in this regard but presents significant magnetostrictive coefficients having effects on their internal stresses. In order to control this magnetostriction, to provide explanations on the behavior at the level of the microstructure of the material and with a view to better characterizing the recovery system, the internal constraints can be evaluated. Therefore, this work first studies incremental directional magnetic permeability as a solution.

For the estimation of internal mechanical stresses, homogeneous external stresses were used in the academic framework of my work. The hysteresis cycles were reconstructed from incremental permeability measurements by a designed sensor; The directional nature of it adds an additional dimension to the observation of the magnetic response. The study reveals that an angle of π/2 between the DC and AC magnetic excitation contributions and a flux density of 10 kA/m is the optimal configuration, exhibiting the maximum correlation with uniformly applied tensile stress. As incremental magnetic permeability is associated with sliding of the domain walls, this study represents a significant advance in the understanding of the fundamental mechanisms of magnetization.

For magnetostrictive energy conversion, we performed magnetic characterization on sheets under mechanical stress, modeling of anhysteretic behavior, as well as evaluation of conversion capabilities using curve-based Ericsson thermodynamic cycles modeled anhysteretics. Under a stress of 480 MPa and a magnetic excitation of 5.5 kA·m-1, a maximum energy density of 10.45 mJ·cm-3 is achieved. Considering losses due to hysteretic cycles, an energy density of 3.52 mJ·cm-3 is obtained under the same conditions. Finally, Ericsson experimental cycles were studied to validate the feasibility of the conversion and confirm the energy level predictions.

The work was concluded by setting up a demonstrator for vibrational energy recovery and a model for estimating the power output from the demonstrator, thus illustrating the feasibility of the recovery system. However, in-depth studies, including the sizing of each of the components of the system, must be carried out in order to obtain optimal results.

Keywords: Magnetostriction, magneto-mechanical coupling, energy conversion, Ericsson cycle, mechanical internal stress, multi-axis magnetization.

TABLE OF CONTENT

LIST OF FIGURES

LIST OF TABLES

LIST OF ABBREVIATIONS

AC	Alternative Current
CMI	Contraintes Mécaniques Internes
CMOS	Complementary Metal Oxide Semi-conductors
CND	Contrôle Non Destructif
Co	Cobalt
DC	Direct Current
DP	Dual-phase
EC	Radio Frequency
ECT	Eddy Current Testing
EC	Eddy-Current
EDM	Electrical Discharge Machining
FET	Faculty of Engineering and Technology
FEIAC	Fédération Evangélique Internationale des Amis du Cameroun
IP	Incremental Permeability
Fe	Iron
FeCo	Iron Cobalt
LGEF	Laboratoire de Génie Electrique et de Férroélectricité
MBN	Magnetic Barkhausen Noise
MIP	Magnetic Incremental Permeability
MNPM	Magnetic Needle Probe Method
MsM	Magnetostrictive material
MATLAB	Matrix Laboratory
MIS	Mechanical Internal Stress
NdFeB	Neodymium
NDT	Non-Destructive Testing
PIM	Perméabilité incrémentale magnétique
Iron-Cobalt	Permendur
PC	Personal Computer

RIT	Radiation Imaging Test
SCAC	Service de la Coopération et de l'Action Culturelle
VLSI	Very Large-Scale Integration

LIST OF SYMBOLS

δ	Angle of the sensor
A	Area
A2	Area of the active zone
A1	Area of the ferrite sensor
Ha	Ascending curve magnetic flux value.
R^2	Coefficient of determination
Hc	Coercive field
A_c	Coil's cross-section
L_{coil}	Coil's inductance
R_{coil}	Coil's resistance
Hd	Descending curve magnetic flux value.
σc	Elastic limit
e(t)	Electromotive force
W	Energy density
$\mu_{MIP\,r}$	FeCo relative permeability
f	Frequency
Z	Impedance
Z''	Impedance imaginary part of Z
Z'	Impedance real part
ΔB_a	Incremental amplitude of the applied alternating magnetic intensity
ΔH_{surf}	Incremental amplitude of the magnetic flux density response
$V_{EMF}(t)$	Induced electrical voltage on the coil windings
L	Inductance of the active part
S_0	Initial prestress
L_0	Initial elongation of the springs
Binterp	Interpolated values of *B*
kA/m	Kilo Ampère/meter

kΩ	Kilo ohms
B_m	Local linearized magnetic flux density of the magnetostrictive material
$\mu_{r\,exp}$	Low field permeability experimental value
$\mu_{r\,sim}$	Low field permeability obtained from the model
H	Magnetic field strength
H_m	Magnetic field strength on the magnetostrictive material
B	Magnetic flux Density
m	Magnetic moments
μ	Magnetic permeability
M	Magnetization
Msat	Magnetization saturation
θ	Magneto elastic coefficient
Vmax_measured	Maximum measured output voltage.
l2	Mean length of the active zone
l1	Mean length of the ferrite sensor
Mpa	Mega pascal
m	Meters
μJ	Microjoules
μW	Microwatts
mm	Millimeters
mJ	Millijoules
mV	Millivolts
mW	Milliwatts
N	Newtons
n_m	Number of magnetic moments
n	Number of turns
N	Number of turns of the ferrite
N_c	Number of turns on the magnetostrictive material
f	Operating frequency
W_{out}	Output electrical energy

Pa	Pascal
$V_{\_EMF\_pk}$	Peak values of the EMF
ρ	Pearson correlation factors
μ_0	Permeability of air
μ	Permeability of the magnetostrictive material
PD	Power density
Q	Quality factor
$\mathcal{R}2$	Reluctance of the active Zone
$\mathcal{R}1$	Reluctance of the ferrite sensor
Br	Remanent flux density or retentivity
f_r	Resonant frequency
Bs	Saturation flux density
s	Sensitivity
IZI	Sensor impedance modulus
C	Series capacitance
S	Specimen cross-section
M	Spontaneous magnetization
K	Spring constant
Hsurf	Tangential surface excitation field
σ	Tensile stress
Vmax_expected	Theoretically expected output voltage
Z_T	Total equivalent series impedance
H_{eq}	Total magnetic field generated by magnets
V_{air}	Total volume of the air
V_{total}	Total volume of the set
$B_{a\ MIP}$	Value of the magnetic flux after integration from the MIP data
V	Vanadium
$d\Phi_m$	Variation of flux in the material
V_a	Volume of active material.
V_{magnet}	Volume of the magnet.
Vd	Volume of the domain

1 GENERALITIES

1.1 Introduction

This chapter constitutes the introductory section of our thesis manuscript, it presents the general context contest in which this thesis is executed: the characterization of magnetostrictive materials and their application to energy harvesting. It will be organized as follows: we are going to first describe the context of our study in section 1.2, followed by the presentation of smart material-based energy harvesting and modeling techniques in section 1.3. Section 1.4 will give more insights on the basics of magnetism while in section 1.5 material characterization and control techniques are going to be presented. Section 1.6 will state the scientific problem to investigate followed by section 1.7 which provides details on objectives and methods adopted to solve the aforementioned problem. Finally, sections 1.8 and 1.9 will respectively give the thesis outline and the conclusion.

1.2 Context

The enthusiasm of the last twenty years concerning ambient energy harvesting is most likely linked to the proliferation of wireless autonomous isolated sensors and wirelessly connected devices (*e.g.*, development of the Internet of Things (IoT) [1]) used to collect real-time information in various environments. Indeed, one of the main keys to the success of any project lies in its ability to predict future events. Using that knowledge, means of action can be put in place to reduce the impact of future disruptive events and to better take advantage of future beneficial events. For instance, a farmer has every interest in being able to predict the weather to perform real-time adjustments on his way of farming, or, in the same way, an airline company has much interest in being able to predict the health state of his planes to program revisions as needed. These predictions are developed by collecting certain relevant information on the parameter to be controlled which, once processed (analysis of trends, occurrence, cause and effect, development of mathematical models, etc.), makes it possible to formulate possible scenarios (for the future as well as the probability that they will occur). The greater the amount of (relevant) data collected, the more accurate the prediction will be and the more likely it will be to come true. It is partly for this reason, coupled with the various advances in electronics and communication (especially in terms of consumption), that wireless isolated sensors, less and less expensive and more and more compact, arouse so much interest and are deployed in the entire networks.

In 2016, a study performed by Rashid and Rehmani listed all major business areas using these wireless sensor networks [2]. The analysis concluded that their use was mainly related to the field of transport (traffic regulation, communication between vehicles, public transport logistics, signaling of free parking spaces, etc.), the meteorological field (volcano monitoring, weather forecasts, etc.), the field of health (implanted sensors, remote monitoring, home help, etc.) or even the field of predictive maintenance (monitoring of structures in civil engineering, machinery in an industrial environment or more broadly components under stress in all environments to plan their future maintenance). The wide variety of fields concerned suggests an increase in the number of these wireless sensor networks in the upcoming years.

The issue of providing reliable and sustainable electrical energy to all of these wireless sensor networks remains an essential challenge. The most common solution used so far to make these systems energy self-sufficient is to embed a primary lithium battery with the sensor (i.e., non-rechargeable)[3]. Those conventional batteries, connected to a large number of sensors have shown several limitations that can be summarized:

- **Short life span** due to their self-discharge over time [4]. From studies performed by Gutierrez et al. [5] the calculated autonomy for an $8cm^3$ battery is approximately three years which remains relatively low compared to the lifespan of wireless sensors. These sensors will therefore require several interventions to change their empty battery and sometimes to check the state of charge of the battery, which might be impossible according to the reachability (*e.g.*, Tire Pressure Monitoring System, remote location and so on).
- **Maintenance costs:** let's consider the case of the management board of a fleet for instance containing several hundred rotating machines each equipped with several wireless sensors for which a battery change is necessary every three years, it represents a significant workload and cost, which may increase the overall running cost of the system.
- **Compactness:** most of the time battery takes up considerable volume space of the wireless sensor. A study conducted by Paradiso and Starner [6] suggests that this congestion tends to worsen in the upcoming years.
- **Temperature:** generally, in moderate to high-temperature environments efficiency and self-discharge of the battery degrades. The upper use limit of primary lithium batteries varies from 60°C for Li-MnO_2 batteries (80% of the market for primary lithium batteries) to 85°C for Li-(CF)x batteries [7].

To address these four issues generated by the use of on-board batteries, the research is currently focused on ambient energy scavenging, leading to the concept of "Energy Harvesting [8]." Through energy harvesting, there is a direct and continuous way to recover the energy in the close environment of the sensors, hence suppressing the necessity to embed a large quantity of energy and therefore dispensing the use of batteries. The sensors thus gain independence and can be forgotten for their entire

lifespan. One important parameter to take into consideration when designing an energy harvester is the conversion medium, *i.e.*, the material. The next section will present the smart materials and their application to vibration energy harvesting.

1.3 Smart Materials Vibration-Based Energy Harvesting Systems

1.3.1 Smart Materials Classification

Smart materials are also known as advanced materials, intelligent materials, or adaptive materials. A standard definition cannot be given to smart materials [9], [10], [11]. For instance, NASA described them as materials that can remember various forms and can react with particular applied stimuli. They are also considered highly engineered materials that can react smartly with their environment [12], [13]. They modify their physical property such as rigidity or viscosity in function of an external stimulus such as mechanical stress, electric or magnetic field, or a temperature change [14]. Smart materials are classified based on their properties; we therefore consider two sets[15]:

1.3.1.1 Passive and Active Materials

Passive smart materials have the property to transfer specific energy types or lack the inherent capability to convert energy from one form to another. Optical fibers can transfer electromagnetic waves

Active smart materials are classified into two subsets.

- **A Class of materials that cannot change their shape, but properties are changed when exposed to external stimuli**

For this case, we may consider photo chromatic glasses: they only change their color when exposed to sunshine.

- **The other category of materials can change their shape or can convert one form of energy (thermal, electrical, chemical, mechanical) into another**

For this category, we can cite piezoelectric materials which can produce an electric charge when submitted to external strain of force.

Smart materials possess some properties that differentiate them from other types of materials, among which[12], [13], [16], [17], [18]:

- **Transiency:** they can respond to many types of stimuli;
- **Responsiveness:** Most smart materials have relatively low response time;
- **Self-actuation (intelligence):** The response can be a change in form/shape or appearance modification depending on the type of externally applied stimuli;
- **Selectivity:** the response is distinct and predictable;
- **Proximity:** Both the source of the stimuli and the smart material are placed at the same location.

1.3.1.2 Classification of Smart Materials based on their response

Depending on their responses to environmental or external excitations, smart materials can be classified into several types, including shape memory alloys (response to temperature and pressure), piezoelectric materials (response to electricity and pressure), electro strictive materials (response to electric field and mechanical solicitation), magnetostrictive materials (response to a magnetic field and /or stress), optical fibers, electrorheological fluid (react with electric field) and magnetorheological fluids (react with magnetic field). Table 1-1 below summarizes the advantages, disadvantages, and some applications of smart materials. Each type of material has different characteristics which are put to best use, depending on the application. Several energy sources are available (solar, thermal, etc.), and mechanical vibrations have many advantages such as large availability and are relatively reliable with wide availability[19].

Magnetostrictive materials provide ways for converting vibrations into electrical energy as they exhibit high allowable stress and superior conversion properties compared to electromagnetic devices[20]. The next section will consist of presenting magnetostrictive materials which is our application case.

1.3.2 Magnetostrictive materials

Magnetostrictive materials (MsM) are those materials that can change their magnetic properties by the application of mechanical excitation and conversely. These materials are used in many applications as actuators (damping…) and sensors. Studies

are being carried out on different materials to optimize them but also to minimize losses in appropriate working conditions. Magnetostrictive materials are a class of smart materials that also convert energy between the magnetic and mechanical states. For this reason, magnetostrictive materials, and devices based on these materials, are often referred to as transducers. Indeed, alloys based on transition metals (iron, nickel, and cobalt) in combination with some rare earth elements are being currently employed in actuation and sensing systems in a broad range of industrial, biomedical, and defense applications. Because magnetostriction is an inherent property of ferromagnetic materials, it does not degrade over time as can be the case with some poled piezoelectric substances. In addition, newer magnetostrictive materials provide strains, forces, energy densities, and coupling coefficients which compete favorably with more established technologies such as those based on piezoelectricity. As evidenced by the ever-increasing number of patented magnetostrictive systems, transducer designers are finding new opportunities to employ magnetostrictive materials in a wide variety of applications ranging from stand-alone transducers to complex smart structure systems[20]. Due to the bidirectional nature of this energy exchange, magnetostrictive materials can be employed both for actuation and sensing and energy harvesting. Some magnetostrictive materials include Terfenol-D ($Tb_xDy_{1-x}Fe_2$), Galfenol, Fe_xGa_{1-x}, and Alfer, Fe_xAl_{1-x}. Another commonly used magnetostrictive composite is the amorphous alloy $Fe_{81}Si_{3.5}B_{13.5}C_2$ with the commercial name Metglas 2605SC. Magnetostrictive materials have many applications amongst which is energy harvesting, more details on the use of magnetostrictive materials in energy harvesting will be given in the next section.

Table 1-1: Advantages, disadvantages, and applications of smart materials[21]

Name of the material	Advantages	Disadvantages	Applications
Piezoelectric	- High frequency response[22] - Generate electrical signal on the application of mechanical force or stress [23] - Structure is simple[24] - No electromagnetic interference [25] - High energy density [25] - Compactness	- Working stroke is limited to several or ten micrometers limits its application as an actuators [23] - Wear and heat generation - Difficult to manufacture	- Used in electronics devices such as transducers and sensors - Used at high temperatures due to their high Curie temperature [24] - Micro positioning - Power gen in auto - Tires pressure sensor - Knock sensor - Fuel injectors
Magnetostrictive	- Higher energy density - Intrinsic robustness [26]	- Magnetostrictive materials increase the complexity of the system [26] - The accuracy of experimental reproduction is not enough [26] - Prone to electromagnetic interference	- Tuned vibration absorber - Damper - Engine mounting - Sensors - Vibration Energy harvester[27]

Name of the material	Advantages	Disadvantages	Applications
Shape memory alloy	- Elastic behavior - High fatigue failure life [28] - High damping capacities - High strength - Corrosion resistant [29]	- Temperature sensitive[29] - High cycle fatigue - Complicated design and high weight [30]	- Biocompatible - Aerospace - Robotics [31] - Clothing and fashion industries
Electro-rheological fluid	- Stable system performance - Simple controller design - Act as power amplifier[32]	- High Density [33] - The fluid becomes thick after prolonged use and needs replacement [32]	- Vibration dampers, Shock absorber - Clutches - Hydraulic valves [32]
Magneto-rheological fluid	- Very low remnant magnetization - Higher permeability - Higher saturation magnetization[34]	- High-quality fluids are expensive - Settling of ferro particles can be problematic	- Vibration absorber - Iron particles deposition - Sealing problems - Environmental contamination [34]
Optical fibers	- Higher bandwidth support - High carrying capacity - Immunity to electromagnetic interference and tapping	- More expansive transmitter and receiver equipment - It cannot carry electrical power to operate terminal devices	- Advanced intrusion detection security systems - Optical chemical sensors and optical biosensors - Used to transmit power using a photovoltaic cell, as light guides in medical and other applications

Name of the material	Advantages	Disadvantages	Applications
	- Flexible optical fiber cables require less space - Resistance to corrosion	- Not suitable at higher optical powers - Installation is costly	- Structural health monitoring, Spectroscopy, Imaging optics

1.3.3 Energy Harvesting

Energy harvesting defines the process by which unused energy source from the surroundings is transformed into useful electrical energy. A complete energy harvesting system includes three main parts: a conversion material (magnetostrictive, magnetocaloric, piezoelectric, thermoelectric, photovoltaic, etc.) [21], a structure (mechanical, thermal, electromagnetic, etc.), and an electrical interface[35], [36]. All energy harvesting systems can be sorted according to the conversion mechanism, corresponding conversion material, and the energy source.

1.3.3.1 Classification of Energy Harvester Based on the Conversion Mechanism

Based on the conversion mechanism, energy harvesters can be roughly divided into piezoelectric, electrostatic induction, magnetostrictive, and electromagnetic [25].

- Electromagnetic energy harvesting device employs the relative motion of a conductor mass in a magnetic field, provided by a permanent magnet. Typically, the mass is wound in a coil to form an inductor. Based on Faraday's Law, an AC voltage is induced by the relative motion between the mass and the pick-up coil.
- The electrostatic energy harvesting relies on the changing capacitance of vibration-dependent varactors, or variable capacitors whose electrodes are moveable to each other and separated by a dielectric to form a capacitor.
- Magnetostriction: MsM has been recently considered in applications of energy harvesting. It utilizes the Villari effect, where the vibration-induced strain of an MsM produces a change in the magnetization of the material. Upon dynamic or cyclic loading, this change in magnetization is converted into electrical energy using a pick-up coil or solenoid surrounding the magnetostrictive layer according to Faraday's law. An in-depth presentation of the principle is done in section 1.3.5.
- At a small scale (millimeters to centimeters), the preferred conversion mechanism remains to date piezoelectricity. It uses the physical properties of piezoelectric materials to change its form due to mechanical vibration and then generates induced charge. More than 200 $mJ \cdot cm^3$ can be expected using piezoelectric material [37], which is larger than any other conversion method. Still, many drawbacks as

presented previously in section 1.3.1.2 can be associated with the piezoelectric solution, including, in the first line, the absence in the market of large-volume production.

1.3.3.2 Classification of Energy Harvester based on the Conversion Materials

The harvester could be classified according to the energy source [38] and corresponding conversion material. Some conversion materials include:

- magnetostrictive alloys for vibrational sources.
- thermoelectric modules for thermal energy [39], [40].
- photovoltaic cells for solar sources [41].

From the conversion material [27] point of view, most of the existing vibrational energy harvesters use piezoelectric, magnetodynamic, or magnetostrictive coupling [42]. Piezoelectric materials are interesting because of their significant voltage output and active nature. On the other hand, magneto dynamic systems show several shortcomings such as low voltage output and predominant resistive losses at low frequencies. Magnetostrictive materials allow addressing such issues due to stress-dependent magnetic characteristics. The solid-state aspect of the magneto-mechanical coupling in magnetostrictive materials also yields more compact devices compared to magneto-dynamic systems, as the latter requires significant dimensional changes to allow the conversion to take place. Most magnetostrictive materials have higher Curie temperatures than piezoelectric materials henceforth they can operate in harder environments[43].

1.3.3.3 Classification of Harvesters based on Energy Sources

All the energy sources produced from the earth cannot be used to generate autonomous power for wireless sensor networks. There are several energy harvesting sources present in the atmosphere[38]. Amongst typically available energy sources we have solar (using photovoltaic materials [44], [45]), thermal (using thermoelectric materials [46]), wind and vibrational (piezoelectric [47] or magnetic/magnetostrictive materials [48], [49], [50]). Solar energy can be directly converted to electrical energy via the photovoltaic effect. Solar energy is inconsistent due to its dependence on weather,

location, and time of day. Mechanical vibrations have many advantages, such as availability despite difficult climate conditions, or energy levels that are compatible with the requirements of autonomous sensors [51], [52].

Temperature difference, or thermal gradient, can generate electrical energy via the thermoelectric effect[8]. Hi-Z Technology developed a commercial prototype of a thermoelectric energy harvester and achieved a power density of 0.29 W/cm^2 from a 200°C temperature difference [53]. One drawback of the device is the proportional degradation of its output power with the temperature difference, as well as thermal Interfacing due to the thermal conductivity of conventional thermoelectric modules.

Another energy source is electromagnetic waves. Radiofrequency (RF) radiation specifically, has been investigated as a possible power source for wireless sensor networks and other low-consumption devices. A typical RF energy harvester is made of an antenna, an impedance-matching circuit, and a voltage rectifier[54]. The available power output from RF energy harvesters is generally a few microwatts and the performance of these devices is highly affected by the (squared) distance from the source. When the distance between the harvester and the RF source increases, the performance drops quadratically[55].

Basagni et al. [56] performed a comparison between the various potential energy sources to supply wireless sensors, the summary is made in Table 1-2 below.

Let's consider a Li-ion battery [57], with an initial capacity of 1000mAh, a voltage of 3.7V, a maximum operating temperature of 85°C, and dimensions 5.2 x 3.3 x 0.5 cm. For a 2-year operating time, without taking into consideration the auto discharge, its average power density is 24.6 $\mu W.cm^{-3}$.

From Table 1-2 we can see that the maximum power density that can harnessed from the other sources is higher than the power density of a Lithium battery. A piezoelectric linear oscillator (mass of 10 g, mechanical damping of 0.10 $N.m^{-1}$, resonance frequency of 160 Hz) placed on a vibration source (acceleration of 10 $m.s^{-2}$ and frequency of 160 Hz) gives a maximum power density seven times greater than that of a battery (respectively 125$\mu W.cm^{-3}$ and 18 $\mu W.cm^{-3}$). This aspect suggests that energy harvesting will improve the compactness of wireless sensors. The second observation is the

maximum operating temperature of the generators associated with all these sources; all the generators can work at higher temperatures compared to a primary lithium battery. Based on the observations presented in this section, a vibration energy harvester is a good candidate for energy harvesting. The next section will present the various vibrations harvesters.

Table 1-2: Comparative study between the various energy sources likely to power isolated wireless sensor networks [56]

Source	Condition	Power density	Efficiency of generators	Harvested Power	Maximum temperature
Solar	Solar	1.5mW.cm^{-2}	5-30%	0,8-4,5 mW.cm^{-2}	Reduction of the efficiency of 4,5% for each +10˚C[d]
	Sky	150µW.cm^{-2}	5-30%	8-45 µW.cm^{-2}	
Thermal	[a]	5.0mW.cm^{-2}	5-30%	5-30 µW.cm^{-2}	600˚C
Vibrations	[b]	200µW.cm^{-3}	10-50%	5-150 µW.cm^{-2}	Piezo 150˚C[e] Electromag 230˚C[f]
Wind	[c]	380µW.cm^{-3}	~5%	~20 µW.cm^{-3}	230˚C[f]

[a] ΔT = 5˚C

[b] Linear Harvester: A = 10 m.s^{-2}, m = 10 g, $\mu_{méca}$ = 0.10 N.m−1.s−1, f_0 = 160 Hz,

$P_{récup\ max}=A^2m^2/8\mu_{méca}$

[c] Wind speed 5 m.s^{-1}

[d] Greater than the normal operating temperature which is 25˚C

[e] Irreversible polarization loss

[f] Irreversible magnetization loss

1.3.4 Vibrational Energy Harvesters

This section reviews the various strategies and prototypes developed in the scientific literature related to the harvesting of vibrational energy. Generators for vibration energy harvesting devices can be divided into two broad distinct categories illustrated in Figure 1-1(a) and (b).

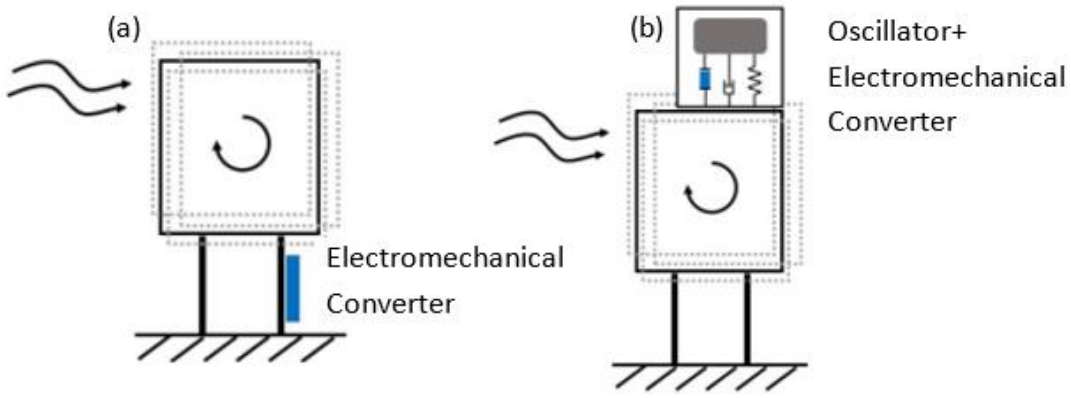

Figure 1-1: The two main principles of vibration energy Harvester. We consider a rotating machine as vibration source and under internal or external stresses [58].

1.3.4.1 Direct Deformation Generator

As illustrated in Figure 1-1(a), direct deformation generators are made of an electromechanical converter (generally piezoelectric), located directly on the path of mechanical stress generated by the vibrations. Thus, they are submitted to the real deformations of the host structure on which they are located. Figure 1-2 shows two examples of direct deformation generator prototypes. These generators offer the advantage of not depending on the operating point of the source (amplitude and frequency) unlike inertial generators. Their efficiency is therefore not affected by a source whose characteristics (frequency, …) vary over time (which is always more or less the case in real conditions).

A drawback of this particular technology is the mechanical coupling i.e., we need many anchor points to faithfully transmit the deformation to the piezo element and maintenance in case of failure.

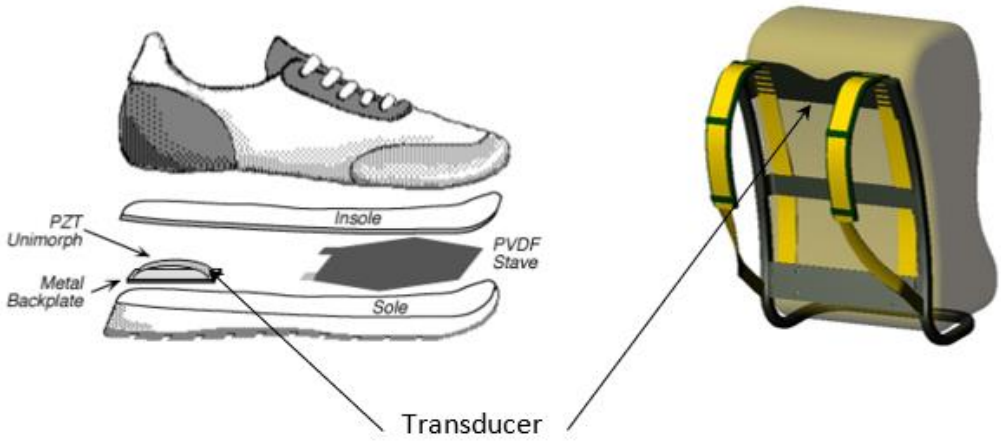

Figure 1-2:Illustration of some direct deformation generators. From left to right:[59],[60]

1.3.4.2 Linear Inertial generators

Inertial generators are devices that generate electrical energy from their inertial motion and have only one mechanical connection with their surroundings. Linear inertial generators are made using a linear mechanical oscillator made of mass-spring (the return force *F* imposed by the spring on the mass is proportional to the deformation *x* of the spring: $F = -kx$). The most common system based on this type of generator is the embedded cantilever-free beam. Figure 1-3 shows their operating principle, and two prototype examples are shown. The most used electromechanical converters for this type of generator are illustrated in the block diagram of Figure 1-3 (electromagnetic converter and piezoelectric converter). This makes them suitable power sources for embedded systems operating in environments that experience some inertial excitation.

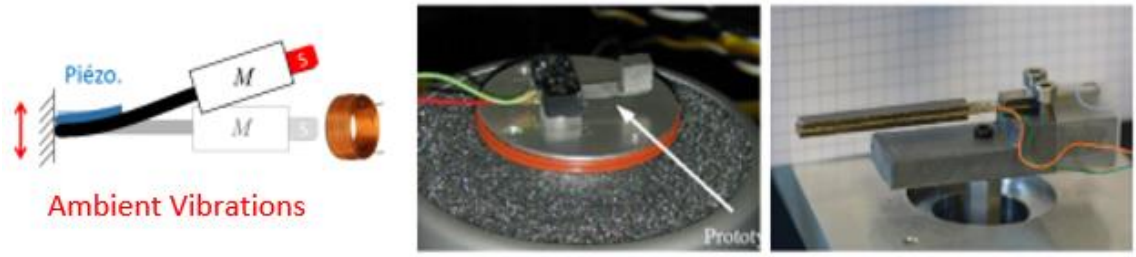

Figure 1-3: Operating principle and examples of linear inertial generators. The electromechanical converter is generally piezoelectric or electromagnetic. From left to right:[61], [62].

For an inertial generator, the maximum average power is highly dependent on the mechanical damping coefficient which is highly dependent on the mass. So, to optimize the generator we need to embark the largest possible mass and adjust its resonant frequency to the resonant frequency of the vibration source. The difficulty with such systems is that the source of vibrations is never purely sinusoidal and its preponderant frequency is never permanently fixed, making their environmental integration difficult. Several solutions like multimodal inertial generators (generators in series with each generator corresponding to a particular frequency) or adequate design of the interface circuit between the linear generator and the load can be considered to address this aspect.

In previously exposed devices, piezoelectric materials are mainly used, but they possess many drawbacks amongst which their fragility. To overcome this, we decided to use magnetostrictive materials. In the next section, we are going to throw more light on the magnetostriction process and its application in vibration energy harvesters.

1.3.5 Magnetostriction and Application to Vibration Energy Harvesting

Historically, magnetostrictive materials were initially exploited based on their ability to change shape under external magnetic fields [63]. Magnetostrictive energy harvesting devices utilize the Villari effect (inverse effect) to convert strain into magnetic energy [64]. By definition, the Pseudo Villari effect (also known as magneto-elastic coupling or inverse magnetostrictive coupling [64], [65],[66]) is the magneto-mechanical coupling corresponding to a change of magnetic flux density due to mechanical stress [64]. In magnetostrictive devices, parameters (*e.g.,* permeability) are changed, so in this situation, we have instead the pseudo-Villari effect.

Magnetostriction is a material property that causes material deformation when subjected to an external magnetic field [67], [68], [69], [70], [71]. It is linked to the presence of magnetic domains (which will be developed in section 1.4.3.1) in the microstructure of the material that is also sensitive to the applied mechanical stress[72].

Magnetostriction is associated with two magnetization mechanisms[72]:

The domain wall motions;

The rotation of the magnetic moments within domains toward the field direction.

Ferromagnetism and magnetostriction are two related phenomena that are often observed within the same material. Ferromagnetism refers to the tendency of certain materials to become permanently magnetized when exposed to a magnetic field. It arises from atomic magnetic moments of electronic origin becoming ordered into small regions known as magnetic domains. Each magnetic domain typically comprises 10^{12} to 10^{18} magnetic moments aligned in the same direction and orientation. At the domain boundaries, known as domain walls, a change in the direction of the atomic magnetic moment progressively takes place over several hundred atoms (the exact number depends on wall energy consideration) [73].

The effect of magnetostriction and inverse magnetostriction could be mostly explained, as a first approximation, by the change of orientation of magnetic moments due to external stimulus. Ferromagnetic materials exhibit both reciprocal features. The magneto-mechanical coupling can be described, for instance, by the Stoner–Wohlfarth approximation, where the magnetostrictive material is assumed to be a collection of non-interacting magnetic domains [8] (Figure 1-4). Each magnetic domain exhibits a uniform local magnetization *Ms*. The bulk magnetization is a weighted sum of local responses, which are determined by stress and field-dependent domain orientations. As shown in Figure 1-4(a), in the initial state all the domains are assumed to be randomly distributed yielding a null magnetization. An application of an external bias magnetic field (Figure 1-4(b)) first leads to a rotation of magnetic moments following the magnetic force, inducing an increase in the length of the sample. When a tensile stress is superimposed (Figure 1-4 (c)) along the same direction, the sample gets elongated, and the magnetic moments continue rotating. This external tensile stress is imposed through mechanical excitation. The magnetic flux in the specimen then varies with the rotation of the magnetic moment.

The magnetostrictive energy conversion principle is presented in Figure 1-4 below. When applying a biased external magnetic field, the element converts electrical energy from mechanical vibration or tensile stress via magneto-mechanical coupling. The magneto-mechanical effect is the change of magnetization of a magnetic material resulting from applying stress and an external magnetic field [74]. Coupling such a

change in the magnetic properties with the electromagnetic effect (e.g., the Lenz effect through a coil) allows energy to be available in the electrical domain. In most cases, in magnetostrictive vibration energy harvesters, the bias magnetic field is usually generated by permanent magnets; the mechanical stress is either applied directly by the vibration source or indirectly by vibration-induced inertia forces.

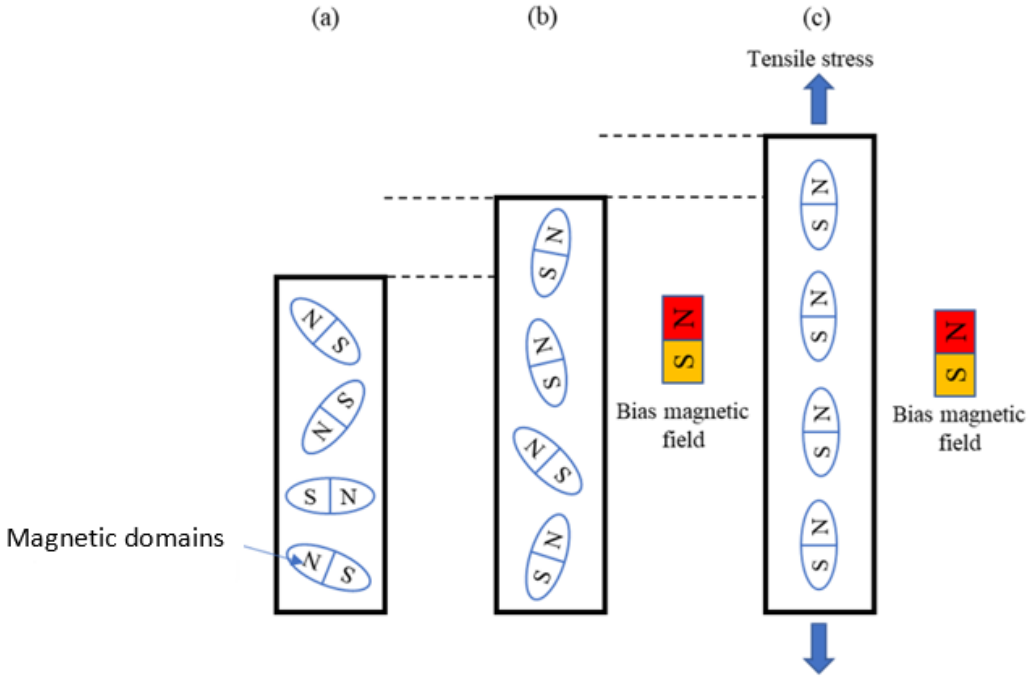

Figure 1-4: Behavior of magnetic domains in magnetostrictive materials under tensile stress.

The magnetostrictive energy conversion principle is depicted in Figure 1-5. When applying an external vibration, the active material converts electrical energy from mechanical vibration change or tensile stress via magneto-mechanical coupling. More precisely, a wrapped coil acting as an electrical generator converts the change in magnetic quantities associated with the magnetic and mechanical stimuli into electrical output through the Faraday law. As we can see, the conversion process depends on the flux variations at the level of materials; hence magnetostrictive energy harvester can be classified based on this criterion.

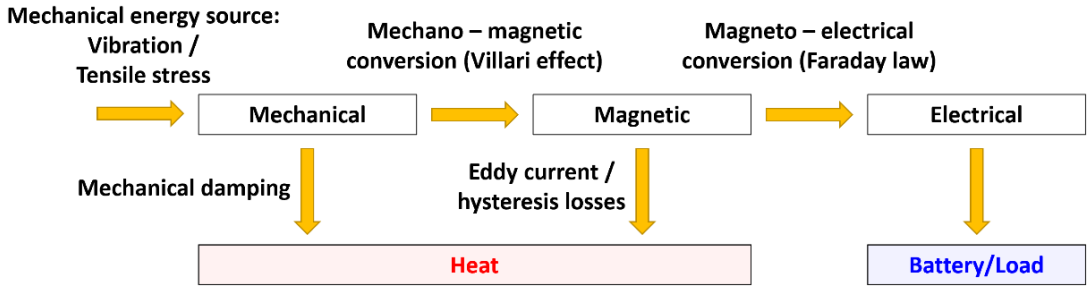

Figure 1-5: Illustration of the energy distribution in a magnetostrictive conversion system.

1.3.5.1 Classification of Magnetostrictive Energy Harvester

Based on material magnetic flux variation at the level of the material, the conversion process in a magnetostrictive energy harvesting system can be done in 2 ways:

- by geometrically-induced reluctance change in the magnetic circuit [75], [76] : The method can be achieved by geometrical adjustment, for instance by varying the distance between the magnetostrictive material and the magnet (with an airgap). This solution can be realized by including an air gap to the magnetic circuit, yielding a loss of integrability; the role of magnetostriction may be secondary compared to the geometry change effect in this case.
- by the direct magnetostrictive effect (Villari effect) [77]. Two main parameters are taken into consideration: the biasing magnetic field and the pre-stress. Those parameters should be optimized according to the material's nature for maximal use of the Villari effect [78], [79], [80]. All ferromagnetic materials react in the presence or when placed near a permanent magnet, that is the magnetism. This will be the object of the next section.

1.4 Basics of Magnetism

1.4.1 Magnetic Field and Origin

Magnetism is a phenomenon that originates from the movement of electrons in the atom, and its effects will be visible even on a macroscopic scale - for example through permanent magnets. The magnetic behavior of a material can be explained by studying it at several scales. Materials can be classified based on their magnetic

behavior. The response of a material when subjected to an external magnetic field is the root of magnetism. Let's consider two current-carrying conductors that are running in parallel. The wires tend to attract one another if the current flowing through both of them is in the same direction, while the phenomena of repulsion are seen if the current is flowing in the opposite direction [81]. The magnetic force is the force that causes attraction or repulsion. The magnetic field determines the magnetic force that acts on such moving charges. The magnetic field is the most fundamental component of magnetism.

Though all materials are affected in some way by a magnetic field, their interaction with a magnetic field differs from one another. This interaction dependents certain factors, such as the atomic and molecular structure of the material and the net magnetic field associated with the atoms.

Nonmagnetic materials are typically made of diamagnetic and paramagnetic as introduced by Paul Langevin in 1905, whereas materials referred to as magnetic are classified as ferromagnetic. This classification of magnetic materials is based on their response to a magnetic field and on their bulk magnetic susceptibility. Nonmagnetic elements such as copper, silver, and aluminum, refer to diamagnetic and paramagnetic materials whose magnetic response to an applied field shows weak, negative, and small positive magnetic susceptibility, respectively.

Other material types experiencing magnetism are antiferromagnetic and ferrimagnetic. Antiferromagnetic are similar to paramagnetic in the sense that their magnetic dipole moments are antiparallel to each other so that in both cases the overall magnetization is zero. Unlike antiferromagnetic, the magnetic microstructure of ferrimagnetic materials allows for a net overall magnetic moment. Thus, ferrimagnetic are equally referred to as magnetic materials. Ferromagnetic materials such as iron, nickel, and cobalt, extensively used as raw materials for engineering components and structures, exhibit a strong attraction to magnetic fields and can retain their magnetic properties after the external field has been removed. The magnetic field sensitivity of these materials lies in the long-range ordering phenomenon at the atomic level which causes a very high degree of alignment of atomic magnetic moments from unpaired electrons to the crystallographic axes. This leads to the formation of regions of magnetic

alignments called domains, which will be discussed in section 1.4.3.1. Figure 1-6 illustrates the orientation of the dipole moments within the various classes of magnetic materials. Nevertheless, ferromagnetic properties are sensitive to many environmental factors like temperature and mechanical stress (residual or applied stress). These effects may lead to misalignment of the atomic magnetic moments and hence, reduce or in the worst-case scenario, nullify the magnetic properties of the material which becomes paramagnetic with subsequent impact on the material integrity.

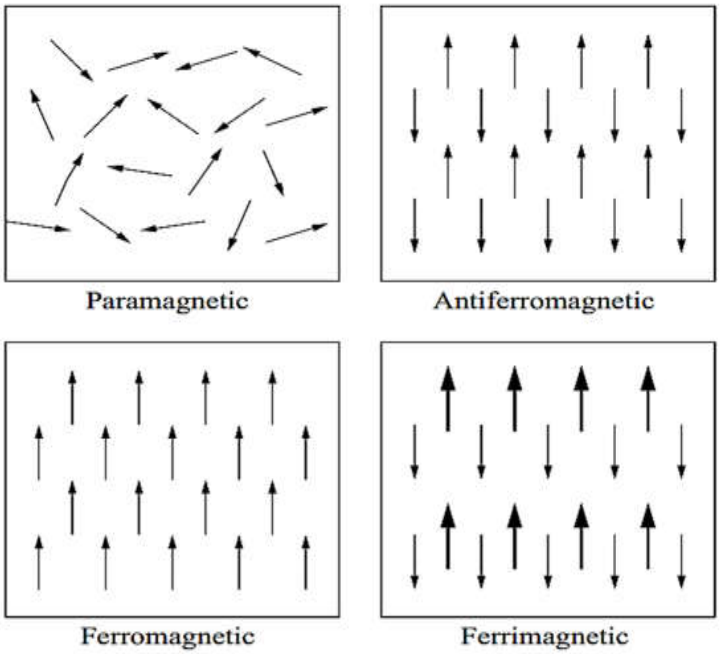

Figure 1-6: Orientation of the magnetic dipoles in different magnetic materials [82]

The patterns of the magnetic fields produced by various sources vary, and they are briefly illustrated in the following section.

1.4.2 Magnetic Field Pattern

The field surrounding a solenoid and a single current loop is comparable to that of a bar magnet, where the field emanates from one end of the magnet (North pole) and travels through the air on its way back to the other end (South pole) [81].

Figure 1-7 below shows a few of the magnetic field patterns produced by various sources.

1.4.3 Ferromagnetic Behavior

1.4.3.1 Domain Theory

The magnetic microstructure of ferromagnetic materials is made of small macroscopic regions called magnetic domains, that are spontaneously or intrinsically magnetized as a result of magnetic moments being parallel aligned to each other[13]. Each domain has a permanent or remanent magnetization. When no external magnetic field is applied, the moments of various domains have random orientation. This is an effect of the existence of magneto-static energy and the magneto-crystalline structure of the material which hinders the global moment of the material to be at saturation.

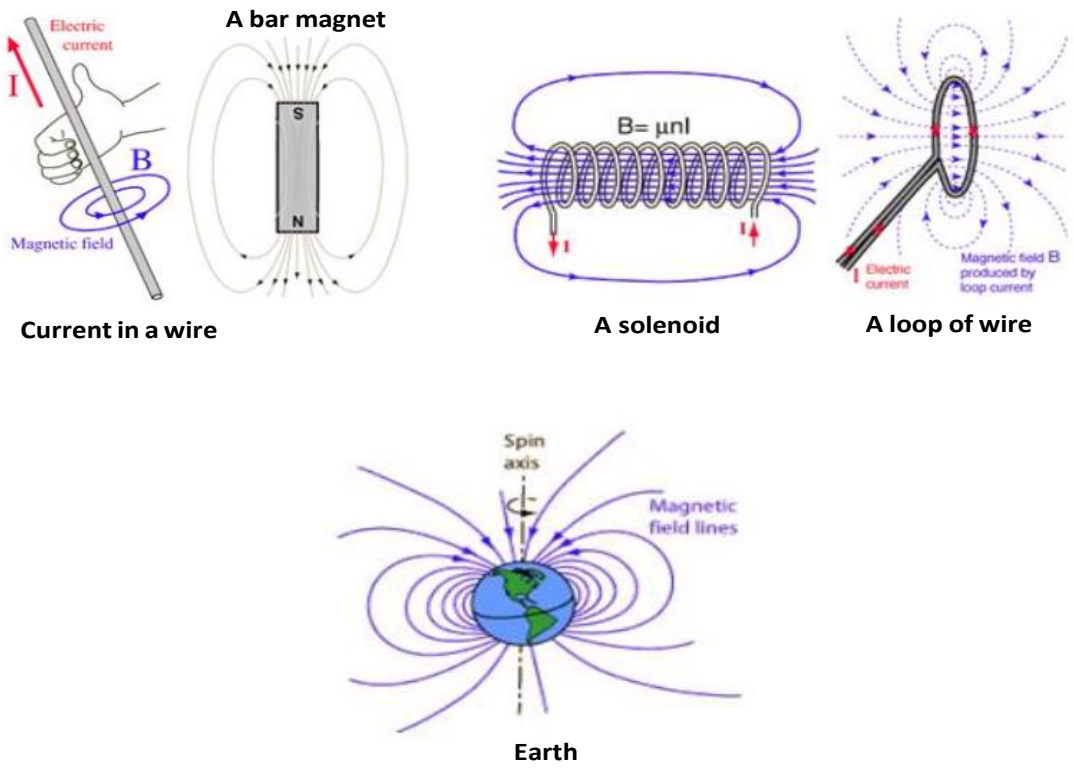

Figure 1-7: Magnetic field pattern[81]

The magneto-crystalline energy favors magnetic moments of each domain to be aligned in its direction of easy magnetization with respect to the structure of materials. Furthermore, magnetic interaction between moments gives way to the creation of magnetic poles (negative and positive poles) within the material: this is referred to as magneto-static interaction. These two different interactions are at the origin of the formation of the Weiss domain and Bloch walls as shown in Figure 1-8.

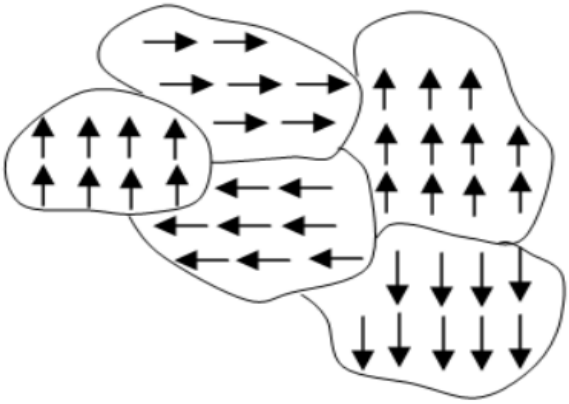

Figure 1-8:Magnetic moments and domains in the ferromagnetic materials at the atomic level

Domain's boundary, i.e., interfaces or junctions between regions where magnetization directions are different are known as domain walls. A Bloch wall is a narrow transition area at the boundary between the magnetic domains, over which the magnetization changes (value/orientation) from the two neighboring domains.

The spontaneous magnetization *M* within a domain of n_m magnetic moments may be expressed as the sum of magnetic moments *m* per volume of the domain v_d:

$$M = \frac{n_m \,.\, m}{v_d} \qquad (1\text{-}1)$$

Therefore, the total magnitude of the magnetism within a ferromagnetic material is the vector sum of the magnetization of the domains.

The degree of atomic magnetic moment alignment decreases as ferromagnetic materials are heated due to the atoms' thermal agitation. The Curie temperature is the point at which the material becomes paramagnetic due to extreme thermal agitation [82].

When an external magnetic field is applied, that complementary energy boost will drive magnetic moments to have the same direction as the external field at the expense of the other domains: that is what is mainly observed in the process of magnetization. Not all magnetic moments will line up at once; the magnetic moments that have a small drift from the direction of the external field will be more inclined to line up first. The remaining domains, with a larger degree of drift, will require more

energy to align their orientation as shown in Figure 1-9. Figure 1-10 shows how a domain transitions from one orientation to the other smoothly rather than abruptly[83].

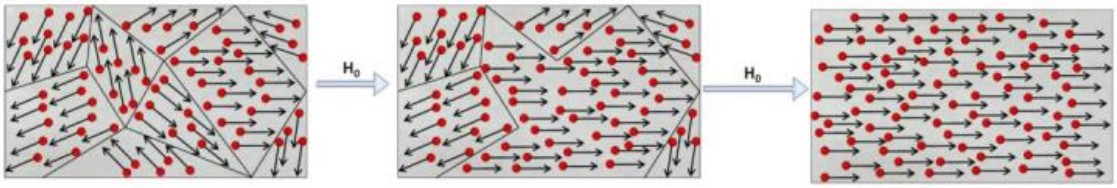

(a) No magnetic field (b) Low magnetic field (c) High magnetic field

Figure 1-9: Change process of domain size and rotation of spontaneous magnetization with increasing applied external magnetic field [84]

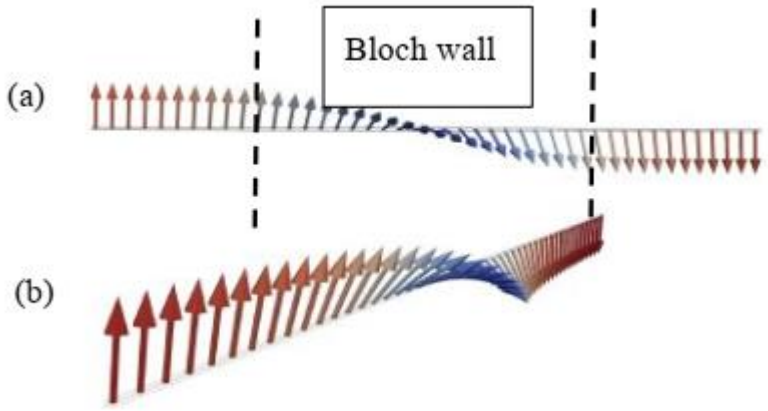

Figure 1-10:Magnetic domain transition at Bloch wall[85] (a) side view on a Bloch wall (b) detailed view

Based on the magnetic scale, a material can be subdivided into three different levels namely: macroscopic, microscopic (magnetic domain), and atomic. At the microscopic scale of the material, the magnetic microstructure is made of magnetic domains and domain walls whereas the mechanical microstructure is composed of grains and grain boundaries. Due to the strong interaction between the two microstructures, the effects on them can be perceived at the macroscopic scale by performing magnetic measurements. The interdependence of mechanical and magnetic properties is called the magneto-mechanical coupling and will be later described in this work (chapter 3).

From what has been previously explained, the magnetic domains are an underlying meaning to many phenomena of the magnetization process within a sample.

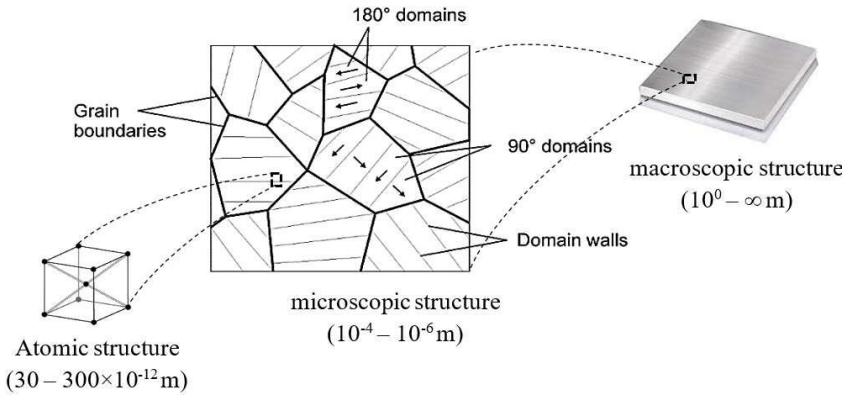

Figure 1-11: Material scales from a magnetic point of view[86]

1.4.3.2 Magnetization Process

Ferromagnetic materials exhibit very strong attraction to the applied external magnetic field, the permeability μ is positive and rather substantial for them. These materials also have unpaired electrons, which produce the net magnetic moment, much like paramagnetic materials do. The application of an external magnetic field has two effects on the material:

- **Motion of domain walls** characterized by an increase of domain size with favorably orientated magnetization vectors ;
- **Rotation of the magnetization vectors in the applied field direction**: the domain walls will remain fixed, but the magnetic dipole moments will rotate to gradually align with the external magnetic field if the latter is strong enough. The domains return spontaneously to their initial orientation if the magnetic field is removed, so the magnetization rotation is considered a reversible phenomenon. This effect explains the ferromagnetic material magnetization process.

The interaction of domains and domain walls during the process of magnetization determines the hysteresis (which is non-linear) behavior of the ferromagnetic materials. A proper description of this nonlinear phenomenon is done in the following section.

1.4.4 Theory of Ferromagnetic Hysteresis and the Anhysteretic Magnetization

1.4.4.1 Hysteresis Loop

The hysteresis loop is a characteristic feature of ferromagnetic materials. Depicted in Figure 1-12, it shows the historical dependent nature of ferromagnetic materials from the magnetization process. Once the material has been driven to saturation flux density B_s, the magnetic field can then be reduced until zero. The alignment of magnetic domains is disrupted but a considerable level of magnetization is still retained in the material. This is referred to as remnant magnetization (remnant flux density or retentivity defined by B_r) and indicates the level of residual magnetism in the material when no field is applied. To completely bring the magnetization in the material to zero, a certain reverse magnetic field value called the coercivity H_c, must be applied. This is the reserve magnetic force required to flip enough Bloch walls to restore the demagnetized state of the domain structure ($B_r = 0$). The loop that is traced out is called the major hysteresis loop at magnetic saturation.

Generally, magnetic hysteresis arises as a result of an increase in the energy lost during the magnetization process caused by energy barriers, due to magneto-crystalline anisotropy, and material imperfections, whether in the form of dislocations or impurity elements. Application of an external field turns to dislodge the magnetic moments from their direction to abide by the crystallographic equivalent axes which are closer to the field direction and hence, of lower energy. The energy required to rotate the spin system (or magnetic moments) of a domain away from the easy direction is just the energy required to overcome the spin-orbit coupling. Hence, the hysteresis effect depends on how freely the Bloch walls can move.

The hysteresis cycle is usually used to classify ferromagnetic materials. Magnetic materials are grouped into two types, soft and hard, depending on the nature of magnetic behavior i.e., magnetic field strength needed to align the magnetic moments of domains constituting the material.

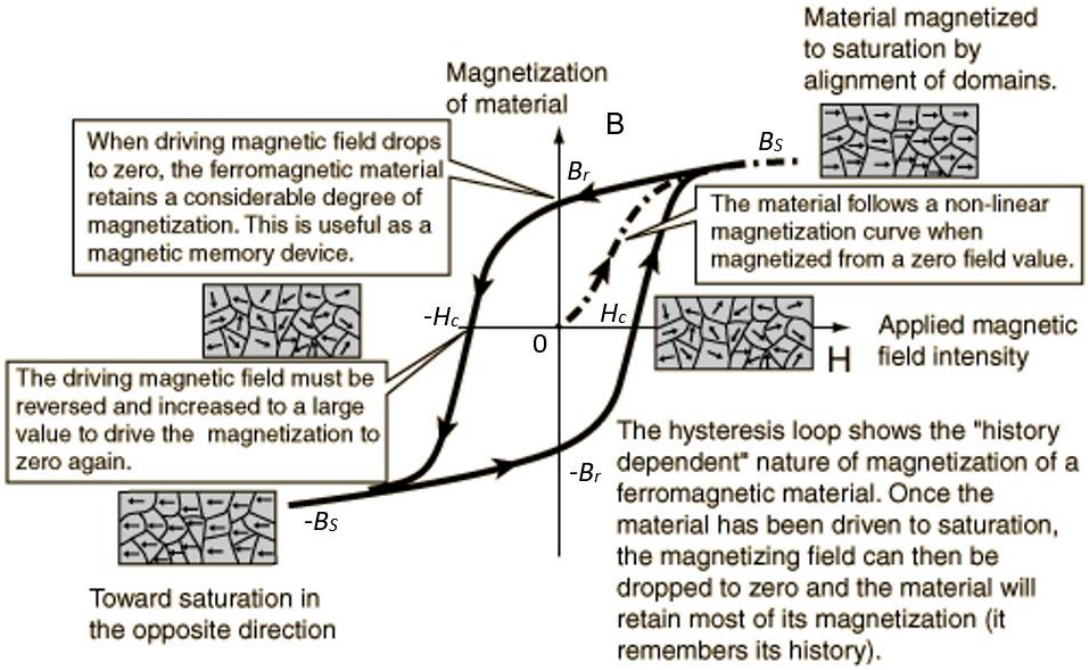

Figure 1-12: Standard Hysteresis Curve and orientation of magnetic dipoles for each phase [87]

A small coercivity characterizes soft magnetic materials like electrical steel, whereas a high coercivity describes hard magnetic materials chosen for permanent magnets. Figure 1-13 illustrates the hysteresis curve of both hard and soft ferromagnetic material.

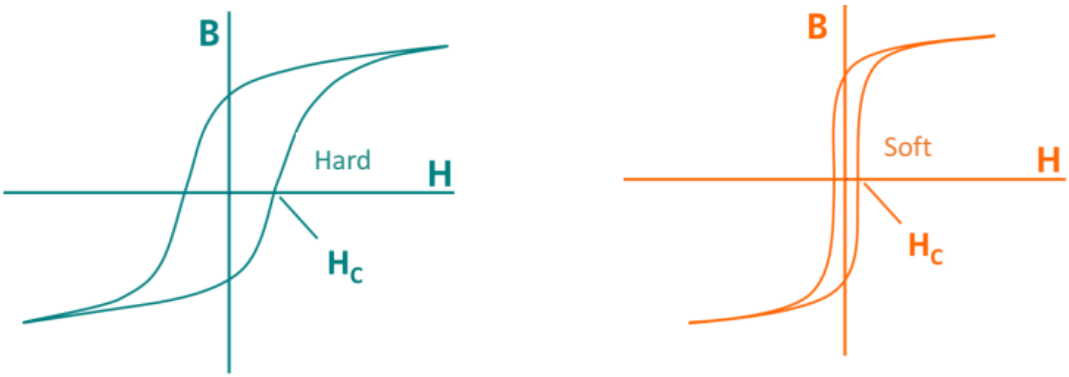

Figure 1-13: Typical Hysteresis curves for Hard as well as soft magnetic materials[88]

Analysis of ferromagnetic materials properties is done using several means. Among them we have hysteresis and anhysteretic magnetization; these are going to be presented in the following section.

1.4.4.2 Anhysteretic Behavior

Given that the hysteresis loop takes its origin from the presence of lattice imperfections acting as pinning sites impeding the domain wall motion, it is worth noting that in the absence of all these imperfections, the ferromagnetic material would be hysteresis-free. In such a situation, the resulting magnetization process only relates to the reversible stochastic motion of Bloch walls. Figure 1-14 shows this type of magnetic behavior illustrated by the anhysteretic curve. The slope of the curve at the origin representing the maximum differential permeability μ_{an} is an important characteristic of the material.

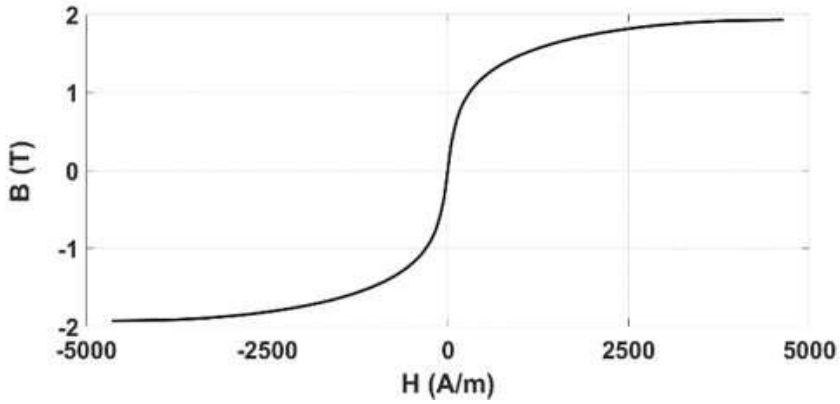

Figure 1-14: A typical anhysteretic magnetization curve of a ferromagnetic material

It constitutes the "ideal" magnetization curve of the ferromagnetic material when no defects or other deficiencies that hinder the magnetization and demagnetization process are present[89].

1.4.5 Magnetic Permeability

The physical property of a magnetic material is known as magnetic permeability (μ); it indicates how a material responds to an externally applied magnetic field and quantifies how magnetically conductive a material is [90]. Another definition of magnetic permeability is the constant in the relationship between the variation of the magnetic induction (ΔB) and the variation of magnetic field strength (ΔH). The number of field lines that flow through a material has a direct correlation with its magnetic permeability. The number of magnetic lines of force that flow through a material

increases with its magnetic permeability. Henry per meter is the unit of the magnetic permeability.

Magnetic permeability is the main factor defining whether the material is magnetized in the direction of the applied magnetic field or the opposite direction. A material's magnetic permeability may not be a constant value but is instead affected by several parameters, including the humidity content of the medium, the medium being utilized, the temperature, the strength, and the direction of the applied magnetic field. As a result, rather than using an absolute value, magnetic permeability is typically expressed in terms of relative permeability.

Depending on their magnetic permeability, materials can be classified as diamagnetic, paramagnetic, or ferromagnetic. Diamagnetic materials resist the applied magnetic field and produce repulsion as a result. Materials that support the imposed magnetic field, on the other hand, and as a result produce an attraction force, are those that are paramagnetic. While in the manufacturing stages or working, the state of the material has to be assessed to ensure proper functioning, which will be mainly presented in the next section.

1.5 Ferromagnetic Materials Characterization and Control Techniques

In this section, we are going to focus only on magnetic-based measurement techniques, and mechanical internal stress estimation techniques have been discussed.

Magnetic methods are part of Non-Destructive Testing and Evaluation techniques of a ferromagnetic material. It is the process of examining and investigating materials for any discontinuities, fractures, or defects that compromise the integrity of the material or structure without compromising its serviceability. As a result, after the test, the material can still be used. Non-destructive testing is mostly used in the fields of fabrication, manufacturing, and in-situ inspections to control the manufacturing process by verifying the integrity of the product/materials.

A comparative analysis made by Modal Shop in [91] has led our choice towards eddy current testing since it uses eddy current which is one of the main properties that

can be easily assessed based on our application (energy harvesting) and has a low processing cost. Eddy Current Testing (ECT) is user-friendly and training an operator for the manipulation of these sensors won't necessarily need a huge cost. Thus, a cost-effective method of technology.

1.5.1 Eddy Current Testing (ECT)

The basic setup for ECT is shown in Figure 1-15 below. According to Faraday's law of electromagnetic induction, an alternating magnetic field is induced in and around a conductor (material 1) or a copper wire anytime an alternating current is applied to it [92]. If another electrically conductive material (material 2) is placed near this alternating magnetic field, currents are also induced in material 2. These currents are referred to as eddy currents because they move in a circular pattern.

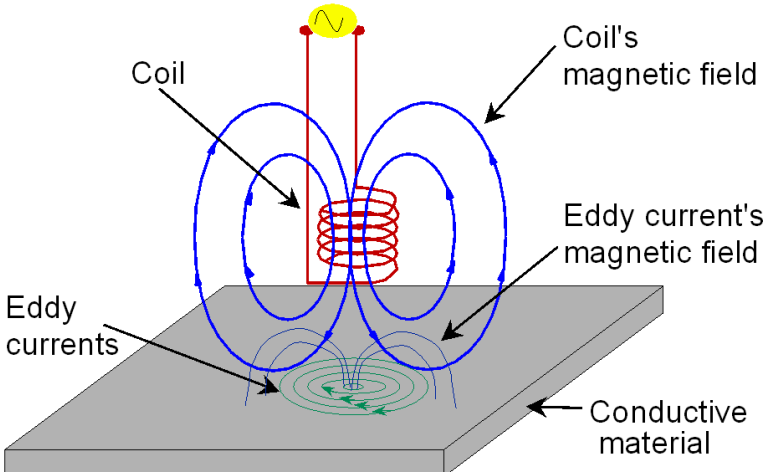

Figure 1-15: Principle Set-up of Eddy Current Testing[93]

A pick-up coil can be used to monitor the path of eddy currents (change in impedance) in the case the material's physical structure has a fault.

Eddy's current testing is widely used in industry to identify flaws and perform material health analysis. Typically, ECT is used to inspect a smaller material zone, and the probes are made specifically depending on the material being tested (in terms of geometry, shapes, etc.). Frequency is crucial since Eddy currents are produced by alternating currents and alternating magnetic fields this then induces the concept of Skin depth. The skin depth, δ, is known as the depth at which the current density is about 37% of the area. The skin depth is associated with the frequency of the current and the

electrical/magnetic properties of the conductor. As a result, the Eddy currents testing method can focus exclusively on a material's surface, making it useful to find local surface and near-surface flaws and therefore can be considered as a micromagnetic NDT technique.

ECT is suitable for all electrically conductive materials, unlike the other micro-magnetic NDT techniques, which are limited to ferromagnetic materials. In the case of ferromagnetic materials, however, measurements and results analysis are more difficult since, in addition to conductivity, permeability change also affects the results. Eddy currents have many uses, one of which is determining the material's thickness. This application is very helpful in identifying corrosion/pitting damage that might result in material thinning. ECT, which is very informative, is used to characterize the tube walls used in assemblies like heat exchangers and to measure the corrosion thinning on aviation parts. The thickness of paints and other coatings can also be measured via eddy current testing. Many sensors can be used to perform the Eddy current testing among which are the search coil, local search coil, and magnetic needle probe; the search coil will be the interest point in the following section.

1.5.2 Encircling or Searching Coil

Encircling coil probes operation is based on the electromagnetic induction principle and they are most of the time made up of a few turns of copper wire wound around a ferrite core or around the sample material to be tested as seen in Figure 1-16a. They possess the advantage of being very cheap and accessible to all.

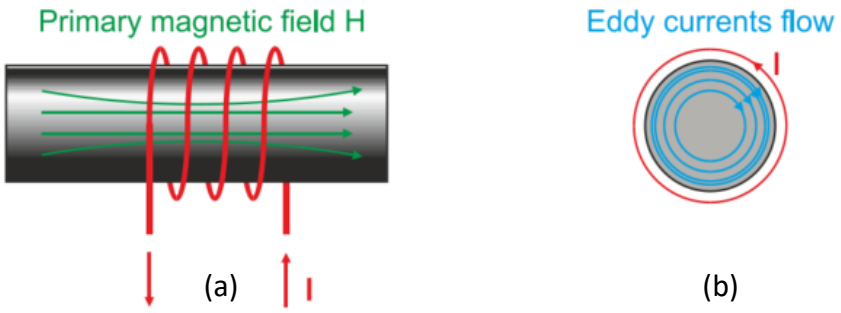

Figure 1-16:(a) Searching coil for a ferrite bar inspection. (b) Eddy currents flow in the measuring system[94]

Eddy currents describe radial circumferences in an opposite direction of currents around the energized coil current, as shown in Figure 1-16b. The time-varying nature of the electromotive force (emf) makes this sensor unable to operate in a constant magnetic field[95].

The response of encircling coils is highly affected by the presence of any parallel discontinuities to the axis of the tube or bar. The precision is enhanced as the number of turns of the coils increases.

The sensitivity *S* of the sensor is expressed by:

$$S = \frac{v}{B} = \frac{N.2\pi f.B.A}{B} \quad (1\text{-}2)$$

Where *N* is the number of turns, *f* is the operating frequency.

The sensitivity depends on the frequency. It is detrimental to work at a relatively low frequency; even though it is at a low frequency that we have a high depth of penetration. This dilemma can be overcome by increasing the number of turns and the diameter of the coils.

Magnetic behaviors of ferromagnetic materials can be influenced by several factors, either internal to the material or external. The internal parameter includes temperature, MIS (Mechanical Internal Stress), etc.… MIS can be one of the sources of unwanted behaviors in magnetostrictive materials, so we need appropriate techniques to assess it. Those techniques will be presented in the next section.

1.5.3 Mechanical Internal Stress Estimation Techniques

1.5.3.1 Mechanical Internal Stress

Residual stresses are those stresses remaining in a material or body after some manufacturing processes in the absence of external forces or thermal gradients [36]. It can also refer to self-equilibrated internal stresses upon plastic deformation in materials [96]. In general, all-in material anomalies expressed as defects may be sufficiently large to cause local yielding and inhomogeneous plastic strains or internal stresses in a structure either at the macroscopic, microscopic, or sub-microscopic levels.

Internal stresses are generally classified based on:

- Their origin [97]
- The scale over which they self-equilibrate [98]
- Their effects on material behavior [99].

We can have three types of internal stress [86]:

❖ **Macro residual stresses.**

They are residual stresses at the macroscopic scale of the material lattice regardless of its microstructure. Macro residual stresses commonly come from the non-uniform plastic flow of mechanical processes such a: peening, bending, rolling, steep thermal gradients, and phase transformations. Generally, material characterization under these residual stress's cuts across several grains in the material and several magnetic domains and domain walls as well. Thus, accessible by most NDT methods.

❖ **Intergranular micro residual stresses**

There are stresses whose impact is perceived at the grain scale due to local crystalline anisotropy.

❖ **Atomic micro residual stresses**

These are short-range micro residual stresses felt at the atomic scale of the material lattice. Yet, no magnetic NDT method is to date capable of experimentally investigating such intrinsic residual stresses in materials.

Most of the time the internal stress within the material is a combination of the three types. Its evaluation requires consideration of the past processing stages in manufacturing and subsequently evolution during life in-service. Thus, the historical difficulties are associated with its measurement and prediction. Several techniques exist to characterize the present state of internal stress within a material, amongst them destructive techniques.

1.5.3.2 Destructive Techniques of Internal Stress Evaluation

All the estimation technologies used so far in MIS are indirect. The first step is a combination of measured physical quantity and then followed by a calculation stage [100]. Destructive techniques have 2 main methods, mechanical and chemical [100].

❖ **Mechanical methods include :**

- The hole-drilling method [101] (see Figure 1-17 for illustration),
- The contour method [102]
- The crack compliance method [103],
- The stripping method [100]

Figure 1-17: Illustration of internal stress evaluation by destructive hole-drilling tests (courtesy of CETIM, Senlis, France).

1.5.3.3 Non-Destructive Techniques of Internal Stress Evaluation

Non-destructive Testing (NDT) methods have also been broadly depicted in [104], [105], [106]. For situations where applications include conductive and/or ferromagnetic parts, the suggested technique is electromagnetic. A current research trend of alternative and/or self-made magnetic sensors for magnetic NDT measurements is perceptible in the literature [107], [108]. Eddy currents testing [109], magneto-acoustic emission [110], [111], electromagnetic acoustic transducer [112], and Magnetic Barkhausen Noise (MBN) [113], [114], [115] are the most popular methods, either alone or combined [116].

Materials such as conventional carbon steels (including mild steel), low alloy steels, and tool steels are all compatible with ferromagnetic and magnetic control techniques. These control methods offer benefits like fast response, low cost, small size, and easy maintenance. Drawbacks reside in their currently reduced industrial developments and their low efficiency. Very few of them have crossed the bridge between academia and industry levels. Based on the principle of MBN measurements, the Stresstech controller (Jyväskylä, Finland) is among them. A significant problem for this device comes from the quasi-impossibility of distinguishing the effect of MIS from other dependent properties (dislocations, grain size, texture, plastic strain, precipitates, phase changes, impurities, etc.).

The micromagnetic, multi-parametric, microstructure and stress analysis (3MA) developed by IZFP Fraunhofer institute (Saarbrücken, Germany) is a promising alternative. 3MA accumulates and combines data from different hysteresis cycles and identifies the ultimate magnetic combination of indicators to a given targeted microstructure property (hardness, internal stress, yield strength, etc.) [117]. Figure 1-18 illustrates the standard 3MA sensor. It consists of a magnetization unit (yoke core with magnetization coil) to generate an alternating magnetic field for the sample under test, a Hall probe for measuring the time signal of the tangential magnetic field component, a coil for detecting the magnetic Barkhausen noise, probe system for detecting the eddy current and the incremental permeability and a preamplifier [118]. 3MA setup is a set of four micromagnetic NDT methods: Magnetic Barkhausen Noise, Eddy Current Analysis, Magnetic Incremental Permeability, and Harmonic Analysis of the tangential component of the magnetic field strength.

3MA is pragmatic and efficient but needs time-consuming experimental campaigns and provides non-transposable results.

It is essential to understand that all magnetic MIS controllers are designed on the same principles, that is, they use a powerful electromagnet applying a unidirectional magnetization coupled with surface sensors which allow the magnetic responses to be observed and recorded. Nevertheless, there are numerous factors impacting the measurement, including primarily the magnetic sensor design parameters [119].

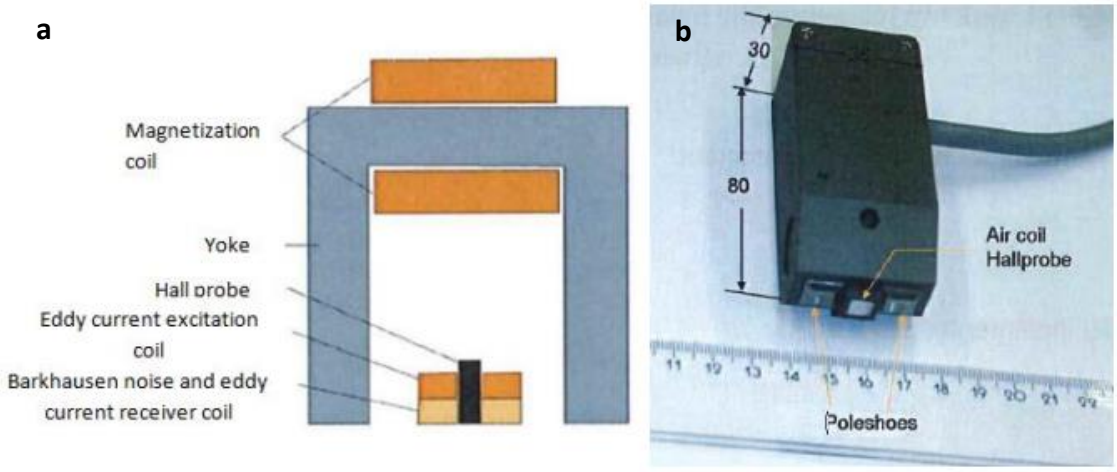

Figure 1-18: 3MA probe: a – Sensor components b- standard 3MA probe with curved pole shoes and spring mounted sensor[120]

Pickup coils stand out among existing sensors as the most popular for magnetic NDT measurement. Research trends in magnetic NDT measurements are evident in the literature in the form of alternative and/or self-made magnetic sensors [107], [108]. Despite their attractiveness in terms of reproducibility and stability, these innovations fail to accurately demonstrate the magnetic sensor's directional selectivity when applied to angular-dependent measurements. Figure 14 of [114] however shows, despite being simulation predictions on FeCo alloys, that effects of stress on the magnetic answer can be more visible when the magnetic excitation and the stress direction are not in the same direction and that the directional sensor would probably bring improvement in the stress observation.

Just a few methods among those described previously can give information on the material's state taking into consideration the direction. Point probes [121], [122], and MBN are some of them [123] but are not tested in this study.

1.6 Problem Statement

As stated previously in section 1.2, the issue of providing a fixed and reliable energy source for wireless sensors remains a problem. So far, the recovery of energy by magnetostrictive elements has been relatively little studied. Understanding the intrinsic mechanisms linked to the application aspect (energy harvesting, etc.) from a global point of view, from the material to the electrical aspect via the mechanical structure has rarely

been considered. In this thesis, we wish to focus in particular on the multiaxial coupling aspect within the material itself and its improvement. We want to develop a characterization device capable of properly informing modeling tools and testing the selected materials to determine the optimum waveforms and operating points in terms of energy efficiency.

The problem of the behavior of magnetostrictive materials concerns two points:

1- The first point is the exact effect of the application of mechanical excitation (stress for our case) on magnetic behavior. Mechanical properties are modified together with a change in magnetic flux in the right direction yielding a much larger electromechanical energy conversion leading to an increase in magnetic losses and a reduction of efficiency. Coupled with this effect, we have a highly nonlinear response of magnetostrictive materials: most studies consider the magnetostrictive material operating up to the intermediary range of magnetic excitation (linear behavior). This consideration strongly limits the application potentials and assessment of the performance of the associated energy harvester.

2- The second point is magnetostriction effects with respect to the material: Iron-Cobalt ferromagnetic alloys are highly promoted for electrical energy conversion in several applications where there is a need for high-power density, but their high magnetostrictive coefficients may result in undesired behaviors such as acoustic noise. Internal stresses which are one of the sources of that noise, can be tuned to limit magnetostriction. Internal stress is also the root cause of various flatness defects of some magnetostrictive plates [124]. However, that evaluation process must be adequately assessed in a non-destructive way for further applications of the material. So, we need a way to reduce the effect of these major concerns. The first step consists of characterizing the material itself to better predict and model the magneto-elastic behavior of electrical equipment.

In that way, we set some objectives and methods to achieve them. These will be presented in the following section.

1.7 Objectives and Methods of The Thesis

In the context of providing a reliable and sustainable energy for supplying remote sensors or wireless connected devices, this thesis aim of is to develop an energy harvesting device capable to replace existing batteries. One of the main components of an energy harvesting device is the conversion material. Following the observation made in (1) and that the most commonly related literature on energy conversion materials for use in magnetostrictive energy harvesters has been mostly focused on highly magnetostrictive materials such as Terfenol and Galfenol. For the purpose of our research work, we will focus on samples of Permendur (Fe_{49}-Co_{49}-V_2) magnetostrictive laminated sheets. Currently available review articles focus more on assessing the overall performance of the magnetostrictive energy harvesting system without exploring the potential energy conversion performance at a material level. In that line we decided to firstly characterize the Permendur.

Preliminary experimental test of Permendur under tensile stress from 0-480 MPa will be performed. A physical model will be developed to estimate the anhysteretic magnetization curves through a fitting process. For energy harvesting assessment 3 approximations were done. Firstly, theoretical thermodynamic Ericsson cycles from modelled anhysteretic cure were used to evaluate the output energy. Considering that previous estimation doesn't considered hysteresis loops a second estimation is proposed considering major loops. Then experimental Ericsson energy cycles will be measured to prove the feasibility of the conversion process and validate Permendur as a relevant material for energy conversion applications. After the validation of the principle for energy harvesting, we proceed the practical step of the energy harvesting based on the same principle as result of the modelling performed at this step, the optimum the theoretical maximum power that can be harvested is not dependent on the mechanical structure, and is only dependent on the stress, magnetic field variations at the optimal frequency and the properties of the magnetostrictive material itself. Magnetostrictive materials performance are affected by the material texture or composition [1], magnetic field strength and orientation [1], geometrical factors and Stress. Since the effect of the stress of the material doesn't depends on the origin

internal stress were replaced by homogeneous external stress, we then proposed a direction sensor for stress level indication.

1.8 Thesis Outline

This work reports on the magneto-mechanical characterization of Permendur laminated magnetostrictive sheets and their applications to energy harvesting. The document will be divided into 5 chapters.

Chapter One introduces the context of the study, the basics of magnetism and its concepts as well as the problem statement. A presentation of smart materials-based energy harvesting, materials characterization, and control techniques is provided. The objectives of this research work and presentation of the thesis outline conclude the chapter.

Chapter two provides a brief review of MIP used as a mechanical stress estimation technique, and then describes the experimental conditions, including sensors and tested specimens, for the validation of the experimental process for further use. We then describe the experimental process used in the tests and preliminary magnetic characterization results. Finally, we will provide an analysis, discussion, conclusion, and future scope on the proposed directional MIP sensor.

Chapter three presents the electromechanical energy conversion models. Afterward, the experimental magnetic characterization and simulation of Permendur sheets under tensile stress are conducted. Based on these experimental measurements, a simulation method of the anhysteretic behavior is proposed and validated and then used to assess the potential energy conversion under tensile stress and magnetic excitation. Then, another estimation of the converted energy density is described taking into account the hysteresis losses. Finally, experimental Ericsson energy cycles are measured to prove the feasibility of the conversion process and validate Permendur as a relevant material for energy conversion applications.

Chapter four briefly presents vibration energy harvesters, then the proposed axial vibration-based energy harvesters. Analysis of the various conversion mechanisms

is performed and improvement technologies of the output voltage are proposed. Necessary comparative analyses are equally presented and discussed.

Chapter Five concludes the research work and areas of potential investigations for further work are given at the end.

1.9 Conclusion

In this chapter, we presented the context of our research which can be summarized as the need for reliable and sustainable energy supply for wireless sensors through the use of ambient and available energy sources. We also presented smart materials and their application in vibration energy harvesting, the class of smart materials we decided to use are magnetostrictive materials. As the energy conversion process matters, we also present the various classifications of energy harvesters, and a special emphasis was laid on magnetostriction as its characteristics such as the " Pseudo Villari effect" in our case are quite profitable in energy harvesting applications. In another section, we presented the generalities of magnetism and ferromagnetic materials characterization and control. Our thesis mainly studies the magneto-mechanical behavior of magnetostrictive materials towards energy production from mechanical vibrations. Energy harvesting systems use smart materials as conversion mediums, but those materials may be subject to stress which may affect the overall performance. The effect of the stress should be properly characterized for the dimensioning of the overall system; more details on the assessment method will be given in the next chapter.

2 CHARACTERIZATION OF TENSILE STRESS-DEPENDENT DIRECTIONAL MAGNETIC INCREMENTAL PERMEABILITY: MECHANICAL INTERNAL STRESS ESTIMATION IN IRON-COBALT MAGNETIC SHEETS

2.1 Introduction

Iron-cobalt (Permendur) alloys are used in several applications because of their high magnetization saturation and high magnetostriction which leads to high-power density gains and, hence, converters with lower volumes. Those materials are also highly used in energy harvesters due to their properties. Tuning Mechanical Internal Stresses (MIS) can be a promising and reliable solution to control high magnetostriction[126]*. Before the tuning process, the internal stress must be properly measured and analyzed. So far, in most harvesting devices the stress and the magnetic excitation are applied within the same direction. Stress effects when applied in different directions with the magnetic field remain to date not studied enough. To this effect, we proposed Directional Magnetic Incremental Permeability (MIP) is proposed as a viable for MIS evaluation.*

This chapter is organized as follows: we first provide a brief literature review of MIP used as a mechanical stress estimation technique (Section 2.2), and then describe the experimental conditions, including sensors and tested specimens for the validation of the experimental process for further use (Section 2.3). Section 2.4 throws more light on the experimental process used in the tests. Section 2.5 will present preliminary magnetic characterization results. Sections 2.6 and 2.7 will provide an analysis and discussion of directional MIP results respectively, while in Section 2.8, the conclusion and future scope of our present study are presented.

2.2 Review of Magnetic Incremental Permeability used as Stress Estimation Techniques

Mechanical internal stress is caused by multiple mechanisms including plastic deformation from industrial machining, temperature gradients, and microstructural changes. Its impact on the magnetic and mechanical performances of ferromagnetic materials cannot be neglected. Magnetic incremental permeability (MIP) provides information on reversible magnetization, which is closely linked to the microstructure of the ferromagnetic material during the entire magnetization and demagnetization process [127]. The microstructure of a ferromagnetic material (magnetic domain, pinning center, etc.) is easily affected by mechanical damage, stress, or strain. These factors justify the use of MIP as a MIS estimation technique. All MIS estimation methods are indirect: they start with the measurement step of a coupled physical quantity and end with the calculation stage [100]. In this section, we present some studies in the literature related to the magnetic incremental permeability used as a stress (as magneto-mechanical coupling manifestations) estimation technique.

Several studies have been conducted to date.

- Kaiyu et al. [125] proposed a non-destructive and fast method to evaluate the yield strength of cold-rolled steel using incremental permeability. Based on the established relationships between Incremental Permeability (IP), eddy-current (EC) impedance, and microstructure, an Incremental Permeability feature based on the prolling direction that indicates the average grain size and lattice friction of materials is presented in this paper. This feature was then used to estimate the yield properly. The feature presented in this paper highly depends on the grain size, which requires a preliminary proper crystallographic analysis and may be a source of error added to computing errors occurring during IP data processing.
- Zeng et al. [128] proposed a transmissive method for non-destructive stress evaluation based on inverse magnetostrictive theory for ferromagnetic materials. The traditional U-shaped sensor was replaced by a quadrupole layout. The authors proposed a method to decrease the power supply instability caused by the change in the air gap by adjusting sensor parameters, such as the sensor

angle, amplitude of the excitation current, and variation of the air gap. The experimental results showed that the transmission quadrupole layout caused the test system to exhibit. A limitation of this system is the shape and size of the sensor, which may be a drawback in industrial applications.

- Mohsen et al. [129] examined the sensitivity of incremental permeability and coercivity when used as magnetic parameters for the correlation method with the tensile strength of DP (dual phase) steel. The results showed that the initial permeability was a slightly more sensitive magnetic parameter (correlation coefficient for the best-fit equation of 0.9693) than the coercivity (correlation coefficient for the best-fit equation of 0.9412) for discriminating and assessing the mechanical properties of DP steels.

All magnetic stress controllers conceived so far are based on principles using unidirectional magnetization (stress and magnetization in the same direction) induced by a powerful electromagnet added to local surface sensors to observe magnetic responses [119]. Many recent research works to seek alternative and/or self-made magnetic sensors for magnetic NDT measurements are present in the literature[107], [108]. With advantages such as sensor reproducibility and stability, these advancements have failed to provide accurate information for applications involving directional/angular–dependent measurements. However, as shown in Figure 14 of [11], numerical predictions of FeCo alloys show that stress effects on the magnetic response can be more visible when the magnetic excitation and the stress direction are from different directions and that a directional sensor would probably bring significant improvement in the stress observation.

In this study, we propose to overcome the directional limitations of previously presented sensors using a miniature U-shaped ferrite magnetic core. The precise control of MIS remains a significant challenge; thus, internal stress has been replaced by externally applied stress. Regardless of the stress origin, the effect on the magnetization process remains the same. The tests were limited to tensile stress, which constitutes the worst-case scenario for the stress observation. As a preliminary step for the validation of the specimens, we performed magnetic characterization of various samples under tensile stress, we are going to talk more about the process in the following section.

2.3 Stress Dependent Magnetic Characterization of Iron-Cobalt

2.3.1 Selection and Preparation of Specimen

Fe_{49}-Co_{49}-V_2, Iron-Cobalt also called Permendur laminations are presented in this section. It has a high yield strength and quasi-isotropic magnetic behavior in the sheet plane under no-stress conditions. It is a soft magnetic steel characterized by its low coercive field H_c (less than 1kA/m) hence, is easy to demagnetize. They are widely used in electric machines or transformers owing to their high magnetic permeability and low hysteresis loss. Iron-cobalt is an alloy of Iron and Cobalt in equal parts, with the addition of other elements such as Vanadium (the composition is 49% Fe, 49% Co, and 2%V) to facilitate its rolling and increase its resistivity, which increases the maximum frequency of use [130]. Its low magneto crystalline anisotropy induces no naturally preferred crystallographic orientation [131], [132], [133].

Three variants were initially characterized: RN, FP6, and FP10. The difference between them lies in their degree of crystallization (RN being completely recrystallized, FP10 being little recrystallized, and FP6 having intermediate states). This recrystallization yields smaller grains for RN than for FP10, which will have an impact on their magnetic and mechanical properties.

The subscript in each notation corresponds to the expected elastic limit. It was 600 MPa for FP6; therefore, for RN, it was different. Iron-cobalt is a material that can be worked in such a way as to minimize its magnetic anisotropy [130], so its magnetic behavior will depend very little on the orientation of the magnetic field. From the same batch, all the tested specimens were extracted. Electrical Discharge Machining (EDM) was used to cut all the strips (Figure 2-1), thus reducing the effects of the residual stress associated with the cutting process. All three samples had the same dimensions. Two specimens from each sample were tested for consistency. The choice of the material was not only based on the coercivity but also on the capacity of the material to withstand to high values of tensile stress and magnetic field without saturation. No matter the materials considered, there will still be the coercivity. The idea is to have the material with high potential. Based on these criteria we decided to consider the material

FP10. The next section presents the experimental setup used to characterize the samples.

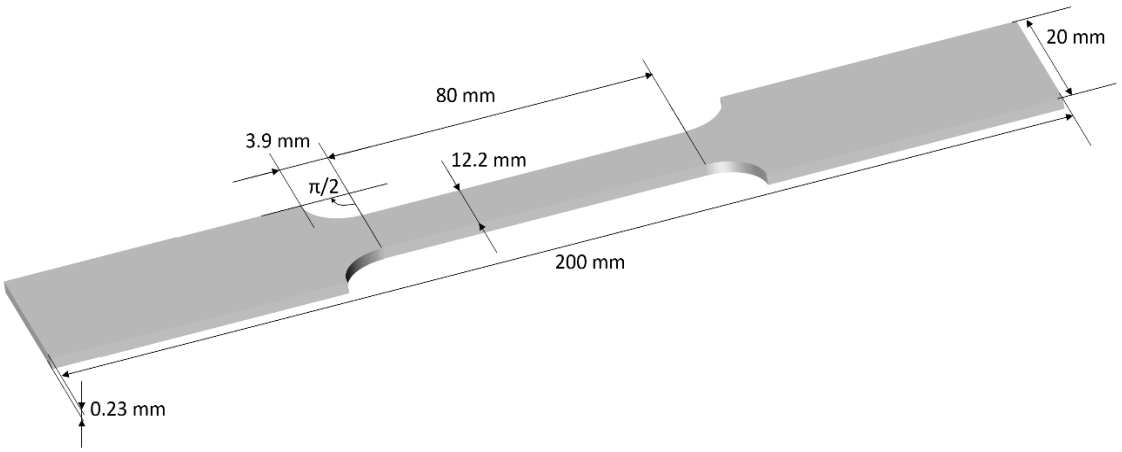

Figure 2-1: Permendur's specimen dimensions

2.3.2 Description of the Experimental Setup

Based on the IEC 60404-3 standard, details are given on the use of a single sheet tester for the magnetic characterization of ferromagnetic lamination sheets [134]. Because of its special geometry, it is impossible to use a tensile stress bench while considering all recommendations. The experimental setup that we developed was inspired by this standard. Figure 2-2 shows sensor pictures and a 2D overview of the test bench.

For tensile stress application, we used a traction-compression machine Shimadzu AGS-X series (Kyoto, Japan)[135]. It can measure stresses up to 10 kN with a resolution of 0.2N and 1 µm. The displacement and force were controlled from a dedicated proprietary software from a PC. The distance between grips was 100 mm. The magnetic field inductor was made of U-shaped electrical steel yokes (Grain-oriented Fe-3%Si). The cross-section of the legs was 12 × 12 mm^2, and the inner distance between the legs was 30 mm. A 500-turn excitation coil is wound around the yoke. A Kepco BOP 100-4 M (New York, USA) current-controlled power amplifier with limits of ±10 A and ±100 V supplied to the coils. We used an RS pro 180 W bench power supply (Corby, UK) for the MIP.

A noise-shielded radiometric linear Hall probe SS94A from Honeywell® (Charlotte, USA) was positioned tangentially to the surface of the tested sample for surface

magnetic field (H_{surf}) measurement. For the calibration of the sensor, we used a Gaussmeter with predefined characteristics. The integrated sensor was selected because of its small dimensions and high-frequency response, and its sensitivity was acceptable for our application. H_{surf} was measured on the left and right sides of the specimen (Figure 2-1), and no difference was observed, confirming the symmetry of magnetic excitation. Data acquisition and analog signal generation were ensured using the DEWESoft X2 (Trbovlje, Slovenia) data acquisition software associated with SIRIUS 8 × CAN data acquisition.

All the tests were performed at room temperature under constant imposed stress conditions without an initial load. Once constant stress was imposed, a minimum of 60s was required before starting the acquisition process to avoid any drift issues.

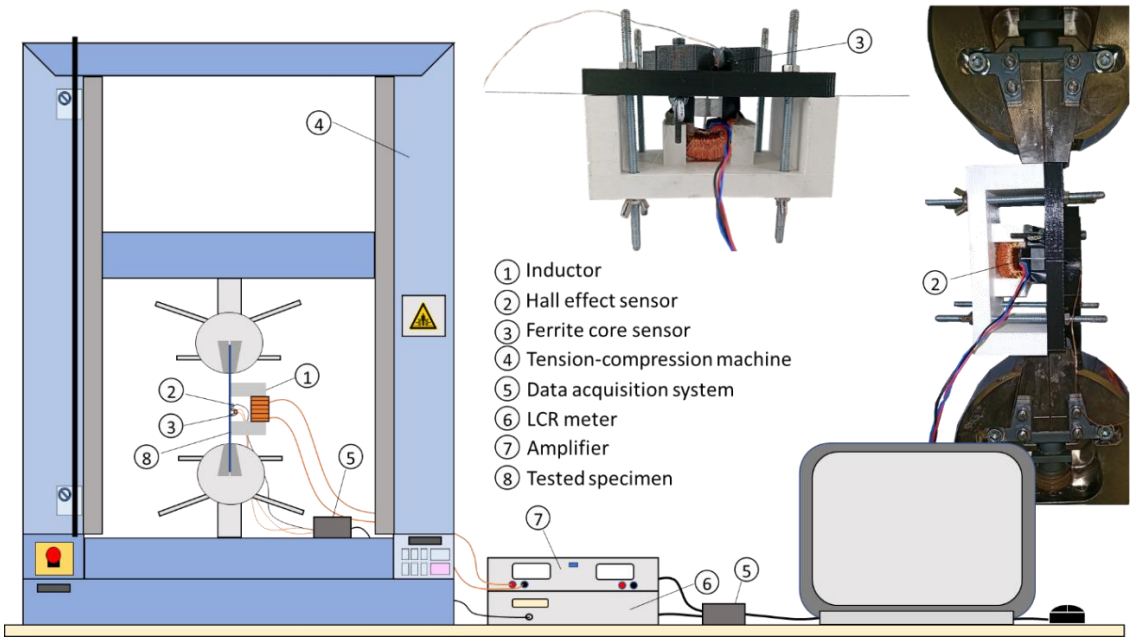

Figure 2-2:2D overview of the experimental setup for magnetic characterization under different tensile stress levels.

2.3.3 Mechanical Excitation

The first step of the experiment involved applying tensile stress to the tested samples. The mechanical constraint was uniform along the active part of the material. Therefore, we can link the stress (denoted *by* σ) to the applied force F and normal surface S of the sample:

$$\sigma = \frac{F}{S} \tag{2-1}$$

The influence of tensile stress on the evolution of $B_a(H_{surf})$ hysteresis loops was evaluated for H_{surf} values of up to 5500 A·m^{-1}. The tensile stress range considered was 0-480 MPa. σ was intentionally set to be lower than 0.5·σ_c (σ_c is the elastic limit) for each of the samples to avoid microplastic strains and maintain the tested specimens in the elastic region. The maximum applied forces are listed in Table 2-1.

Table 2-1: Samples' maximum mechanical tensile stress values

Materials	σ_c(Mpa)	Max (σ)(Mpa)	S(mm2)	F(N)
FeCo RN	370	185	2.5	463
FeCo FP6	600	300	2.5	750
FeCo FP10	1000	500	2.5	1250

The absence of residual strain was confirmed by verifying the reproducibility of the *B(H)* curves after all the tensile tests. Two sensors were used for the magnetic measurements, which are presented in the next section.

2.3.4 Magnetic sensors

Figure 2-3 shows a 3D illustration of the solutions implemented for magnetic characterization. Two sensors were used to evaluate and assess the magnetic state of the tested specimens, as described in Section 2.3.1.

2.3.4.1 Sensor for the Local Magnetic Flux Density B_a

The measurement of the local surface magnetic flux density B_a is based on the encircling coil method, its operating principle has been presented in Section 1.5.2. As shown in Figure 2-3 (a), wound coils were made of n = 50 turns of pick-up coil wrapped around the tested samples to measure the magnetic flux density. B_a is obtained by numerical integration (Eq. (2-2)) of the electromotive force *e(t)* measured by the pick-up coils during the magnetization cycle:

$$B_a(t) = -\frac{1}{n \cdot S}\int_0^t e(t)dt \tag{2-2}$$

Where *S* is the specimen cross-section.

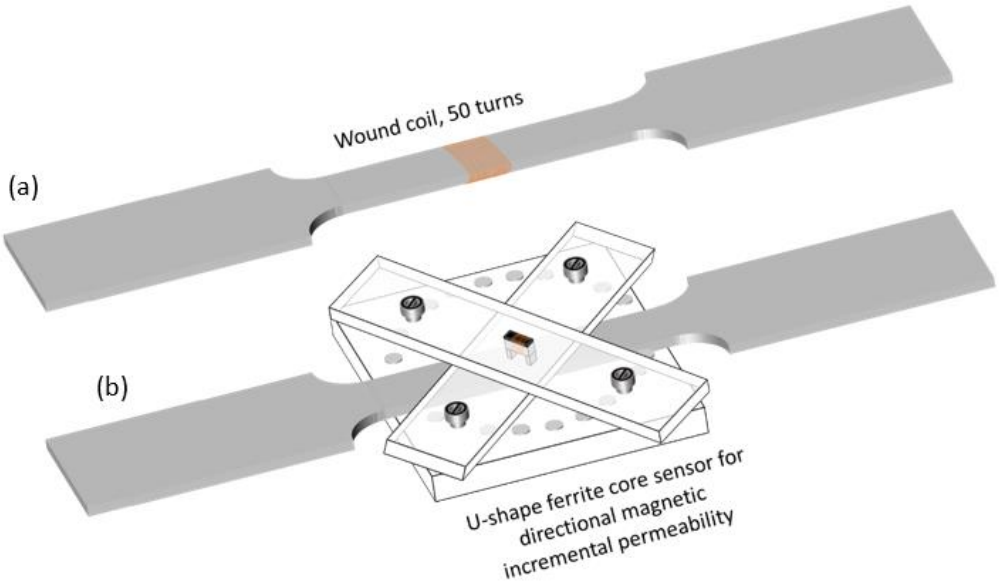

Figure 2-3: 3D illustration of the sensors used (a) magnetic flux density sensor (b) Directional MIP sensor

2.3.4.2 Sensor for the Local Directional MIP

The local magnetization processes are highly dependent on the distribution of the residual stresses, and local micromagnetic characterization is a particularly effective sensing technique for mapping the distribution of these residual stresses. In this way, the second sensor (Figure 2-3 (b)) combines a U-shaped half-toroidal ferrite core (WE-TOF EMI from Würth Elektronik, Künzelsau, Germany) and a 54 turns wound coil. A black PLA polymer 3D-printed specific support (Figure 2-3 and Figure 2-4) was designed and printed using a Flashforge Dreamer (Jinhua, China). The support helps in holding the sensor and authorizing plane measurements at every $\Delta\delta = \pi/18$ rad angle step, and has no magnetic influence on the performed measurements.

A precision Keysight LCR meter (Santa Rosa, CA, USA) was used to record the impedance *Z* of the sensor during the experimental phase. The sensors presented, in the next section will explain the experimental magnetic characterization process.

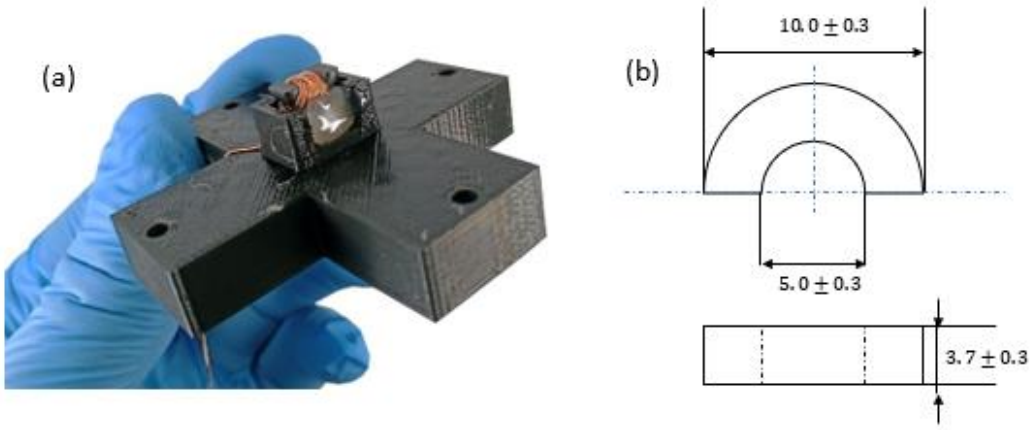

Figure 2-4: (a)Photograph and (b) Dimensions of the directional MIP sensor.

2.4 Magnetic Characterization Experimental Processes

The experimental magnetic characterization campaign was divided into two linked phases.

- Classic Hysteresis Cycles
- Directional Magnetic Incremental Permeability

2.4.1 Classic Hysteresis Cycles

This phase consisted of the evaluation of the tensile stress effect on the classic $B_a(H_{surf})$ hysteresis cycles (where H_{surf} is the tangential surface excitation field). The process is illustrated in Figure 2-5 and can be summarized by the following steps:

- After calibration of the tensile stress bench, the 1st step consists of setting the corresponding force value on the dedicated tensile bench software via a PC.
- The value of the force reached and held until stability, we start the function generator and the amplifier and set the desired value to be sent through the exciting; in our case, it was current imposed.
- The signals of both the magnetic field and flux from the Hall sensor and coil sensor, respectively, in the form of voltage, were acquired on the DAQ Dewesoft and used in the final post-processing step.

The effect of stress on magnetic behavior has been thoroughly described in scientific literature [133]. The objective of this preliminary experiment is to validate the conformity of the specimens. The results are presented in the next section.

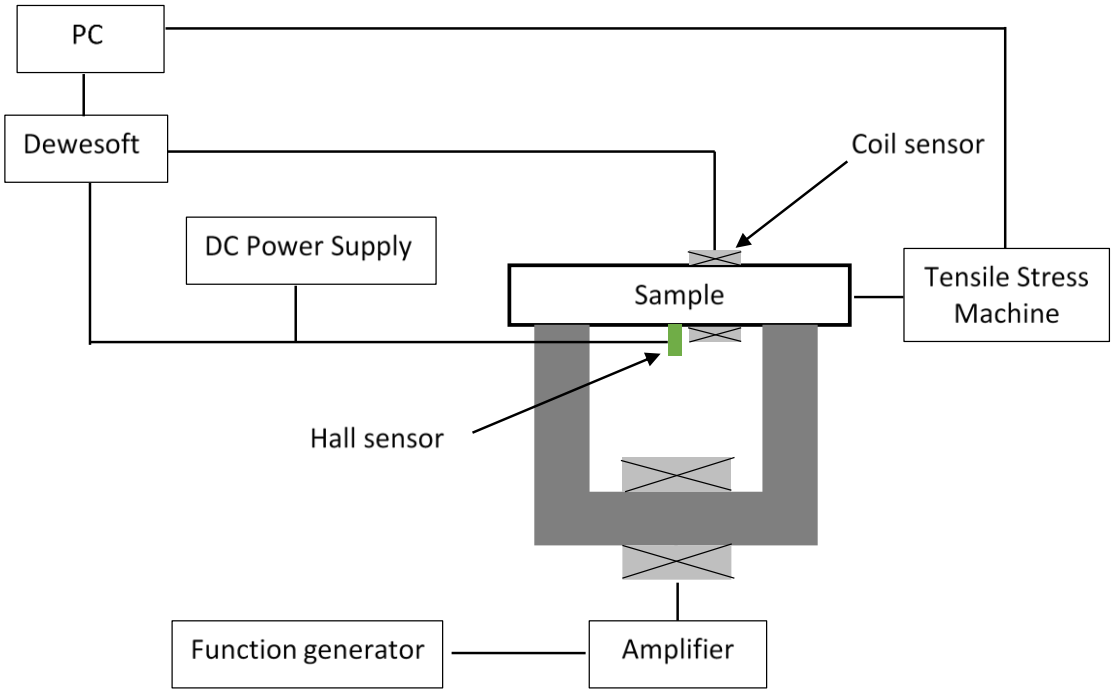

Figure 2-5:Process of the classic $B_a(H_{surf})$ hysteresis cycles

2.4.2 Directional Magnetic Incremental Permeability

A similar tensile stress sequence and process were performed in this second phase of the experiment. The difference in this situation is that the magnetic measurement (magnetic field) was combined with directional magnetic incremental permeability measurements, both still under stress. In this situation, we did not consider the measurement of the magnetic flux. For each stress level, a set of ten $Z(H_{surf})$ curves were plotted (for different values of the angle δ from 0 to $\pi/2$ with a $\Delta\delta = \pi/18$ step). The measurement principle is illustrated in Figure 2-6. The next section presents the results of a preliminary test on the effects of stress on magnetic behavior.

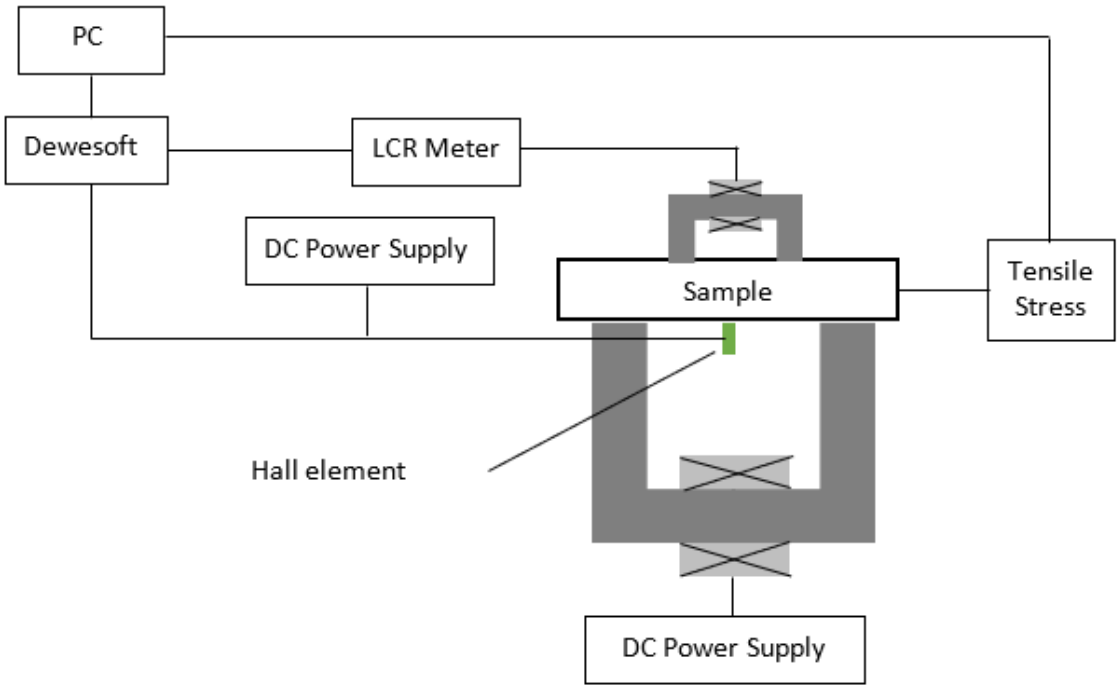

Figure 2-6: Schematic for measuring Incremental Permeability using LCR meter

2.5 Magnetic Characterization Results: Classical *Ba* (H_{surf}) Curves

This section details the various operations performed on the measured data to obtain a correct display of the final curves. The first step is linear drift correction. From Eq.(2-2), the computation of B_a (H_{surf}) involves the integration of the voltage induced across the terminals of the coil. After the integration of induced voltage, the drift correction step was followed by centering the obtained curves across the axis.

Different levels of tensile stress were tested for each sample, and characterizations were performed in the elastic zone of the material. Figure 2-7 shows the hysteresis behavior and the coercive field value of the various samples under tensile stress.

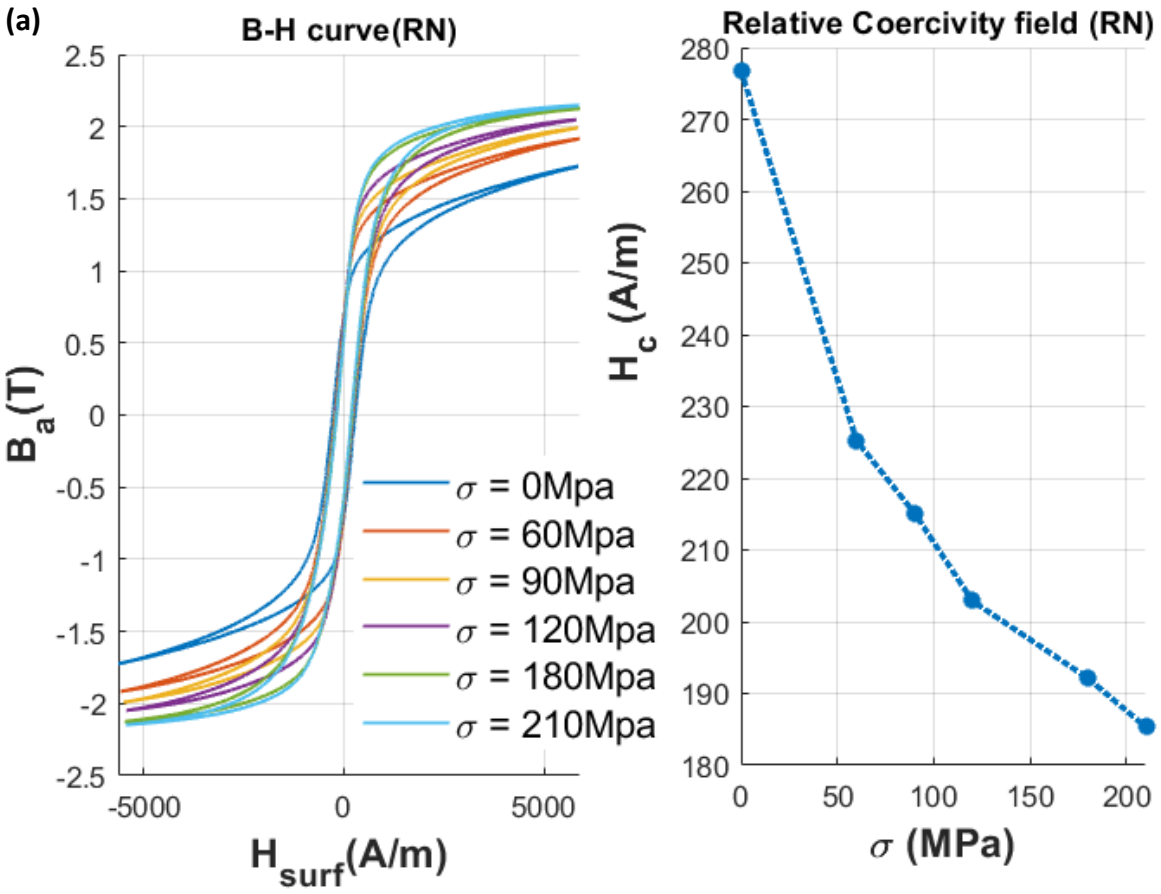
(a)
B-H curve(RN)
B_a(T)
H_surf(A/m)
σ = 0Mpa
σ = 60Mpa
σ = 90Mpa
σ = 120Mpa
σ = 180Mpa
σ = 210Mpa
Relative Coercivity field (RN)
H_c (A/m)
σ (MPa)

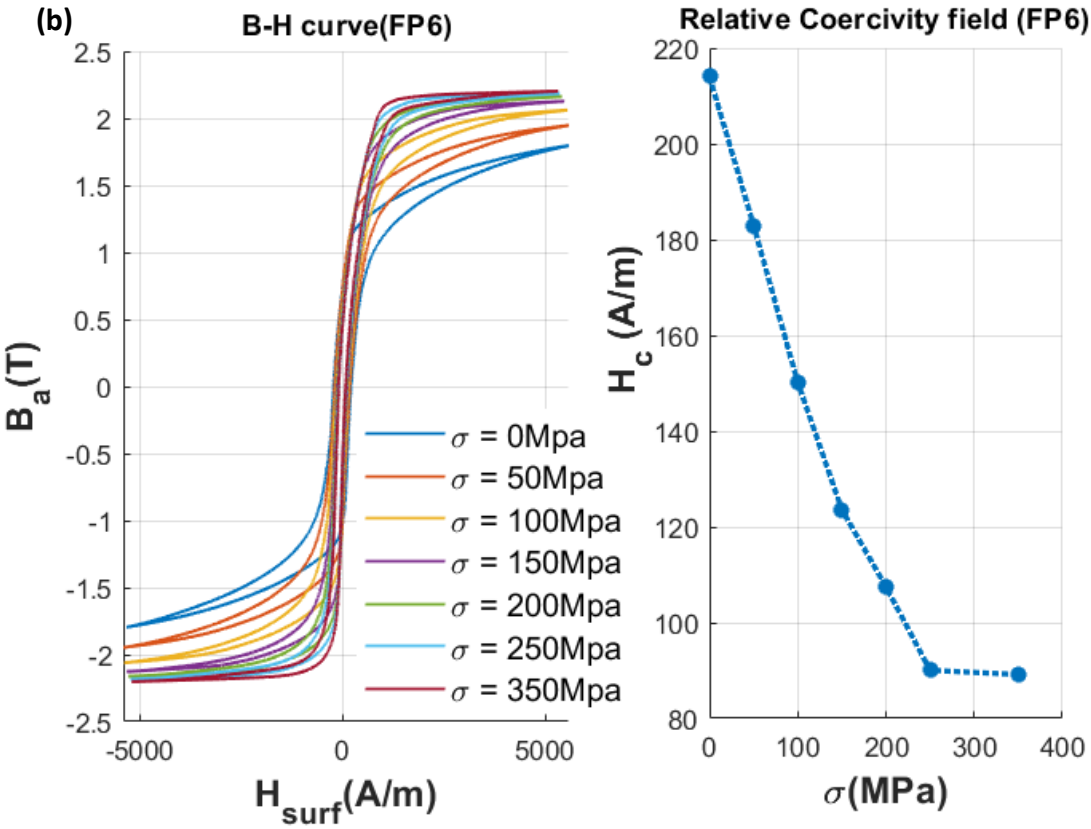
(b)
B-H curve(FP6)
B_a(T)
H_surf(A/m)
σ = 0Mpa
σ = 50Mpa
σ = 100Mpa
σ = 150Mpa
σ = 200Mpa
σ = 250Mpa
σ = 350Mpa
Relative Coercivity field (FP6)
H_c (A/m)
σ(MPa)

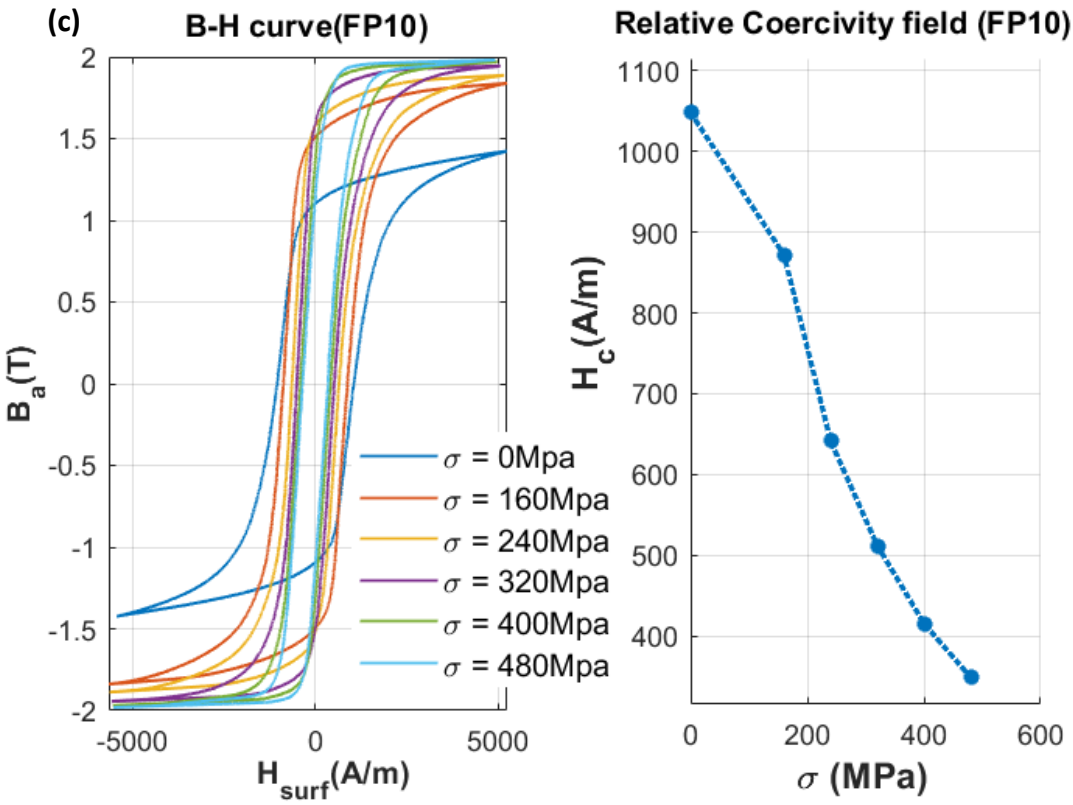

Figure 2-7:Experimental measurements for the tensile stress-dependent Ba(Hsurf) hysteresis cycles of samples (a)RN (b) FP6 (c)FP10

According to the literature, the tensile stress σ on iron-cobalt ferromagnetic materials softens its magnetic behavior. In the low-frequency range, softer magnetic behavior indicates higher permeability at a low magnetic field (near zero) but lower coercivity. This behavior is well known and has already been demonstrated in previous scientific works on positive magnetostriction coefficient materials (Fig. 6 in [114], Fig. 2.34 in [133], [136], and [137]).

Another indicator of the effects of stress on the magnetic behavior of a material is the coercive field. This can be explained by the effects of stress which reduces the domain volume hence reducing the hysteresis losses. Figure 2-7 also shows the experimental evolution of the coercive field for each stress value. This behavior can be approximated by a decreasing experimental law. The value of the coercive field can also be used to determine the value of the stress on the material [138].

The experimental results depicted in Figure 2-7 confirm our expectations; they validate the conformity of our test bench with the tested specimens.

After the first magneto-mechanical experimental step was performed, the results showed that sample FP10 has the highest coercive field value at no stress condition and can exhibit higher stress compared to RN and FP6, which are good attributes for energy harvesting applications. Based on these criteria, only sample FP10 was used in further experiments.

B_a *(H_{surf})* hysteresis cycles showed stress dependency and thus could be considered stress observation tools. Still, the difficulty of using wound coils in an industrial context where large and complex surfaces have to be controlled is worth mentioning. This limitation prompted us to use other methods, including the directional MIP test described below.

2.6 Directional Magnetic Incremental Permeability

2.6.1 Magnetic Incremental Permeability

Generally, magnetic permeability can be described as a measure of a material's response to an applied magnetic field. More precisely, according to the German standard DIN1324 (Part II: magnetic field for material quantities [139]), the Magnetic Incremental Permeability (MIP) is defined as the slope of the inner asymmetric loops (Eq. (2-3), Figure 2-8). These loops, also called minor cycles, originate from reversible changes due to reversible magnetization vector rotations and domain wall bowing around the pinning sites[140]. As illustrated in Figure 2-9, they were obtained when the tested ferromagnetic material was exposed to the superimposition of two magnetic contributions [127]:

1. a low-frequency (steady-static), high-amplitude magnetic excitation,
2. high-frequency low-amplitude magnetic excitations.

Mathematically, the relative MIP, μ_{MIP_r}, can be defined as [141]:

$$\mu_{MIP_r} = \frac{1}{\mu_0} \cdot \frac{\Delta B_a}{\Delta H_{surf}} \tag{2-3}$$

Where, μ_0 is the permeability of air, ΔB_a is the incremental amplitude of the magnetic flux density response, which is generated and measured by the LCR meter connected to

the sensor described in Figure 2-4, and ΔH_{surf} is the incremental amplitude of the applied alternating magnetic intensity of relatively high frequency measured by the Hall effect sensor.

To obtain minor loops, the frequency of the sensor must be significantly higher than the hysteresis frequency. In addition, the ΔH_{surf} the value should be less than half that of the coercivity to ensure that the magnetization changes, responsible for ΔB_a, are reversible, that is Bloch walls do not jump if applying ΔH_{surf}. In this case, the absolute value of coil impedance is proportional to μ_{MIP_r} if ΔH_{surf} is constant [142].

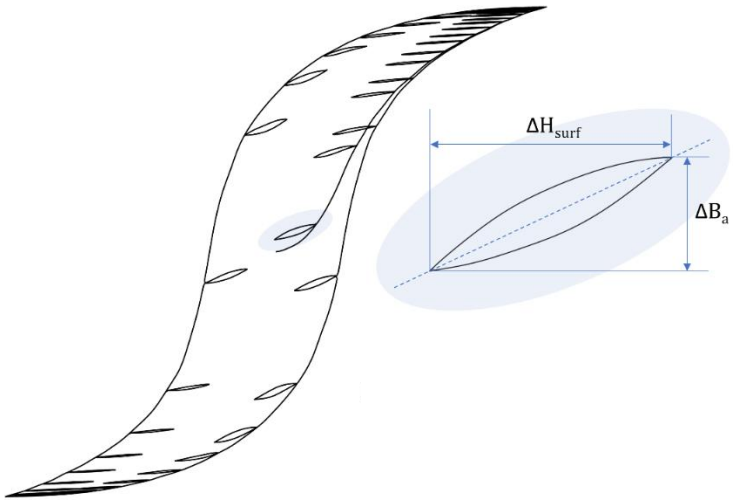

Figure 2-8: Illustration of MIP [143].

Figure 2-9 represents the structure of the MIP system, on it we can see the various magnetic fields on the sample.

Mechanical damages such as plastic deformation and fatigue damage have a lot of effects on the microstructural features (magnetic domains) of a ferromagnetic material. Therefore, the MIP method is considered a potential NDT technique for the evaluation of residual stress. The step before the plotting of the curve will be the appropriate setting of the parameters that's the frequency and magnetic field, this will be the object of the next section.

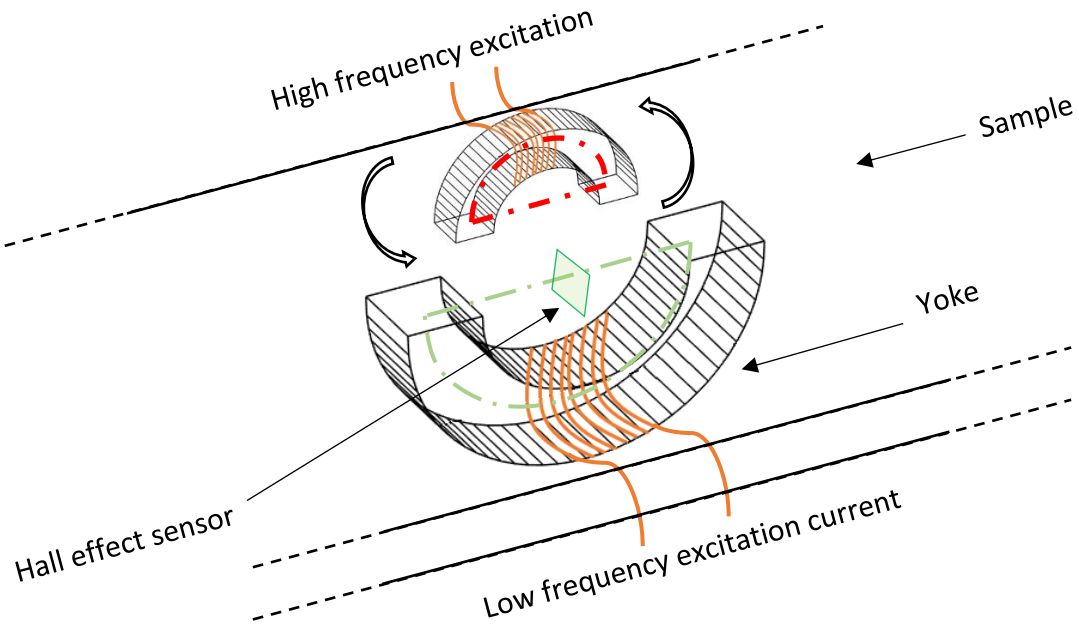

Figure 2-9:Structure of the MIP system

2.6.2 Frequency and Magnetic Field Dependence

As previously explained, the MIP measurements are performed with the superimposition of two frequencies: The excitation frequency for magnetizing the material and the high AC frequency. For the frequency dependence, based on Fig 12-a of [143], we decided for the future characterizations to adopt the lowest frequency (DC signal) as the excitation frequency for driving the maximum possible flux into the specimen under test.

For the amplitude of the magnetic field, we decided to still consider the parameters used for the classic hysteresis curve considering that from Figure 2-7 (c) we already have a moderate saturation for the sample FP10 at no stress conditions. Taking the same condition, the same result will be obtained for the MIP curves. A frequency of 10kHz was selected for the low-amplitude alternating field. From [143] a higher frequency ($> 20Hz$) doesn't yield any significant changes in the MIP signatures. For the temperature, all the experiments are still performed at room temperature. Having set our parameters, the next paragraph will present the $Z(H_{surf})$ butterfly loops.

2.6.3 Evolution of the *Z(H_{surf})* Butterfly Loops based on the Tensile Stress

The previously described experimental setup in section 2.3.2 measures the impedance of the MIP sensor shown in Figure 2-3 and Figure 2-4. Figure 2-10 shows the evolution of the sensor impedance modulus *IZI* vs. the quasi-static magnetic excitation at four levels of tensile stress σ. For the curve (Figure 2-10) plotted below, the sensor is aligned with the length of the tested specimen and with the magnetic excitation ($\theta = 0\ rd$, as illustrated in Figure 2-10 upper left-hand corner). Since the *Z(Hsurf)* butterfly loops cannot provide to us the informations we are looking we will pass through an intermediate conversion process from the Impedance *IZI* to the FeCo Permeability μ_{MIP}, this will be the subject of the next section.

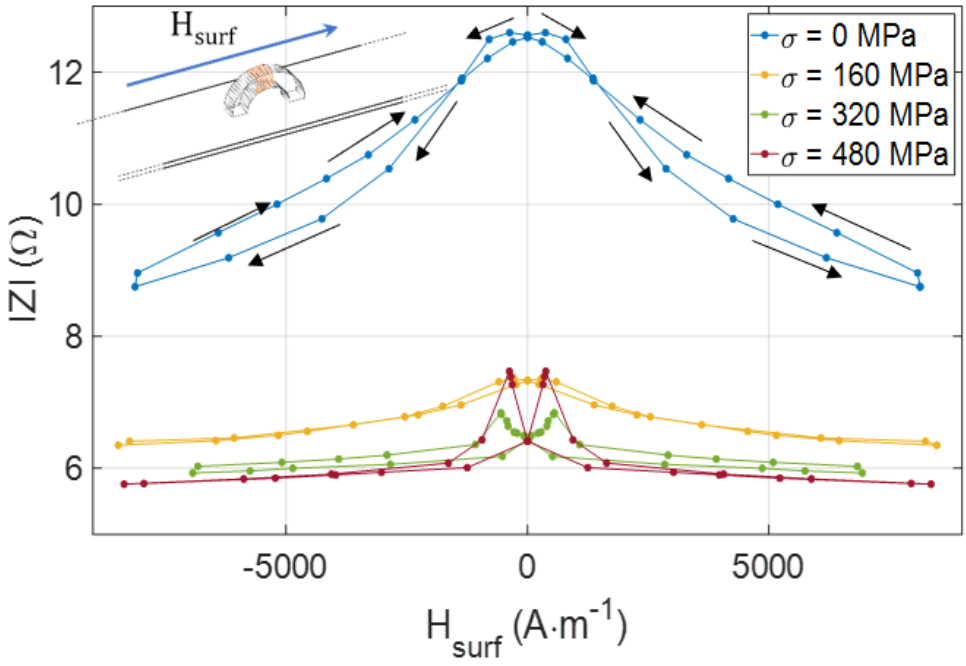

Figure 2-10:IZI (H_{surf}) for different tensile stress levels and with the MIP sensor aligned at $\delta = 0\ rd$.

2.6.4 Conversion from the Impedance *IZI* to the FeCo relative permeability μ_{MIP_r}

As previously stated, the data from the impedance measurements performed in Section 2.6.3 cannot directly be interpreted. To overcome it, we have to return to

physical quantities. For this, the relationship between *IZI* and μ_{MIP_r} for the FeCo sheet MIP needs to be established.

A magnetic reluctance scheme was used in this study as a proposed solution for the conversion.

Figure 2-11 depicts the simplified reluctance scheme used to establish the relationship between *Z''* and the relative permeability μ_{MIP_r}. The magnetic contact between the ferrite core and the sheet is supposed ideal meaning no air gap.

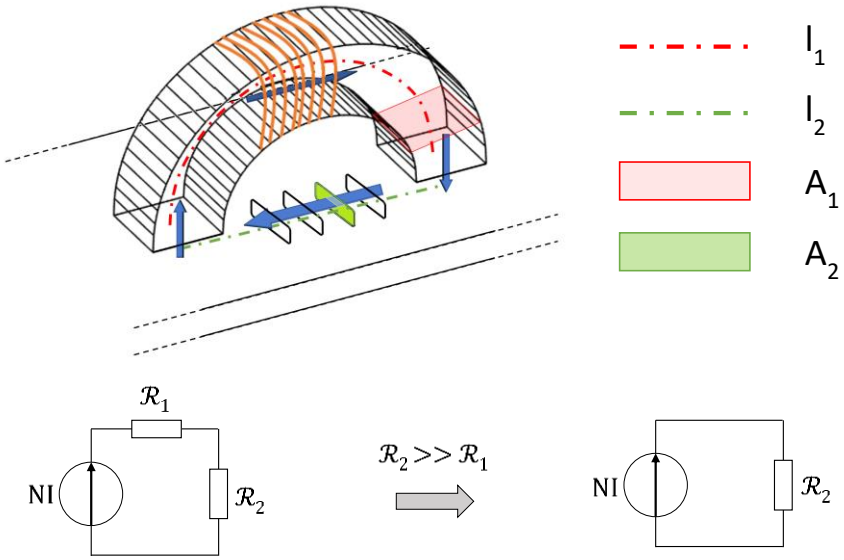

Figure 2-11: Simplified reluctance conversion scheme and parts of the magnetic circuit

For the magnetic flux tube, the width is defined as the mean length of the ferrite core denoted l_2 and the depth is the width of the active zone of the magnetostrictive material;

Let's define by $\mathcal{R}_1$ and $\mathcal{R}_2$, respectively the reluctances referring to the ferrite sensor and FeCo sample. Considering $\mathcal{R}_2$ >> $\mathcal{R}_1$, the inductance of the active part of the sample is given by :

$$L = \frac{N^2}{\mathcal{R}_2} \tag{2-4}$$

The reluctance of the active part is defined by:

$$\mathcal{R}_2 = \frac{l_2}{\mu_0 \mu_{MIP_r} A_2} \tag{2-5}$$

Replacing Eq (2-5) into Eq (2-4) leads to:

$$L = \frac{N^2 \mu_0 \mu_{MIP_r} A_2}{l_2} \tag{2-6}$$

$$\mu_{MIP_r} = \frac{L l_2}{N^2 \mu_0 A_2} \tag{2-7}$$

Based on the early assumption made, the impedance of the device is written as :

$$Z = R + jLw = Z' + jZ'' \tag{2-8}$$

Performing variable identification in Eq(2-8), the inductance is :

$$L = \frac{Z''}{w} \tag{2-9}$$

Combine Eq (2-9) and Eq (2-7), the linear relationship between the impedance imaginary part of Z'' and the relative permeability μ_{MIP_r} is :

$$\mu_{MIP_r} = \frac{Z'' \cdot l_2}{\mu_0 \cdot N^2 \cdot A_2 \cdot \omega} \tag{2-10}$$

Where l_2 and A_2 are respectively the mean length and area of the active zone of the material.

For the magnetic flux tube, the width is defined as the mean length of the ferrite core denoted l_2 and the depth is the width of the active zone of the magnetostrictive material;

Table 2-2 below gives the values of both Ferrite and sample constant parameters.

Table 2-2: Physical parameters values

Parameters	Ferrite	FeCo Active Zone
μ_r	800	500
l_1	0.0236m	-
l_2	-	0.0075m
$\mathcal{R}_1$	1.27×10^6 H^{-1}	-
$\mathcal{R}_2$	-	1.4×10^7 H^{-1}
A_1	1.85×10^{-5} m^2	-

A_2	-	8.51×10^{-7} m^2

Based on results from Figure 2-10 we ran comparisons between incremental and differential permeabilities at high values of magnetic field (greater than 4500A.m^{-1}) where they are supposed to be similar. These comparisons are available in Table 2-3 below. Though the conversion scheme may be inexact as it relies on simplifying assumptions, it allows rapid estimation of the permeability with satisfactory accuracy. We performed several post-processing operations to check the validity of the resulting MIP values. Based on comparisons performed in Table 2-3, values confirm our expectations and the relatively similar permeabilities in the saturated range.

Table 2-3:Comparisons between the incremental permeability (μ_{MIP_r}) and differential permeability ($\mu_{r\ Diff}$) in the high H_{surf} amplitude range

σ (MPa)	***H_{surf} (A·m^{-1})***	***μ_{MIP_r}***	***$\mu_{r\ Diff}$***
0	4500	37.5	40
160	4500	12	17
320	4500	9	10
480	4500	7	9

Figure 2-12 gives the resulting μ_{MIP_r} *(H_{surf})* for all Figure 2-10 tests. From the behavior of the obtained curve, it can be highlighted that its shape is similar to the impedance modulus $|Z|$, this behavior is the consequence of low electrical losses in the device.

The intermediary conversion step is done, and the next step is to convert the obtained curve into the classical *B-H* curve.

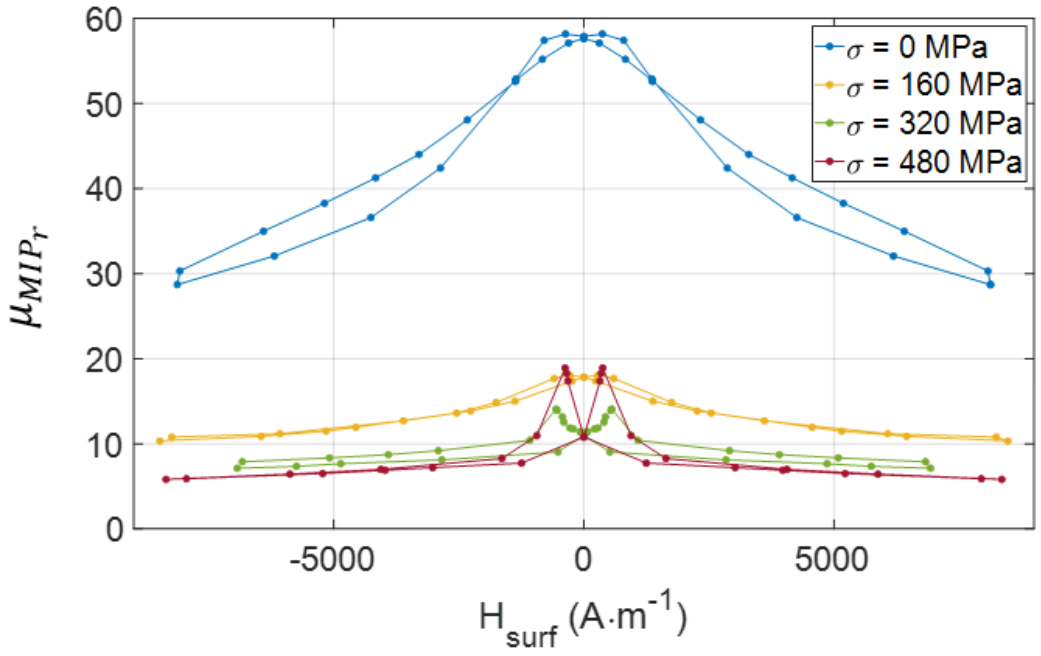

Figure 2-12: Resulting $\mu_{MIP_r}(H_{surf})$ for different tensile stress levels and with the MIP sensor aligned at $\delta = 0\ rd$.

2.6.5 Conversion from $\mu_{MIP_r}(H_{surf})$ to $B_{a\ MIP}(H_{surf})$ Classical Hysteresis Cycles

The MIP method's conventional signature is the butterfly loop (as illustrated in Figure 2-12). In NDT, defining indicators coming directly from this signature and plotting them vs. the targeted properties (i.e., the property to be assessed, MIS, microstructural information, etc.) is common. For MIP tests, those indicators include:

- the maximum amplitude
- the amplitude at the remanence point
- and the curve width at 50% of max($\mu_{r\ MIP}$), to name some [144].

For comparison purposes and in the context of this research, the indicator definition step is pushed to a final step consisting of the reconstruction of a MIP hysteresis cycle from butterfly loops. We decided to assess this approach for several reasons amongst which, the same indicators can be used for both classic and MIP hysteresis cycles, and the comparison of the stress effects on both these magnetic signatures can be easily studied. The resulting induction field name $B_{a\ MIP}$ is obtained from Eq.(2-11):

$$B_{a\,MIP} = \int \mu_0 \mu_{r\,MIP}.dH_{surf} \tag{2-11}$$

The integration in Eq.(2-11) process brings more stability and eases the determination of the indicators. Figure 2-13 below depicts the $B_{a\,MIP}(H_{surf})$ for the various stress values as illustrated previously in Figure 2-10.

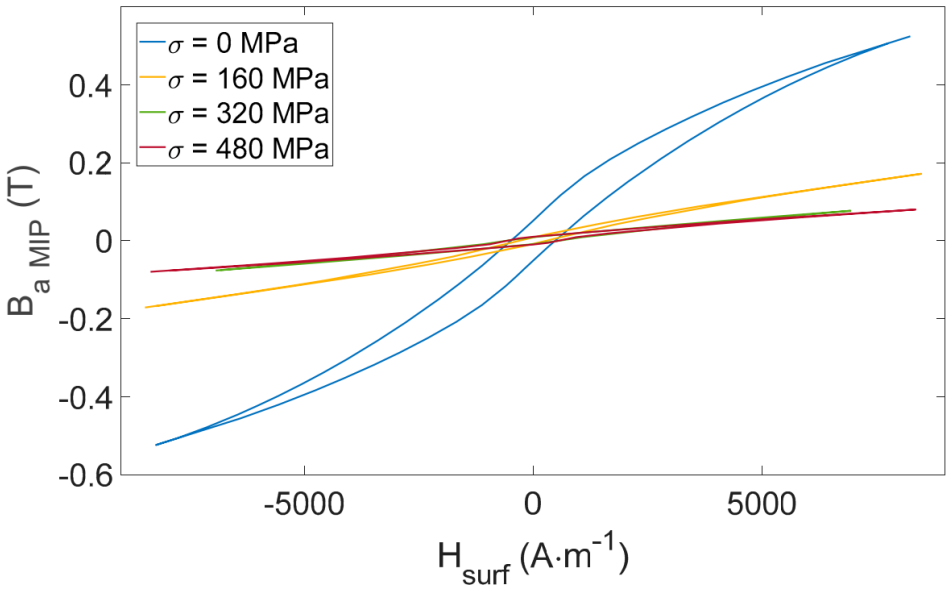

Figure 2-13: $B_{a\,MIP}(H_{surf})$ hysteresis cycles from Figure 2-10 measurements.

2.6.6 Directional $B_{a\,MIP}(H_{surf})$ Hysteresis Loop

In the series of tests below, five tensile stress levels and for different values of angle δ from 0 to π/2 with a $\Delta\delta$ = π/18 step were performed (as illustrated in Figure 2-14). The applied tensile stress on the sample is limited to 250 MPa. For saturation reasons, the stress effect is especially weak beyond the [0 – 250] MPa range. The results are shown in Figure 2-16.

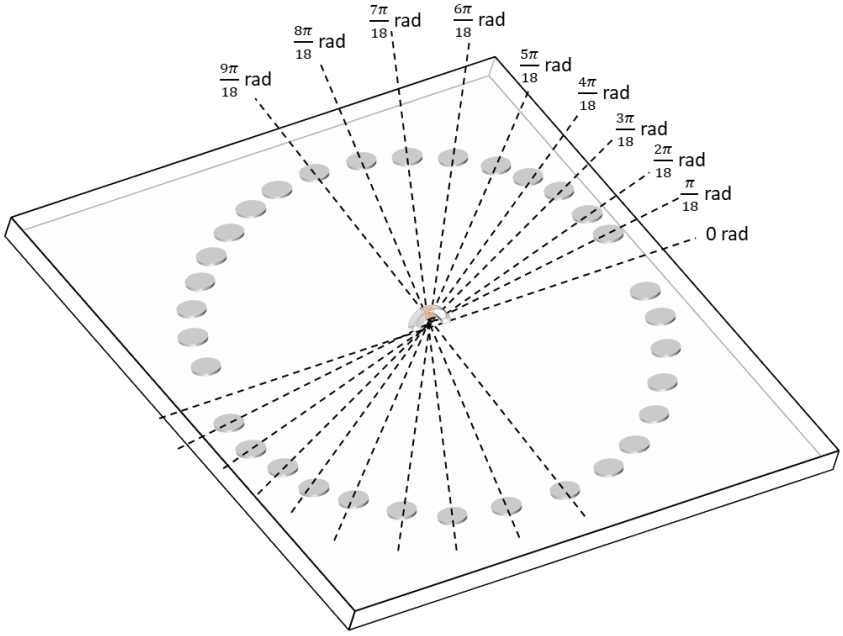

Figure 2-14: Angles repartition on the 3D printed piece for sensor orientation

2.7 Analysis of the Reconstructed $B_{a\ MIP}(H_{surf})$ Hysteresis Loop

Figure 2-16 is the reconstructed $B_{a\ MIP}(H_{surf})$ hysteresis loop. Its analysis reveals many differences with the standard $B_a(H_{surf})$ curve plotted previously. Those differences will be presented below:

- From Figure 2-7 the external tensile stress straightened the classical $B_a(H_{surf})$. But for $B_{a\ MIP}(H_{surf})$ loops it is the opposite behavior, the resulting hysteresis loop is laying down when the tensile stress increases (Figure 2-16).
- Due to the positive magnetostriction property of Iron-Cobalt alloys, their magnetic behavior is supposed to be softened by the application of tensile stress. As an already soft material, tensile stress effects on $B_a(H_{surf})$ are limited. Oppositely, a strong influence can be observed on the general shape of the cycles: the laid down of $B_{a\ MIP}(H_{surf})$ cycles is remarkable.

The nature of the magnetic signature tested ($B_a(H_{surf})$, Barkhausen noise, MIP, etc.) is expected to have no effects on the coercivity field. Therefore, comparing $H_c(\sigma)$ and $H_{c\ MIP}(\sigma)$ (at δ = 0 rad) can be considered as a way to check the reliability of the MIP measurements. Figure 2-15 illustrates this comparison for a tensile stress range of 0 – 250 MPa.

- Results from Figure 2-15 confirm our expectations that coercivities of both characterizations ($B_a(H_{surf})$ and $B_{a\ MIP}(H_{surf})$) remain close all along σ variations.

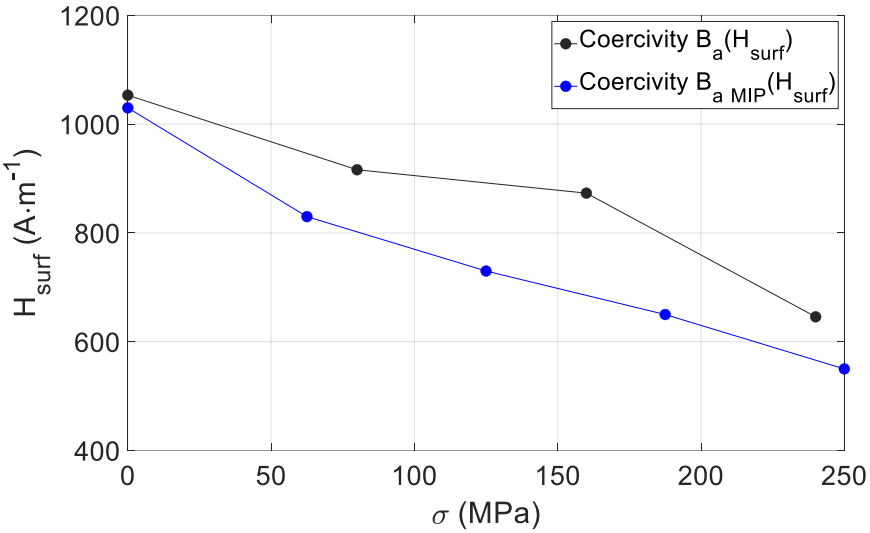

Figure 2-15:Coercivity vs. stress for $B_a(H_{surf})$ and $B_{a\ MIP}(H_{surf})$ hysteresis cycles.

Magnetization in ferromagnetic steel depends on several factors, from its atomic source to its perception at the human scale. Each mechanism has a unique time constant, geometric scale, and sensitivity to the outside world (magnetic, mechanical, thermal, etc.). It is difficult to separate and list these systems because of their overlap. However, three classifications can be made clear:

1- Magnetic domain structure and kinetics (10^{-4} to 10^{-6} m):

- Burst domain walls (reversible, in the low excitation range).
- Domain wall vibrations that are irreversible (middle excitation range).
- Annihilation and nucleation (high-range).

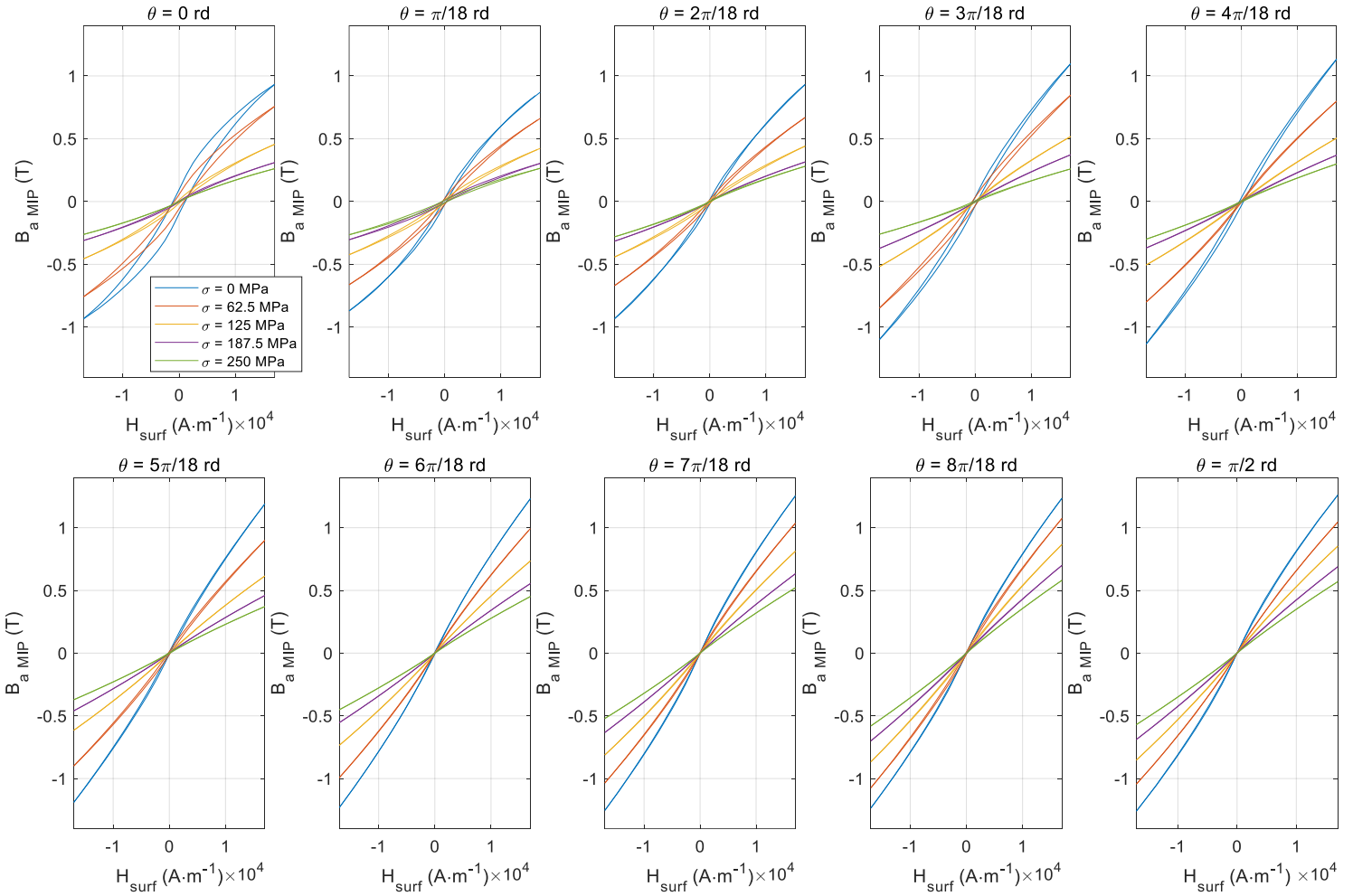

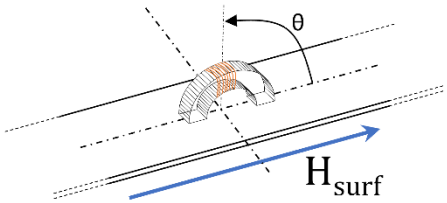

Figure 2-16:$B_{a\ MIP}(H_{surf})$ hysteresis cycles in the [0 – π/2] angle range

2- Atomic magnetic moments' orientation and amplitude (10^{-11}- 10^{-9} m)
   - Unplanned Rotation (high and very high magnetic excitation).
3- Mechanisms on a human scale:
   - eddy currents on a macro scale.

It is hard to identify the impact of stress on a specific mechanism from a single observation of typical $B_a(H_{surf})$ hysteresis loops due to overlap. The unique access for domain wall bulging provided by MIP experimental observation is the exact opposite of its counterpart $B_a(H_{surf})$ hysteresis loops. The scientific literature [142], [145], advises MIP to be operated in an alternating magnetic field with an amplitude half that of the coercivity, restricting the domain wall movements to reversible ones. Low-amplitude magnetic stimulation has an impact on domain wall bulging. We are encouraged to test its sensitivity in a modest range of stress via scaling methodologies and analogies.

There is disagreement over the direction of domain wall bulging. Even though the manufacturer claims that the crystallographic texture of FeCo laminations is not very noticeable, every material has some degree of anisotropy in its magnetic response, so MIP should also have this property. This claim is supported by Figure 2-16 large fluctuations over the tested angles.

To determine which indicators are most suited for estimating tensile stress, five indicators directly read on the δ-dependent $B_{a\,MIP}(H_{surf})$ cycles have been tested:

- Coercivity $H_{c\,MIP}$
- Remanence $B_{r\,MIP}$
- $B_{a\,MIP}(H_{surf})$ Hysteresis area
- $B_{a\,MIP}$ at H_{surf} = 2 kA·m^{-1}
- $B_{a\,MIP}$ at H_{surf} = 10 kA·m^{-1}

The best indication, according to a more thorough analysis based on Pearson correlation factors ρ, is $B_{a\,MIP}$ at H_{surf} = 10 kA·m^{-1}. For the 10 sensor angles evaluated, Figure 2-17 shows its fluctuations vs. σ and at $\delta = \pi/2$, the astounding 0.99 linear correlation is attained. $H_{c\,MIP}$ depends on all magnetization mechanisms, even when read on the $B_{a\,MIP}(H_{surf})$ cycles. Contrarily, B_{aMIP} at H_{surf} = 10 kA·m^{-1} offers a cumulative

reflection throughout the domain wall bulging mechanism occurring during the magnetization cycle.

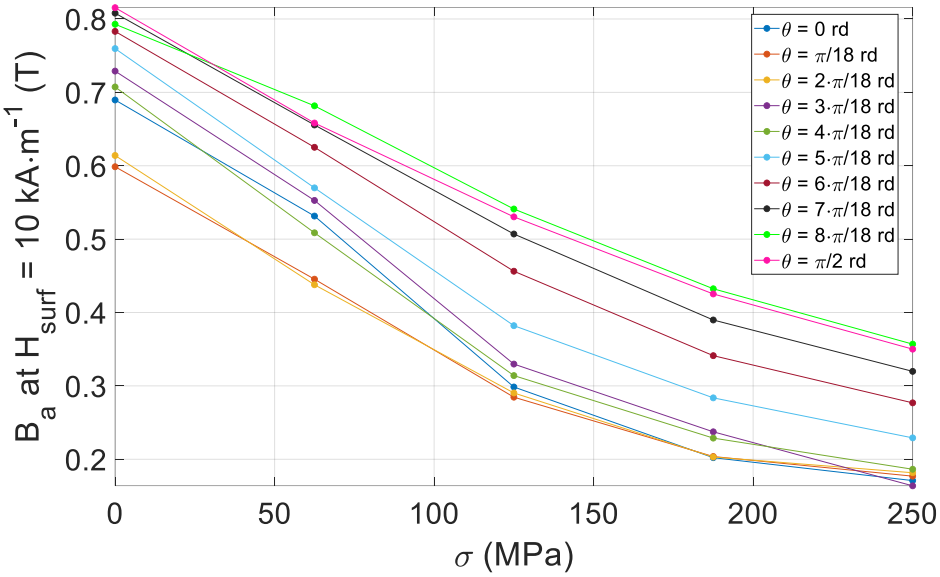

Figure 2-17:B_a at H_{surf} = 10 kA·m^{-1} for δ in the [0 ; π/2] range.

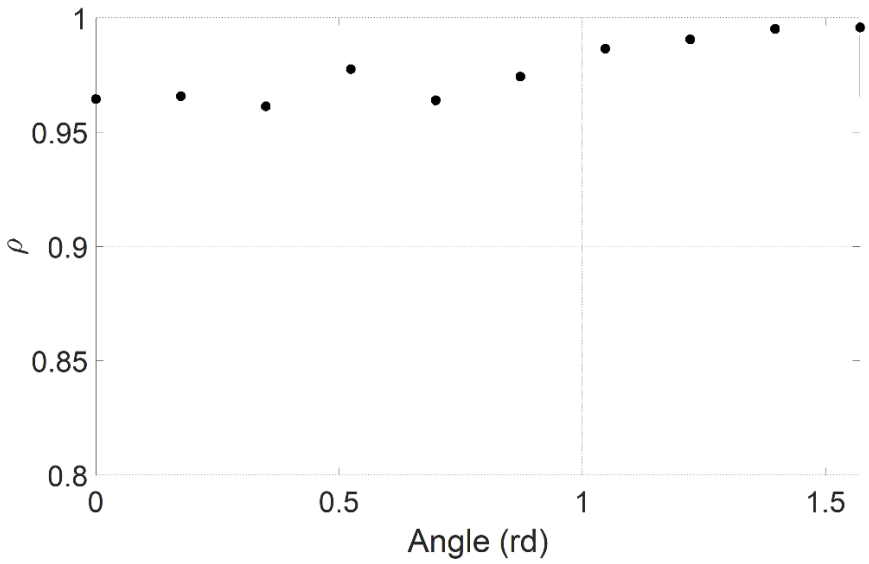

Figure 2-18:Related Pearson correlation factors.

Regarding the sensor orientation, the domain wall of a theoretically isotropic material should not bulge differently in either direction for energy reasons.

First, with σ and H_{surf} parallel, if δ = 0 rad, the static and dynamic contributions overlaid, intensifying the softer behavior and highlighting the impact on the material as well as the changes in behavior across the stress levels. The sensor measurement is less impacted by the softener effect and becomes quasi-linearly dependent on σ when δ= 0

rad, in contrast, where the static and dynamic contributions work in quadratic directions.

2.8 Conclusion

The directionality of the MIP sensor has never been investigated. Giving the experimental method a greater level of flexibility opens up new avenues for the interpretation of the outcomes. It enables the definition of NDT optimal circumstances, for example, for the observation of a linked targeted physical property.

The optimal circumstances are identified in this study when the DC and AC H_{surf} contributions have quadratic orientations. This study focuses especially on detecting mechanical internal stress replaced here by tensile stress, and the results show that this is the case.

Conventional traditional $B_a(H_{surf})$ Hysteresis cycles were plotted. The experimental conditions are very clearly described for purposes of repeatability. Since it is hard to establish these conditions in an NDT setting, companies are exploring alternatives. It has previously been extensively researched how $B_a(H_{surf})$ vs. stress-related indices, such as coercivity, remanence, etc., have changed over time. We link MIP with related indicators by recreating hysteresis cycles from MIP data. Regarding these traditional inclinations, their dependence on stress is addressed.

$H_{c\,MIP}$ is dependent on all of the magnetization processes, much as traditional H_c. Its dependence is clear, although not always in a linear fashion. To evaluate the impact of this process, one can employ other $B_{a\,MIP}(H_{surf})$ markers that are better tailored to the domain wall bulging mechanism.

The scope of NDT based on the magnetization mechanism is wider than that of this study, which is restricted to FeCo alloys. The development of new sensor designs will help us better understand the connections between magnetization mechanisms and the intended attributes. The high energy density property of Iron-Cobalt materials makes them good candidates for energy conversion, this will be the object of the next chapter of this document.

3 MAGNETOSTRICTIVE ENERGY CONVERSION, MODELLING, AND VALIDATION ON PERMENDUR ALLOY

3.1 Introduction

This chapter presents the magneto-mechanical characterization of the magnetostrictive sheets in view of magnetostrictive energy conversion, and methods are presented for optimal conversion. In that scope, we first present some magneto-mechanical models and some existing electromechanical energy conversion models. Afterward, the experimental magnetic characterization and simulation of Permendur sheets under tensile stress are conducted. Based on these experimental measurements, a simulation method of the anhysteretic behavior is proposed and validated and then used to assess the potential energy conversion under tensile stress and magnetic excitation. Then, another estimation of the converted energy density is described taking into account the hysteresis losses. Finally, experimental Ericsson energy cycles are measured to prove the feasibility of the conversion process and validate Permendur as a relevant material for energy conversion applications. We also give the orders of magnitude of the converted energy density under various applied mechanical stresses and fixed excitation magnetic fields, allowing drawing insights concerning conventionally and non-conventionally used materials for such applications.

Let's note that the contents presented in this chapter have been already published explaining the similarities in some figures and graphs.

3.2 Electromechanical Energy Conversion Models

Vibration energy harvesters can supply power continuously or (more often) intermittently to electronic devices by scavenging useful electrical energy from ambient vibrations. In this domain, magnetostrictive materials for converting mechanical vibrations into electrical energy in a cost-effective way remain to be determined. Iron-Cobalt-Vanadium (Permendur, Co_{49}-Fe_{49}-V_2) is a promising candidate: it is a soft ferromagnetic material with high magnetization saturation, high magnetostrictive coefficients coupled with large elasticity limit (which favors energy harvesting), low price, and good availability.

The electromechanical energy conversion model describes the relationship between the mechanical displacement of the energy harvester and the electrical voltage generated. This energy conversion model considers the harvester's mechanical properties, such as its stiffness and damping, and the electrical properties, including the capacitance and resistance of the energy harvesting circuit.

In the literature, several energy conversion models are developed to analyze the influence of some parameters [146] on the harvester performances. Amongst the works available in the literature, Davino et al. [147] proposed a model for the description of a magnetostrictive harvesting device. The system consists of an N-turns coil wound around a magnetostrictive rod which experiences a compressive periodic mechanical stress. The model took into consideration the effects of hysteresis. Those effects were highlighted and compared to the predictions of the linear modeling. Modelling equations were coupled with circuit equations which then led to a differential equation depending on hysteresis. The equation can provide an effective macroscopic description of the internal energy conversion mechanism in the prototype. The tests have shown the effect of a magnetic field bias on the generated electric power.

Mizukawa et al. [148] described a linearized model of a Fe-Ga (Galfenol) rod-based magnetostrictive energy harvester operating under a small-signal vibration excitation imposed over a constant prestress and magnetic bias using linear constitutive equations. The energy loss due to eddy currents is also considered for high-frequency applications.

The influence of the permeability and magnetostrictive constant variation on the output power is investigated from the algebraically obtained output power, and the existence of an optimal value in resistance and capacitance of the electric circuit is discussed. These optimal design parameters are also presented in the form of an algebraic solution. The estimation method of the permeability and magnetostrictive constant in the paper is not described and may be a source of errors in the model development and validation since those values greatly affect the optimal mechanical and magnetic biases applied to the harvester. Linearized models are effective when the mechanical variations are sufficiently small [149].

Another recent work is presented by Liu et al. [76] who investigated the energy conversion abilities of Metglas 2605SA1 by performing experimental Ericsson cycles as well as through dedicated theoretical model predictions of the magnetic curves. As a result, the output electrical energy density varies between 0.1 and 1 mJ/cm^3/cycle under stress values less than 100 Mpa and magnetic excitation up to 4 kA/m.

Still, in the same framework of energy conversion models, Palumbo et al. [150] focused on the change of magnetostrictive properties under different mechanical prestresses (vibrations amplitude and frequency), load resistance, and magnetic bias, and experimentally investigated the effect of parameters variations. The optimal operating condition and output power were obtained from these experiments. The experiments were performed by varying the magnetic bias applied to the coils; it was proved that the relationship between output power (or voltage) and magnetic field bias is always described by a "bell" curve; which shows that a well-defined optimal condition can always be identified through the tuning of the mechanical prestress as a function of the magnetic bias. The variation of the parameters of influence (mechanical preload, vibration frequency, amplitude, load resistance) changes the values of the output quantities but does not modify the shape of the function output power (or voltage) versus magnetic bias. Such a result is particularly important because it highlights how an optimal output voltage/power can always be reached with low permanent magnets remanence, provided that the preload and the electrical load impedance are adequately tuned. Indeed, keeping constant the other parameters, low magnetic bias should be coupled with a low mechanical prestress, and vice versa. The maximum output average

power obtained with permanent magnets was 796 mW, that is 6.5 mW/cm^3 with a sinusoidal vibration amplitude of 40 MPa at 100 Hz.

Overall, these models are important tools for designing and optimizing vibration energy harvesters but numerical calculations generally performed require a great deal of time and computational cost while potentially hiding the physical meaning of parameters. Hence an alternative analytical modeling tool in which the characteristics of magnetostrictive energy harvesters can be reasonably described is of great interest. In the next part, we are going to present the preliminary experimental characterization of the magnetostrictive sheet including the experimental setup, material selection, and the obtained experimental results.

3.3 Experimental Characterization of Permendur

As a first step towards the investigation of the energy conversion capabilities of Permendur, this section aims at first making a presentation of the used material and experimental setup and then assessing the experimental magnetic responses (hysteretic and anhysteretic behaviors) of the considered material.

3.3.1 Material Selection and Experimental Setup

3.3.1.1 Material Selection

Even if a vast family of magnetostrictive materials exists, most energy harvesting systems described in the scientific literature rely on giant magnetostriction materials like TbDyFe (commercial name Terfenol) and Galfenol [151], [152], [153] (Table 3-1). They are highly used because of their merits in terms of high magneto-mechanical coupling coefficient, high energy density, and excellent applicability to harsh environments [154]. However, they are not quite suitable for energy harvesting due to their brittleness, and difficulty to bend and miniaturize attributed to the fact that TbDyFe is usually a cylinder or cuboid [155]. Another drawback of these materials is extremely high prices (Table 3-1, right column), and a large-scale development for such energy harvesters would be a financial oddity. Other materials like Iron-Cobalt-Vanadium show high magnetostrictive activity and much lower prices but have never really been tested in an energy harvesting context.

Table 3-1: Characteristics of the magnetostrictive materials for energy harvesting

Material	**Magnetostriction coefficient λ_s (ppm)**	**Magnetization saturation P_s (T)**	**Energy density at the material scale W_{mat} (μJ·cm^{-3})**	**Mechanical Preload σ (MPa)**	**Magnetic Bias**	**Price**
Galfenol	400-500 [156]	1.75 [157]	49 [158]	No preload	1.1T [158]	10 $ / g
Terfenol-D	1500-2000 [156]	1 [159]	40.7 [160]	6MPa	1.2T [160]	15 $ / g
Permendur	80 [156]	2.35 [161]	*Purpose of the present study*	No preload	5.5kA/m	0.1 $ /g

Based on the characterization made in Section 2.5 of the previous chapter, sample FP10 is still considered. Table 3-2 below gives a more detailed chemical composition and mechanical and physical properties of the sample under study.

Table 3-2:Composition, physical, and mechanical properties of the tested specimen

• ***Composition***					
C (Mass %)	*Si*	*Mn*	*Co*	*V*	*Fe*
<0.015	<0.1	<0.15	<49	2	Balanced
• **Physical Properties**					
Density (g.cm3)	Electrical Resistivity(μΩ.cm)	Thermal Expansion	Thermal Conductivity	Curie Temp. (°C)	
8.12	40	9.10^{-6}	0.3	950	
• **Mechanical Properties**					
Yield Strength (Mpa)		Tensile Strength	Young Modulus	Hardness (HV10)	
1000		1345	250	300	

Understanding all the conversion stages involved in the energy harvesting process and their interactions starts with the proper selection and knowledge of the

magnetostrictive material. The problem of the behavior of magnetostrictive materials concerns two points:

- The application of mechanical stress to a soft ferromagnetic material can lead to a rise in magnetic losses and a decrease in efficiency, as it changes the material's microstructure and alters its magnetic properties. Hence there is a need the properly assess the stress effects on the material
- Most studies on magnetostrictive materials focus on their behavior in the middle range of magnetic excitation, which is considered linear. This limitation restricts the potential applications and evaluation of the performance of associated energy harvesters.

Following these last observations and that most recently related works mainly focus on evaluating the overall performance of the magnetostrictive energy harvesting system without exploring the potential energy conversion performance at a material level, this thesis aims to assess the energy harvesting capability of Permendur laminated sheets.

3.3.1.2 Experimental Setup

The experimental process, the functional principle and the role of components in the experimental setup are almost the same as presented in section 2.4.1 of the previous chapter. The difference resides in that in Figure 3-1, to enhance the stability in the tensile stress bench, 2 U-magnetic yokes in series we used to provide the magnetic field. This was mainly implemented for the sake of the stability of the overall experimental bench within the tension-compression machine and to avoid the shearing of the sample.

3.3.2 Experimental Magnetic Behavior

Figure 3-2 depicts B_a (H_{surf}) hysteresis loops measured at different tensile stress levels where H_{surf} is the tangential surface excitation field and B_a is the magnetic flux density. The tests were performed within the elastic zone of the material. The tensile stress σ was varied randomly from lower to high values by the tensile stress machine represented in.

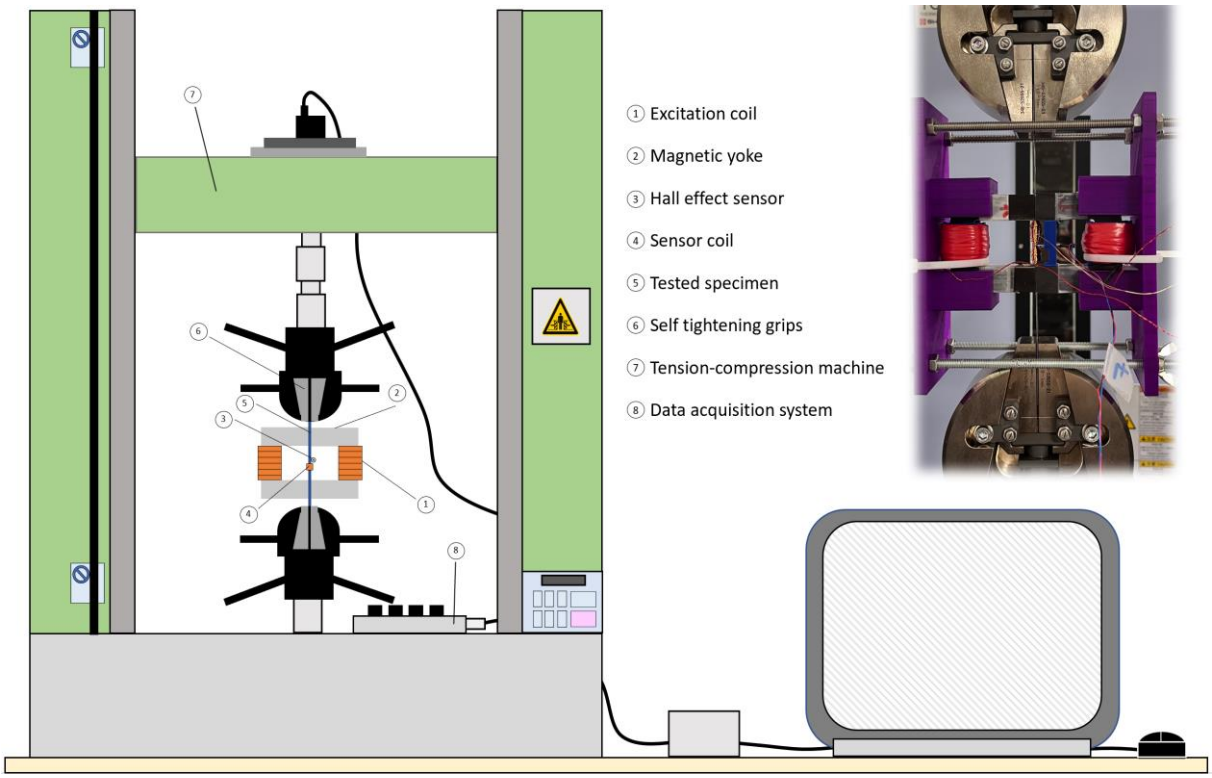

Figure 3-1: Experimental setup for the magnetic characterization under different tensile stress levels.

As an expected consequence, the magnetic behavior of the specimens is softened as the magnetic moments gain a preferential direction (easy axis of magnetization direction) with the stress application (Figure 3-2). However, applying a high magnetic field tends to align these moments in the applied field direction. The number of moments being constant, saturation magnetization is a material property that will eventually be reached when H_{surf} is strong enough to compensate for the effect of stress.

In the low-frequency range, softer magnetic behavior means higher permeability and lower coercivity; this behavior is well-known and has already been discussed in the literature (*e.g.*, Fig. 2.34 in [133]). As expected, the material's permeability increases when the stress increases, and the cycle is straightened.

Another behavior seen is that all the curves do not reach the same final magnetic field. This is explained by the fact that the excitation remains in a medium field region. Increasing the excitation would eventually lead to all the curves having the same saturation but the saturation value is fixed no matter the value of the exciting field

because its value only depends on the composition of the material and the material is unchanged. However, such a high-field region is barely reached in energy harvesting systems which usually rely on permanent magnets with a significant air gap. For our study, we will not further develop the various parameters of the energy harvester.

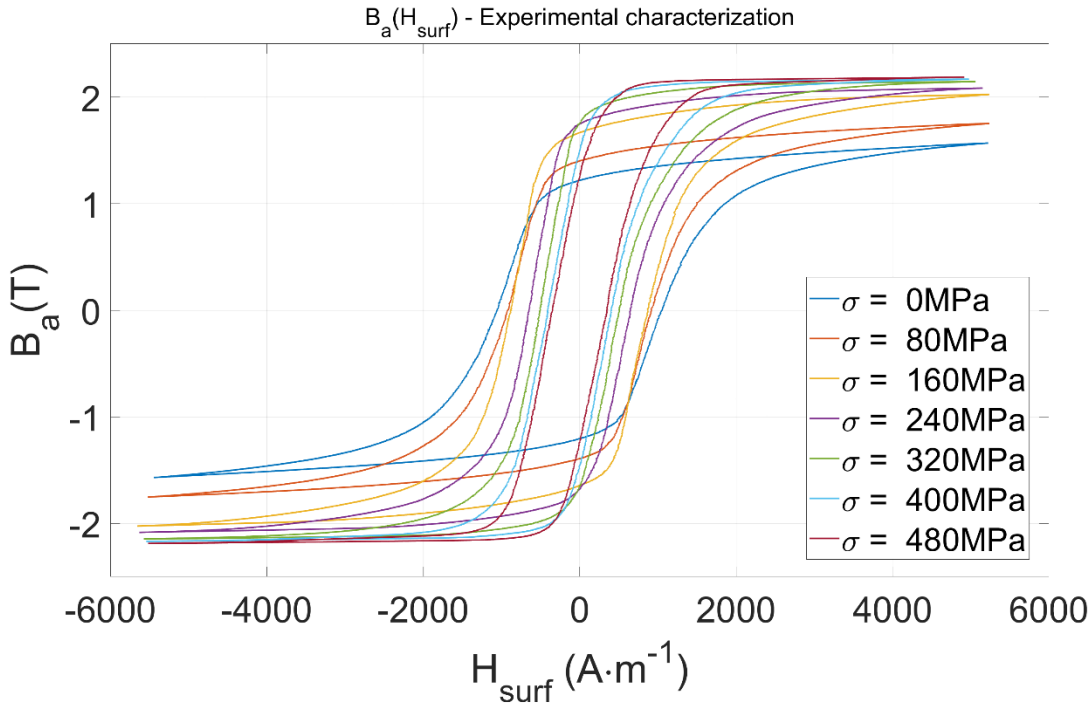

Figure 3-2: Fe-Co-V: B_a (H_{surf}) experimental hysteresis loops for different tensile stress levels.

3.3.3 Experimental Anhysteretic Behavior

The numerical anhysteretic behavior is estimated by performing the averaging of the magnetic excitation field for a given magnetic flux density between ascending and descending magnetic responses of the major hysteresis curves. We assumed no changes in the external conditions during each complete magnetization cycle.

To perform it, the 1st step consisted of separating the ascending and descending parts (Figure 3-3) from the anhysteretic curve plotted in Figure 3-2 for any particular value of the stress. For the calculation, we assumed no variations in the external conditions during each complete magnetization cycle. We assumed that no variations occurred in the external conditions during each complete magnetization cycle.

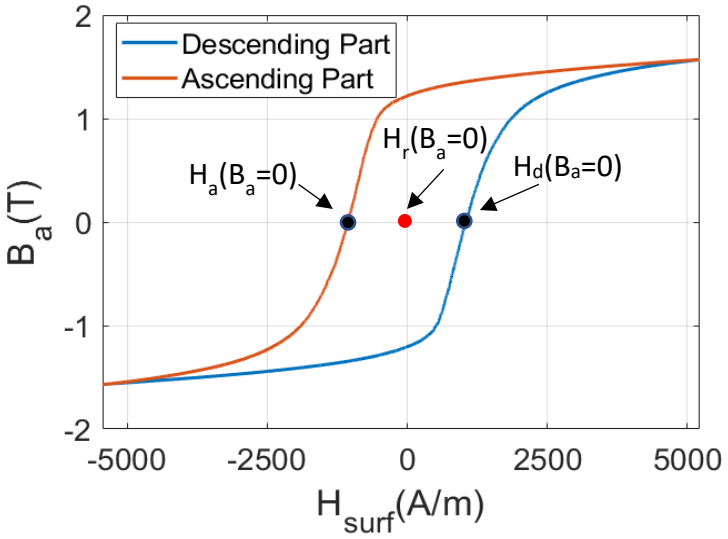

Figure 3-3:Illustration of the ascending and descending curves for σ = 0Mpa

In Figure 3-3, $H_d(B_a=0)$ and $H_a(B_a=0)$ respectively denote the descending and ascending values of the magnetic flux when $B_a=0$.

The resulting anhysteretic point *Hr* corresponding to a value of B_a is given in Eq.(2-2).

$$H_r(B = B_i) = \frac{H_a(B = B_i) + H_d(B = B_i)}{2} \quad (3\text{-}1)$$

The resulting anhysteretic curves $(H_r(B = B_i)(B_i))$ are the collection of the corresponding points and are plotted in Figure 3-4. It can be noted that the experimental plotted anhysteretic curves follow the same trend as the hysteresis curves.

Based on these experimental measurements, a simulation method of the anhysteretic behavior is proposed and will be used to assess the potential energy conversion under tensile stress and magnetic excitations. Then, another estimation of the converted energy density will be described to account for the hysteresis losses. Finally, experimental Ericsson energy cycles will be performed to prove the feasibility of the conversion process and validate Permendur as a relevant material for energy conversion applications

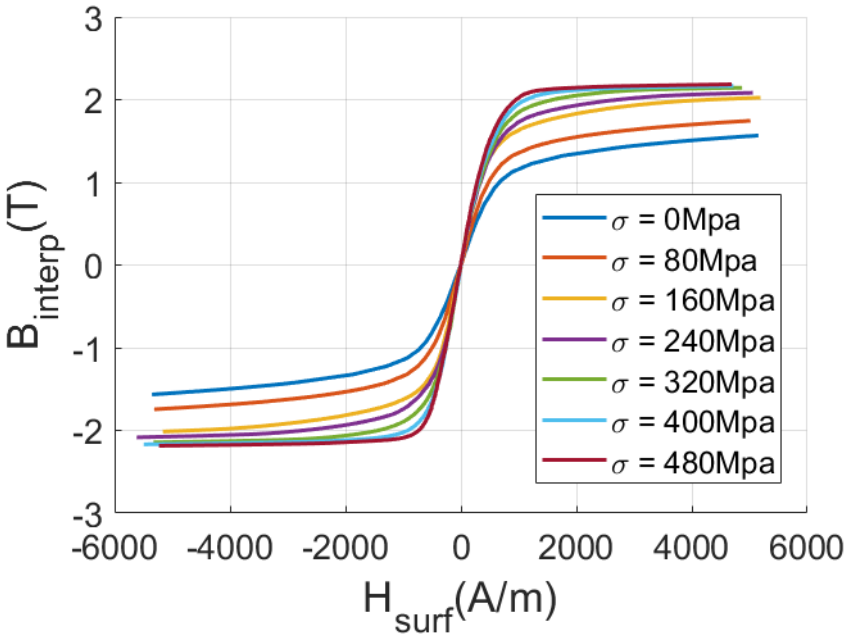

Figure 3-4: Obtained experimental Anhysteretic Curve

3.4 Simulation Method of The Tensile-Stress-Dependent Anhysteretic Behavior

3.4.1 Magnetomechanical Behavior Models

Any shift in the magnetization of a magnetic material resulting from the application of mechanical stress; either compressive or tensile stresses, is considered as a magnetomechanical effect. The fundamental coupling between the mechanical stress and magnetic properties of ferromagnetic materials tells of the reciprocity between the magnetic microstructure (magnetic domains and domain walls) and the mechanical microstructure (stress and strain fields) as well as its magnetostrictive dependence. Thus, the magneto-mechanical behavior of magnetic material in mechanical stress[162]. The magnetic hysteresis plays an important role in the field of magnetism, so the pertinence of a magnetic model to adequately replicate the intrinsic behavior of ferromagnetic materials. Magnetomechanical models are important for magnetostrictive materials due to their non-linear behavior, hysteresis, and coupling, which severely reduce their related device design and applications[163]. So far, several complex models have been developed in the literature to reproduce the behavior of

these materials under the effect of mechanical stress[150]. In this part, we are going to focus only on anhysteretic behavior models. Early investigations in the field of magnetism considered several possible explanations for the phenomenon of ferromagnetic hysteresis. These hypotheses fell broadly into two categories [164], one of which suggested that a frictional type force is responsible and the other considering hysteresis as due entirely to the strong mutual interactions between the individual magnetic moments.

It is known to be a tough task to describe the behavior of magnetic materials under the influence of an applied field and its field exposure history by hysteresis modeling. The complexity arises because of the multiplicity of magnetization processes that can occur simultaneously within a magnetic material when exposed to a magnetic field. These processes can be reversible and irreversible and can arise from domain magnetization rotation, domain boundary motion, or both; at least four types of magnetization processes usually occur at any given time. So far, to study the magneto-mechanical effect, an analytical approach and a theoretical approach have been adopted.

For the analytical approach, models represent the non-linear behavior of ferromagnetic materials as determined from empirical data. Nevertheless, several analytical simulations of magnetic materials are introduced with limited validity. Analytical models share little or no theoretical base for physical interpretation.

Theoretical methods of approach are based on the mathematical description of hysteresis of any physical nature (where the parameters are obtained by fitting model parameters to experimental data), or on micro-magnetics theory. These methods are arbitrary and are time-intensive[165].

For instance, in [36][37], the multiaxial effect of stress is performed using an equivalent stress concept and uniaxial models. Even though this modeling approach can be successful for some configurations, it does not give a general description of the magneto-elastic behavior and can be inaccurate in in case of high exciting field values [137].

A modeling approach is a multiscale approach, where local free energy at the domain scale is considered to get the macroscopic magneto-elastic behavior [114].

Another approach is obtained by defining a Helmholtz free energy density, i.e., a function of five scalar invariants of the magneto-mechanical loading [78]. Here, the constitutive relationships of the material are obtained by minimizing this energy.

In [168] and [169] nonlinear function was proposed to describe the magnetic behavior of Terfenol-D. A biphasic model was developed in [170] for Metglas 2605SA1, which emphasizes a mathematical description rather than a phenomenological approach. This approach uses a hyperbolic tangent function and a linear term to describe the sigmoid shape that fits well with the magnetic hysteretic curves of considered magnetostrictive materials.

All these modeling methods are accurate and, most of them are time-predictive, but remain challenging to implement because of their computational cost, the required input data, and the delicate identification process. In this study, where the experimental tests were limited to uniaxial tensile stress, we left them aside and opted for a simplified physical method described in the next section.

3.4.2 Proposed Model of Anhysteretic Behavior

This section focuses on the investigation of an analytical method for the characterization and prediction of the Permendur sheets' converted energy density under different stress levels based on the performed experimental measurements. The simulation method will be used afterwards to assess nonlinear effects like saturation, and permeability to check its validity.

As the ultimate goal of the present study lies in the energy conversion assessment in the framework of energy harvesting, the hysteresis property was not considered first. Indeed, only unipolar magnetization variations (anhysteretic behavior) are induced by energy harvesting applications, limiting the hysteresis losses. This approach has already been proven effective since it allows obtaining analytical equations describing the energy conversion mechanism [171], thus facilitating the whole system optimization.

Among the already existing modeling possibilities and considering the material characteristics (effect of stress and negligible hysteresis among others), we decided to

adopt a simplified anhysteretic model based on a thermodynamic approach presented by Agayan in [171] to relate the anhysteretic behavior of Permendur under mechanical stress. This model focuses more on a mathematical formulation rather than a phenomenological approach, which allows for describing the physical meaning of each variable as well as highlighting potential interconnections in the different physical domains.

Based on that, the objective is to obtain a fitting curve describing the anhysteretic behavior obtained through curves reconstructed from experimental measurements shown in Figure 3-4. These data are limited to the intermediate H_{surf} excitation level, and so is the simulation method. We decided to limit the simulated excitation level because the behavior of the material for the high-level excitation field remains unknown. The anhysteretic curves obtained from experimental measurements are denoted as interpolated curve $B_{interp}\ (H_{surf})$ in Figure 3-4 and are similar to sigmoid functions. Multiple analytical functions were tested. Hyperbolic Arctangent gave the best results. The expression inside the function is the magnetostriction effects on the magnetic behavior. The resulting analytical expression, including the stress σ and the magnetic field H_{surf} dependency [172], is presented by Eq.(2-2).

$$B_{model}(H_{surf},\sigma) = \{(1 + d \cdot tanh(e \cdot \sigma)) \times \alpha atan[\beta \cdot H_{surf} \times tanh\,(\kappa \cdot \sigma + 1)]\} \qquad (3\text{-}2)$$

Where α is the magnetic flux density saturation of the nonlinear part of the curve, β is the small signal slope of the nonlinear part, κ describes stress effects on the magnetic permeability in the linear range, and *d* and *e* are two material parameters.

The impact and significance of the parameters in Eq. (3-2) are presented in the following section.

3.4.3 Determination and Evolution of the Model Parameters

The model parameters were determined using the MATLAB® Curve Fitting Toolbox. To do it, the reasonable range of the parameter values was first estimated, along with a consistent and realistic working point. The conditions filled, using the Nonlinear Least Squares Method and the True-Region algorithm, the toolbox provided

the optimal set of parameters to align the equation with the anhysteretic curves derived from the experimental data at various stress levels.

The various model parameters are presented below:

- **The Parameter α**

α represents the maximal flux density at H_{surf} = 5000 A·m^{-1} (intermediate H_{surf}) and σ = 0. For very soft magnetic materials, where saturation is reached at very low magnetic excitation, α can be assimilated to $\mu_0 \cdot M_{sat}$, where M_{sat} is the magnetization saturation [172]. It is not the case for the Permendur, and both quantities must be distinguished.

- **The Parameter β**

β is the small signal slope of the nonlinear part. It is associated with the material's permeability in the Rayleigh region (i.e., in the low magnetic field amplitude).

- **The parameters d and e**

The influence of stress σ on the magnetic flux density B_α is considered through two contributions:

  - The first contribution consists in the modulation of parameter α by the hyperbolic ($1 + d \cdot tanh\ (e \cdot \sigma)$) function, where d and e are two material parameters: d is associated with the maximal flux density variation that tensile stress can induce, while e is its variation rate. We opted for a sigmoid shape function as the influence of stress is high in the low range of σ, then decreases and saturates for very high σ due to domains' reorganization.
  - The second contribution comes from the modulation of parameter β by the tanh($\kappa \cdot \sigma + 1$) function. It's the stress effect on domain alignment at low magnetic field region.

- **The Parameter κ**

κ denotes how stress affects the magnetic permeability in the linear range, and can also be seen as the manifestation of magnetostriction.

Finally, Eq. (3-2) parameters have been identified by performing a curve fitting from the preliminary experimental results, leading to values in Table 3-3.

Table 3-3: Simulation method parameters

Parameters	Value
α	*1.02 T*
β	*0.002 A·m^{-1}*
κ	0.0023×10^{-6} *Pa^{-1}*
d	*0.464*
e	0.0043×10^{-6} *Pa^{-1}*

Figure 3-6 represents the experimental and the modeled curves for $\sigma \in [0 – 480]$ MPa. Good agreement is observed between the anhysteretic curves derived from the experimental measurements and the model prediction.

Since the obtained model was based on some assumptions, its validation is consolidated through the investigation of some typical physical parameters of Permendur, common to both anhysteretic and hysteresis behaviors. That will be the purpose of the next section.

3.5 Validation of the Model

To validate our model many studies were performed and a comparative analysis was conducted with those of the literature.

3.5.1 Error Analysis between Modelling and Experimental Curves

For comparative analysis, we computed the error analysis between the modeled and the experimentally derived anhysteretic curves for a particular stress value.

To assess the error, we used the coefficient of determination defined by R^2. It is a statistical measurement that examines how differences in one variable can be explained by the difference in a second variable when predicting the outcome of a given event. In other words, assesses how strong the linear relationship is between two variables and is heavily relied on by investors when conducting trend analysis[173]. The model's coefficient of determination R^2 was given by MATLAB and it was used to check the simulation method's accuracy. An R^2 value closer to 1 is an indication of better data

fitting [174]. The given value was **0.9991,** which confirms the simulation method's high accuracy.

3.5.2 Effects of Tensile stress on the relative permeability in the low magnetic field region.

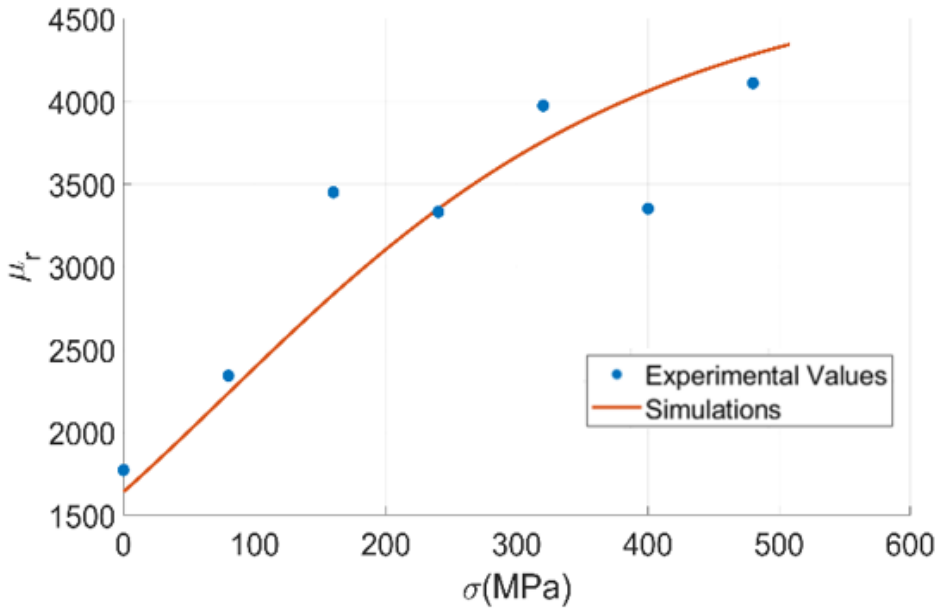

depicts the low-field relative permeability as a function of the applied stress and magnetic field. The low field permeability experimental value $\mu_{r\,exp}$ (Eq. (3-3)) was obtained by measuring the slope of the B_a (H_{surf}) curve for H_{surf} = 0 A·m^{-1}:

$$\mu_{r\,exp}(\sigma) = \frac{\Delta B_a(H,\sigma)}{\mu_0 \cdot \Delta H_{surf}} \tag{3-3}$$

The value $\mu_{r\,sim}$ which is the low field permeability obtained from the model by performing the first-order derivation of $the\ B_{model}$ is given by Eq.(3-4).

$$\mu_{r\,sim}(\sigma) = \frac{dB_{model}(H,\sigma)}{dH_{surf}} \tag{3-4}$$

Eq.(3-5) shows the final resulting value of the modeled value of permeability at a low field.

$$\mu_{r\,sim}(\sigma) = \frac{\{(1 + dtanh(e\sigma)) \times [\beta H_{surf} \times tanh\,(\kappa\sigma + 1)]\}}{\mu_0} \tag{3-5}$$

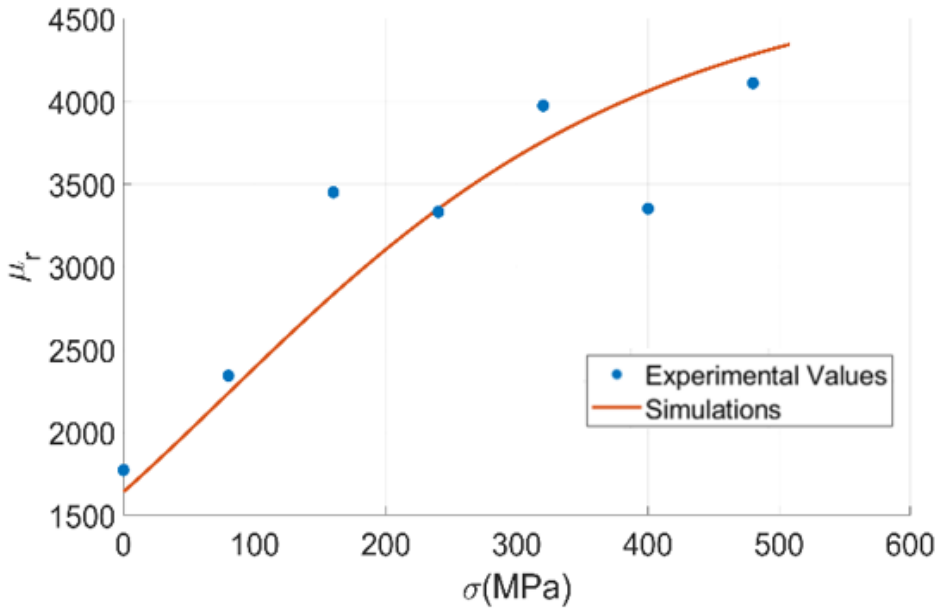

Figure 3-5: Tensile stress dependency of the relative permeability in the low magnetic field region.

shows good agreement between the fitted curve and the theoretical predictions. However, since we are working at a relatively high value of the magnetic field, meaning a relatively constant value of permeability, the observed deviations are considered negligible. It can be noted that, in the considered elastic stress region, low-field permeability increased with the tensile stress following the physical mechanisms behind magnetostriction explained previously in Section 3.3.2.

This low-field equivalent permeability thus ranged from $1350 \times 10^6 \mu_0$ for the stress of 0 MPa to approximately $3340 \times 10^6 \mu_0$ for 480 MPa. This effect has already been studied in reference [175], which is consistent with the effect of stress on the magnetic moment, as previously stated. Therefore, the effect of stress on the variation of magnetic flux density is not linear, which has also been observed in other materials such as FeCo-2V and FeSiNO studied in [133].

Another parameter to study is the value of the magnetic flux density for a maximum magnetic field intensity.

3.5.3 Value of Ba at Hsurf = 5000A.m^{-1}

Figure 3-7 shows the flux density B_a level when H_{surf} is maximum. Again, both modeled and observed values follow the same trend. While strong nonlinearity in the form of the hysteresis effect is not considered, as it could be considered negligible in the situation of energy conversion, soft nonlinearities arose as the magnetic responses started saturating above 3200 A/m. Similarly, the application of tensile stress tended to widen the range of the excitation field where the response can be considered linear. Such behavior is again consistent with the previously exposed physical effects. Yet, no clear and pronounced saturation was observed in the range of the excitation field of interest. The figure confirms that the material does not reach saturation for the same magnetic excitation. In that zone, we are still at the pre-saturation level. Another noticeable point is the tendency of magnetization to converge for all mechanical stresses for excitation fields around a certain point. The point may be the subject of further studies. While such results are qualitatively predictable, as the fully saturated magnetic state is independent

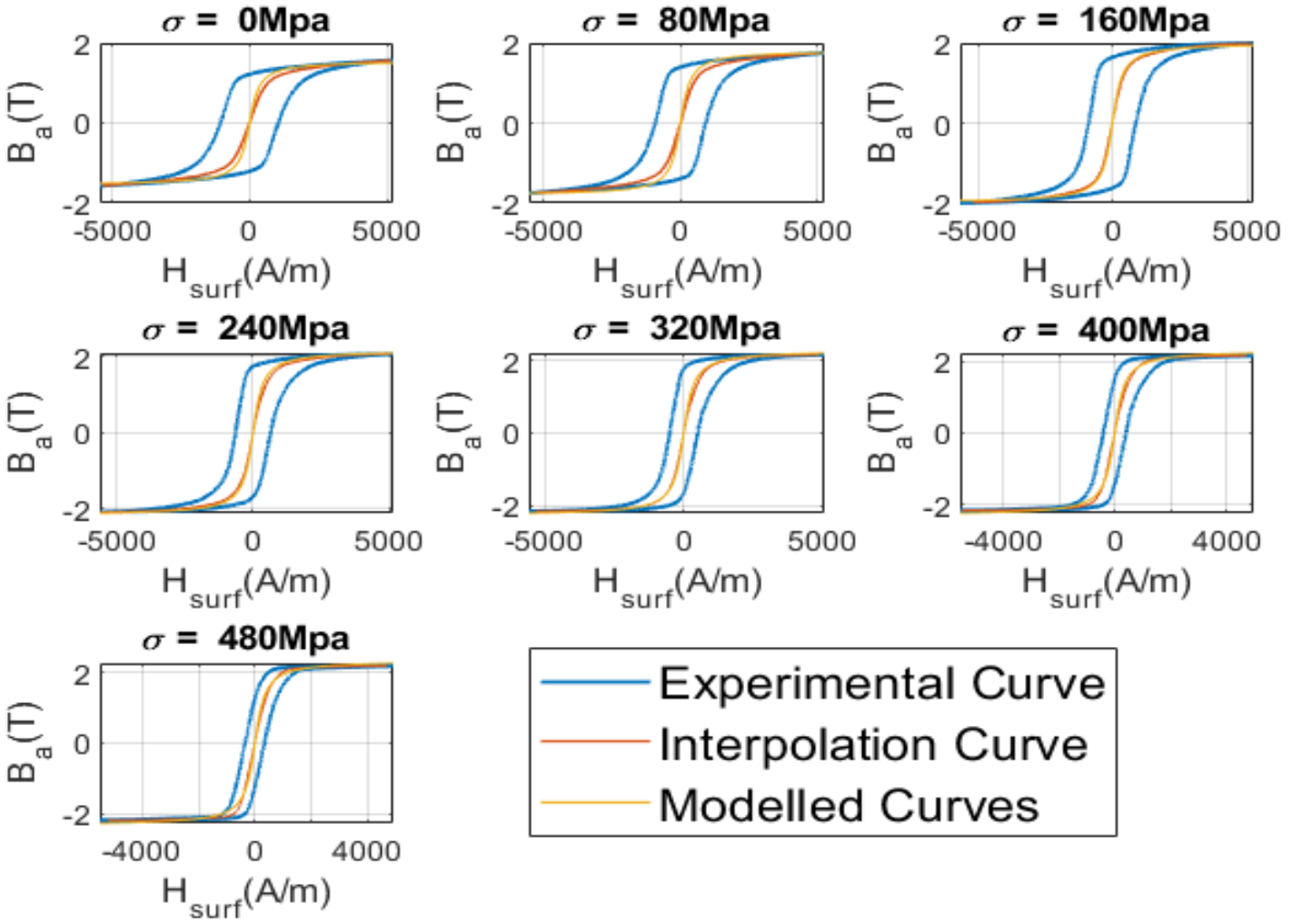

Figure 3-6: Comparisons between the experimental measurements, the reconstructed anhysteretic curves, and the simulation results.

of mechanical excitation, these results give relevant quantitative considerations for practical harvester applications.

From the previous analysis, we saw that the model encompassing tensile stress could fit well with anhysteretic curves derived from experimental results, not only for the linear part in the low magnetic field range but also considering the 'pre-saturation' part for higher magnetic field levels. Finally, a good agreement between experimentally derived and modeling results can also be observed as the stress is varied, although some slight discrepancies appear. However, these discrepancies are negligible so the proposed model can provide a relevant theoretical framework for the energy conversion ability assessment of Permendur. The next section of the chapter will then be consecrated to investigate the energy conversion capabilities of the Permendur under mechanical stress using the validated model and the experimental anhysteretic curve.

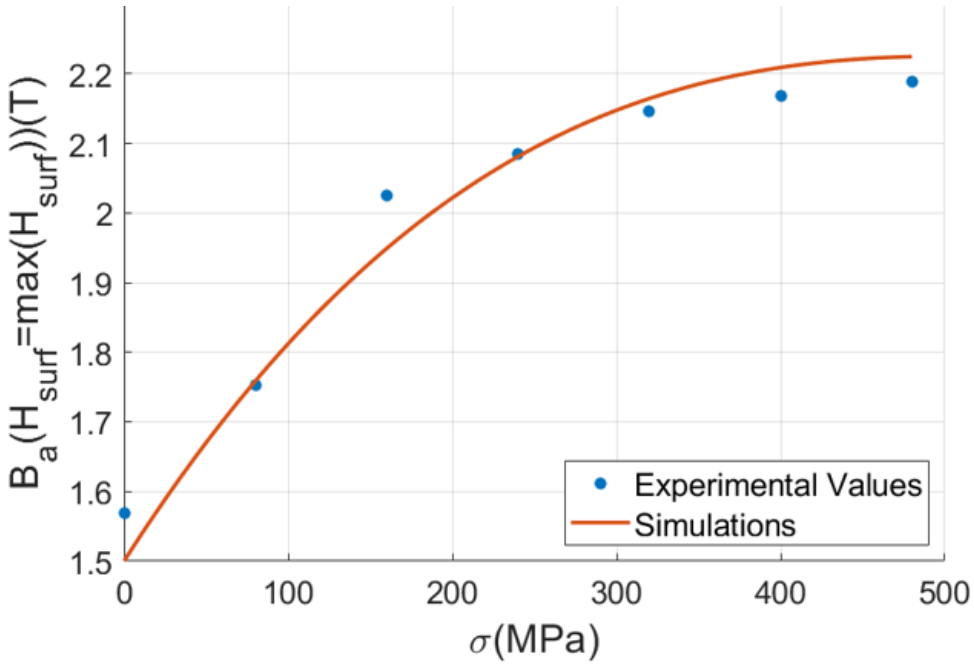

Figure 3-7: Tensile stress dependency of the flux density at Hsurf = 5000 A·m-1

3.6 Energy Conversion Density Assessment

Based on measurements previously performed on Permendur and the general theoretical framework exposed in the previous section, this part investigates the energy conversion potential of the material for energy harvesting applications using 3 approaches:

- Energy estimation from simulated anhysteretic Curves
- Energy estimation from hysteresis cycles
- Energy estimation from Experimental Ericsson cycles

3.6.1 Estimation from the simulated anhysteretic curves

Experimental results (section 3.3) showed an explicit dependency between the magnetic flux density B_a, the applied tensile stress σ, and the excitation field H_{surf}. This section investigates how these relations can be optimally exploited from the material electromechanical energy conversion point of view. More specifically, the converted energy (available energy for extraction in a harvesting process) by the Permendur will be assessed, emphasizing the nonlinear effect of both the magnetic and mechanical excitations.

For simplicity, we considered only the purely magneto-mechanical conversion without the electromagnetic one, similar to other studies devoted to magneto-rheological elastomers [172]. Although it forbids taking into account the effect of harvesting, it allows being independent of the number of turns of the coil, for instance, hence giving a fair basis for material comparison.

The calculation of the ultimate converted energy during one cycle was considered to assess the energy conversion capability [17][55]. More precisely, this assessment was performed assuming a thermodynamic cycle close to the equivalent Ericsson cycle. An Ericsson cycle consists of two steps that are performed under constant stress and two other steps that are performed under constant magnetic excitation as illustrated in Figure 3-8.a. [33][34]. By performing an analogy between Figure 3-8 (b) and Figure 3-8 (a), it shows there is a possibility to reconstruct an Ericsson cycle from a pair of anhysteretic curves acquired at various stress levels. The constant stress steps follow the anhysteretic trajectories. The constant field steps represent vertical jumps from one anhysteretic curve to the other. The area enclosed by the resulting Ericsson cycle then represents the converted energy density. Beyond a threshold level in the high field range, the stress and no-stress anhysteretic curves merge, as depicted in Figure 3-8 (b). Application of larger fields will thus not modify the energy density beyond this level and the resulting Ericsson cycle area can be regarded as the material's ultimate energy density.

During the first step (1 – 2), the magnetic excitation field is increased to a value H_M while the stress is kept constant at σ_{max}. During the second step (2 – 3), the excitation field H_M is kept constant, and the stress on the material is reduced to σ_{min}. The magnetic induction field decreases in this stage, as shown in Fig. 8 of [172]. During the third step (3 – 4), the excitation field decreased to zero while the stress remained constant at σ_{min}.

The closed loop area in the $B_a(H_{surf})$ diagram (cycle 1 - 2 - 3 - 4 in our case) corresponds to the energy converted from mechanical to magnetic energy. The maximum potential extractable energy between σ [0 - 480 MPa] and H_{surf} [0 - 5500 A·m^{-1}] is then determined, as shown in Figure 3-8. b.

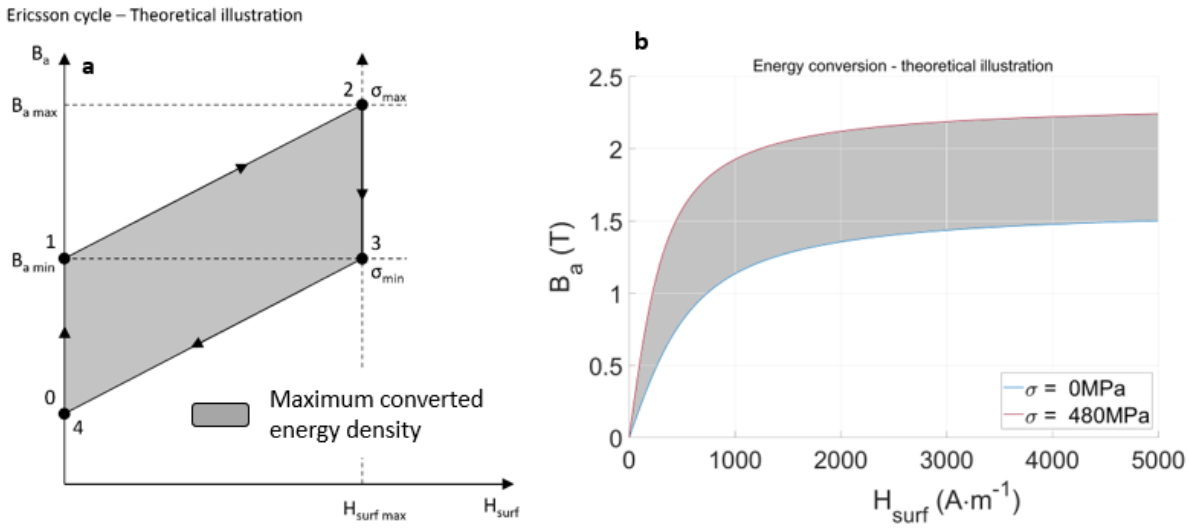

Figure 3-8. a) – Illustration of the thermodynamic Ericsson cycles used to estimate the energy conversion capability; b- Extractable energy vs. H_{surf} and for different tensile stress levels.

For a single cycle, the energy density W is given by Eq(3-6) and Eq(3-7) :

$$-W = \int H_{surf} \cdot dB_{loop} \tag{3-6}$$

$$W = \int_0^{H_M} -\Delta B_a \cdot dH_{surf} \tag{3-7}$$

Eqs. (3-6) and (3-7) are the ferromagnetic dual expression of Eq. 2 in [179] and Eq. 1 in [180], where the Ericsson cycle principle is applied to a ferroelectric conversion. Eq. (3-7) leads to the graph shown in Figure 3-9 beyond a threshold of approximately H_{surf} = 250 A·m^{-1}. For all stress levels, the converted energy follows a quasi-linear

trajectory as the magnetic flux density does not vary significantly for a given stress level. The relatively weak difference between both extreme values of stress is noteworthy.

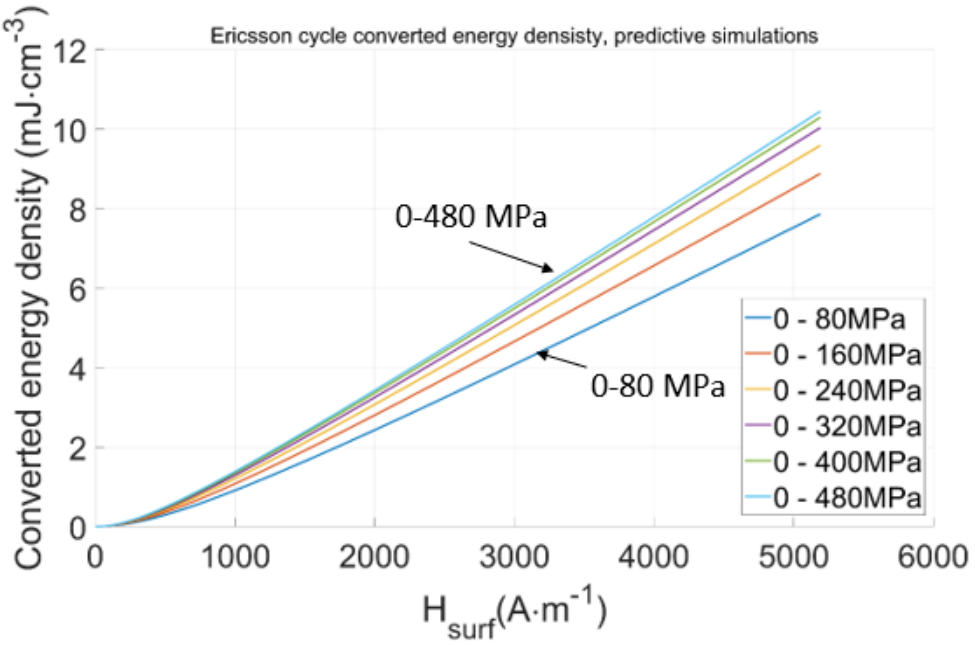

Figure 3-9:Ericsson cycle converted energy density vs. H_{surf}, based on the reconstructed anhysteretic curves and for different stress levels.

Table 3-4 summarizes the maximum converted energy obtained with the anhysteretic curves method, considering a magnetic excitation field of max (H_{surf}) = 5500 A·m^{-1} and different stress levels. As observed in Figure 3-9, Table 3-4 confirms the relatively weak influence of the stress level beyond 240 MPa.

3.6.2 Direct energy estimation from the $B_a(H_{surf})$ hysteresis cycles

The previous section described a method to estimate the Ericsson cycle energy densities using the anhysteretic curves reconstructed from $B_a(H_{surf})$ cycles under low and high stresses, respectively (1 – 2 – 3 – 4 cycles in Figure 3-8. a). However, this estimation is inaccurate as the hysteresis losses are not considered. This section proposes a further step to truly evaluate the energy conversion through an alternative semi-empirical estimation (Figure 3-10). The red curve represents the area between the descending curves for two various values of stress. The ascending curve of the $B_a(H_{surf})$ hysteresis loop under high tensile stress, denoted $f(H_{surf})$, is shifted upward to become $g(H_{surf})$ and is considered equivalent to a first-order reversal curve [181]. Hence, the estimated Ericsson cycle became the B1 – g(H_{surf}) – C – D – B1 cycle (Figure 3-10), and $g(H_{surf})$ is

calculated from $f(H_{surf})$ according to Eq(3-8). This equation has not been derived from any other equation and was proposed to reproduce closely the first-order reversal curve shape.

$$g(H_{surf}) = f(H_{surf}) \cdot \frac{B_2 - B_1}{B_2 - B_3} + B_1 - B_3 \cdot \frac{B_2 - B_1}{B_2 - B_3} \quad (3\text{-}8)$$

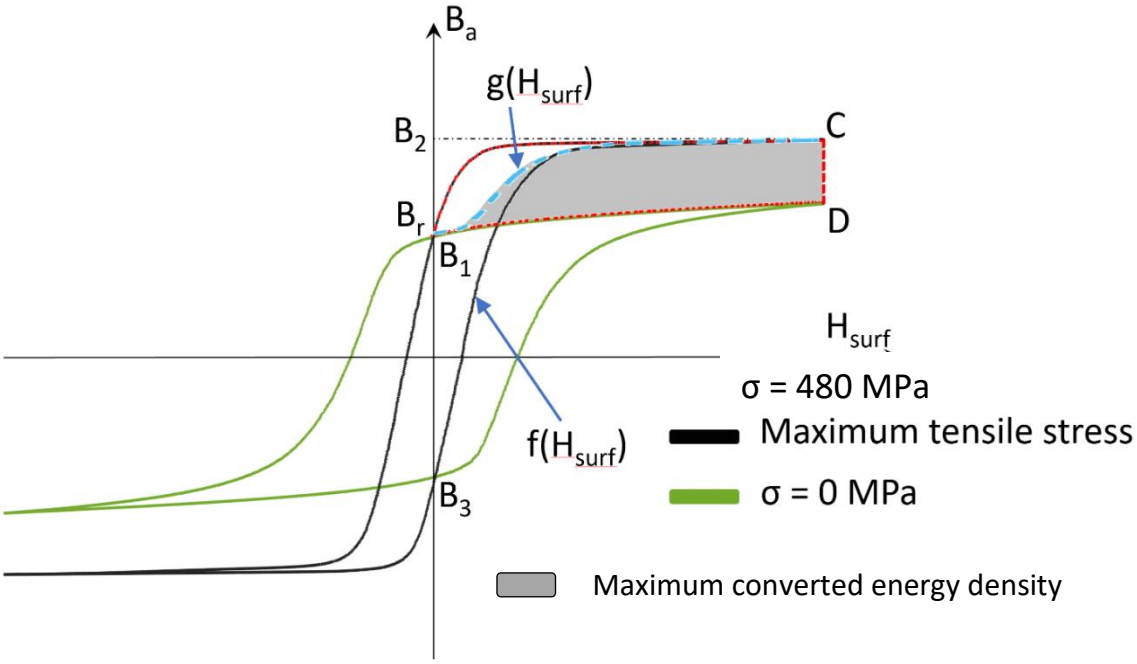

Figure 3-10: $B_a(H_{surf})$ hysteresis loops at σ = 0 MPa and high tensile stress. Illustration of the B1- $g(H_{surf})$ -C-D-B1 Ericsson cycle as obtained from these curves.

Table 3-4: Maximum Ericsson cycle converted energy density for different stress levels, as obtained with the reconstructed anhysteretic curve and the hysteresis loop methods.

σ (MPa)	Max. energy density – anhysteretic method (mJ·cm^{-3})	Max. energy density – hysteresis loop method (mJ·cm^{-3})
0-80	7.86	1.37
0-160	8.89	2.59
0-240	9.6	2.95
0-320	10.04	3.28
0-480	10.45	3. 52

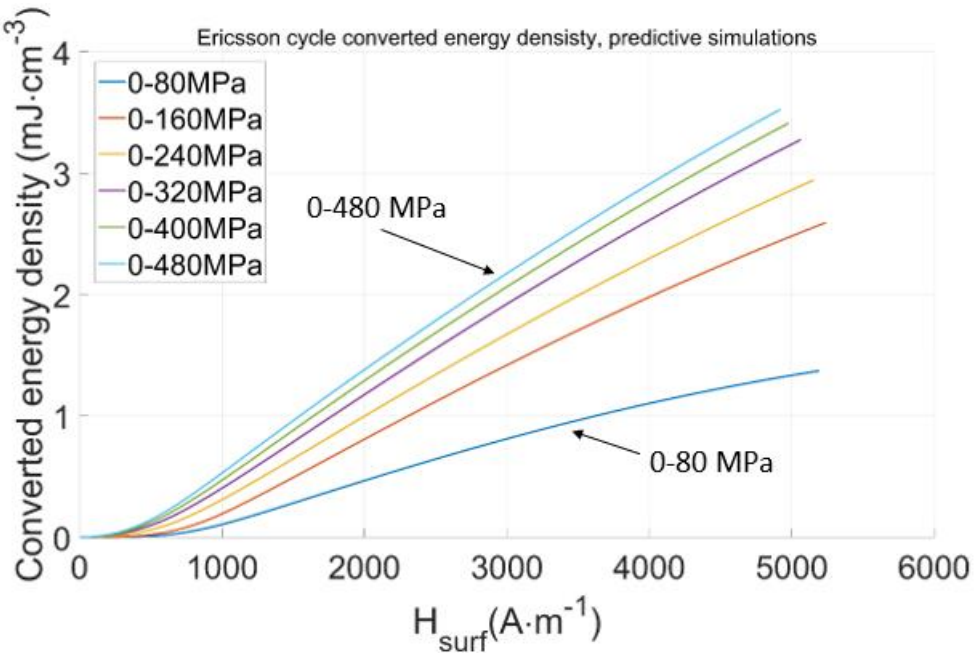

Figure 3-11:Ericsson cycle converted energy density vs. H_{surf}, based on the hysteresis loop measured at different stress levels.

The semi-empirical estimation method shows a larger stress influence yet a much lower converted energy. However, beyond a threshold level close to 300 MPa, a pseudo-saturation is reached, and the variation from one stress level to the other is less significant. Comparing Figure 3-9 and Figure 3-11 allows us to highlight the hysteresis loss impact on the level of converted energy. The dependency is especially remarkable under low-stress levels, dividing the amount of harvested energy by more than 30% when σ is lower than σ = 160 MPa. Table 3-4 establishes a comparison between the maximum energy converted between the anhysteretic and the hysteresis loop methods (max (H_{surf}) = 5500 A·m^{-1}).

3.7 Experimental validation of the Ericsson Cycle

The final stage of this study consisted of the practical implementation of Ericsson cycles and measurement for the feasibility validation as an energy conversion system and confirmation of the theoretical energy level predictions. The experimental setup described above is versatile and allows magnetic and mechanical stress excitation to be imposed simultaneously. In the case of the Ericsson cycle, the magnetic field and mechanical stress chronograms are depicted in Figure 3-12.

Figure 3-13 shows the resulting Ericsson cycle (in terms of relative values, as the initial magnetic state of the tested specimen was unknown), and Figure 3-14 shows the evolution of the harvested energy density for σ = 175 MPa. It is worth mentioning that the tensile stress level was limited to avoid drifts observed beyond σ = 175 MPa, which yield open Ericsson cycles.

As forecasted, the semi-empirical estimation from the hysteresis loops is more accurate in its prediction than the anhysteretic ones. More than 4 mJ·cm^{-3} is reached, and it seems reasonable to anticipate up to two times this amount in higher stress conditions. Working points 1 to 4 in Figure 3-12 are reported in Figure 3-13 for illustration.

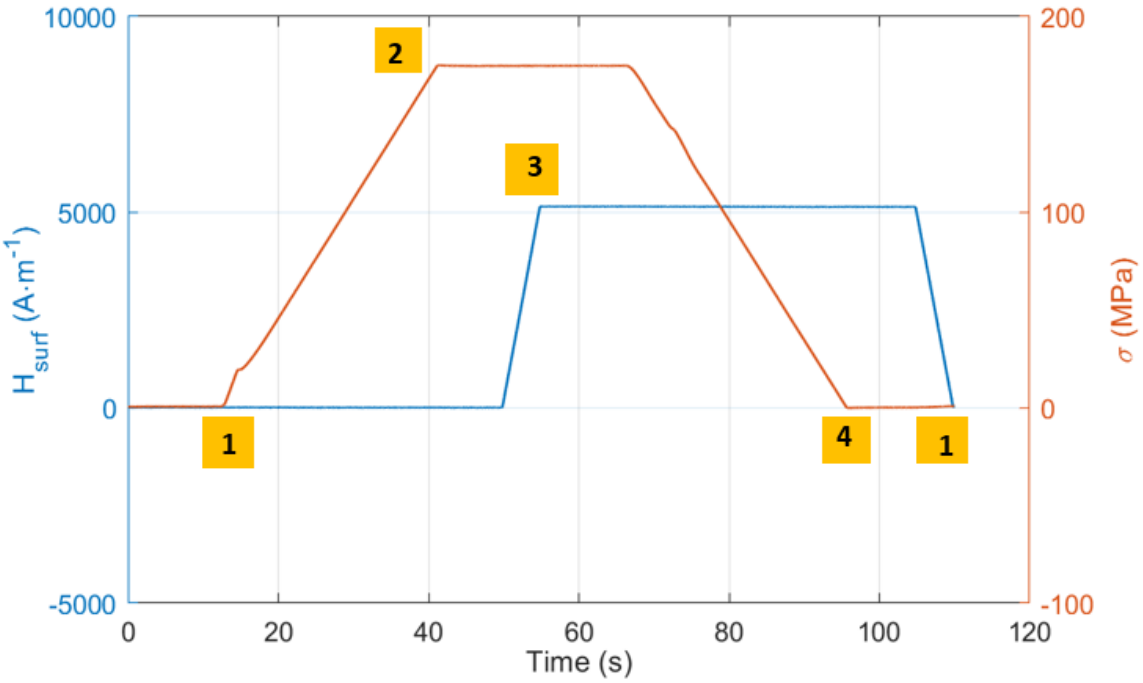

Figure 3-12: Experimental Ericsson cycle magnetic field H_{surf} and stress σ chronograms.

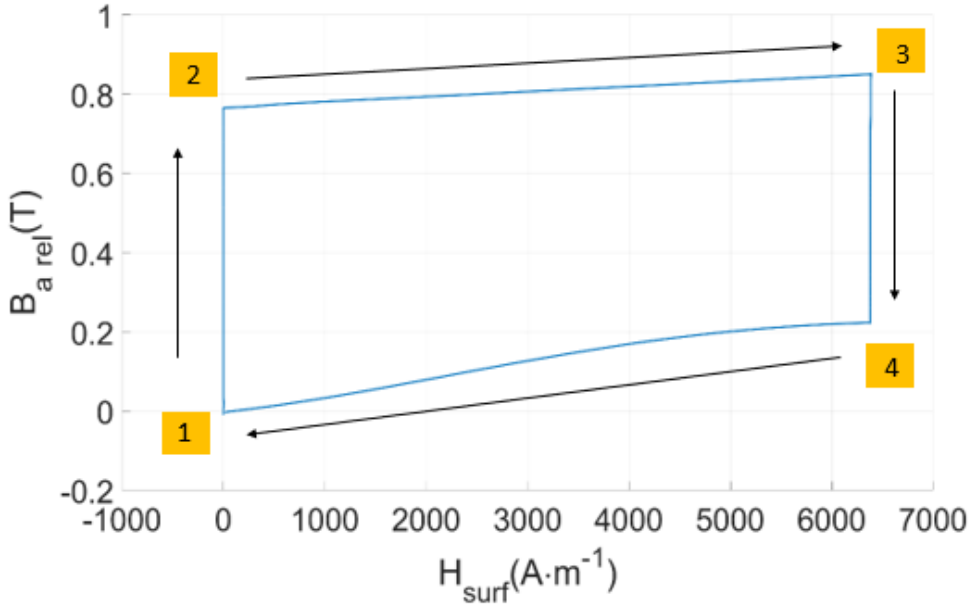

Figure 3-13:Experimental Ericsson cycle (max(H_{surf}) = 6400 A·m^{-1}, σ = 175 MPa).

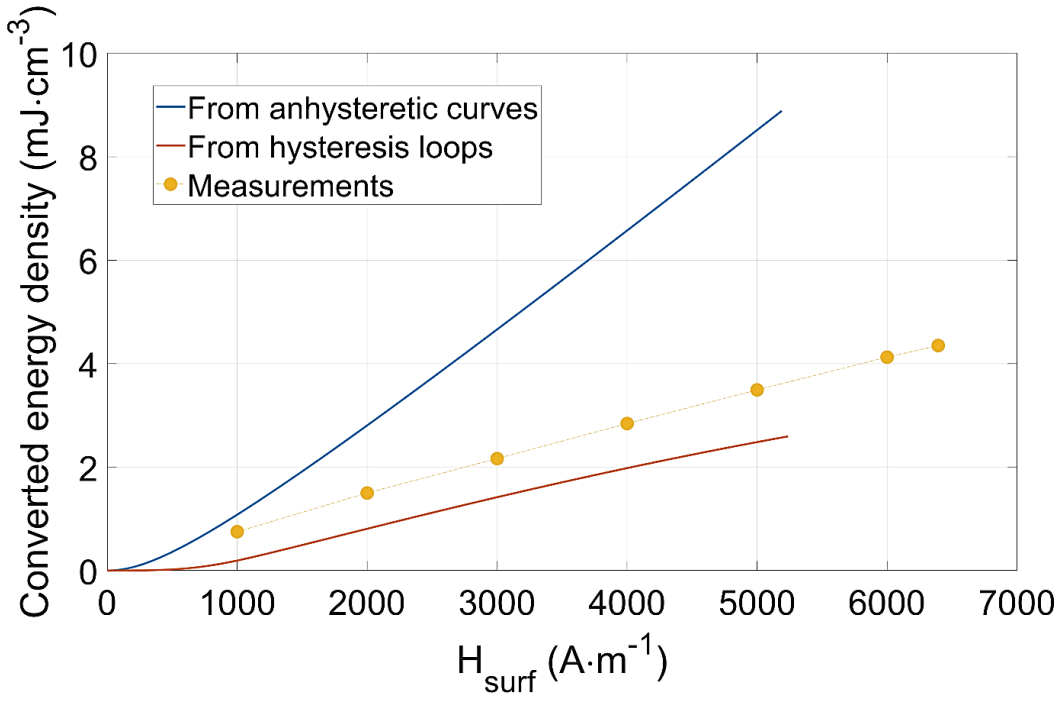

Figure 3-14:Converted energy density vs. H_{surf}, comparisons predictions/measurement (σ = 175 MPa)

The estimation method based on the Ericsson cycle helps give a proper description of the ideal energy harvesting process and estimate the maximum energy for a specified range of magnetic fields and stress levels. An appropriate system for ultimate Ericsson

cycle assessment could potentially be envisaged for higher power cases similar to electrical machines (kW range) but is not reasonable within the energy harvesting framework (which currently is far below 1W). Therefore, it cannot provide information about the feasibility of electrical/magnetic interfaces and can only be used to perform basic comparisons between the materials

3.8 Conclusions

Due to their robustness and potential electromechanical coupling, magnetostrictive materials are a competitive solution for vibrational energy harvesters. Yet, their realistic implementation, mainly due to the material price as well as a deep understanding of their conversion efficiency, is still an open question. Low-frequency mechanical energy conversion based on tensile stress application to magnetostrictive Permendur material was investigated in this part. Permendur is highly magnetostrictive, low-cost, and abundant, yielding an ideal candidate for energy conversion applications in microgenerators. Tensile stress tests were performed as a first step and used as experimental bases for establishing theoretical tools. A simulation method was proposed based on an analytical function describing the effects of stress and magnetic field on the anhysteretic magnetization curve. The formula requires only two material parameters with high-level physical meaning (saturation field and permeability). The obtained simulation results were proved to be in good agreement with experimental ones. Then, using Ericsson cycles, the energy conversion was predicted from the calculated anhysteretic curves. A maximum of converted magnetic energy was forecasted to be equal to 10.45 $mJ \cdot cm^{-3}$ under a tensile stress of σ = 480 MPa and a magnetic excitation of 5.5 $kA \cdot m^{-1}$. Yet, Permendur coercivity is not so small and will result in core losses that greatly reduce the conversion efficiency. Still, when the stress is tensile, the comparison with recent results on a very soft Metglas material [170] shows that the influence of coercivity on the energy conversion process is minor. The effect of the stress when saturation starts is much more influential, though. Hence, a relevant solution consists of a permanent magnet bias field to shift the working condition in the saturation zone where hysteresis is significantly reduced and the stress influence is still substantial.

Then, to consider hysteresis, another experimental estimation of the converted energy density was proposed based on hysteresis loops. An energy density of up to 3.52 $mJ \cdot cm^{-3}$ was obtained in the same conditions. This value appears to be excessive compared to the Galfenol and Terfenol-D results depicted in Table 3-1, but the experimental conditions are entirely different ($\sigma < 10$ MPa in [160], for example), making the comparison delicate. This value can also be compared to other energy conversion processes, such as piezoelectric conversion, where the energy density may reach hundreds of $mJ \cdot cm^{-3}$ [37]. The difference in the order of magnitude may be attributed to the relatively high electro strictive strain of ferroelectrics that may reach thousands of ppm or even close to 1% in some compounds.

Then, experimental Ericsson cycles were experimentally assessed to prove the feasibility and confirm the energy level predictions. The comparison between the predictive methods and the experimental tests showed an overestimation of the model based on the anhysteretic curve, especially in the high field range. The prediction based on the major hysteresis loops was much more accurate, especially in terms of the slope of the converted energy vs. magnetic field curve. The predicted value of converted energy as a function of the excitation field amplitude slightly underestimated the experimental result (4 $mJ \cdot cm^{-3}$) by a constant term, which can be attributed to the level of mechanical stress (slightly lower in the simulation: $\sigma = 160$ MPa vs. 175 MPa) or an overestimation of the hysteresis losses.

One of the limits of the magnetostrictive energy harvester is the need for significant stress variations and high magnetic field bias. But to overcome it, one can work on the optimum magnetic field value at the maximum magnetoelastic coefficient. Recently, a study [170] verified this on a magnetostrictive Metglas material where these ideal working conditions were obtained at a low magnetic excitation zone compared to Terfenol and Galfenol, which usually require bias fields higher than 20 kA·m-1 (Table 1 of [170]). For Metglas 2605SA1, a magnetoelastic coefficient of nearly 15 mT·MPa-1 was obtained at 100 kA·m-1, illustrating a realistic implementation of magnetostrictive harvesters. The development of a real energy harvester (*i.e.*, mechanical device and electrical interface) and assess the material effect on the next stages and conversely. This will be developed in the next chapter.

4 MAGNETOSTRICTIVE VIBRATION ENERGY HARVESTING: A DEMONSTRATOR

4.1 Introduction

Energy harvesting systems are a great alternative to batteries and their associated drawbacks, such as environmental concerns in the framework of self-powered wireless sensors [182], [183], [184] *and sensor networks in health monitoring* [185]*, cardio pacemakers* [186]*, transportation…. This chapter gives details on the principle, analysis, and characterization of an axial-type vibration energy harvester based on a magnetostrictive sheet Permendur (Fe_{49}-Co_{49}-V_2) sheet. We will start by presenting a review of some implemented vibration energy harvesters based on magnetostrictive materials in section 4.2 followed by the presentation and the modelling of our proposed vibration-based energy harvester (Section 4.3). In section 4.4, an improvement means of the output voltage is proposed. Finally, sections 4.5 and 4.6 respectively discuss obtained results and conclude the chapter.*

4.2 Review of Vibration Energy Harvesters

Vibration energy harvesting is a research field that attempts to study the process of generating electrical energy from wasted ambient energy or through recycling the discarded vibration energy that is usually lost or dissipated. This field of research could benefit from many practical issues; therefore, it brings a lot of interest from academic researchers as well as industrial companies. Presently, the output power of harvesting devices is still less than that of conventional batteries. However, recent developments in integrated circuit manufacturing, low-power CMOS circuits, and VLSI designs have significantly reduced the power demand of commercial wireless sensors from mW to μW [187]. Those changes improve the feasibility of vibration energy harvesting technology for practical applications and promote the creation of self-powered sensor nodes and other self-powered electronic devices. However, there are still few commercial products being used effectively. Wireless sensors have reduced power requirements of hundreds of μW in Mica (class of wireless sensor nodes) with projections into tens of μW. The maximum power for most wireless nodes is typically 200 mW, which strongly depends on the sensor node's sampling rate, transmission range, and transmission speed [3]. The energy consumption of a self-powered device usually requires a few mJ to perform its operation (Scavenger Transmitter Module). According to [4] typical power demands for temperature sensors lie between 0.5-5mW, and 2-3 mW for acceleration sensors.

As a non-exhaustive energy generation method, vibration energy harvesting can be categorized as a micro energy production technique, which converts vibrations induced by human motion, fluid flow, and mechanical equipment, among others, into usable electric energy [188]. While batteries are still used in the large majority of devices, the guarantee of long-term operations is made very complex due to the self-discharge of such energy storage systems. The multifunctional nature of the problem also permits the use of energy conversion devices for vibration suppression from the view of energy conservation [10,11]. In addition, the output voltage can be considered as a signal that carries data information depending on some situations, making the harvester into a special all-in-one self-powered sensor [12,13]. Nevertheless, the energy

harvesting capability and performance of the device are typically the priority in most applications. Presently, TbDyFe (commercial name Terfenol) is the most used magnetostrictive material because of its merits already presented in section 3.3.1 of chapter 3.

Regarding energy harvesting from a mechanical vibration source, several solutions have been proposed so far. Some make use of electromagnetic induction due to the linear relative motion of a permanent-magnet core into an external coil [12,13]. Other harvesting systems make use of the electrostatic conversion induction between capacitive movable plates [14,15]. But recently there has been a trend of exploiting the intrinsic properties of some materials like magnetostrictive materials which are capable of coupling mechanical variables with electrical ones. Based on this, vibration energy harvesters can be categorized into two classed based on the direction of applied stress or vibrations on the active materials. We can name them bending-type harvesters and axial-type harvesters.

4.2.1 Bending energy harvesters

Bending-type energy harvesters can extract electrical energy efficiently from any kind of vibrating surface [63]. The bending-type structure usually applies stress and strain to a beam made of a magnetostrictive material by bending [197]. The bending type can be classified into 2 subclasses:

4.2.1.1 Bimorph type

Bimorph energy harvesting devices use two beams or two pieces of the same material for the harvesting process. Ueno et al. [198] developed a Galfenol-based bending-type harvester. It was made of two parallel strips. The system is shown in Figure 4-1. A voltage is generated across the coils when a bending force is exerted on the mover. When the force is exerted, the structure bends like a cantilever, i.e., a compressive stress is applied to one beam, and a tensile stress is applied to the other in the longitudinal direction. The compression causes the magnetic flux to decrease while the tension increases as a result of the inverse magnetostrictive effect.

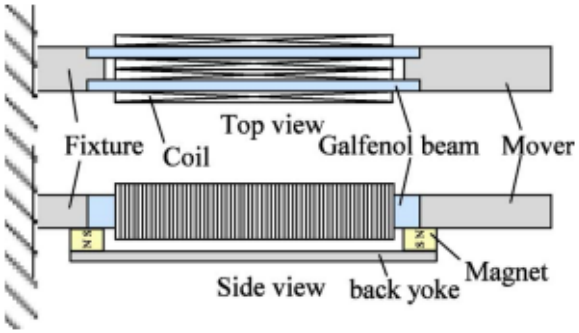

Figure 4-1:Configuration of the device [198]

From the experimental results, it has been shown that the efficiency of energy conversion of this device was 16% at 395 Hz. The experimental results also show that the maximum output power of 2 mW can be obtained at a resonant frequency of 395 Hz. the harvester can generate a maximum power of 3.5 mW. The limit of the work is that to obtain the resonant frequency we need a mechanical force at the mover to trigger. The efficiency of the system reduces with the frequency and in most real-life situations the frequency is really low. This then limits the application of the work for practical harvesters.

4.2.1.2 Unimorph type

Unimorph-type technology uses a single cantilever sheet to harvest electricity. Several prototypes have been implemented using this technology.

Zucca et al. [160] used a combined experimental and modeling approach to analyze the behavior of a transducer based on a rod of Terfenol-D. They developed a bending-type energy harvester where a longitudinal force was applied at the head of the moving part of the beam. In the paper, the influence of frequency, amplitude of vibrations, coupled electrical circuit, preload, mechanical, and magnetic biases on the output power and electrical current is presented. Added to it, the effects of coil characteristics and type of permanent magnets on the output power are also studied. Figure 4-2 presents a detailed and full view of the transducer and experimental setup.

The output power of the energy harvester was found to be 18 mW at an input frequency of 300 Hz. The existence of the mechanical preload increases the generated output power and is obtained for a maximum magnetic remanence of the magnets. The paper did not deeply investigate the effects of frequency, amplitude of the dynamic

stress, and electrical load. The effects of the magnetic bias were studied from modeling where details were not given.

Adly et al. [199] proposed a device for energy harvesting using vibrations from the environment using a magnetostrictive material. Even if most of the modeling efforts were focused on a linear approach, more complex and nontrivial phenomena like the behavior of the magnetization *M* are experimentally observed. It shows that the amplitude variation in *M* is linked to the converted power and is circumscribed within the anhysteretic curves of lower and upper-stress values and depends on the magnetic bias, the mechanical prestress and stress amplitudes. A sample of such nontrivial behaviors, suggesting the definition of potentially more effective models, is described and discussed. The obtained system had a maximum power of 0.44 mW at 50 Hz frequency at 8 MPa stress. The paper laid more emphasis on the accurate modeling of the material; which is also important in situations where we need an accurate description of phenomena happening during the energy harvesting at the material level.

Figure 4-2: Detail and full view of the transducer and experimental setup[199]

Wang et al. [187] proposed a vibration energy harvesting device using Metglas 2605SC. The developed system contains two submodules: an MsM (magnetostrictive material) harvesting device and an energy harvesting circuit. To increase the energy conversion efficiency and alleviate the need for a bias magnetic field, Metglas ribbons are transversely annealed by a strong magnetic field along their width direction this implies no need for a bias magnetic field hence reducing the harvester size. The system is shown in Figure 4-3 below.

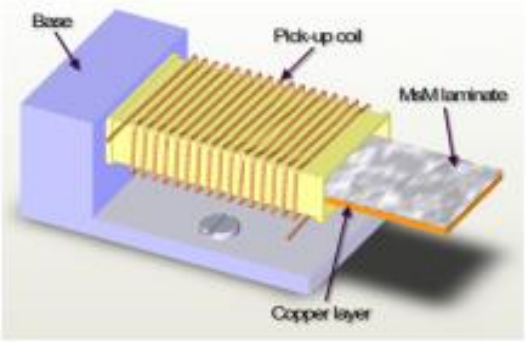

Figure 4-3: Prototype of the energy harvesting device[187]

Experimentally, the maximum output power and power density on the resistor can reach 200 µW, at a low frequency of 58 Hz. For a working prototype under vibration with a resonance frequency of 1.1 kHz, the average power during charging the ultracapacitor can achieve 576 µW and 606 $\mu W.cm^{-3}$ (based on the active material volume). The study doesn't mention the harvester conversion efficiency.

Kita et al. [200] have developed an unimorph-type Galfenol-based bending-type energy harvester. The operation principle is the same as described in [198]. A maximum of 35% conversion efficiency was achieved at an input frequency of 202 Hz and they had a maximum instantaneous power of 0.73 W and energy of 4.7 mJ. 25N impulse force was applied at the tip of the device. They also found that energy conversion efficiency not only depends on the force factor (conversion ratio of the electromotive force to velocity); but also, on the damping (mechanical loss due to inner mechanical properties such as viscous damping coefficient of the material) of the device. The study didn't specify or take into consideration the prestress and the magnetic field bias which are core elements in a magnetostrictive energy harvester.

4.2.2 Axial-type harvesters

Many axial-type harvesters have also been developed. Frequency bandwidth for axial-type harvesters is very limited and their optimal performance can be found only when these harvesters are installed along the load path.

Yamaura et al. [197] proposed a Fe-Co-V alloy vibration energy harvester with an impact-sliding structure. A magnetostrictive rod is fixed magnetically, not mechanically. The rod vibrates longitudinally at its inherent frequency as free vibration excited by an impulsive force. Figure 4-4 shows a schematic of the harvesting system.

The maximum output energy obtained in this work was 1.59 mJ, which was generated by a harvester with 3000 coil turns and two magnets under a load resistance of 3 kΩ. It was found that the maximum output energy was generated when the load resistance was close to the coil impedance at the inherent frequency of the axial vibration of the rod.

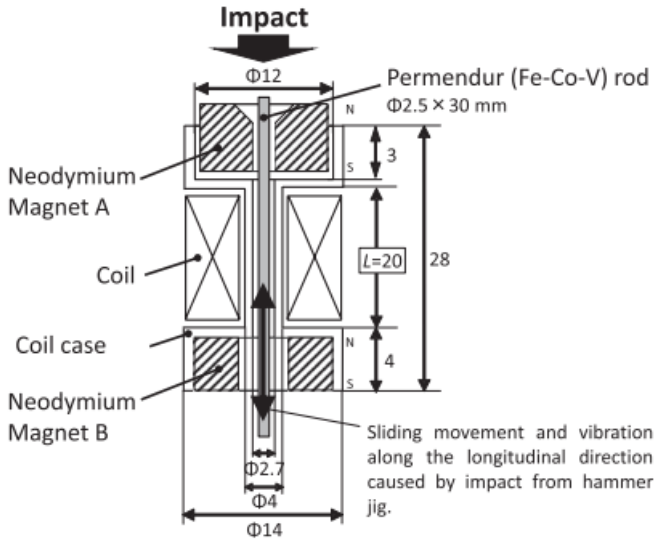

Figure 4-4:Schematic illustration of proposed power generation device with impact-sliding structure[197]

Liu et al. [201] made a similar structure using a pre-stress mechanism and the obtained energy harvester was installed and tested inside vehicle tires. To accurately describe the relationship between vibration force (stress) and output voltage in the giant magnetostrictive vibration-power generation process, a mathematical model is established based on the core principle of inverse magnetostrictive effect. To compute the energy conversion efficiency of the device, the authors proposed a computing

method of power generation efficiency. The obtained energy conversion efficiency of the prototype was 32.6%.

From the experiment, it was observed that the energy conversion efficiency first increased and then decreased as the resistance increased. One limitation of the paper is the restriction of the analysis at the level of experimental studies. Such a harvester for a practical case will need proper dimensioning.

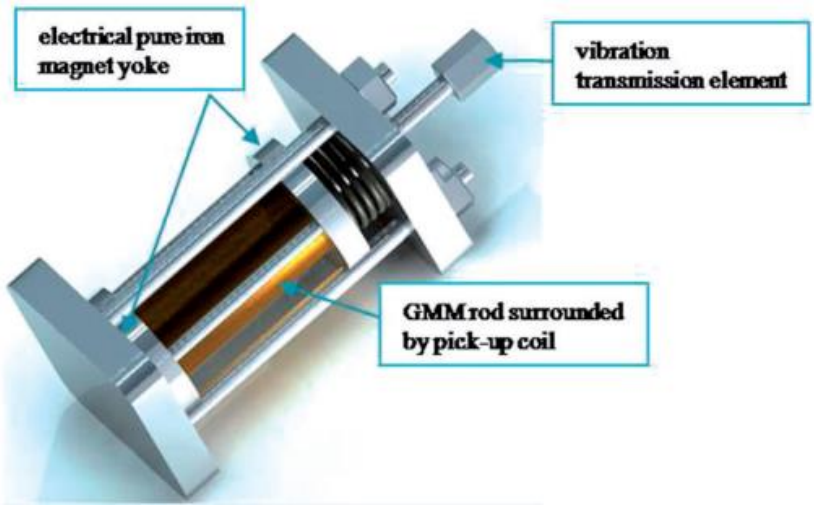

Figure 4-5: General structure of giant magnetostrictive vibration-power generation device developed in [201]

Ueno [202] developed a U-shaped vibrational Galfenol-based energy harvesting device made of a coil, permanent magnet, and U-shaped frame. The bending deformation of the frame induces in the magnetostrictive material successive tensile and compression stresses hence variation of the magnetic flux. At the first resonance of 166Hz, the average output power in that structure was 3.7 mW, and the maximum power was 9.1 mW for a load of 400Ω. One advantage of the developed conversion systems is that they are miniature, they can be easily moved from one application to another and is a good step towards commercialized energy harvesting devices. An efficient power management circuit can also be necessary for the system.

Berbyuk [203] developed an axial-type harvester. He inserted a 50 mm long and a 6.35 mm diameter Galfenol (at 18.4 % Ga) rod into a 4000-turn copper coil. The experimental setup is shown in Figure 4-6. Under optimized operational conditions and external excitations with a frequency of 50Hz the designed transducer generates about

10 V and harvests about 0.45 W power under a 50 Hz, 55 MPa amplitude sinusoidal stress. Within the running conditions, the Galfenol rod power density was estimated to be 340 mW/cm^3.

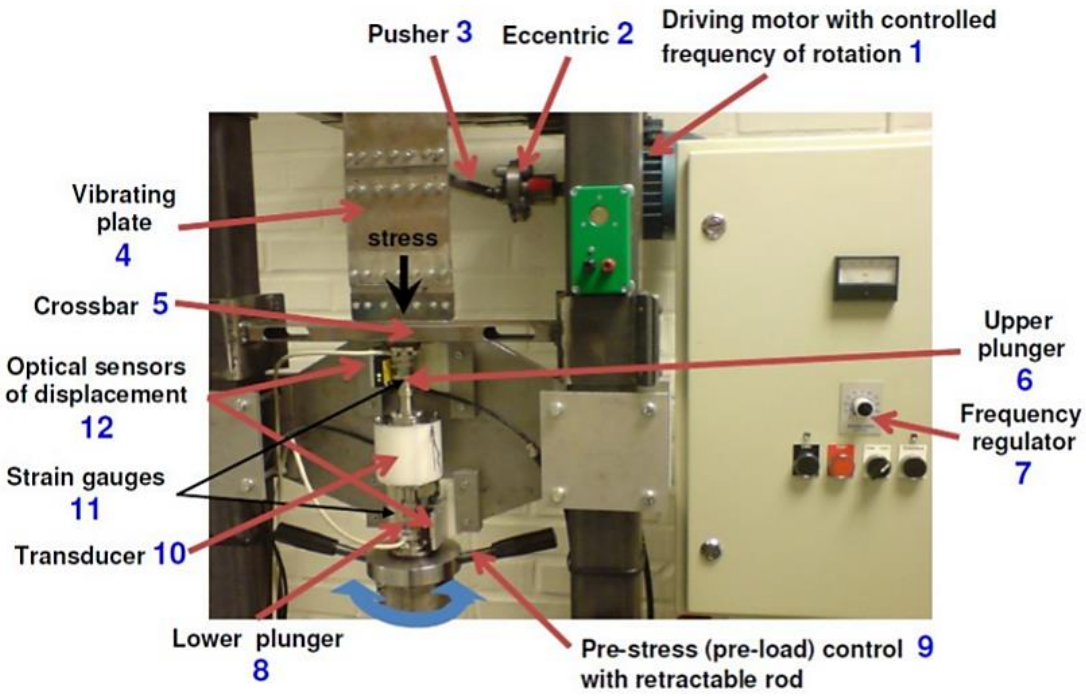

Figure 4-6: Closed view of VIBEL machine [203]

Mori et al. [204] made an embodiment of a Terfenol-D-based energy harvester to extract electrical energy for a broad range of frequencies. However, in most of the energy harvesters in previous studies, input vibration was given by using an electromagnetic shaker and the effect of leakage magnetic flux created from the solenoid of the shaker affects the performance of the harvester.

Axial-type vibration magnetostrictive harvesters are also relatively easy to manufacture and can be customized to suit specific application requirements. However, there are some limitations to the performance of axial-type vibration magnetostrictive harvesters. The energy conversion efficiency of these devices is typically low, which means that they are not suitable for high-power applications. In addition, the performance of these devices is affected by factors such as temperature, magnetic field strength, and mechanical pre-stress. Taking into consideration those parameters, we developed an axial vibration-based harvester which is going to be presented in the next section.

4.3 Proposed Axial vibration-based Energy Harvester

4.3.1 Description of the Used Samples

The samples are still the same as presented in the section 2.3.1 of Chapter 2. In the Fe-Co alloy, Permendur ($Fe_{49}Co_{49}V_2$ alloy) is commonly used due to its good soft magnetic properties [205]. Permendur has high permeability with little loss and high flux density at the magnetic saturation point, it also has the advantage of having a low price compared to other magnetostrictive elements like Terfenol, Galfenol… It is thus one of the most commonly used commercially available soft magnetic alloys in the application of energy harvesting. It also has moderately good magnetostriction, making it an excellent candidate for use as a low-cost magnetostrictive material for energy harvesting.

4.3.2 Experimental Setup of the Vibration Energy Harvester

Based on previous works from the literature and the specifications of the various available components, we decided to build a longitudinal axial vibration-based energy harvester. Figure 4-7 shows a schematic diagram of the proposed experimental setup used for the energy generation prototype. The structure is made of two vertically oriented parallel $Fe_{49}Co_{49}V_2$ magnetostrictive sheets with a wound coil of n=2500 turns each. The diameter of the copper wire used for the coils was 0.2 mm. To maximize the output voltage, the coils on the 2 sheets were connected in series. Holes were made on the sheets for connection with the magnets.

For motion application, an LDS V406 magnetic vibration shaker was used. The vibration amplitude and frequency are provided by a KEYSIGHT 33500B Series waveform generator and the produced waveform is amplified by an LDS amplifier PA 100E which feeds the voltage to the coils installed in the shaker.

Three similar vertical springs were used for prestress application and to ensure that the sheets were always in tension hence avoiding buckling. An IQS 452 inductive displacement sensor was mounted to monitor the displacement and quantify the mechanical power in the sheet. The resolution of the sensor is 4mV/µm.

The voltage waveforms were visualized using a KEYSIGHT EDUX 1002G Digital oscilloscope.

Six NdFeB (Neodymium) magnets, three on each end of the sheet were connected in series and were used to provide an adequate bias magnetic field for the system, increase the magnetization level of the sheets, and close the magnetic circuit. The screw-on channel magnets are square flat countersunk block magnets, embedded in a U-shaped steel profile. We decided to choose those magnets because of their high strength compared to their small size and their screw-fastening characteristics. The magnetic field variations are caused by reluctance variations and induced currents in the coils, which act as a secondary magnetic field source in addition to the permanent magnet.

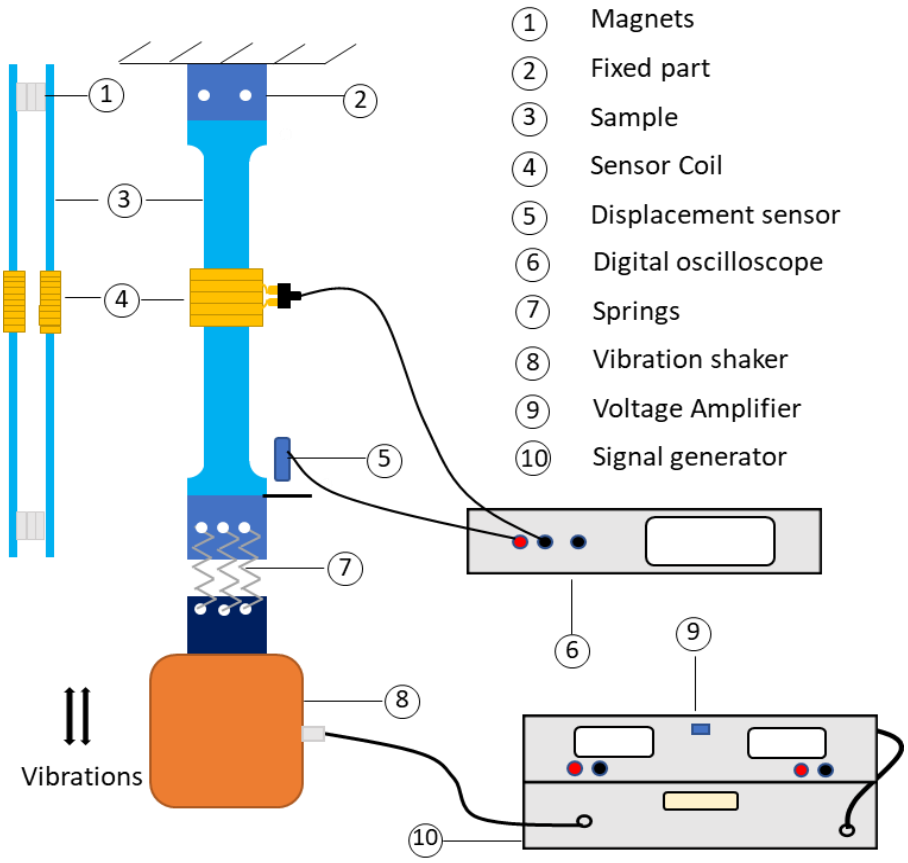

Figure 4-7: Experimental Setup

4.3.3 Experimental Energy Harvesting Process

The general principle behind the energy harvesting process has been describe in section 1.3.5 of Chapter 1. The developed harvesting device receives base vibration with any frequency or free excitation, and based on the inverse magnetostrictive effect a voltage is generated on the pick-up coils as follows: when a vibration is applied to the sheet through the base, in our case through a mechanical shaker, the structure will repetitively be stretched and relaxed around a functioning point due to the initial prestress from the springs on the magnetostrictive sheets. Vibration strain caused by those moves will result in a change of the magnetic flux in the sheets through the pseudo-Villari effect or inverse magnetostrictive effect (which refers to a change of the magnetic susceptibility of a material when the material is subjected to mechanical stress and induces a change in magnetization inside the material). By vibrating the device dynamically or cyclically, the time variation of fluxes caused by periodic tensile deformation generates a voltage across the pick-up coils according to Faraday's law of electromagnetic induction [206]. Then, the induced voltage is measured. Several mechanisms occur in the system during the energy conversion process either at the mechanical, magnetic, or electrical levels, more insights on these will be given in the next section.

4.3.4 Analysis of the Energy Conversion Mechanism

Let's note that the initial output voltage of the signal generator responsible for vibration is 200mVpp. The amplification factor of the voltage amplifier was used to study the behavior of the system according to the variation of the vibration amplitude of the shaker.

Considering Figure 1-5 in chapter one the principle is applied for the practical demonstrator presented in this chapter. Within the device, three main coupling domains exist:

- The mechanical section hosting the active magnetostrictive material
- The magnetic circuit hosted by the active material
- The electric domain is characterized by the induced voltage across the coil.

Mechanical energy, i.e., vibration, force, or motion, first acts on the vertically oriented sheets, which leads to the repetitive Fe-Co-V stretching process. Those moves then

produce strain and stress in the mechanical domain. The stress or strain induces a pseudo-Villari effect (due to magnets) in the Fe-Co-V sheet which leads to the modification of the magnetic flux around the sheet. At this stage, the mechanical domain is coupled with the magnetic domain, and mechanical energy is transformed into magnetic energy. Any change of magnetic flux will result in a Faraday electromagnetic induction effect, and correspondingly an induced electromotive force is generated across the pick-up coils. The magnetic domain is coupled with the electric domain, and thus, magnetic energy is converted into electric energy. From the above explanation, we can see three phenomena taking place at various locations of the system:

- The mechanical section is characterized by the mechanical stretching of the sheets.
- The active material is characterized by the magnetization of the sheets in the magnetic circuit. Stress variation affects the reluctance of the magnetostrictive sheet
- The electric part is characterized by the production of electrical energy in the coil's windings.

Figure 4-8 describes the conversion mechanism principle.

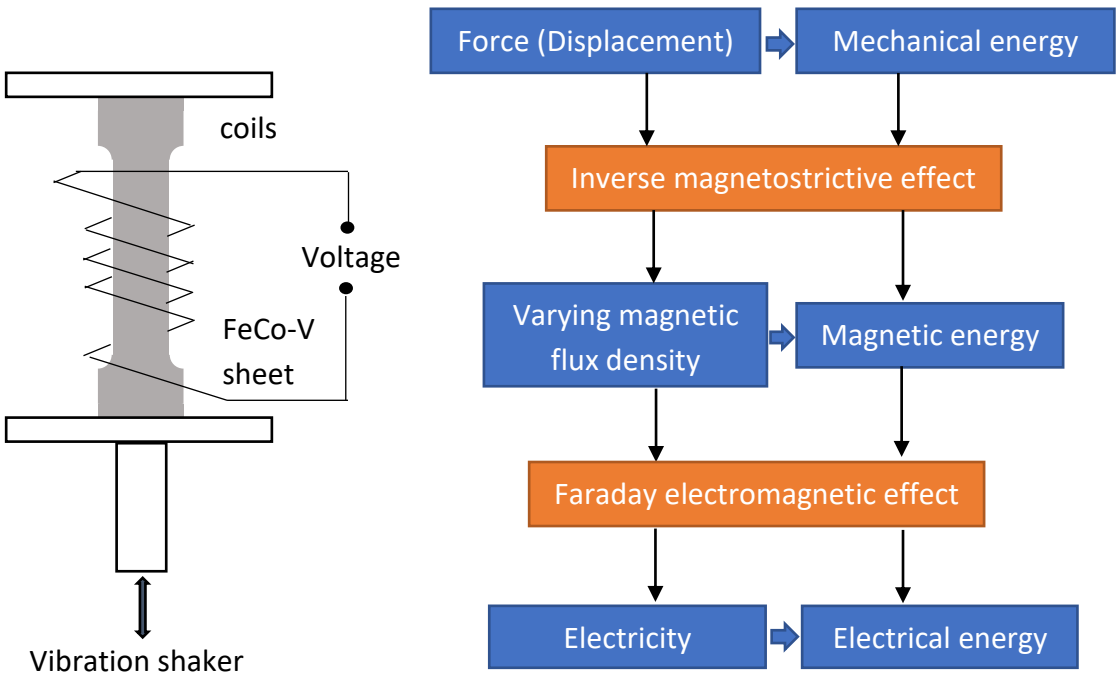

Figure 4-8: Energy conversion mechanism

In the following parts, we are going to detailed present the various levels of energy conversion.

4.3.4.1 Prestress: Mechanical Stretching by the Springs

For prestress generation, an initial manual mechanical stretch is exerted by springs on the sheets. The springs are connected to the shaker. To characterize the springs, we performed a simple experiment by connecting at their ends variable weight masses; this done their respective displacements were measured. For experimental purposes, we assumed an equal repartition of the force between all three springs implying they have the same displacement depending on the amplitude and frequency of the vibrations. Figure 4-9 shows the behavior of the spring with masses. We can see from it that the plotted points have a non-linear tendency; this gives as a main possibility for approximation, a non-linear quadratic expression. To make it simpler and regarding our goal, we will consider a linear fitting since the error between the 2 approaches (linear and non-linear) for our case is relatively low. The slope of the line represents the spring constant K, whose value is found to be K =1.3 kN.m^{-1}.

For the physical harvester, due to geometrical reasons, the springs were initially elongated by L_0 = 2.5 cm. So, the initial and fixed force F_0 on the spring is 35 N corresponding to an initial prestress S_0 of 1.21 MPa which is relatively low due to the hard nature of the material. The elastic limit of the sample used is 1000 Mpa. Meaning the applied stress is low and its effects may not be visible enough on the behavior.

In Table 4-1 below we have a summary of the initial mechanical parameters of the springs

Table 4-1: Summary of initial mechanical parameters

Parameters	Value
K	*1.3 kN.m^{-1}*
L_0	*2.5 cm*
F_0	*35 N*
P_0	*1.21MPa*

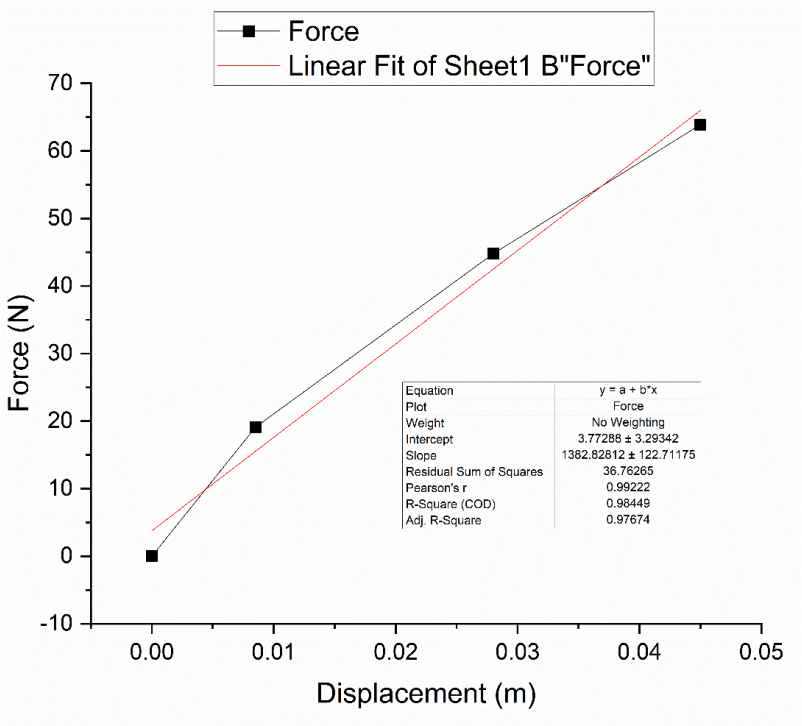

Figure 4-9: Characterization of the spring

4.3.4.2 Modeling Magnetization of the Sheet within Magnetic Circuit

To properly analyze the energy-harvesting phenomenon and to design a reliable energy conversion system, a key role is played by the material modeling in terms of its constitutive relations that relate the mechanical and magnetic inputs to the outputs[207]. Magnetic flux variation appears in the sheet as it is stretched, which indicates that there is a coupling between the mechanical domain and the magnetic domain. Accordingly, we need to characterize the magnitude of magnetization and magnetic flux density caused by the change of stress. There have been several models developed for describing the mathematical relationship between stress and magnetization of magnetostrictive materials, including the linear piezomagnetic equation [208], uncoupled and coupled finite element model [32,33], and the distributed-parameter dynamic coupled model [211].

In our demonstrator, the magnetic field is due to the contributions of three factors:

- Reluctance variations in the sheets due to the variations of stress.

- Induced currents in the coils can be considered as a secondary source of magnetic field.
- Permanent magnets generate a constant magnetic field.

Based on the variation of both the stress level (depending on vibration source) and magnetic field, the magnetic performance is within a small elliptical BH loop, with structure-dependent magnetic field and stress variations that cannot be predicted or controlled precisely. To harness energy density the cycle will be positioned and the point corresponding to the bias magnetic field and under mechanical prestress.

The magnetic circuit consists of permanent magnets, coils windings, and the magnetostrictive material which exhibits a positive magnetostriction in a fixed magnetic field. Neglecting leakage, one flux loop arises; it consists of magnets and magnetostrictive sheets. A steel screw is used to connect the sheets and the magnets.

For the following calculations, we have assumed we have assumed that the load resistance is equivalent to the internal resistance of the coil. We also neglected the reluctance of all other materials or components other than the magnetostrictive magnetic materials. Based on these assumptions, the equivalent magnetic circuit described by the harvester is shown in Figure 4-10 below.

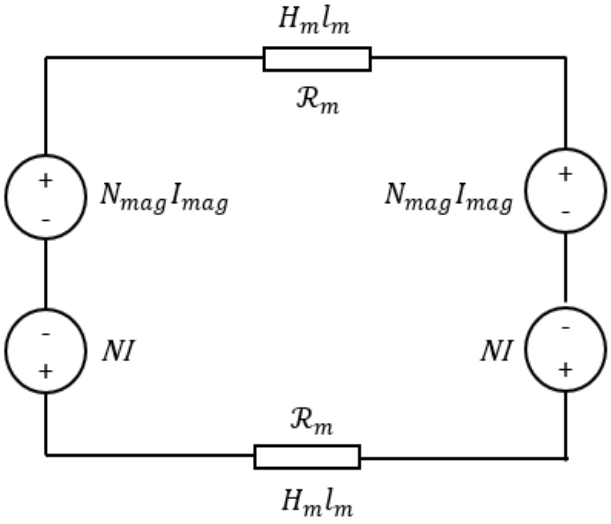

Figure 4-10: Equivalent magnetic circuit

Where H_m and l_m represent the magnetic field and the magnetostrictive material length and $N_{mag} I_{mag}$ and NI are respectively the magnetomotive force (mmf) of the magnet

block and that of the coil windings. $\mathcal{R}_m$ is the reluctance of the magnetostrictive material.

For the magnetic circuit defined in Figure 4-10, we have Eq. (4-1) below :

$$H_m l_m = N_{mag} I_{mag} - NI \quad (4\text{-}1)$$

The mmf of the magnet can still be written as:

$$N_{mag} I_{mag} = H_{eq} l_{mag} \quad (4\text{-}2)$$

With H_{eq} is the equivalent field generated by the magnets block and $l_{mag}$the total length of magnets.

Magnets are used in the circuit as the source of the bias magnetic field. As stated, we are using Neodymium grade N38 magnets. For such magnets, the coercive field varies from 860 to 915 kA/m, and the remanent induced field varies from 1.22-1.26T [212]. For experimental purposes, we are going to take the value *Hc* = 888 kA/m for a single magnet. The total magnetic field H_{eq} generated by a block of 3 magnets is given by Eq.(4-3) below:

$$H_{eq} = \frac{H_c \times V_{magnet}}{V_{magnet} + V_{air}} \quad (4\text{-}3)$$

Where:

- V_{magnet} is the volume of the magnet.
- V_{total} is the total volume of the set.
- V_{air} is the total volume of the air.

Table 4-2 below shows summarizes the calculated values of the volumes.

Table 4-2: Calculated values of volumes and equivalent magnetic field

Parameters	Value
V_{total}	$1.6 \times 10^{-6}\ m^3$
V_{magnet}	$1.46 \times 10^{-6}\ m^3$
V_{air}	$1.38 \times 10^{-7}\ m^3$
H_{eq}	$810.3 \times 10^3 A/m$

Let's assume the linearized from of Eq. (3-2) defining the anhysteretic magnetic behavior of the magnetostrictive material in function of the magnetic field H_m and the mechanical stress σ around the functioning point to be :

$$B_m = \mu_{r\,sim} H_m + \theta\sigma \tag{4-4}$$

$$\theta = \frac{\partial B_{model}}{\partial \sigma} \tag{4-5}$$

$$\mu_{r\,sim} = \frac{\partial B_{model}}{\partial H} \tag{4-6}$$

here θ is the magneto elastic coefficient which is related to the magnetic field and the mechanical stress. B_m and μ are respectively the local linearized magnetic flux density and the permeability of the magnetostrictive material.

After development,

$$\theta = -\alpha de \times atan\big(\beta H(tanh(\kappa\sigma)+1)\big)(tanh(e\sigma)^2-1) - \frac{[\alpha\beta\kappa H * (tanh(\kappa\sigma)^2-1)(d2 * tanh(\sigma * e2)+1)]}{(\beta H)^2(tanh(\sigma c)+1)^2+1} \tag{4-7}$$

$$\mu_{r\,sim} = \frac{\big\{\big(1+dtanh(e\sigma)\big) \times \big[\alpha\beta H_{surf} \times tanh\,(\kappa\sigma+1)\big]\big\}}{\mu_0(\beta H)^2(tanh(\sigma c)+1)^2+1} \tag{4-8}$$

In Figure 4-11 is shown the equivalent electrical circuit of the coil. Where R_{coil} and L_{coil} are respectively the coil resistance and inductance, and $i(t)$ the current flowing in the electrical circuit.

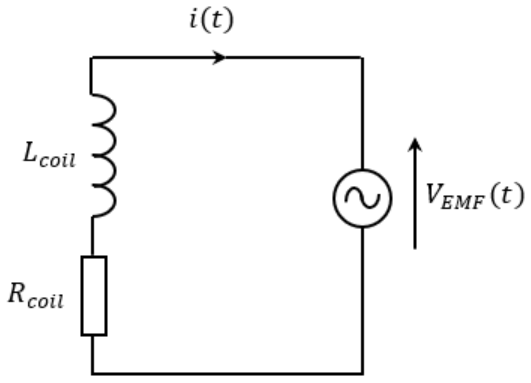

Figure 4-11: Equivalent circuit of the coil on the sample

The electromagnetic coupling connecting magnetic and electric systems is provided by coils around the magnetostrictive sheets. According to Faraday's law of induction, the electrical voltage $V_{EMF}(t)$induced by the variation mechanical input is shown in Eq. (4-9) below:

$$V_{EMF}(t) = N_c \frac{d\Phi_m}{dt} = (R_{coil} + jL_{coil}\omega) \times i(t) \tag{4-9}$$

$$\Phi_m = B_m A_c \tag{4-10}$$

Where:

- A_c is the coil's cross-section
- $\mathrm{N_c}$ is the total number of turns.
- $d\Phi_m$ is the variation of flux in the material.

Replacing Eqs(4-5), (4-9), (4-4) and (4-2) in (4-1) we have:

$$\frac{\frac{\Phi_m}{A_c} - \theta\sigma}{\mu} l_m = H_{eq} l_{mag} - \frac{{N_c}^2 \frac{d\Phi_m}{dt}}{R_{coil} + jL_{coil}\omega} \tag{4-11}$$

By assuming only small variations around a bias value for the following variables:

$$\sigma = \sigma_0 e^{j\omega t} \tag{4-12}$$

$$\Phi_m = \Phi_0 + \Phi_{dyn} e^{j\omega t} \tag{4-13}$$

$$B_m(t) = B_{m_0} + B_{dyn} e^{j\omega t} \tag{4-14}$$

$$H_m(t) = H_{m_0} + H_{dyn} e^{j\omega t} \tag{4-15}$$

Where Φ_0, B_{m_0}, H_{m_0} are respectively the magnetic flux, magnetic field density, and intensity at the functioning point.

Using Eq. (4-11), and for less complexity let's consider only the varying terms with $e^{j\omega t}$ only, we obtain:

$$\frac{\frac{\Phi_{dyn} e^{j\omega t}}{A_c} - \theta\sigma_0 e^{j\omega t}}{\mu} l_m = H_{eq} l_{mag} - \frac{{N_c}^2 j\omega\, \Phi_{dyn} e^{j\omega t}}{R_{coil} + jL_{coil}\omega} \tag{4-16}$$

A simplification of Eq. (4-11) leads to:

$$\theta\sigma_0 A_c = \Phi_{dyn}\left(1+\frac{{N_c}^2\mu j\omega}{l_m(R_{coil}+jL_{coil}\omega)}\right) \tag{4-17}$$

From Eqs. (4-4) and (4-10) we can extract the following expression for the dynamic magnetic field density and field intensity

$$B_{dyn} = \frac{\theta\sigma_0}{1+\frac{{N_c}^2\mu j\omega}{l_m(R_{coil}+jL_{coil}\omega)}} \tag{4-18}$$

$$H_{dyn} = \frac{\theta\sigma_0}{\mu}\left(\frac{1}{1+\frac{{N_c}^2\mu j\omega}{l_m(R_{coil}+jL_{coil}\omega)}}-1\right) \tag{4-19}$$

The converted power and its average can be defined as :

$$P(t) = H_m(t)\frac{dB_m(t)}{dt} \tag{4-20}$$

$$< P(t) >= \frac{1}{2}Re\{H_{dyn}e^{j\omega t}\overline{J\omega B_{dyn}e^{J\omega t}}\} = \frac{\omega}{2}Re\{-jH_{dyn}\overline{B_{dyn}}\} \tag{4-21}$$

The energy over a small cycle is derived as:

$$W = T < P(t) >= \frac{2\pi}{\omega}\times\frac{\omega}{2}Re\{-jH_{dyn}\overline{B_{dyn}}\} = \pi Re\{-jH_{dyn}\overline{B_{dyn}}\} \tag{4-22}$$

Under the assumption that $L\omega \ll R_{coil}$, and the reference angular velocity defined as:

$$\omega_0 = l_m\frac{R_{coil}}{A_c\mu{N_c}^2} \tag{4-23}$$

Using (4-23), Eqs (4-18) and (4-19) can be rewritten as:

$$B_{dyn} = \frac{\theta\sigma_0}{1+\frac{j\omega}{\omega_0}} \tag{4-24}$$

$$\overline{B_{dyn}} = \theta\sigma_0\left(\frac{\frac{\theta\sigma_0}{1+\frac{j\omega}{\omega_0}}}{1+\left(\frac{\omega}{\omega_0}\right)^2}\right) \tag{4-25}$$

$$H_{dyn} = \frac{\theta\sigma_0}{\mu}\left(\frac{1}{1+\frac{j\omega}{\omega_0}} - 1\right) \tag{4-26}$$

The final expression of the energy over a small cycle can then be given as in Eq.(4-27) below:

$$W = -\pi\frac{\theta^2{\sigma_0}^2}{\mu} \times \frac{\frac{\omega}{\omega_0}}{1+\left(\frac{\omega}{\omega_0}\right)^2} \tag{4-27}$$

From Eq.(4-27), the maximum energy can be determined when $\frac{\omega}{\omega_0}$ = 1, and the maximum energy is:

$$W_{max} = -\pi\frac{\theta^2{\sigma_0}^2}{2\mu} \tag{4-28}$$

Eq. (4-28) shows that the theoretical maximum power that can be harvested is not dependent on the mechanical structure, and is only dependent on the stress and magnetic field variations at the optimal frequency and the properties of the magnetostrictive material itself. This conclusion is in accordance with the conclusions in the literature [213].

4.3.5 Electrical Energy Production

Recalling Eq.(4-9), consider the case of our harvester where the output voltage mainly depends on the vibration frequency. The induced voltage is illustrated in Figure 4-12 below. The process consisted of varying the frequency at a constant amplitude of vibrations of then measuring the RMS voltage at the coil.

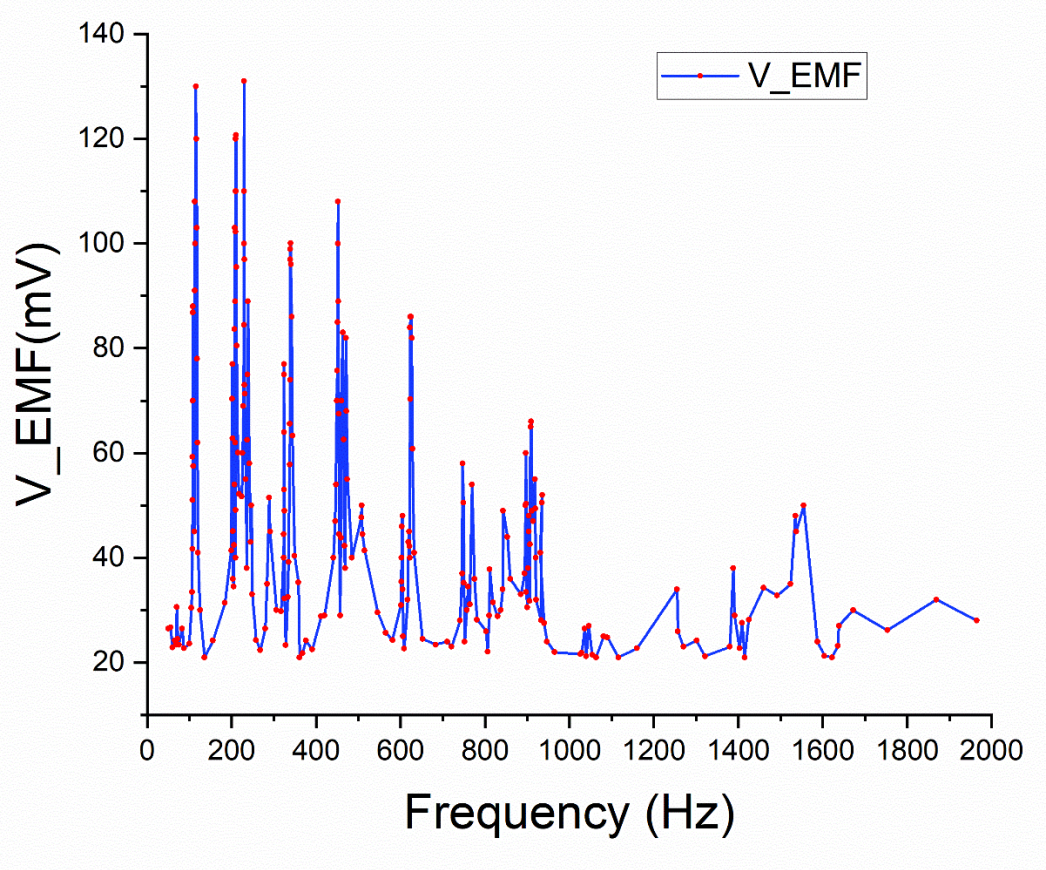

Figure 4-12: Variation of output voltage with the frequency

The voltage is recorded at different vibration frequencies varying from 0 -2000Hz spectrum. We can observe some peak values of voltage at some frequencies. During the process, many vibration modes appear.

To check the repeatability of results, successive tests were performed under the same conditions and for the same value of frequency. Values of voltage plotted are averaged values concerning the applied input frequency. The figure shows some peaks of voltage at some frequencies. Those frequencies cannot be called resonant frequencies due to the presence of several mechanic oscillations. The study of those frequencies is not within the scope of this work. Having collected the output voltage; we investigated ways to improve it to increase the efficiency of the system. This will be the object of the next part.

Table 4-3 represented below shows the peak values of voltage and their related frequency.

Table 4-3: Peaks values of voltage and corresponding frequency

Frequency (Hz)	202	210.3	229.1	232.3	238.6	339.3
V_EMF_pk(mV)	40	100	116	102	78	70
Frequency (Hz)	461.7	626.5	912.5	935.2	1527.8	1830
V_EMF_pk (mV)	60	91	71	21	25	24

4.4 Improvement of the Output Voltage

After voltage generation across the coil's windings, in practical harvesters, several techniques are currently being used as voltage amplification means; amongst them, we can have dedicated power electronics circuits... But for our case, we decided to use capacitors. This part will describe in detail the improvement technique of the output voltage using capacitors. From Figure 4-12, we observe some voltage peak values due to resonant frequency. The goal of the work is to work at those peak values to harvest the maximum energy. During the experimental process, it was seen that coils' inductance and impedance are related to the frequency, the first step consists in studying the effect of the frequency on those parameters.

4.4.1 Variation of Coil's Impedance and Resistance with Frequency

Resistance and inductance and intrinsic properties of the coil. Figure 4-13 and Figure 4-14 below show the variation of the inductance and the impedance respectively with the frequency. From Figure 4-14, we can see an increase in resistance is partly due to the high-frequency skin effect. And as a consequence of the skin effect, the inductance decreases.

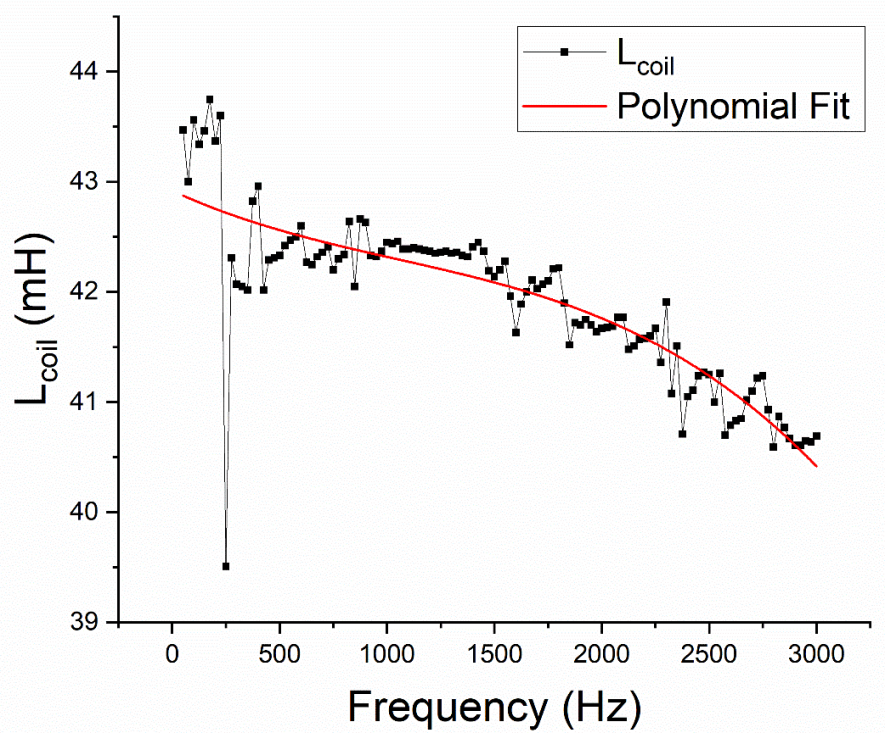

Figure 4-13: Variation of inductance with the frequency

Within the boundary of applied frequencies, the non-linear interpolation was done using the software ORIGIN employing the Nonlinear Least Square method, and the expression with the fitting coefficients of the behavior of the series inductance L_{coil} is represented by Eq. (4-29) below:

$$L_{coil} = -1.38 \times 10^{-10}.f^3 + 4.35 \times 10^{-7}.f^2 - 8.97 \times 10^{-4}.f + 42.91\ H \quad (4\text{-}29)$$

Where f is the frequency. The R^2 of the fitting is 0.7.

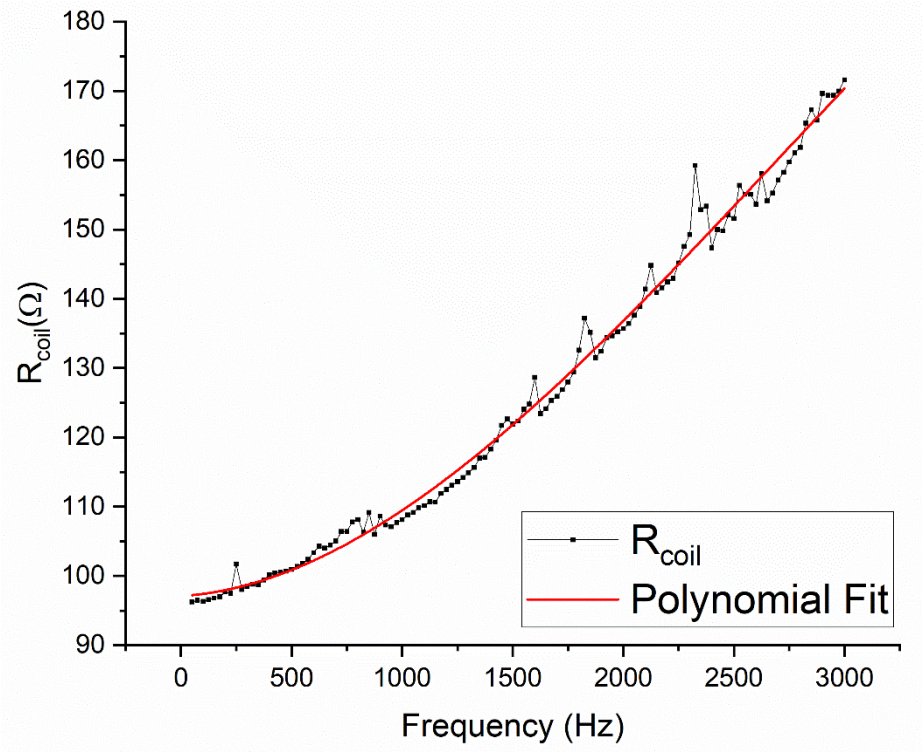

Figure 4-14: Variation of the resistance with the frequency

In the range of frequency applied, by still using the same principles and tools as the inductance, the behavior of the resistance of the coil R_{coil} was approximated to a cubic function as shown in Eq. (4-30) below:

$$R_{coil} = -1.562 \times 10^{-9}.Freq^3 + 1.24 \times 10^{-5}.Freq^2 + 1.15 \times 10^{-3}.Freq + 97.43\ \Omega \quad (4\text{-}30)$$

Where *f* is the frequency. The R^2 of the fitting is 0.99.

The linear approximations for *Lcoil* and *Rcoil* will be used in the next section for the choice of the appropriate series capacitance for amplification.

4.4.2 Parallel Capacitance

To amplify the output voltage of the coils we decided to implement a simple method which is the impedance matching. Since we have to do with a series RL circuit, we opted to add capacitors in series with the coil; the resultant is a series RLC circuit and then we supposed the system is oscillating at resonance at the specified frequency (we have low impedance value since the reactance is zero) and in that situation, maximum energy is transferred to the resistor. Assuming the circuit is in resonance at the corresponding frequency peak points, the resonant frequency f_r is given by Eq. (4-31) below:

$$f_r = \frac{1}{2\pi\sqrt{L_{coil}C}} \tag{4-31}$$

Where *L* is the inductance of the coils and *C* is the series capacitance

From Eq. (4-31) the value of the capacitance *C* is:

$$C = \frac{1}{4{f_r}^2\pi^2 L_{coil}} \tag{4-32}$$

The *quality factor Q* of the resulting RLC circuit is defined by:

$$Q = \frac{\sqrt{\frac{L_{coil}}{C}}}{R_{coil}} \tag{4-33}$$

The *output voltage* V_c of the capacitor in a series RLC circuit is defined in Eq. (4-34) below:

$$V_c = Z_c I = Z_c \frac{U}{Z_T} \tag{4-34}$$

Where *U* is the voltage across the coil, Z_T is the total equivalent series impedance of the coil and resistance.

Since we assumed it to be at the resonant frequency,

$$Z_T = R \tag{4-35}$$

Replacing Eq. (4-35) in Eq. (4-34) gives:

$$V_c = QU \tag{4-36}$$

From Figure 4-14 plotted before, we can see that the values of resistance are relatively high, so to have a positive quality factor (*Q*>1), the value of the frequency has to be high as far as *L* is decreasing and *R* increasing.

Table 4-4 presents a summary of the output voltage values, quality factor, capacitors values, and Quality factor of the collected peak values from Figure 4-12 previously presented. In the table, the values *Rtotal* and *Ltotal* were obtained using Eqs. (4-29) and (4-30) are presented before for each corresponding frequency. The values of capacitances were also calculated using Eq. (4-32). *Vmax_expected* is the theoretical

expected output voltage. It is the product of *Vmax* and the quality factor *Q. Vmax_measured* is the actual measured output voltage.

From the table, we note some differences between the actual and the expected values of the output voltage. Those differences are due to many factors including:

- the tolerance on the values of capacitances.
- the fluctuations in the value of voltages since the plotted value of voltage was obtained by performing the mean around several three sets of measurements.
- The data were collected manually.

Based on those reasons the differences may be negligible.

The amplified voltage values *Vmax_measured* at the peaks from Figure 4-12 are shown in Figure 4-15.

At 913 Hz, the waveform of the AC-generated voltage is presented in Figure 4-16*. V_SC* is the output voltage with no capacitor connected while *V_AC* is the output voltage when the capacitor is connected. The peak voltage with no capacitance is 0.0715V and with capacitance is 0.13V. We note a difference of 30mV 'with capacitors and no difference of 'without capacitors' voltages. The difference between these values and those presented in Table 4-4 is explained by the fact that values presented in the table are averaged while values in the figure are just a set of values. The difference is therefore negligible.

Table 4-4: Summary Values of the output voltage

Frequency (Hz)	202	210.3	229.1	232.3	238.6	339.3	461.7	626.5	912.5	935.2	1527.8	1830
Vmax (mV)	40	100	116	102	78	70	60	91	71	21	25	24
Rtotal (Ω)	91.37	91.59	92.10	92.17	92.35	95.01	98.20	102.56	110.09	110.70	126.28	134.27
Ltotal (H)	0.0429	0.0429	0.0428	0.0428	0.0428	0.0428	0.0427	0.0426	0.0424	0.0423	0.0419	0.0417
C (F)	1.45E-05	1.34E-05	1.13E-05	1.10E-05	1.04E-05	5.15E-06	2.79E-06	1.52E-06	7.19E-07	6.85E-07	2.59E-07	1.82E-07
Q (Quality Factor)	0.60	0.62	0.67	0.68	0.69	0.96	1.26	1.63	2.20	2.25	3.19	3.57
Vmax Expected (mV)	23.80	61.79	77.63	69.15	54.21	67.13	75.60	148.57	156.54	47.17	79.63	85.67
Vmax_measured (mV)	22.5	61.3	60.7	62	48	82	80	116	130	51	86	82.4

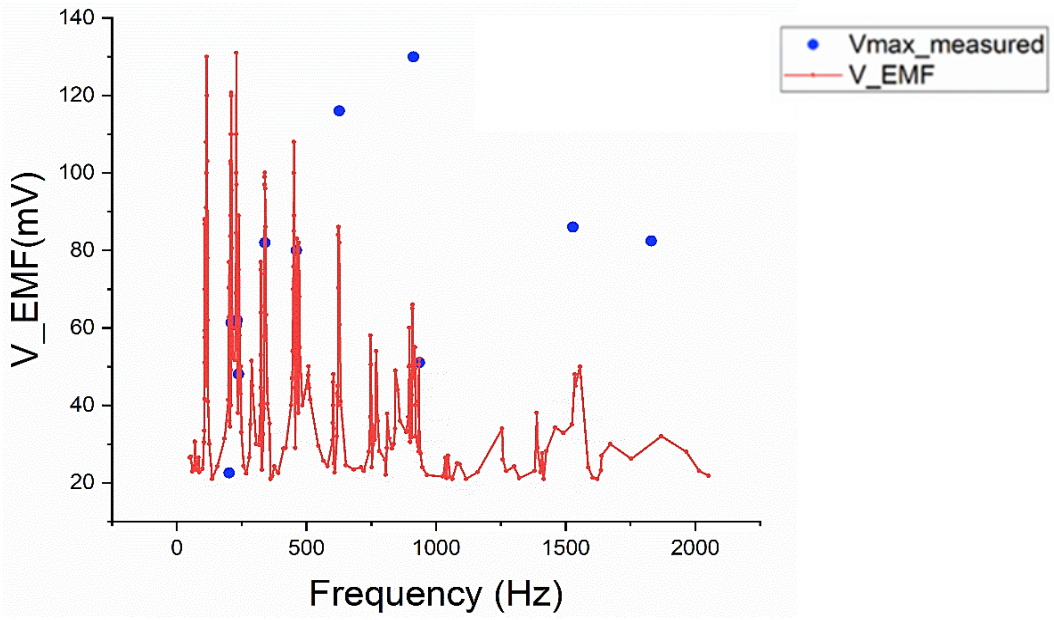

Figure 4-15: Effect of amplification of the output voltage with the input frequency

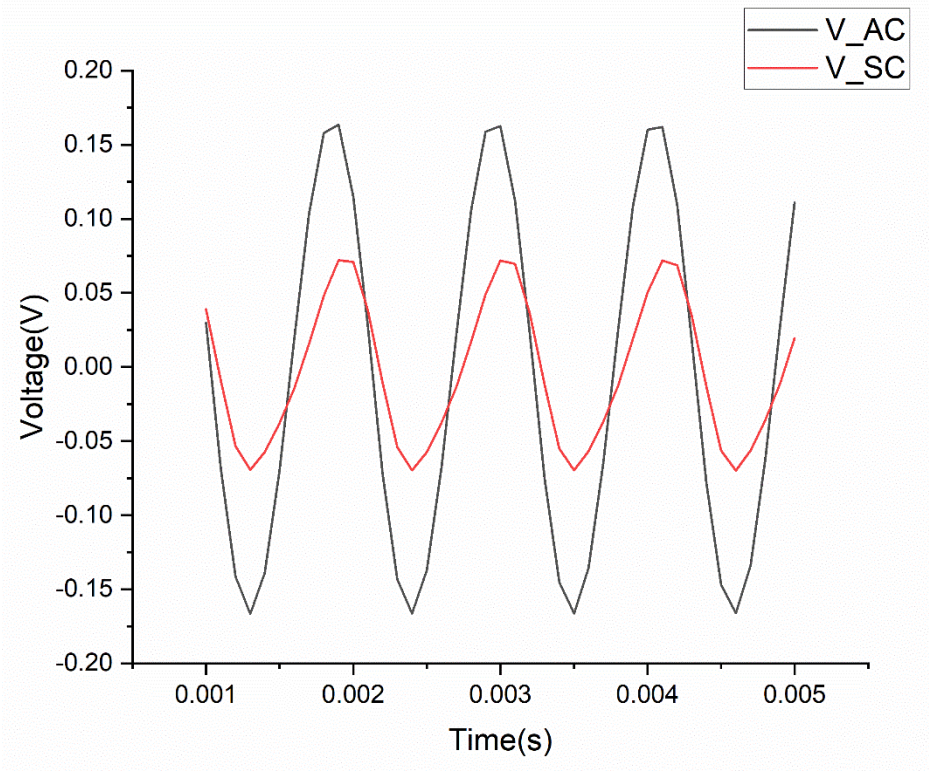

Figure 4-16:Generated AC voltage at f=913Hz, V_SC without capacitor, V_AC with capacitor

4.4.3 Power Density of the System

The system implemented in the study is a typical axial-type magnetostrictive energy harvester. For the sake of simplicity, we considered the internal resistance of the coil as load and we assimilated it to the energy harvesting capability to the joule heat dissipated in the resistance.

Amongst the performance characteristics of a harvesting device, we have the output power. Let's note by P_{out} and W_{out} respectively the electrical power and energy delivered by the coils

$$P_{out} = \frac{{V_{coil}}^2}{R_L} \tag{4-37}$$

$$W_{out} = \int_0^{T_0} \frac{V_{coil}(t)^2}{R_{coil}} dt \tag{4-38}$$

Where T_0 is the period of the input stress.

Based on Eq. (4-37), Table 4-5 presents the various output power in function of the applied frequency.

Table 4-5: Output electrical power in function of frequency

Frequency (Hz)	202	210.3	229.1	232.3	238.6	339.3
Pout (µW)	5.54	41.02	40	41.7	24.94	70.77
Frequency (Hz)	461.7	626.5	912.5	935.2	1527.8	1830
Pout (µW)	65.17	131.2	152.66	23.49	58.56	50.56

The maximum output power that can be harvested after amplification is **0.15 mW** and without amplification **45.78 µW** is reached at a frequency of 912.5Hz.

The obtained electrical energy W_{out} at a frequency of 912.5Hz from Eq. (4-38) at 912.5Hz is **0.15 µJ/cycle**.

The other performance metric for the harvester is the power density *PD*, which describes the output power generated by a unit volume of magnetostrictive materials. The power density *PD* is

$$PD = \frac{W_{out}}{T_0 V_a} \tag{4-39}$$

where V_a is the volume of active material and is 0.22 cm^3.

The obtained power density *PD* at a frequency of 912.5Hz from Eq. (4-39) at 912.5Hz is **0.6mW.cm^{-3}** with amplification and at that same frequency the PD without amplification is **0.2mW.cm^{-3}.**

4.5 Results and Discussion

Table 4-6 below shows comparative results of some similar energy harvesting devices currently present in the literature. From the table, we can see that most of the results in the literature were obtained at relatively low frequencies. It's not the case with our demonstrator. The developed system presented in this chapter shows a low output

power compared to others, it can be explained by the fact the material is mechanically excited at high frequency, and at such frequencies, the material is almost static.

With the use of a vibration shaker, we are limited in terms of stress amplitude, the applied stress value used here is insignificant and is far below the elastic limit of the material hence the effects on the material are not visible and the obtained results cannot be optimal. Nevertheless, the order of merit of those results is significant.

Table 4-6:Comparative results table with literature

Authors	**Types of Harvesters**	**Magnetostrictive Material**	**Frequency**	**Output Power**
Ueno et al. [198]	Bending	Galfenol	395Hz	3.5mW
Zucca et al. [160]		Terfenol-D	300Hz	18mW
Adly et al. [199]			50Hz	0.44mW
Wang et al. [187]		Metglas	58Hz	200µW
			1.1kHz	576µW
Kita et al. [200]		Galfenol	202Hz	0.73W
Yamaura et al. [197]	Axial	Permendur		
Zhang [214]		Terfenol		
Berbyuk [203]		Galfenol	60 Hz	0,45 W
Ueno [202]		Terfenol		3.7 mW
Our Proposed System		**Fe-Co-V**	**913Hz**	**0.15 mW**

4.6 Conclusion

Due to their robustness and potential electromechanical coupling, magnetostrictive materials are a competitive solution for vibrational energy harvesters. Yet, their realistic implementation, mainly due to the material price, as well as the deep understanding of their conversion efficiency, is still an open question. Most of the harvesters designed so far are still in the research stage and few products have been commercialized. The reasons are low power output of the order of microwatts, low efficiency, and low endurance. The output power delivered by a vibrational

magnetostrictive energy harvester depends on several parameters; some of them linked to the mechanical vibration source (amplitude and frequency) others related to design quantities, like mechanical preload, magnetic bias, coil turns, and load impedance. We proposed an axial vibration energy harvester based on the pseudo-Villari effect which is a magnetostrictive material property. We first presented the existing vibration energy harvester; It was followed by the operation principle of the developed system and then we proposed an energy estimation model of the harvested electrical energy to be collected based on mechanical, magnetic, and electric parameters. Obtained experimental results were presented and we present an improvement method of the output voltage based on the impedance matching. Due to skin effects coil resistance and inductance were approximated. Series capacitors were added to the harvesting circuit. Experimentally, the maximum output voltage that can be harvested from the system is at 912.5 Hz without amplification 71 mV and after amplification 130 mV. It is at the same frequency that we have the highest power output which is 152.66µW. The maximum energy that can be obtained from the harvesting device is 0.15 µJ. $cycle^{-1}$ corresponding to a power density of 0.6 $mW.cm^{-3}$. It has been really difficult to interpret the significance of the frequency (1^{st} order, second, 3^{rd} order, …). The reason has been linked to the mechanical system which was not stable at some frequency the system was oscillatory. The high operating frequency makes the analysis difficult because at such frequency we may have many types of noise and disturbances.

5 CONCLUSION AND FUTURE WORKS

5.1 Conclusion

This chapter attempts to bring an overall conclusion to the work developed during this thesis. Our primary motivation is as follows: to be able to offer an alternative to the use of conventional batteries for autonomous wireless sensors. By recovering energy from the direct environment of these sensors for their power supply, the latter could gain in compactness (no longer need to carry a large quantity of energy), autonomy (no longer need to regularly change the empty batteries), and uniform in severe environments (at high temperatures for example). This work focuses more specifically on the harvesting of vibrational energy, which is promising in terms of power available per unit volume in an industrial environment, compared to thermal, solar, or wind energy (the sensors being regularly located in a closed space). Moreover, the emphasis here is on the magneto-mechanical energy conversion using Iron-Cobalt magnetostrictive sheets. This manuscript is thus articulated around three main axes:

(i) Magnetostrictive materials are highly used because of their high-power density gains and high magnetization saturation. But those good properties can be the source of unwanted acoustic noise during their operation. Tuning Mechanical Internal stress can be a solution to a solution to reduce the high magnetostriction. We proposed to overcome the directional limitations of magnetic sensors used so far by a MIP miniature U-shaped ferrite magnetic core. The precise control of MIS remains a significant challenge; thus, internal stress has been replaced by externally applied stress. The tests were limited to tensile stress, which constitutes the worst-case scenario for the stress

observation. Results showed that internal stress can be replaced by external. Preliminary $Z(H_{surf})$ butterfly loops were plotted, but are limited because they can't provide magnetic information on the process hence, we pass through a conversion of Impedance *IZI* to the FeCo relative permeability μ_{MIP_r} using a reluctance conversion scheme. The final conversion step is the conversion from $\boldsymbol{\mu_{MIP_r}}(H_{surf})$ to $B_{a\ MIP}(H_{surf})$ classical hysteresis cycles. The link between MIP and related indicators established by recreating hysteresis cycles, we study the trend of $B_{a\ MIP}(H_{surf}$ =10 kA·m^{-1}*)* markers that are better tailored to the domain wall bulging mechanism. The analysis of the Pearson Correlation factor for the 10 sensor angles evaluated revealed that for $\theta = \pi/2$, the astounding 0.99 linear correlation is attained. Hence this orientation favors the measurement.

(ii) The increasing demand for autonomous devices has made the concept of energy harvesting a significant industrial and academic interest point. Iron Cobalt Vanadium constitutes a sustainable channel to convert mechanical vibration into electrical energy. In this part, we initially performed the experimental magnetic characterization as the basis of the analytical modeling of the anhysteretic behavior of sheets under tensile stress. The validity of the model was checked using many tests amongst which the model's coefficient of determination was closer to 1 based on them the validity of our model was established. and their energy conversion capabilities were assessed. The energy conversion ability was assessed in 3 ways:

- Using thermodynamic Ericsson cycles from proposed modeled anhysteretic curves. A maximum of 10.45 mJ·cm^{-3} energy density was forecasted under a tensile stress of 0-480 MPa and a magnetic excitation of 5.5 kA·m^{-1}.
- Then, an additional estimation was proposed to account for the hysteresis losses induced by the existence of a coercive field within the material. For this, major hysteresis loops at different stress levels were considered, yielding an energy density of 3.52 mJ·cm^{-3}.
- Finally, experimental Ericsson cycles were performed to prove the feasibility of the conversion and corroborate the energy level predictions.

The comparison between the various predictive methods and the experimental tests showed an overestimation of the proposed model based on the anhysteretic curve, especially in the high field range. The prediction considering the major hysteresis losses was much more accurate, especially in terms of the slope of the converted energy vs. magnetic field curve.

(iii) Due to their robustness and potential electromechanical coupling, magnetostrictive materials are a competitive solution for vibrational energy harvesters. Yet, their realistic implementation, mainly due to the material price, as well as the deep understanding of their conversion efficiency, is still an open question. For the practical harvester we set, the maximum output voltage that can be harvested from the system is at 912.5 Hz without amplification 71 mV and after amplification 130 mV. It is at the same frequency that we have the highest output voltage which is 152.66µW. The maximum energy that can be obtained from the harvesting device is 0.15 µJ. $cycle^{-1}$ corresponds to a power density of 6.13mW.cm^3. The addition of the stability robustness criterion to characterize the different behaviors thus improving the precision of this model;

We have presented a summary of the development proposed around these three axes we will propose perspectives concerning the future work that can be envisaged in the continuity of this thesis work.

5.2 Future Scope

Concerning energy conversion, many perspectives can be listed for this work to take advantage of the material nonlinearity to design efficient energy harvesters (structure and electrical interface); those include:

- For a better approximation of the ultimate energy density, we should study the correlation between the magnetostriction and ultimate energy density properties.
- Perform the complete dimensioning of the system at high bias field values and study the behavior of the conversion process.
- the test of predictive methods under compressive stress,

- the consideration of different stress levels,
- For real energy harvesting devices, magnetic bias is provided by magnets which induce an additional dynamic magnetic field hence we may investigate the dynamic behavior of the sample.

As a follow-up of MIS estimation, several hypotheses might be enumerated which include:

- the short-term impact of homogenous compressive stress.
- Additionally, MIS of already described specimens should be used to corroborate the suggested conclusions (by X-ray diffraction, for instance).
- In the future, it may be possible to test additional kinds of materials and, in the even longer term, to see how well the directional MIP performs on other typical magnetic NDT targeted attributes, such as microstructural characteristics and aging.

Based on the weaknesses of the demonstrator, we propose as future scope:

- Proper dimensioning of the full harvesting system takes into consideration the inner behavior of the material, the effects of the number of turns, and the biased magnetic field.
- Increase the stress value and see the effect on the output voltage.
- build a model to better predict the behavior of the harvester.
- Design an electrical interface able to output sufficient DC voltage (along with sufficient power).

6 RÉSUMÉ ÉTENDU (EXTENDED SUMMARY)

6.1 Chapitre 1 : Généralités

6.1.1 Introduction générale

Les progrès en microélectronique ont conduit à une multiplication d'appareils connectés sans fil (Internet des Objets …) au cours des dernières années conduisant à une demande croissante des dispositifs pour leur alimentation ainsi la notion de récupération d'énergie. Parmi les sources d'énergie typiquement disponibles (solaire, thermique...), les vibrations mécaniques présentent de nombreux avantages tels que leur ubiquité et une disponibilité [19].

6.1.2 Contexte

Dû à leurs nombreuses applications, notamment dans les domaines du transport, santé, génie civil, etc. La problématique de fournir une énergie électrique fiable et durable à l'ensemble de ces systèmes reste un enjeu d'actualité. Alors que les batteries conventionnelles présentent des limites (leurs durées de vie limitées dues à leur autodécharge, l'espace occupé pour leur stockage, les frais de maintenance…), le recours aux sources d'énergie ambiantes constitue une solution alternative attrayante, conduisant au concept de « récupération de l'énergie ».

6.1.3 Matériaux Intelligents et Application à la Récupération d'Énergie

Les matériaux intelligents sont ceux-là qui changent leur forme ou ont une réponse définie en fonction du stimulus externe qui leur est appliqué. Ces matériaux présentent de nombreuses propriétés, certaines de celles-ci sont mises en contribution pour la conversion d'énergie. À petite échelle (de l'ordre du centimètre), les mécanismes

de conversion privilégiés sont l'électromagnétisme ou la piézoélectricité. Toutefois, chacune de ces solutions présente des inconvénients (fragilité, haute impédance de sortie pour les dispositifs piézoélectriques, faible tension, pertes élevées et problèmes d'intégration pour les dispositifs électromagnétiques) ce qui limite leur développement dans certaines applications dans la vie courante. Le choix de la source dépend des facteurs tels que la résistance à température, le rendement du système de conversion, la puissance récupérable, le volume du capteur + unité de récupération.

Dans le cas de la conversion de l'énergie vibratoire, les matériaux magnétostrictifs présentent des avantages permettant de surmonter les limites évoquées plus haut notamment, ils présentent une contrainte admissible élevée et des propriétés de conversion supérieures par rapport aux dispositifs électromagnétiques [76]. Pour ce qui est de la magnétostriction, la principale caractéristique utilisée est l'effet de Villari.

6.1.4 Le Magnétisme

Le magnétisme est la force exercée par les aimants lorsqu'ils s'attirent ou se repoussent. L'électromagnétisme est le terme mis en évidence par Michael Faraday ; il a démontré qu'un aimant en mouvement crée un courant électrique dans une bobine placée à proximité : c'est l'induction électromagnétique. Cette section présente donc les propriétés du champ magnétique, le paramètre perméabilité du matériau et les propriétés des matériaux ferromagnétiques. Elle décrit aussi le phénomène de domaine magnétique.

6.1.5 Caractérisation du Matériau et Techniques de Contrôle du matériau

Dans cette partie, nous présentons les différentes techniques de détection de fissures sur un composant. Ces techniques peuvent être non destructives et destructives. Un accent est mis sur celles non destructives tel l'essai par courants de Foucault (ECT). Ensuite a été présenté le principe des courbes hystériques et anhystérétiques qui représentent les signatures magnétiques uniques des matériaux nous permettant ainsi d'évaluer leur état comparé à un état initial. Dans l'optique de la caractérisation du stress mécanique résiduel du matériau, plusieurs techniques ont été

présentés et celle retenue fut la Perméabilité incrémentale magnétique au vu de ses nombreux avantages. Un point ajouté sera l'utilisation du facteur directionnel de la mesure par rapport à l'application du champ ; des dispositifs existants tels que le capteur 3MA a été présenté.

6.1.6 Énoncé du Problème

Jusqu'à présent, la récupération d'énergie par éléments magnétostrictifs a été relativement peu étudiée. La compréhension des mécanismes intrinsèques liés à l'aspect applicatif (récolte d'énergie …) d'un point de vue global, du matériau à l'aspect électrique en passant par la structure mécanique, n'a presque jamais été envisagée. Dans cette thèse nous souhaitons nous intéresser en particulier à l'aspect couplage au sein même du matériau et à son amélioration. Nous souhaitons développer un dispositif de caractérisation capable de renseigner proprement des outils de modélisation et de tester les matériaux sélectionnés afin de déterminer les formes d'ondes et points de fonctionnement optimal quant au rendement énergétique. Pour la mise sur pied du système de récupération d'énergie magnétostrictive, le comportement du matériau en lui-même soulève quelques interrogations :

1- Le premier point est l'effet exact de l'application d'une excitation mécanique (contrainte dans notre cas) sur le comportement magnétique du matériau. La variation des propriétés mécaniques conduit à une variation du flux magnétique ceci entraînant une conversion d'énergie électromécanique beaucoup plus considérable. Cette variation d'énergie a des effets sur le matériau tels que l'augmentation des pertes magnétiques et la réduction de son rendement. Couplées à cet effet, nous avons la non-linéarité du comportement magnétique du matériau réduisant ses applications dans des plages intermédiaires d'excitation magnétique. Cette réduction limite fortement les potentielles applications et l'évaluation des performances des systèmes de récupération y associés.
2- Le deuxième point concerne les effets de la magnétostriction sur le matériau : les alliages ferromagnétiques fer-cobalt sont fortement utilisés pour la conversion de l'énergie électrique dans plusieurs applications où une densité de

puissance élevée est nécessaire, mais leurs coefficients magnétostrictifs élevés peuvent entraîner des comportements indésirables tels que le bruit acoustique. Les contraintes internes, qui sont l'une des sources de ce bruit, peuvent être ajustées pour limiter la magnétostriction. Mais ce processus d'évaluation de la contrainte doit être effectué de manière adéquate et non destructive pour une utilisation ultérieure du matériel.

6.1.7 Objectifs de la Thèse

Nous nous concentrerons sur des éprouvettes magnétostrictives de Permendur.

Suite à l'observation faite en (1) et que les travaux récents se concentrent principalement sur l'évaluation des performances globales du système de récupération d'énergie sans explorer les performances de conversion d'énergie au niveau matériel, dans un premier temps, nous allons évaluer l'énergie pouvant être potentiellement récoltée des feuilles laminées Permendur. Le comportement magnétique sous contrainte de traction dans le domaine élastique sera évalué. Ensuite, sur la base de ces mesures expérimentales, un modèle (une grande importance sera accordée au modèle, c'est-à-dire la complexité et la précision) pour l'approximation du comportement anhystérétique sera proposé et utilisé pour évaluer la conversion d'énergie potentielle sous contrainte de traction et excitation magnétique. Ensuite, une autre estimation de la densité d'énergie convertie sera décrite en tenant compte des pertes hystérétiques. Des cycles énergétiques expérimentaux d'Ericsson seront mesurés pour prouver la faisabilité du processus de conversion et valider le Permendur en tant que matériau pertinent pour les applications de conversion d'énergie. Une dernière étape sera la conception d'un récupérateur d'énergie basé sur les vibrations axiales pour étudier la faisabilité pratique du dispositif et un ordre de mérite sera proposé pour comparer le système.

La méthode PIM (Perméabilité Incrémentale Magnétique) semble être très sensible aux contraintes mécaniques internes (MIS). Jusqu'à récemment, le MIP était presque observé avec des bobines en crêpe ou enroulées empêchant l'accès aux informations directionnelles. Cette limitation sera dépassée dans cette étude par un capteur renseignant sur la perméabilité magnétique incrémentale directionnelle avec

l'utilisation d'un noyau magnétique miniature en ferrite en forme de U. À des fins académiques, les contraintes internes seront remplacées par des contraintes externes homogènes, plus faciles à contrôler à l'aide d'un banc d'essai de traction/compression et entraînant des effets similaires. Les tests seront limités aux stimuli de contrainte de traction qui constituent le pire des cas pour l'observation de contraintes magnétiques sur des matériaux à coefficient de magnétostriction positif. Les cycles d'hystérésis seront reconstruits à partir de la mesure de perméabilité incrémentale. Le caractère directionnel du capteur offre un degré de liberté supplémentaire dans l'observation de la réponse magnétique. À partir des courbes hystériques reconstituées la corrélation entre les valeurs du flux magnétique pour des valeurs de champs magnétiques ont été évaluées pour chaque orientation.

6.1.8 Organisation de la Thèse

Ce travail porte sur la caractérisation magnéto mécanique des tôles magnétostrictives laminées de Fe-Co-V et de leur application à la récupération d'énergie. Le document est divisé en 5 chapitres.

Le premier chapitre présente les généralités sur le magnétisme, les matériaux intelligents et leur application à la récupération d'énergie, et les méthodes de caractérisation et de contrôle des matériaux.

Le chapitre deux fournit un aperçu de la PIM utilisé comme technique d'estimation des contraintes mécaniques, puis décrit les conditions et le processus expérimental et les résultats préliminaires de la caractérisation magnétique en utilisant le capteur directionnel PIM qui est proposé.

Le chapitre trois présente quelques modèles de conversion électromécanique d’énergie. Ensuite, la caractérisation magnétique expérimentale des tôles sous contrainte de traction est réalisée. Sur la base de ces mesures, une modélisation du comportement anhystérétique est proposée et validée puis utilisée pour évaluer la conversion d'énergie potentielle sous contrainte et excitation magnétique. Ensuite, une autre estimation de la densité d'énergie convertie est décrite en tenant compte des pertes hystérétiques. Enfin, les cycles énergétiques expérimentaux d'Ericsson sont

mesurés pour prouver la faisabilité du processus de conversion et valider le Permendur en tant que matériau pertinent pour les applications de conversion d'énergie.

Le chapitre quatre présente brièvement les récupérateurs d'énergie vibratoire, puis les récupérateurs d'énergie basés sur les vibrations axiales proposées. Une analyse des différents mécanismes de conversion présents dans le système est effectuée et une méthode d'amélioration de la tension de sortie est proposée.

Le chapitre cinq présente la conclusion du travail de recherche et les domaines d'investigation potentiels pour des travaux ultérieurs sont indiqués à la fin.

6.2 Chapitre 2 : Caractérisation de la Perméabilité Incrémentale Magnétique Directionnelle Dépendante de la Contrainte de Traction : Estimation de la Contrainte Mécanique Interne dans une Tôle de Fer-Cobalt

Les alliages Fer-Cobalt (Permendur) sont utilisés dans plusieurs domaines en raison de leurs valeurs élevées de saturation, ceci conduit à des gains de densité de puissance élevés et, par conséquent, à des convertisseurs avec des volumes réduits. Dans la microstructure de ces matériaux plusieurs phénomènes influent sur leurs performances notamment les contraintes mécaniques internes (CMI). L'ajustement de celles-ci peut être une solution prometteuse et fiable pour réduire la forte magnétostriction dans l'optique d'une meilleure caractérisation du système de récupération global mettant l'accent sur le matériau [126]. Avant ce processus d'ajustement, la contrainte interne doit être correctement mesurée et analysée, car elle est importante pour l'assurance qualité et l'inspection des charges supportables par le matériau. Dans ce chapitre, la perméabilité incrémentale magnétique directionnelle (PIM) est proposée comme solution de contrôle non destructif (CND) viable pour l'évaluation des contraintes mécaniques internes.

6.2.1 Revue sur la Perméabilité incrémentale magnétique utilisée comme Techniques d'Estimation des Contraintes mécaniques internes

Les CMI sont causées par de multiples mécanismes, notamment les déformations plastiques dues à l'usinage industriel, les gradients de température et les changements dans la microstructure. La perméabilité magnétique incrémentale (PMI) fournit des informations sur le processus d'aimantation réversible, qui est étroitement liée à la microstructure du matériau ferromagnétique pendant tout le processus d'aimantation et de démagnétisation [127]. La microstructure d'un matériau ferromagnétique (domaine magnétique, centre de fixation, etc.) est facilement affectée par des dommages mécaniques, des contraintes ou des déformations. Ces facteurs justifient l'utilisation de la PMI comme technique d'estimation des CMI. Dans cette section, nous avons ensuite présenté quelques travaux effectués dans la littérature présentant la PIM

comme technique d'estimation des contraintes (en tant que manifestations de couplage magnéto mécanique).

De la littérature, nous avons remarqué que tous les outils/méthodes de contrôle des CMI conçus jusqu'à présent sont basés sur des principes utilisant la magnétisation unidirectionnelle induite par un puissant électro-aimant ajouté aux capteurs de surface locaux pour observer les réponses magnétiques et ne renseignent pas sur des mesures multi directionnelles [119]. Les prédictions numériques des alliages Fe_{49}-Co_{49}-V_2 montrent que les effets des contraintes sur la réponse magnétique peuvent être plus visibles lorsque l'excitation magnétique et la direction de la contrainte proviennent de directions différentes et qu'un capteur directionnel apporterait probablement des résultats significatifs [215].

Dans cette optique, nous avons proposé de surmonter les limitations directionnelles des capteurs existants en utilisant un petit noyau magnétique en ferrite en forme de U. Le contrôle précis des CMI reste un défi important ; ainsi, la contrainte interne a été remplacée par une contrainte externe car les effets de la contrainte sur le matériau est indépendante de la nature de celles-ci. Les essais se sont limités à la contrainte de traction, qui constitue le pire des cas pour l'observation des contraintes.

6.2.2 Caractérisation Magnétique des Tôles Sous Traction

En guise d'étape préliminaire à la validation des éprouvettes et du banc de caractérisation, nous avons effectué des caractérisations magnétiques sur les différents échantillons sous contrainte de traction. Trois classes (RN, FP6, FP10) de Fer-Cobalt ont été initialement caractérisées, la différence entre les trois réside principalement dans le niveau de cristallisation. Ainsi, RN a des grains plus petits que FP10. L'usinage par électroérosion a été utilisé pour couper toutes les éprouvettes (Figure 2-1), réduisant ainsi les effets de la contrainte résiduelle associée au processus de découpe. Tous les tests ont été effectués en dessous de la moitié de la valeur de limite élastique de chacune des tôles. Le dispositif expérimental est présenté dans la Figure 6-1 ci-dessous. Pour la collecte des données plusieurs appareils et capteurs son utilisés.

La première étape après la collection des données fut la correction de la dérive ensuite le recentrage de la courbe. Selon la littérature, la contrainte de traction σ sur les

matériaux doux tels que le Fer-Cobalt adoucit le comportement magnétique. Dans la gamme des basses fréquences, un comportement magnétique plus doux indique une perméabilité plus élevée à un champ magnétique faible (proche de zéro), mais une coercivité plus faible.

Un autre indicateur est le champ coercitif, son comportement peut être approximé par une loi expérimentale décroissante. La valeur du champ coercitif peut également être utilisée pour déterminer la valeur de la contrainte sur le matériau [138].

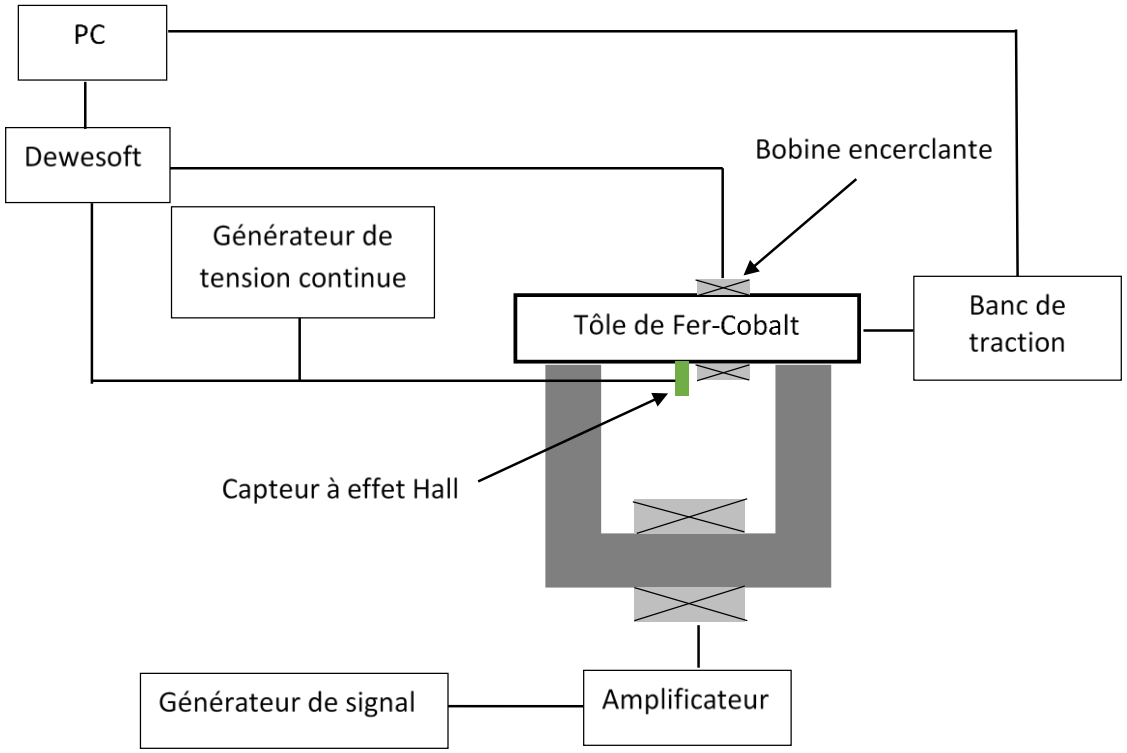

Figure 6-1: Système expérimental pour l'acquisition des courbes hystérétiques B_a (H_{surf}) classiques

Les résultats expérimentaux représentés dans la Figure 2-7 ont confirmé nos attentes ; ils valident la conformité de notre banc d'essai avec les éprouvettes testées ; les résultats ont également montré que l'échantillon FP10 possède la valeur de champ coercitif la plus élevée sans contraintes que les autres échantillons et peut supporter une contrainte plus élevée. Sur la base de ces critères, seul l'échantillon FP10 a été utilisé pour les autres expériences.

6.2.3 Perméabilité Incrémentale Magnétique Directionnelle

La différence dans cette caractérisation et présentée précédemment est que la mesure du champ magnétique est combinée avec des mesures de perméabilité magnétique incrémentale directionnelle sous contrainte. Pour chaque niveau de contrainte, un ensemble de dix courbes $Z(H_{surf})$ a été tracé (pour différentes valeurs de l'angle θ de 0 à $\pi/2$ avec un pas de $\Delta\theta = \pi/18$). Le principe de mesure est illustré dans la Figure 6-2 ci-dessous.

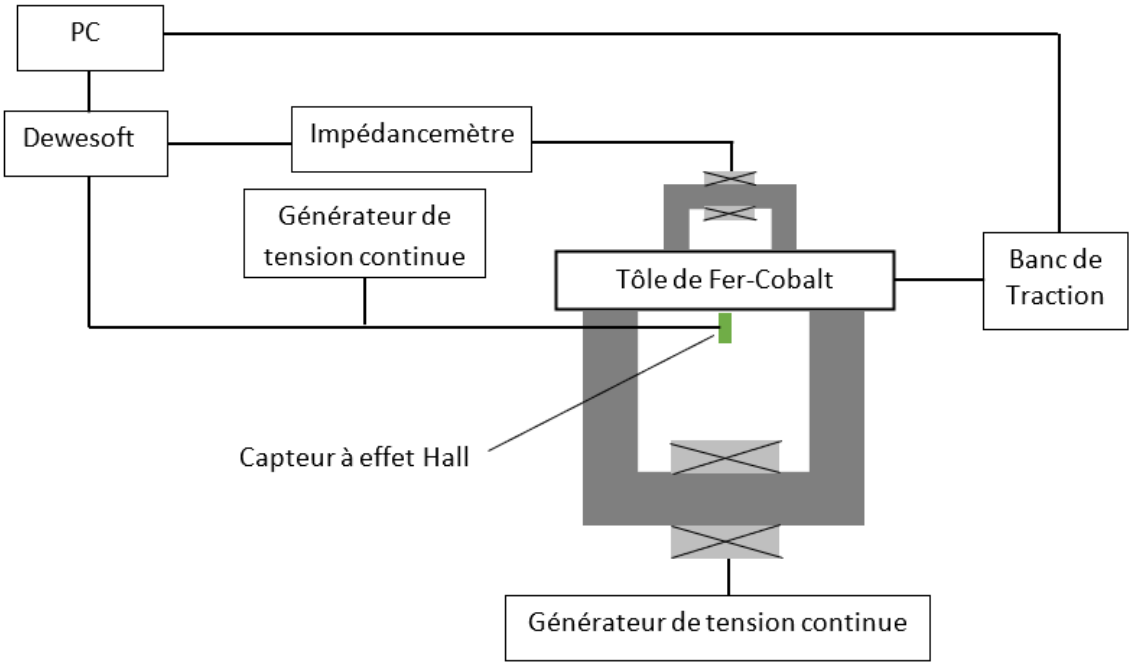

Figure 6-2:Principe de mesure de la perméabilité incrémentale différentielle avec l'impédance mètre

Les mesures de PMI sont réalisées par la superposition de deux fréquences : une basse fréquence d'excitation pour magnétiser le matériau (amplitude la même que pour les cycles *B-H)* et la haute fréquence AC (10KHz pour notre cas).

La première étape de mesure les cycles en ailes de papillon *Z(Hsurf),* et ensuite nous continuons avec une étape de conversion intermédiaire de *Z* (module de l'impédance) vers $\mu_{MIP,}$ définie comme la perméabilité relative des cycles mineurs. Pour cette conversion, un schéma de réluctance magnétique a été établi ainsi que les vérifications basées sur les perméabilités incrémentales et différentielles pour une valeur de champ

de 4500A.m^{-1} ; ces valeurs étaient presque similaires et ont prouvé la pertinence du schéma.

La signature conventionnelle de la méthode MIP est la courbe en aille de papillon, mais pour des fins de comparaison et dans le cadre de ces travaux, l'étape de définition de l'indicateur est poussée vers la reconstruction des cycles d'hystérésis MIP à partir des courbes en aile de papillon. Ainsi toutes les courbes hystérétiques ont été obtenues pour différentes valeurs d'orientation et de traction.

6.2.4 Analyse du Cycle D'hystérésis $B_{a\ MIP}(H_{surf})$ Reconstitué

L'analyse du cycle d'hystérésis reconstitué $B_{a\ MIP}(H_{surf})$ révèle de nombreuses différences avec la courbe $B_a\ (H_{surf})$ classique telles que :

- La contrainte de traction externe tend à redresser la courbe le $B_a\ (H_{surf})$ classique. Mais pour les cycles $B_{a\ MIP}(H_{surf})$, c'est le comportement inverse.
- En tant que matériau déjà doux, les effets de la contrainte de traction sur $B_a\ (H_{surf})$ sont limités. Mais à contrario, on note une forte influence de la traction sur la forme générale des cycles : l'affaissement des cycles $B_{a\ MIP}(H_{surf})$ est facilement perceptible.

La nature de la signature magnétique testée ($B_a\ (H_{surf})$, bruit de Barkhausen, MIP, etc.) ne devrait pas avoir d'effet sur-le-champ coercitif. Les analyses faites ont confirmé nos attentes selon lesquelles les champs coercitifs des deux caractérisations ($B_a\ (H_{surf})$, $B_{a\ MIP}\ (H_{surf})$) restent proches tout au long des variations de σ pour un angle précis ceci confirmant ainsi la fiabilité des mesures MIP au travers des cycles reconstitués.

6.2.5 Conclusion

Plusieurs indicateurs issus de la courbe hystérétique peuvent être utilisés afin de déterminer les effets de la contrainte mécanique dans le matériau, pour notre cas la meilleure indication, selon une analyse plus approfondie basée sur les coefficients de corrélation de Pearson ρ, est l'étude de la valeur du flux $B_{a\ MIP}$ pour une valeur de champ surfacique H_{surf} = 10 kA·m^{-1}. Pour les 10 angles de capteur évalués, la valeur $\theta = \pi/2$, révèle une étonnante corrélation linéaire de 0,99.

$B_{a\ MIP}$ pour H_{surf} = 10 kA·m^{-1} offre une réflexion cumulative tout au long du mécanisme d'augmentation de volume des parois du domaine se produisant pendant le cycle d'aimantation. Concernant l'orientation du capteur, la paroi du domaine d'un matériau théoriquement isotrope ne devrait pas se gonfler différemment dans les deux sens pour des raisons énergétiques.

6.3 Chapitre 3 : Conversion d'Energie magnétostrictive, Modélisation et Validation pour l'Alliage Fer-Cobalt Valdanium

La demande croissante d'appareils autonomes a fait du concept de récupération d'énergie un point d'intérêt croissant. Dans ce sens, les matériaux magnétostrictifs constituent un candidat idéal pour la conversion des vibrations mécaniques en énergie électrique de manière rentable (c'est-à-dire concurrencer le prix des batteries primaires). Dans ce chapitre nous avons tout d'abord présenté quelques modèles magnéto mécaniques et électromécaniques de conversion d'énergie existants. Sur la base des mesures expérimentales, un modèle du comportement anhystérétique des tôles est proposé et validé puis utilisé pour évaluer la conversion d'énergie des tôles sous contraintes de traction et excitation magnétique. Ensuite, une autre estimation de la densité d'énergie convertie est décrite en tenant compte des pertes dues au phénomène d'hystérésis. Enfin, les cycles énergétiques expérimentaux d'Ericsson sont mesurés pour prouver la faisabilité du processus de conversion et valider le Permendur en tant que matériau pertinent pour les applications de conversion d'énergie.

6.3.1 Modèles écrivant le Comportement Magnéto mécanique

Le couplage entre les contraintes mécaniques et les propriétés magnétiques des matériaux ferromagnétiques témoigne de la réciprocité entre la microstructure magnétique (domaines magnétiques et parois de domaines) et la microstructure mécanique (contraintes et de déformations). La complexité du processus de modélisation vient de la multiplicité des processus de magnétisation qui peuvent se produire simultanément au sein d'un matériau magnétique lorsqu'il est exposé à un champ magnétique. Basés sur ce principe de réciprocité plusieurs modèles ont été établi. Jusqu'à présent, pour étudier l'effet magnéto mécanique, une approche analytique (approche empirique de la modélisation et absence de base théorique pour l'interprétation physique) et une approche théorique (description mathématique de l'hystérésis à partir des données expérimentales) ont été adoptées. Les méthodes de modélisation sont pour la plupart précises et prédictives sur le temps, mais restent

difficiles à mettre en œuvre en raison de leur temps de calcul, des données d'entrée requises et leur processus d'identification délicat.

6.3.2 Modèles de Conversion d'Énergie Electromécanique

Le modèle de conversion d'énergie électromécanique décrit la relation entre le déplacement mécanique du système de récupération d'énergie et la tension électrique générée. Ces modèles prennent en compte les propriétés mécaniques du système de récupération, telle que sa rigidité et son amortissement, la fréquence de vibration, le type d'alimentation en champs, ainsi que les propriétés électriques, notamment la capacité et la résistance du circuit de récupération d'énergie. Dans la suite du chapitre nous avons des travaux, prototypes et quelques densités d'énergie pour des systèmes de récupération utilisant des matériaux magnétostrictifs présents dans la littérature.

6.3.3 Caractérisation expérimentale du Permendur

Le Permendur a été choisi dans le cas de notre étude due à son faible coût, sa disponibilité, sa solidité tout ceci pour des coûts financiers bien en dessous de ceux du Terfenol, Galfenol ou du Metglas ayant des propriétés mécaniques, magnétiques et magnétostrictives quasi similaires. Et de plus, ce matériau n'a jamais vraiment été utilisé pour des applications de récupération d'énergie. Les cycles *B(H)* (Figure 3-2) de la tôle sous contraintes de traction ont été obtenus expérimentalement. Comme attendu, le comportement magnétique des échantillons est adouci et ceci s'explique par le fait que les moments magnétiques prennent une direction préférentielle (axe facile de direction de magnétisation) avec l'application de la contrainte combinée à l'effet du champ d'excitation qui tend aussi à aligner ces moments dans sa direction.

6.3.4 Méthode de Simulation du Comportement Anhystérétique Associé à la Contrainte de Traction

Pour l'établissement du modèle, nous avons dans un premier temps obtenu le comportement anhystérétique expérimental. Il est obtenu en effectuant la moyenne des valeurs de champ d'excitation magnétique correspondant aux pentes ascendantes et descendantes des courbes principales d'hystérésis pour une densité de flux

magnétique donnée. Les courbes anhystérétiques résultantes sont la combinaison des différents points correspondants obtenus.

Parmi les différents modèles existants et compte tenu des caractéristiques du matériau (effet de contrainte et hystérésis négligeable entre autres), nous avons décidé d'adopter un modèle anhystérétique simple basé sur une approche thermodynamique présentée par Agayan [171] pour obtenir le comportement anhystérétique. Ce modèle est concentré davantage sur une expression mathématique plutôt que sur une approche phénoménologique, qui permet de décrire la signification physique de chaque variable ; l'expression du modèle est ainsi définie par l'Eq.(3-2).

Les paramètres du modèle ont été obtenus à l'aide de l'outil Curve Fitting Tools de MATLAB®. Pour ce faire, une plage raisonnable de valeurs des paramètres a d'abord été estimée, ainsi qu'un intervalle de valeurs cohérentes et réalistes. Les paramètres dans la Table 3-3 ; le modèle ainsi présenté a été validé sur la base d'un certain nombre de caractérisation présenté ci-après.

6.3.5 Validation du Modèle.

Pour la validation du modèle, nous avons effectué trois tests :

- Le coefficient de détermination R^2 du modèle ; il est donné par le logiciel, une valeur proche de 1 signifie un modèle précis ; nous avons une valeur de 0.9991 confirmant la précision du modèle.
- Effet de la contrainte de traction sur la perméabilité relative dans la région du faible champ magnétique : à bas champ nous avons une perméabilité maximale, cette valeur augmente avec la traction. Dans la Figure 3-6, nous remarquons une même tendance entre les points expérimentaux et la courbe obtenue par modélisation.
- Valeur de B_a à H_{surf} = 5000A.m^{-1} : Dans cette zone, nous sommes toujours au niveau de pré-saturation. Un autre point notable est la tendance de la magnétisation à converger pour toutes les contraintes mécaniques des champs d'excitation autour d'un certain point. Ce point pourrait faire l'objet d'études complémentaires.

6.3.6 Évaluation de la Conversion énergétique

Dans cette partie, nous avons étudié le potentiel de conversion énergétique du matériau pour des applications de récupération d'énergie en utilisant 3 approches :

- **Estimation d'énergie à partir de courbes anhystérétiques simulées :**

Les résultats expérimentaux (section 3.3) ont montré une dépendance explicite entre la densité de flux magnétique, la contrainte de traction appliquée et le champ d'excitation. Par souci de simplicité, nous avons considéré uniquement la conversion purement magnéto mécanique sans la conversion électromagnétique. Cette évaluation a été réalisée en supposant un cycle thermodynamique proche du cycle équivalent d'Ericsson (Figure 3-8). L'analyse des résultats a montré une influence relativement faible du niveau de contrainte au-delà de 240 MPa. Une densité d'énergie maximale de 10.45 mJ.cm $^{-3}$ sous une contrainte de traction entre 0 et 480 MPa et une excitation magnétique de 5.5 kA.m^{-1}.

- **Estimation d'énergie à partir de cycles d'hystérésis**

Cette méthode prend en compte les pertes hystérétiques dues au processus d'aimantation sous contrainte. Une méthode d'estimation d'énergie semi-empirique est proposée afin de reproduire fidèlement la forme de la courbe d'inversion du premier ordre représentant la densité d'énergie pouvant être convertie. Cette méthode d'estimation révèle une influence de contrainte plus importante, mais une énergie convertie beaucoup plus faible. La prise en compte des pertes engendre une chute du taux de conversion de 30 %. Une densité d'énergie allant jusqu'à 3.52 mJ.cm^{-3} a été obtenue dans les mêmes conditions que dans le cas précédent.

- **Validation expérimentale du cycle Ericsson**

Cette étape consistait à la reconstruction expérimentale des cycles d'Ericsson pour la validation de la faisabilité du principe en tant que système de conversion d'énergie. Cette partie consistait aussi la confirmation des prévisions théoriques du niveau d'énergie pouvant être récolté. Le banc expérimental est resté inchangé. Mais toutefois, la variation de traction a été limité entre 0-175MPa. Passé cette valeur maximale nous avons obtenu des dérives marquées ce qui nous empêchait d'obtenir un cycle fermé.

6.3.7 Conclusion

En raison de leur robustesse et de leur fort potentiel de couplage électromécanique, les matériaux magnétostrictifs constituent une solution compétitive pour les récupérateurs d'énergie vibratoire. Des essais sous contrainte ont été réalisés dans un premier temps et utilisés comme base expérimentale pour établir des outils théoriques. Une méthode de simulation a donc été présentée et validée. Ensuite, à l'aide des cycles d'Ericsson, la densité d'énergie pouvant être récupérée a été prédite à partir des courbes anhystérétiques obtenues par simulation. En considérant les effets des pertes hystérétiques, une seconde méthode d'estimation a été présentée. Les valeurs obtenues par cette approche semblent excessives par rapport aux résultats obtenus par des matériaux conventionnels tels que le Galfenol ou le Terfenol entre autres dû aux conditions expérimentales (valeurs de traction) qui ne sont pas les mêmes. La comparaison entre les méthodes prédictives et les tests expérimentaux a montré une surestimation du modèle basé sur la courbe anhystérétique, notamment pour les cas des valeurs de champs élevés. La prédiction basée sur les boucles d'hystérésis majeures était beaucoup plus précise, notamment en termes de pente de la courbe énergie convertie en fonction du champ magnétique. Le prochain chapitre constitue la mise sur pied d'un démonstrateur illustrant le principe de récolte de l'énergie vibratoire.

6.4 Chapitre 4 : Récolte de l'Énergie vibratoire à partir des Matériaux magnétostrictifs : Cas pratique d'un Démonstrateur

6.4.1 Systèmes de Récupération d'Energie Vibratoires présent dans la Littérature

En tant que méthode de génération d'énergie non exhaustive, la récupération d'énergie vibratoire peut être classée comme une technique de production de micro énergie, qui convertit les vibrations induites par diverses sources en énergie électrique utilisable[188]. Actuellement, la puissance produite par ces systèmes de récuperation est encore inférieure à celle des batteries conventionnelles majoritairement utilisées jusqu'ici. Plusieurs dispositifs ont été développés jusqu'ici allant des systèmes en poutre aux systèmes à contraintes axiales (horizontales ou verticales). La plupart de ces systèmes utilisent le principe d'électromagnétisme pour générer une différence de potentiel entre les bornes d'une bobine.

Les systèmes de récupération à vibrations axiales sont relativement faciles à implémenter et peuvent être ajustées afin de répondre aux exigences spécifiques fonction des applications. Cependant, ces systèmes présentent globalement des limites telles que le faible rendement de conversion énergétique ; ce qui les rend incompatibles aux applications nécessitant de fortes puissances, ces systèmes aussi ont besoin des circuits électroniques adéquats pour une amplification et stabilisation de la tension en sortie. De plus, les performances de ces dispositifs sont affectées par des facteurs tels que la température, l'intensité du champ de bias et la contrainte mécanique. En tenant compte de ces paramètres, nous avons développé un démonstrateur basé sur les vibrations axiales qui sera brièvement présenté dans la section suivante.

6.4.2 Présentation du Démonstrateur Conçu

Le démonstrateur est illustré par la Figure 4-7. Les échantillons utilisés sont toujours les tôles de Fer-Cobalt. Deux tôles parallèles orientées verticalement avec chacune une bobine de 2500 spires. Afin d'optimiser la tension en sortie, les bobines ont été connectées en série. Six aimants en Néodyme dont 3 à chacune des extrémités de la

tôle assurent la fermeture du circuit magnétique et la création du champ de bias. Pour l'application des vibrations, nous avons utilisé un pot vibrant. Trois ressorts verticaux similaires ont été utilisés pour appliquer la contrainte initiale et garantir que les tôles soient toujours sous tension, évitant ainsi le flambement. Les formes d'onde de tension ont été visualisées à l'aide d'un oscilloscope numérique.

Les variations de champ magnétique dues aux variations de réluctance dues à la vibration et des courants induits dans les bobines agissent comme une source de champ magnétique secondaire en plus des aimants déjà présents.

6.4.3 Processus Expérimental de Récupération d'Energie

Le dispositif de récupération développé reçoit des vibrations par sa base avec en fonction de la fréquence de vibration, et d'après le principe de l'effet magnétostrictif inverse, une tension est générée dans les bobines comme suit : lorsqu'une vibration est appliquée, la structure est étirée et relâchée de manière répétitive autour d'un point de fonctionnement en raison de la contrainte initiale des ressorts sur les tôles. Les contraintes vibratoires provoquées par ces mouvements entraîneront une modification du flux magnétique dans les tôles par effet pseudo-Villari ou effet magnétostrictif inverse et induit un changement d'aimantation à l'intérieur du matériau. En faisant vibrer le dispositif de manière dynamique ou cyclique, la variation temporelle du flux provoquée par la déformation périodique en traction génère une tension aux bornes des bobines selon la loi de Faraday sur l'induction électromagnétique [206].

6.4.4 Analyse du Mécanisme de Conversion d'Énergie

Trois domaines de couplage principaux existent :

- La section mécanique abritant le matériau magnétostrictif actif composé des ressorts et du pot vibrant.
- Le circuit magnétique hébergé par le matériau actif
- Le domaine électrique caractérisé par la tension induite aux bornes de la bobine.

6.4.4.1 Contrainte initiale : Étirement mécanique par les Ressorts

Pour la génération de la contrainte initiale, un premier étirement mécanique manuel est exercé par des ressorts sur les tôles. Après caractérisation des ressorts, nous avons le tableau synthétique ci-dessous :

Table 6-1: Synthèse des paramètres mécaniques initiaux

Paramètres	Valeur
K	$1.3\ kN\ m^{-1}$
L_0	$2,5\ cm$
F_0	$35N$
P_0	$1,21MPa$

6.4.4.2 Magnétisation de la Tôle : Circuit Magnétique

Dans notre démonstrateur, la création du champ magnétique est due aux contributions de trois facteurs :

- Variations de réluctance dans les tôles dues aux variations de contrainte.
- Courants induits dans les bobines qui peuvent être considérés comme source secondaire de champ magnétique.
- Aimants permanents qui génèrent un champ magnétique constant.

Pour l'établissement du modèle, nous avons supposé que la résistance de charge soit équivalente à la résistance interne de la bobine. Nous avons également négligé la réluctance de tous les autres matériaux ou composants autres que le matériau magnétostrictif.

Le modèle ainsi conçu nous a permis de faire des estimations sur l'énergie théorique pouvant être produite en fonction des différentes parties du système et des propriétés magnétiques, électriques et mécaniques.

Éq. (4-28) révèle que la puissance maximale théorique pouvant être récoltée ne dépend pas de la structure mécanique, mais uniquement des variations de contraintes, du champ magnétique à la fréquence optimale et des propriétés du matériau magnétostrictif lui-même. Cette conclusion est conforme aux conclusions des travaux

effectués dans [213]. Un développement poussé dans ce sens et de calcul de valeurs en cours d'exécution.

6.4.4.3 Production d'Energie Electrique

Le procédé de collecte de données consistait à faire varier la fréquence à une amplitude constante des vibrations puis à mesurer la tension RMS au niveau de la bobine à l'aide d'un oscilloscope. La tension est prise à différentes fréquences de vibration variant du spectre 0 à 2000 Hz. Nous avons observé des valeurs maximales de tension à certaines fréquences. La Figure 4-12 illustre le spectre tension obtenue aux bornes de la bobine. Les valeurs de tension tracées sont des valeurs moyennes par rapport à la fréquence d'entrée appliquée. La figure révèle quelques pics (Table 4-3) de tension à certaines fréquences. Ces fréquences ne peuvent pas vraiment être appelées fréquences de résonance en raison de la présence de plusieurs oscillations mécaniques.

6.4.5 Amélioration de la Tension de Sortie

Dû à la variation de fréquence nous notons l'effet de Peau au niveau des valeurs de la résistance et de l'inductance de la bobine. Dans la gamme de fréquence utilisée, nous avons fait une approximation de leur comportement. Pour chaque valeur de fréquence, le modèle renseigne sur les valeurs correspondantes de résistance et d'inductance. Pour amplifier la tension, nous avons connecté un condensateur en parallèle à la bobine et supposé que le système oscille en résonance à chaque pic de tension et en s'appuyant sur le facteur de qualité du circuit RLC.

À 913 Hz, nous avons un facteur de qualité de 2.20, la tension de maximale sans condensateur est de 0,0715 V et avec un condensateur est de 0,13 V. On note une différence de 58.5mV entre les deux valeurs.

La puissance en sortie maximale pouvant être récupérée est de 0.15 mW et est atteinte à une fréquence de 913 Hz. L'énergie électrique obtenue à cette même fréquence est de 0.15 µJ/cycle, pour une densité de puissance de 6.13 $mW.cm^{-3.}$

6.4.6 Discussion

La plupart des résultats présents dans la littérature ont été obtenus à des fréquences relativement basses. Ce n'est pas le cas de notre système. Le système développé montre une faible puissance de sortie par rapport aux autres, cela peut s'expliquer par le fait que le matériau est excité mécaniquement à haute fréquence et à de telles fréquences, le matériau est presque statique.

Avec l'utilisation d'un pot vibrant, nous sommes limités en termes d'amplitude de contrainte, la valeur de contrainte appliquée ici est insignifiante, et est bien en dessous de la limite élastique du matériau ; donc les effets sur le matériau ne sont quasiment pas visibles et les résultats obtenus ne peuvent pas être optimaux. Néanmoins, l’ordre de mérite de ces résultats est significatif.

6.5 Conclusion

6.5.1 Conclusion

Ce manuscrit s'articule ainsi autour de trois axes principaux :

(i) Les matériaux magnétostrictifs sont très utilisés en raison de leur saturation de magnétisation élevée. Mais ces bonnes propriétés peuvent être à l'origine de bruits acoustiques indésirables lors de leur fonctionnement. L'obtention des informations contraintes mécaniques internes constitue une solution pour réduire la magnétostriction élevée ainsi améliorer les performances du matériau. Nous avons proposé de surmonter les limitations directionnelles des capteurs magnétiques utilisées jusqu'à présent par un noyau magnétique miniature en ferrite en forme de U. Le contrôle précis des CMI reste un défi important ; ainsi, la contrainte interne a été remplacée par une contrainte appliquée de l'extérieur. Les essais se sont limités à la contrainte de traction, qui constitue le pire des cas pour l'observation des contraintes. Les résultats ont montré que le stress interne peut être remplacé par un stress externe. Des courbes en ailes de papillon $Z(H_{surf})$ préliminaires ont été tracées, mais sont limitées, car elles ne peuvent pas fournir d'informations magnétiques sur le processus. Nous sommes donc ensuite passés par une conversion de l'impédance *IZI* en perméabilité relative FeCo μ_{MIP_r} En utilisant un schéma de conversion de réluctance. L'étape finale de conversion est la conversion de $\boldsymbol{\mu_{MIP_r}}(H_{surf})$ en cycles d'hystérésis classiques, $B_{a\ MIP}\ (H_{surf})$. Le lien entre PIM et les indicateurs associés étant établi en reconstituant des cycles d'hystérésis, nous étudions le comportement des indicateurs notamment $B_{aMIP}\ (H_{surf})$= 10 kA·m^{-1} qui sont les mieux adaptés et associés au mécanisme de gonflement des parois du domaine. L'analyse du facteur de corrélation de Pearson pour les 10 angles de capteur évalués a révélé que pour δ = π/2, l'étonnante corrélation linéaire de 0,99 est atteinte. Cette orientation favorise donc la mesure.

(ii) La demande croissante d'appareils autonomes a fait du concept de récupération d'énergie un point d'intérêt industriel et académique important. Dans cette partie, nous avons initialement réalisé la caractérisation magnétique expérimentale comme base de la modélisation analytique du comportement anhystérétique des tôles sous contrainte de traction. La validité du modèle a été vérifiée à l'aide de nombreux tests parmi lesquels le coefficient de détermination du modèle. C'est sur cette base que la validité de notre modèle a été établie. La capacité de conversion d'énergie a été évaluée de 3 manières :

- Utilisation de cycles thermodynamiques d'Ericsson à partir de courbes anhystérétiques modélisées proposées. Une densité d'énergie maximale de 10.45 $mJ.cm^{-3}$ a été prévue sous une contrainte de traction de 0 à 480 MPa et une excitation magnétique de 5.5 $kA.m^{-1.}$

- Ensuite, une estimation supplémentaire a été proposée tenant en compte des pertes par hystérésis induites par l'existence d'un champ coercitif au sein du matériau. Pour cela, des boucles d'hystérésis majeures à différents niveaux de contrainte ont été considérées, donnant une densité d'énergie de 3.52 $mJ{\cdot}cm^{-3}$.

- Enfin, des cycles expérimentaux d'Ericsson ont été réalisés expérimentalement afin de prouver la faisabilité de la méthode de conversion et corroborer avec les prédictions du niveau d'énergie.

La comparaison entre les différentes méthodes prédictives et les tests expérimentaux a montré une surestimation du modèle proposé basé sur la courbe anhystérétique modélisé, notamment dans le domaine des champs élevés. La prédiction prenant en compte les pertes majeures par hystérésis était beaucoup plus précise, notamment en termes de pente de la courbe énergie convertie en fonction du champ magnétique.

(iii) En raison de leur robustesse et de leur potentiel de couplage électromécanique, les matériaux magnétostrictifs constituent une solution compétitive pour les récupérateurs d'énergie vibratoire. Pourtant, leur mise en œuvre réaliste, principalement en raison du prix des matériaux, ainsi que de la compréhension approfondie de leur efficacité de conversion, reste un

challenge. Pour le récupérateur pratique que nous avons implémenté, la tension de sortie maximale pouvant être récupérée du système est de 912.5 Hz sans amplification, 71 mV et après amplification, 130 mV. C'est à la même fréquence que l'on a la tension de sortie la plus élevée qui est de 152,66µW. L'énergie maximale pouvant être obtenue à partir du dispositif de récolte est de 0,15 µJ/Cycle^{-1} correspondant à une densité de puissance de 0.6mW.cm^{-3}. L'ajout du critère de robustesse de stabilité pour caractériser les différents comportements améliorant ainsi la précision de ce modèle ;

Nous avons présenté une synthèse des développements proposés autour de ces trois axes et proposerons des perspectives concernant les travaux futurs qui peuvent être envisagés dans la continuité de ce travail de thèse.

6.5.2 Perspectives

Concernant la conversion d'énergie, de nombreuses perspectives peuvent être répertoriées pour ce travail afin de tirer parti de la non-linéarité des matériaux pour concevoir des récupérateurs d'énergie efficaces (structure et interface électrique) ; ceux-ci incluent :

- Pour une meilleure approximation de la densité d'énergie ultime, nous devrions étudier la corrélation entre les propriétés de magnétostriction et de densité d'énergie ultime.
- Effectuez le dimensionnement complet du système à des valeurs de champ de polarisation élevées et étudiez le comportement du processus de conversion.
- Les tests sur des méthodes prédictives sous contrainte de compression.
- La prise en compte des différents niveaux de stress,
- Pour les véritables dispositifs de récupération d'énergie, la polarisation magnétique est assurée par des aimants qui induisent un champ magnétique dynamique supplémentaire, ce qui nous permet d'étudier le comportement dynamique de l'échantillon.

En guise de suivi de l'estimation des CMI, plusieurs travaux d'amélioration pourraient être énumérés, notamment :

- L’impact à court terme d’une contrainte de compression homogène.
- À l'avenir, nous comptons tester d'autres types de matériaux et, à long terme, de voir dans quelle mesure le MIP directionnel fonctionne sur d'autres attributs ciblés par les méthodes de CND magnétiques typiques, tels que les caractéristiques microstructurales et le vieillissement.

Sur la base des faiblesses du démonstrateur, nous proposons comme perspectives futures :

- Le dimensionnement approprié du système de récolte complet en tenant compte du comportement interne du matériau, des effets du nombre de tours et du champ magnétique polarisé.
- L’augmentation de la valeur de contrainte et la caractérisation des effets sur la tension de sortie.

REFERENCES

[1] I. C. L. Ng and S. Y. L. Wakenshaw, “The Internet-of-Things: Review and research directions,” *International Journal of Research in Marketing*, vol. 34, no. 1, pp. 3–21, Mar. 2017, doi: 10.1016/j.ijresmar.2016.11.003.

[2] B. Rashid and M. H. Rehmani, “Applications of wireless sensor networks for urban areas: A survey,” *Journal of Network and Computer Applications*, vol. 60, pp. 192–219, Jan. 2016, doi: 10.1016/j.jnca.2015.09.008.

[3] M. Teresa Penella, J. Albesa, and M. Gasulla, “Powering wireless sensor nodes: Primary batteries versus energy harvesting,” in *2009 IEEE Intrumentation and Measurement Technology Conference*, Singapore. Singapore: IEEE, May 2009, pp. 1625–1630. doi: 10.1109/IMTC.2009.5168715.

[4] J. VanZwol, “Designing battery packs for thermal extremes,” *Power Electronics Technology*, pp. 40–45, Jul. 2006.

[5] Á. Gutiérrez, C. González, J. Jiménez-Leube, S. Zazo, N. Dopico, and I. Raos, “A Heterogeneous Wireless Identification Network for the Localization of Animals Based on Stochastic Movements,” *Sensors*, vol. 9, no. 5, pp. 3942–3957, May 2009, doi: 10.3390/s90503942.

[6] J. A. Paradiso and T. Starner, “Energy Scavenging for Mobile and Wireless Electronics,” *IEEE Pervasive Comput.*, vol. 4, no. 1, pp. 18–27, Jan. 2005, doi: 10.1109/MPRV.2005.9.

[7] “Lithium battery,” *Wikipedia*. Jun. 26, 2023. Accessed: Aug. 28, 2023. [Online]. Available: https://en.wikipedia.org/w/index.php?title=Lithium_battery&oldid=1162036535

[8] Z. Deng and M. J. Dapino, “Review of magnetostrictive vibration energy harvesters,” *Smart Mater. Struct.*, vol. 26, no. 10, p. 103001, Oct. 2017, doi: 10.1088/1361-665X/aa8347.

[9] J. McCabe, Z. Yan, O. Al Naimi, G. Mahmoud, and S. Rolland, “Smart materials in dentistry: Smart materials in dentistry,” *Australian Dental Journal*, vol. 56, pp. 3–10, Jun. 2011, doi: 10.1111/j.1834-7819.2010.01291.x.

[10] R. Bogue, “Smart materials: a review of recent developments,” *Assembly Automation*, vol. 32, no. 1, pp. 3–7, Feb. 2012, doi: 10.1108/01445151211198674.

[11] M. U. Hensel, “Performance-oriented Architecture and the Spatial and Material Organisation Complex. Rethinking the Definition, Role and Performative Capacity of the Spatial and Material Boundaries of the Built Environment,” *FormAkademisk*, vol. 4, no. 1, Mar. 2011, doi: 10.7577/formakademisk.125.

[12] D. M. Addington and D. Schodek, “Smart materials and new technologies : for the architecture and design professions,” 2005. Accessed: Aug. 27, 2023. [Online]. Available: https://www.semanticscholar.org/paper/Smart-materials-and-new-technologies-%3A-for-the-and-Addington-Schodek/e597b6724a2b6d41038bf4e9f69cacb666c0619f

[13] “Smart Materials and Technologies: For the Architecture and Design Professions,” Routledge & CRC Press. Accessed: Aug. 27, 2023. [Online]. Available: https://www.routledge.com/Smart-Materials-and-Technologies-For-the-

Architecture-and-Design-Professions/Addington-Schodek/p/book/9780750662253

[14] CHETOUH Samir, “CARACTERISATION MECANIQUE DES MATERIAUX INTELLIGENTS DE TYPE MAGNETOSTRICTIFS ET LEUR APPLICATION,” UNIVERSITÉ MENTOURI - CONSTANTINE, 2010.

[15] M. Kök, İ. N. Qader, F. Dağdelen, and Y. Aydoğdu, “Akıllı Malzemeler üzerine derleme: araştırmalar ve uygulamaları,” *El-Cezeri Fen ve Mühendislik Dergisi*, Sep. 2019, doi: 10.31202/ecjse.562177.

[16] A. S. Y. Mohamed, “Smart Materials Innovative Technologies in architecture; Towards Innovative design paradigm,” *Energy Procedia*, vol. 115, pp. 139–154, Jun. 2017, doi: 10.1016/j.egypro.2017.05.014.

[17] Y. Song, W. Wei, and X. Qu, “Colorimetric Biosensing Using Smart Materials,” *Adv. Mater.*, vol. 23, no. 37, pp. 4215–4236, Oct. 2011, doi: 10.1002/adma.201101853.

[18] M. Sadeghi, P. Masudifar, and F. Faizi, “The Function of Smart Material’s behavior in architecture,” 2011. Accessed: Jan. 24, 2024. [Online]. Available: https://www.semanticscholar.org/paper/The-Function-of-Smart-Material's-behavior-in-Sadeghi-Masudifar/43d34325b3707ce4b7bbd02d4b92898a7a8b769d

[19] C. Wei and X. Jing, “A comprehensive review on vibration energy harvesting: Modelling and realization,” *Renewable and Sustainable Energy Reviews*, vol. 74, pp. 1–18, Jul. 2017, doi: 10.1016/j.rser.2017.01.073.

[20] M. J. Dapino, “Magnetostrictive Materials,” in *Encyclopedia of Smart Materials*, 1st ed., M. Schwartz, Ed., Wiley, 2002. doi: 10.1002/0471216275.esm051.

[21] S. Bahl, H. Nagar, I. Singh, and S. Sehgal, “Smart materials types, properties and applications: A review,” *Materials Today: Proceedings*, vol. 28, pp. 1302–1306, 2020, doi: 10.1016/j.matpr.2020.04.505.

[22] S. Wang, W. Rong, L. Wang, H. Xie, L. Sun, and J. K. Mills, “A survey of piezoelectric actuators with long working stroke in recent years: Classifications, principles, connections and distinctions,” *Mechanical Systems and Signal Processing*, vol. 123, pp. 591–605, May 2019, doi: 10.1016/j.ymssp.2019.01.033.

[23] J. Li, H. Huang, and T. Morita, “Stepping piezoelectric actuators with large working stroke for nano-positioning systems: A review,” *Sensors and Actuators A: Physical*, vol. 292, pp. 39–51, Jun. 2019, doi: 10.1016/j.sna.2019.04.006.

[24] T. Zheng, J. Wu, D. Xiao, and J. Zhu, “Recent development in lead-free perovskite piezoelectric bulk materials,” *Progress in Materials Science*, vol. 98, pp. 552–624, Oct. 2018, doi: 10.1016/j.pmatsci.2018.06.002.

[25] X. Zhang, G. Li, W. Wang, and S. Su, “Study on the energy conversion mechanism and working characteristics of a new energy harvester with magnetic liquid,” *Sensors and Actuators A: Physical*, vol. 359, p. 114409, Sep. 2023, doi: 10.1016/j.sna.2023.114409.

[26] V. Apicella, C. S. Clemente, D. Davino, D. Leone, and C. Visone, “Review of Modeling and Control of Magnetostrictive Actuators,” *Actuators*, vol. 8, no. 2, p. 45, May 2019, doi: 10.3390/act8020045.

[27] F. Narita and M. Fox, “A Review on Piezoelectric, Magnetostrictive, and Magnetoelectric Materials and Device Technologies for Energy Harvesting Applications,” *Adv. Eng. Mater.*, vol. 20, no. 5, p. 1700743, May 2018, doi: 10.1002/adem.201700743.

[28] M. A. A. Farsangi, F. Cottone, H. Sayyaadi, M. R. Zakerzadeh, F. Orfei, and L. Gammaitoni, “Energy harvesting from structural vibrations of magnetic shape memory alloys,” *Applied Physics Letters*, vol. 110, no. 10, p. 103905, Mar. 2017, doi: 10.1063/1.4978258.

[29] K. K. Alaneme, E. A. Okotete, and J. U. Anaele, “Structural vibration mitigation – a concise review of the capabilities and applications of Cu and Fe based shape memory alloys in civil structures,” *Journal of Building Engineering*, vol. 22, pp. 22–32, Mar. 2019, doi: 10.1016/j.jobe.2018.11.014.

[30] N. G. Garafolo and G. R. McHugh, “Mitigation of flutter vibration using embedded shape memory alloys,” *Journal of Fluids and Structures*, vol. 76, pp. 592–605, Jan. 2018, doi: 10.1016/j.jfluidstructs.2017.09.013.

[31] P. Nnamchi, A. Younes, and S. González, “A review on shape memory metallic alloys and their critical stress for twinning,” *Intermetallics*, vol. 105, pp. 61–78, Feb. 2019, doi: 10.1016/j.intermet.2018.11.005.

[32] C.-J. Lin, C.-Y. Lee, and Y. Liu, “Vibration Control Design for a Plate Structure with Electrorheological ATVA Using Interval Type-2 Fuzzy System,” *Applied Sciences*, vol. 7, no. 7, p. 707, Jul. 2017, doi: 10.3390/app7070707.

[33] X. Dong, C. Niu, and M. Qi, “Enhancement of electrorheological performance of electrorheological elastomers by improving TiO_2 particles/silicon rubber interface,” *J. Mater. Chem. C*, vol. 4, no. 28, pp. 6806–6815, 2016, doi: 10.1039/C6TC01447J.

[34] H. Li, C. Yu, R. Chen, J. Li, and J. Li, “Novel ionic liquid-type Gemini surfactants: Synthesis, surface property and antimicrobial activity,” *Colloids and Surfaces A: Physicochemical and Engineering Aspects*, vol. 395, pp. 116–124, Feb. 2012, doi: 10.1016/j.colsurfa.2011.12.014.

[35] D. Guyomar and M. Lallart, “Recent Progress in Piezoelectric Conversion and Energy Harvesting Using Nonlinear Electronic Interfaces and Issues in Small Scale Implementation,” *Micromachines*, vol. 2, no. 2, pp. 274–294, Jun. 2011, doi: 10.3390/mi2020274.

[36] A. Li *et al.*, “Energy harvesting using a magnetostrictive transducer based on switching control,” *Sensors and Actuators A: Physical*, vol. 355, p. 114303, Jun. 2023, doi: 10.1016/j.sna.2023.114303.

[37] N. Thanh Tung *et al.*, “Ultimate electromechanical energy conversion performance and energy storage capacity of ferroelectric materials under high excitation levels,” *Applied Energy*, vol. 326, p. 119984, Nov. 2022, doi: 10.1016/j.apenergy.2022.119984.

[38] F. K. Shaikh and S. Zeadally, “Energy harvesting in wireless sensor networks: A comprehensive review,” *Renewable and Sustainable Energy Reviews*, vol. 55, pp. 1041–1054, Mar. 2016, doi: 10.1016/j.rser.2015.11.010.

[39] I. Petsagkourakis, K. Tybrandt, X. Crispin, I. Ohkubo, N. Satoh, and T. Mori, “Thermoelectric materials and applications for energy harvesting power generation,” *Science and Technology of Advanced Materials*, vol. 19, no. 1, pp. 836–862, Dec. 2018, doi: 10.1080/14686996.2018.1530938.

[40] M. R. Gokana, C.-M. Wu, K. G. Motora, J. Y. Qi, and W.-T. Yen, “Effects of patterned electrode on near infrared light-triggered cesium tungsten bronze/poly(vinylidene)fluoride nanocomposite-based pyroelectric

nanogenerator for energy harvesting," *Journal of Power Sources*, vol. 536, p. 231524, Jul. 2022, doi: 10.1016/j.jpowsour.2022.231524.

[41] J. Zhao *et al.*, "Self-Powered Implantable Medical Devices: Photovoltaic Energy Harvesting Review," *Adv. Healthcare Mater.*, vol. 9, no. 17, p. 2000779, Sep. 2020, doi: 10.1002/adhm.202000779.

[42] S. Valadkhan, K. Morris, and A. Khajepour, "Review and Comparison of Hysteresis Models for Magnetostrictive Materials," *Journal of Intelligent Material Systems and Structures*, vol. 20, no. 2, pp. 131–142, Jan. 2009, doi: 10.1177/1045389X08093563.

[43] C. Qinghua, C. Dingfang, L. Chuan, L. Quanguo, and Z. Yulu, "A Review of the Magnetomechanical Modeling of Magnetostriction Materials," in *Pervasive Computing and the Networked World*, vol. 8351, Q. Zu, M. Vargas-Vera, and B. Hu, Eds., in Lecture Notes in Computer Science, vol. 8351. , Cham: Springer International Publishing, 2014, pp. 1–7. doi: 10.1007/978-3-319-09265-2_1.

[44] D. Hao *et al.*, "Solar energy harvesting technologies for PV self-powered applications: A comprehensive review," *Renewable Energy*, vol. 188, pp. 678–697, Apr. 2022, doi: 10.1016/j.renene.2022.02.066.

[45] F. F. Ahmad, C. Ghenai, and M. Bettayeb, "Maximum power point tracking and photovoltaic energy harvesting for Internet of Things: A comprehensive review," *Sustainable Energy Technologies and Assessments*, vol. 47, p. 101430, Oct. 2021, doi: 10.1016/j.seta.2021.101430.

[46] R. Kishore and S. Priya, "A Review on Low-Grade Thermal Energy Harvesting: Materials, Methods and Devices," *Materials*, vol. 11, no. 8, p. 1433, Aug. 2018, doi: 10.3390/ma11081433.

[47] M. Safaei, H. A. Sodano, and S. R. Anton, "A review of energy harvesting using piezoelectric materials: state-of-the-art a decade later (2008–2018)," *Smart Mater. Struct.*, vol. 28, no. 11, p. 113001, Nov. 2019, doi: 10.1088/1361-665X/ab36e4.

[48] K. B. Hathaway and A. E. Clark, "Magnetostrictive Materials," *MRS Bull.*, vol. 18, no. 4, pp. 34–41, Apr. 1993, doi: 10.1557/S0883769400037337.

[49] J. Siang, M. H. Lim, and M. Salman Leong, "Review of vibration-based energy harvesting technology: Mechanism and architectural approach," *Int J Energy Res*, vol. 42, no. 5, pp. 1866–1893, Apr. 2018, doi: 10.1002/er.3986.

[50] G. Engdahl, *Handbook of giant magnetostrictive materials*. in Electromagnetism. San Diego, CA: Academic Press, 2000.

[51] K. V. Selvan and M. S. Mohamed Ali, "Micro-scale energy harvesting devices: Review of methodological performances in the last decade," *Renewable and Sustainable Energy Reviews*, vol. 54, pp. 1035–1047, Feb. 2016, doi: 10.1016/j.rser.2015.10.046.

[52] J. Krikke, "Sunrise for energy harvesting products," *IEEE Pervasive Comput.*, vol. 4, no. 1, pp. 4–5, Jan. 2005, doi: 10.1109/MPRV.2005.23.

[53] "Home - Hi-Z Technology - San Diego." Accessed: Jun. 26, 2023. [Online]. Available: https://hi-z.com/

[54] T. Le, K. Mayaram, and T. Fiez, "Efficient Far-Field Radio Frequency Energy Harvesting for Passively Powered Sensor Networks," *IEEE J. Solid-State Circuits*, vol. 43, no. 5, pp. 1287–1302, May 2008, doi: 10.1109/JSSC.2008.920318.

[55] M. Hata, “Empirical formula for propagation loss in land mobile radio services,” *IEEE Trans. Veh. Technol.*, vol. 29, no. 3, pp. 317–325, Aug. 1980, doi: 10.1109/T-VT.1980.23859.

[56] S. Basagni, M. Y. Naderi, C. Petrioli, and D. Spenza, “Wireless Sensor Networks with Energy Harvesting,” in *Mobile Ad Hoc Networking*, 1st ed., S. Basagni, M. Conti, S. Giordano, and I. Stojmenovic, Eds., Wiley, 2013, pp. 701–736. doi: 10.1002/9781118511305.ch20.

[57] “Retevis RT22 RT622 RT15 Talkie Walkie Batterie Lithium 1000mAh 3,7V Talkie Walkie Batterie (1 Pack) : Amazon.fr: High-Tech.” Accessed: Oct. 13, 2023. [Online]. Available: https://www.amazon.fr/Retevis-Batterie-Lithium-1000mAh-Compatible/dp/B07VYG7FVJ/ref=sr_1_7?crid=1PB1AXM1YKK0O&keywords=batterie+lithium+3.7v+1000mah&qid=1697193359&sprefix=batterie+lithium+3.7v+1000%2Caps%2C510&sr=8-7

[58] T. Huguet, “Vers une meilleure exploitation des dispositifs de récupération d’énergie vibratoire bistables : Analyse et utilisation de comportements originaux pour améliorer la bande passante,” phdthesis, Université de Lyon, 2018. Accessed: Aug. 28, 2023. [Online]. Available: https://theses.hal.science/tel-01957377

[59] J. Kymissis, C. Kendall, J. Paradiso, and N. Gershenfeld, “Parasitic power harvesting in shoes,” in *Digest of Papers. Second International Symposium on Wearable Computers (Cat. No.98EX215)*, Pittsburgh, PA, USA: IEEE Comput. Soc, 1998, pp. 132–139. doi: 10.1109/ISWC.1998.729539.

[60] J. Granstrom, J. Feenstra, H. A. Sodano, and K. Farinholt, “Energy harvesting from a backpack instrumented with piezoelectric shoulder straps,” *Smart Mater. Struct.*, vol. 16, no. 5, pp. 1810–1820, Oct. 2007, doi: 10.1088/0964-1726/16/5/036.

[61] S. Roundy and P. K. Wright, “A piezoelectric vibration based generator for wireless electronics,” *Smart Mater. Struct.*, vol. 13, no. 5, pp. 1131–1142, Oct. 2004, doi: 10.1088/0964-1726/13/5/018.

[62] A. Badel and E. Lefeuvre, “Wideband Piezoelectric Energy Harvester Tuned Through its Electronic Interface Circuit,” *J. Phys.: Conf. Ser.*, vol. 557, p. 012115, Nov. 2014, doi: 10.1088/1742-6596/557/1/012115.

[63] S. Dey, D. Roy, S. Patra, and T. Santra, “Performance of a modified magnetostrictive energy harvester in mechanical vibration,” *Heliyon*, vol. 5, no. 1, p. 01135, Jan. 2019, doi: 10.1016/j.heliyon.2019.e01135.

[64] X. Zhao and D. G. Lord, “Application of the Villari effect to electric power harvesting,” *Journal of Applied Physics*, vol. 99, no. 8, p. 08M703, Apr. 2006, doi: 10.1063/1.2165133.

[65] M. J. Dapino, R. C. Smith, F. T. Calkins, and A. B. Flatau, “A Coupled Magnetomechanical Model for Magnetostrictive Transducers and its Application to Villari-Effect Sensors,” *Journal of Intelligent Material Systems and Structures*, vol. 13, no. 11, pp. 737–747, Nov. 2002, doi: 10.1177/1045389X02013011005.

[66] A. Bieńkowski and J. Kulikowski, “The magneto-elastic Villari effect in ferrites,” *Journal of Magnetism and Magnetic Materials*, vol. 19, no. 1–3, pp. 120–122, Apr. 1980, doi: 10.1016/0304-8853(80)90570-3.

[67] Y. Kai, Y. Tsuchida, T. Todaka, and M. Enokizono, “Influence of Biaxial Stress on Vector Magnetic Properties and 2-D Magnetostriction of a Nonoriented Electrical Steel Sheet Under Alternating Magnetic Flux Conditions,” *IEEE Trans. Magn.*, vol. 50, no. 4, pp. 1–4, Apr. 2014, doi: 10.1109/TMAG.2013.2287875.

[68] P. I. Anderson, A. J. Moses, and H. J. Stanbury, “Assessment of the Stress Sensitivity of Magnetostriction in Grain-Oriented Silicon Steel,” *IEEE Trans. Magn.*, vol. 43, no. 8, pp. 3467–3476, Aug. 2007, doi: 10.1109/TMAG.2007.893534.

[69] M. Rekik, O. Hubert, and L. Daniel, “Influence of a multiaxial stress on the reversible and irreversible magnetic behaviour of a 3%Si-Fe alloy,” *JAE*, vol. 44, no. 3–4, pp. 301–315, Mar. 2014, doi: 10.3233/JAE-141793.

[70] O. Perevertov, “Influence of the applied elastic tensile and compressive stress on the hysteresis curves of Fe-3%Si non-oriented steel,” *Journal of Magnetism and Magnetic Materials*, vol. 428, pp. 223–228, Apr. 2017, doi: 10.1016/j.jmmm.2016.12.040.

[71] O. Perevertov, J. Thielsch, and R. Schäfer, “Effect of applied tensile stress on the hysteresis curve and magnetic domain structure of grain-oriented transverse Fe-3%Si steel,” *Journal of Magnetism and Magnetic Materials*, vol. 385, pp. 358–367, Jul. 2015, doi: 10.1016/j.jmmm.2015.03.040.

[72] A. Hubert and R. Schäfer, *Magnetic Domains*. Berlin, Heidelberg: Springer Berlin Heidelberg, 1998. doi: 10.1007/978-3-540-85054-0.

[73] B. D. Cullity and C. D. Graham, *Introduction to Magnetic Materials*. Hoboken, NJ, USA: John Wiley & Sons, Inc., 2008. doi: 10.1002/9780470386323.

[74] D. C. Jiles, “Theory of the magnetomechanical effect,” *J. Phys. D: Appl. Phys.*, vol. 28, no. 8, pp. 1537–1546, Aug. 1995, doi: 10.1088/0022-3727/28/8/001.

[75] X. Dai, Y. Wen, P. Li, J. Yang, and M. Li, “Energy harvesting from mechanical vibrations using multiple magnetostrictive/piezoelectric composite transducers,” *Sensors and Actuators A: Physical*, vol. 166, no. 1, pp. 94–101, Mar. 2011, doi: 10.1016/j.sna.2010.12.025.

[76] H. Liu, C. Cao, X. Sun, L. Zhao, and C. Cong, “Magnetostrictive iron–gallium alloy harvester with efficient two-mode AC–DC converting technology for effective vibration energy harvesting,” *AIP Advances*, vol. 10, no. 11, p. 115304, Nov. 2020, doi: 10.1063/5.0025550.

[77] A. Mohanty, S. Parida, R. K. Behera, and T. Roy, “Vibration energy harvesting: A review,” *J. Adv. Dielect.*, vol. 09, no. 04, p. 1930001, Aug. 2019, doi: 10.1142/S2010135X19300019.

[78] C. S. Clemente, A. Mahgoub, D. Davino, and C. Visone, “Multiphysics circuit of a magnetostrictive energy harvesting device,” *Journal of Intelligent Material Systems and Structures*, vol. 28, no. 17, pp. 2317–2330, Oct. 2017, doi: 10.1177/1045389X16685444.

[79] M. Zucca, O. Bottauscio, C. Beatrice, A. Hadadian, F. Fiorillo, and L. Martino, “A Study on Energy Harvesting by Amorphous Strips,” *IEEE Trans. Magn.*, vol. 50, no. 11, pp. 1–4, Nov. 2014, doi: 10.1109/TMAG.2014.2327169.

[80] Z. Deng, J. J. Scheidler, V. M. Asnani, and M. J. Dapino, “Quasi-static major and minor strain-stress loops in textured polycrystalline Fe81.6Ga18.4 Galfenol,” *Journal of Applied Physics*, vol. 120, no. 24, p. 243901, Dec. 2016, doi: 10.1063/1.4972479.

[81] “Magnetic fields of currents.” Accessed: Aug. 23, 2023. [Online]. Available: http://hyperphysics.phy-astr.gsu.edu/hbase/magnetic/magcur.html

[82] N. A. Spaldin, *Magnetic Materials: Fundamentals and Applications*, 2nd ed. Cambridge University Press, 2010. doi: 10.1017/CBO9780511781599.

[83] P. Brissonneau, *Magnétisme et matériaux magnétiques pour l'électrotechnique*. Paris: Hermès, 1997.
[84] "science des materiaux de l`electrotechnique," studylibfr.com. Accessed: Sep. 16, 2023. [Online]. Available: https://studylibfr.com/doc/2641217/science-des-materiaux-de-l-electrotechnique
[85] N. Sommer, "Critical domain wall behavior in chiral magnetic nanowires induced by spin polarized currents," Master, Johannes Gutenberg-Universität Mainz, 2019.
[86] Y. A. Tene Deffo, "NON-DESTRUCTIVE TESTING AND CONTROL FOR LOCAL MAGNETIC CHARACTERIZATION OF MATERIAL STEEL BY THE NEEDLE PROBE TECHNIQUE." University of Buea.
[87] "Hysteresis in magnetic materials." Accessed: Aug. 24, 2023. [Online]. Available: http://hyperphysics.phy-astr.gsu.edu/hbase/Solids/hyst.html
[88] G. Bhaawan, "Advanced Electromagnetic Nondestructive Testing on Creep Degraded High Chromium Ferritic Steels: Characterization, Modelling and Physical Interpretation." TOHOKU UNIVERSITY, Jul. 30, 2019.
[89] A. Mousavi, A. Krings, G. Engdahl, and A. Bissal, "Measurement and Modeling of Anhysteretic Curves," presented at the 19th COMPUMAG Conference on the Computation of Electromagnetic Fields, Budapest: Royal Institute of Technology (KTH), Jun. 2013.
[90] D. John, "Environmental Magnetic Susceptibility Using the Bartington MS2 System." Bartington Instruments, 1999. [Online]. Available: https://gmw.com/wp-content/uploads/2019/03/JDearing-Handbook-OM0409.pdf
[91] "Comparison of Non-Destructive Testing Methods," The Modal Shop. Accessed: Sep. 16, 2023. [Online]. Available: https://www.modalshop.com/ndt/learn/compare-testing-methods
[92] W. H. Hayt and J. A. Buck, *Engineering electromagnetics*, 8th ed. New York, NY: McGraw-Hill, 2012.
[93] G. Marin-Garcia, G. Vazquez-Guzman, J. M. Sosa, A. R. Lopez, P. R. Martinez-Rodriguez, and D. Langarica, "Battery Types and Electrical Models: A Review," in *2020 IEEE International Autumn Meeting on Power, Electronics and Computing (ROPEC)*, Ixtapa, Mexico: IEEE, Nov. 2020, pp. 1–6. doi: 10.1109/ROPEC50909.2020.9258711.
[94] A. Skarlatos, G. Pichenot, D. Lesselier, M. Lambert, and B. Duchêne, "Electromagnetic Modeling of a Damaged Ferromagnetic Metal Tube by a Volume Integral Equation Formulation," *Magnetics, IEEE Transactions on*, vol. 44, pp. 623–632, Jun. 2008, doi: 10.1109/TMAG.2008.918206.
[95] H. S. NGUEDJANG KOUAKEUO, "Internal characterization of magnetic cores: A route for dimensioning and real time condition monitoring." UNIVERSITE DE LYON, Nov. 14, 2022.
[96] T. Mura, *Micromechanics of defects in solids*, vol. 3. in Mechanics of Elastic and Inelastic Solids, vol. 3. Dordrecht: Springer Netherlands, 1987. doi: 10.1007/978-94-009-3489-4.
[97] P. J. Withers and H. K. D. H. Bhadeshia, "Residual stress. Part 2 – Nature and origins," *Materials Science and Technology*, vol. 17, no. 4, pp. 366–375, Apr. 2001, doi: 10.1179/026708301101510087.

[98] I. C. Noyan and J. B. Cohen, *Residual stress: measurement by diffraction and interpretation*. in Materials research and engineering. New York Berlin Heidelberg London Paris Tokyo: Springer, 1987.

[99] P. J. Bouchard, "Identification of Residual Stress Length Scales in Welds for Fracture Assessment," in *Residual Stress and Its Effects on Fatigue and Fracture*, A. G. Youtsos, Ed., Dordrecht: Springer Netherlands, 2006, pp. 163–176. doi: 10.1007/1-4020-5329-0_14.

[100] J. Guo, H. Fu, B. Pan, and R. Kang, "Recent progress of residual stress measurement methods: A review," *Chinese Journal of Aeronautics*, vol. 34, no. 2, pp. 54–78, Feb. 2021, doi: 10.1016/j.cja.2019.10.010.

[101] "Standard Test Method for Determining Residual Stresses by the Hole-Drilling Strain-Gage Method." Accessed: Jul. 24, 2023. [Online]. Available: https://www.astm.org/e0837-20.html

[102] P. Pagliaro, M. B. Prime, H. Swenson, and B. Zuccarello, "Measuring Multiple Residual-Stress Components using the Contour Method and Multiple Cuts," *Exp Mech*, vol. 50, no. 2, pp. 187–194, Feb. 2010, doi: 10.1007/s11340-009-9280-3.

[103] M. B. Prime, "Residual Stress Measurement by Successive Extension of a Slot: The Crack Compliance Method," *Applied Mechanics Reviews*, vol. 52, no. 2, pp. 75–96, Feb. 1999, doi: 10.1115/1.3098926.

[104] C. Hellier, *Handbook of nondestructive evaluation*, 2nd ed. New York: McGraw-Hill, 2013.

[105] P. Höller, V. Hauk, G. Dobmann, C. O. Ruud, and R. E. Green, Eds., *Nondestructive Characterization of Materials: Proceedings of the 3rd International Symposium Saarbrücken, FRG, October 3–6, 1988*. Berlin, Heidelberg: Springer Berlin Heidelberg, 1989. doi: 10.1007/978-3-642-84003-6.

[106] W. Du, Y. Zhao, R. Roy, S. Addepalli, and L. Tinsley, "A review of miniaturised Non-Destructive Testing technologies for in-situ inspections," *Procedia Manufacturing*, vol. 16, pp. 16–23, 2018, doi: 10.1016/j.promfg.2018.10.152.

[107] J. Capó Sánchez, M. F. De Campos, and L. R. Padovese, "Comparison Between Different Experimental Set-Ups for Measuring the Magnetic Barkhausen Noise in a Deformed 1050 Steel," *J Nondestruct Eval*, vol. 36, no. 4, p. 66, Dec. 2017, doi: 10.1007/s10921-017-0445-1.

[108] S. Santa-aho, A. Laitinen, A. Sorsa, and M. Vippola, "Barkhausen Noise Probes and Modelling: A Review," *J Nondestruct Eval*, vol. 38, no. 4, p. 94, Dec. 2019, doi: 10.1007/s10921-019-0636-z.

[109] F. Yu, M. P. Blodgett, and P. B. Nagy, "Eddy Current Assessment of Near-Surface Residual Stress in Shot-Peened Inhomogeneous Nickel-Base Superalloys," *J Nondestruct Eval*, vol. 25, no. 1, pp. 16–27, Mar. 2006, doi: 10.1007/s10921-006-0003-8.

[110] F. Su, "Methodology for the Stress Measurement of Ferromagnetic Materials by Using Magneto Acoustic Emission," *Exp Mech*, vol. 54, no. 8, pp. 1431–1439, Oct. 2014, doi: 10.1007/s11340-014-9920-0.

[111] M. Shibata and K. Ono, "Magnetomechanical acoustic emission — a new method for non-destructive stress measurement," *NDT International*, vol. 14, no. 5, pp. 227–234, Oct. 1981, doi: 10.1016/0308-9126(81)90075-4.

[112] J. A. Szpunar and D. L. Atherton, "Magnetostriction and the Effect of Stress and Texture," in *Nondestructive Characterization of Materials II*, J. F. Bussière, J.-P.

Monchalin, C. O. Ruud, and R. E. Green, Eds., Boston, MA: Springer US, 1987, pp. 577–584. doi: 10.1007/978-1-4684-5338-6_59.

[113] J. Gauthier, T. W. Krause, and D. L. Atherton, “Measurement of residual stress in steel using the magnetic Barkhausen noise technique,” *NDT & E International*, vol. 31, no. 1, pp. 23–31, Feb. 1998, doi: 10.1016/S0963-8695(97)00023-6.

[114] P. Fagan, B. Ducharne, L. Daniel, A. Skarlatos, M. Domenjoud, and C. Reboud, “Effect of stress on the magnetic Barkhausen noise energy cycles: A route for stress evaluation in ferromagnetic materials,” *Materials Science and Engineering: B*, vol. 278, p. 115650, Apr. 2022, doi: 10.1016/j.mseb.2022.115650.

[115] D. M. Stewart, K. J. Stevens, and A. B. Kaiser, “Magnetic Barkhausen noise analysis of stress in steel,” *Current Applied Physics*, vol. 4, no. 2–4, pp. 308–311, Apr. 2004, doi: 10.1016/j.cap.2003.11.035.

[116] J. W. Wilson, G. Y. Tian, V. Moorthy, and B. A. Shaw, “Magneto-Acoustic Emission and Magnetic Barkhausen Emission for Case Depth Measurement in En36 Gear Steel,” *IEEE Trans. Magn.*, vol. 45, no. 1, pp. 177–183, Jan. 2009, doi: 10.1109/TMAG.2008.2007537.

[117] D. Gerd, A. Iris, and K. Rolf, “Industrial Applications of 3MA – Micromagnetic Multiparameter Microstructure and Stress Analysis,” in *Volume 31: Electromagnetic Nondestructive Evaluation (XI)*, in Studies in Applied Electromagnetics and Mechanics. Timiscora: IOP, Jan. 2008, pp. 18–25.

[118] O. Stupakov, J. Pal’a, T. Takagi, and T. Uchimoto, “Governing conditions of repeatable Barkhausen noise response,” *Journal of Magnetism and Magnetic Materials*, vol. 321, pp. 2956–2962, 2009.

[119] O. Stupakov, J. Pal’a, T. Takagi, and T. Uchimoto, “Governing conditions of repeatable Barkhausen noise response,” *Journal of Magnetism and Magnetic Materials*, vol. 321, no. 18, pp. 2956–2962, Sep. 2009, doi: 10.1016/j.jmmm.2009.04.065.

[120] Fraunhofer IZFP, “3MA for monitoring and controlling sheet metal forming,” Fraunhofer Institute for Nondestructive Testing IZFP Sensor and Data Systems for Safety, Sustainability and Efficiency. Accessed: Aug. 25, 2023. [Online]. Available: https://www.izfp.fraunhofer.de/en/produkte-dienstleistungen/Produkte/steuerung-und-ueberwachung-der-blechumformung-mit-3ma.html

[121] S. H. Nguedjang Kouakeuo *et al.*, “Non-invasive local magnetic hysteresis characterization of a ferromagnetic laminated core,” *Journal of Magnetism and Magnetic Materials*, vol. 527, p. 167783, Jun. 2021, doi: 10.1016/j.jmmm.2021.167783.

[122] S. H. Nguedjang Kouakeuo *et al.*, “Embedded printed magnetic needle probes sensor for the real-time control of the local induction state through a laminated magnetic core,” *Journal of Magnetism and Magnetic Materials*, vol. 505, p. 166767, Jul. 2020, doi: 10.1016/j.jmmm.2020.166767.

[123] B. Ducharne, Y. A. Tene Deffo, P. Tsafack, and S. H. Nguedjang Kouakeuo, “Directional magnetic Barkhausen noise measurement using the magnetic needle probe method,” *Journal of Magnetism and Magnetic Materials*, vol. 519, p. 167453, Feb. 2021, doi: 10.1016/j.jmmm.2020.167453.

[124] F. D. Fischer, F. G. Rammerstorfer, and N. Friedl, “Residual Stress-Induced Center Wave Buckling of Rolled Strip Metal,” *Journal of Applied Mechanics*, vol. 70, no. 1, pp. 84–90, Jan. 2003, doi: 10.1115/1.1532322.

[125] K. Li *et al.*, “A fast and non-destructive method to evaluate yield strength of cold-rolled steel via incremental permeability,” *Journal of Magnetism and Magnetic Materials*, vol. 498, p. 166087, Mar. 2020, doi: 10.1016/j.jmmm.2019.166087.

[126] Y. Ke *et al.*, “Tuning magnetostriction of Fe–Ga alloys via stress engineering,” *Journal of Alloys and Compounds*, vol. 822, p. 153687, May 2020, doi: 10.1016/j.jallcom.2020.153687.

[127] H.-E. Chen *et al.*, “Numerical simulation of magnetic incremental permeability for ferromagnetic material,” *JAE*, vol. 45, no. 1–4, pp. 379–386, May 2014, doi: 10.3233/JAE-141854.

[128] J. Zeng, Y. Xu, S. Liang, and Z. Long, “An Improved Transmissive Method of Stress Nondestructive Measurement Based on Inverse Magnetostrictive Theory for the Ferromagnetic Material,” *Magnetochemistry*, vol. 7, no. 7, p. 106, Jul. 2021, doi: 10.3390/magnetochemistry7070106.

[129] M. Aghadavoudi Jolfaei, L. Zhou, and C. Davis, “Consideration of Magnetic Measurements for Characterisation of Ferrite–Martensite Commercial Dual-Phase (DP) Steel and Basis for Optimisation of the Operating Magnetic Field for Open Loop Deployable Sensors,” *Metals*, vol. 11, no. 3, p. 490, Mar. 2021, doi: 10.3390/met11030490.

[130] G. Couderchon, “Alliages fer-nickel et fer-cobalt - Propriétés magnétiques,” *Conversion de l’énergie électrique*, Jun. 1994, doi: 10.51257/a-v1-d2130.

[131] P. Fagan, B. Ducharne, L. Daniel, and A. Skarlatos, “Multiscale modelling of the magnetic Barkhausen noise energy cycles,” *Journal of Magnetism and Magnetic Materials*, vol. 517, p. 167395, Jan. 2021, doi: 10.1016/j.jmmm.2020.167395.

[132] B. Toutsop, B. Ducharne, M. Lallart, L. Morel, and P. Tsafack, “Characterization of Tensile Stress-Dependent Directional Magnetic Incremental Permeability in Iron-Cobalt Magnetic Sheet: Towards Internal Stress Estimation through Non-Destructive Testing,” *Sensors*, vol. 22, no. 16, p. 6296, Aug. 2022, doi: 10.3390/s22166296.

[133] R. Mahmoud, “Mesure et modélisation du comportement magnéto-mécanique dissipatif des matériaux ferromagnétiques à haute limite élastique sous chargement multiaxial: application aux génératrices à grandes vitesses pour l’aéronautique,” ECOLE NORMALE SUPERIEURE DE CACHAN, 2014.

[134] IEC 60404-3, “INTERNATIONAL STANDARD,” *INTERNATIONAL ELECTROTECHNICAL COMMISSION*.

[135] “Autograph AGS-X Series.” Accessed: Jul. 26, 2023. [Online]. Available: https://www.shimadzu.com/an/products/materials-testing/uni-ttm/autograph-ags-x-series/index.html

[136] C. Miguel, A. P. Zhukov, and J. Gonz﷽lez, “Stress and/or Field Induced Magnetic Anisotropy in the Amorphous Fe73.5Cu1Nb3Si15.5B7 Alloy: Influence on the Coercivity, Saturation Magnetostriction and Magneto-Impedance Response,” *phys. stat. sol. (a)*, vol. 194, no. 1, pp. 291–303, Nov. 2002, doi: 10.1002/1521-396X(200211)194:1<291::AID-PSSA291>3.0.CO;2-L.

[137] U. Aydin *et al.*, “Magneto-mechanical modeling of electrical steel sheets,” *Journal of Magnetism and Magnetic Materials*, vol. 439, pp. 82–90, Oct. 2017, doi: 10.1016/j.jmmm.2017.05.008.

[138] R. Hu, A.-K. Soh, G.-P. Zheng, and Y. Ni, “Micromagnetic modeling studies on the effects of stress on magnetization reversal and dynamic hysteresis,” *Journal of Magnetism and Magnetic Materials*, vol. 301, no. 2, pp. 458–468, Jun. 2006, doi: 10.1016/j.jmmm.2005.07.023.

[139] Y. Gabi, K. Jacob, B. Wolter, C. Conrad, B. Strass, and J. Grimm, “Analysis of incremental and differential permeability in NDT via 3D-simulation and experiment,” *Journal of Magnetism and Magnetic Materials*, vol. 505, p. 166695, Jul. 2020, doi: 10.1016/j.jmmm.2020.166695.

[140] K. H. J. Buschow, Ed., *Encyclopedia of materials: science and technology*. Amsterdam ; New York: Elsevier, 2001.

[141] T. Matsumoto, T. Uchimoto, T. Takagi, and G. Vertesy, “Evaluation of chill structure in ductile cast iron by incremental permeability method,” *JAE*, vol. 52, no. 3–4, pp. 1599–1605, Dec. 2016, doi: 10.3233/JAE-162106.

[142] T. Matsumoto *et al.*, “Investigation of electromagnetic nondestructive evaluation of residual strain in low carbon steels using the eddy current magnetic signature (EC-MS) method,” *Journal of Magnetism and Magnetic Materials*, vol. 479, pp. 212–221, Jun. 2019, doi: 10.1016/j.jmmm.2019.01.103.

[143] B. Gupta, T. Uchimoto, B. Ducharne, G. Sebald, T. Miyazaki, and T. Takagi, “Magnetic incremental permeability non-destructive evaluation of 12 Cr-Mo-W-V steel creep test samples with varied ageing levels and thermal treatments,” *NDT & E International*, vol. 104, pp. 42–50, Jun. 2019, doi: 10.1016/j.ndteint.2019.03.006.

[144] B. Wolter, Y. Gabi, and C. Conrad, “Nondestructive Testing with 3MA—An Overview of Principles and Applications,” *Applied Sciences*, vol. 9, no. 6, p. 1068, Mar. 2019, doi: 10.3390/app9061068.

[145] B. Gupta, B. Ducharne, T. Uchimoto, G. Sebald, T. Miyazaki, and T. Takagi, “Comparison of electromagnetic inspection methods for creep-degraded high chromium ferritic steels,” *NDT & E International*, vol. 118, p. 102399, Mar. 2021, doi: 10.1016/j.ndteint.2020.102399.

[146] U. Ahmed, U. Aydin, L. Daniel, and P. Rasilo, “3-D Magneto-Mechanical Finite Element Analysis of Galfenol-Based Energy Harvester Using an Equivalent Stress Model,” *IEEE Trans. Magn.*, vol. 57, no. 2, pp. 1–5, Feb. 2021, doi: 10.1109/TMAG.2020.3011875.

[147] D. Davino, A. Giustiniani, and C. Visone, “Analysis of a magnetostrictive power harvesting device with hysteretic characteristics,” *Journal of Applied Physics*, vol. 105, no. 7, p. 07A939, Apr. 2009, doi: 10.1063/1.3077208.

[148] Y. Mizukawa, U. Ahmed, M. Zucca, D. Blažević, and P. Rasilo, “Small-signal modeling and optimal operating condition of magnetostrictive energy harvester,” *Journal of Magnetism and Magnetic Materials*, vol. 547, p. 168819, Apr. 2022, doi: 10.1016/j.jmmm.2021.168819.

[149] C. Xin, C. Baixin, L. Han, and A. G. M, “An Accurate Linearization of Electromagnetic Force of Heteropolar Magnetic Bearings With Redundant Structures,” *Journal of Engineering for Gas Turbines and Power*, vol. 142, no. 9, p. 091002, Sep. 2020, doi: 10.1115/1.4046703.

[150] S. Palumbo, P. Rasilo, and M. Zucca, “Experimental investigation on a Fe-Ga close yoke vibrational harvester by matching magnetic and mechanical biases,” *Journal of Magnetism and Magnetic Materials*, vol. 469, pp. 354–363, Jan. 2019, doi: 10.1016/j.jmmm.2018.08.085.

[151] M. E. Staley and A. B. Flatau, “Characterization of energy harvesting potential of Terfenol-D and Galfenol,” presented at the Smart Structures and Materials, A. B. Flatau, Ed., San Diego, CA, May 2005, p. 630. doi: 10.1117/12.604871.

[152] X. Dai, Y. Wen, P. Li, J. Yang, and G. Zhang, “Modeling, characterization and fabrication of vibration energy harvester using Terfenol-D/PZT/Terfenol-D composite transducer,” *Sensors and Actuators A: Physical*, vol. 156, no. 2, pp. 350–358, Dec. 2009, doi: 10.1016/j.sna.2009.10.002.

[153] Y. Zhu and J. W. Zu, “A Magnetoelectric Generator for Energy Harvesting From the Vibration of Magnetic Levitation,” *IEEE Trans. Magn.*, vol. 48, no. 11, pp. 3344–3347, Nov. 2012, doi: 10.1109/TMAG.2012.2199289.

[154] Y. Zeng *et al.*, “Structural optimization design on composite cantilever-beam-type actuator withTbDyFe alloy:,” presented at the 2015 International Conference on Automation, Mechanical Control and Computational Engineering, Shunhe, China, 2015. doi: 10.2991/amcce-15.2015.91.

[155] Liu, Cong, Zhao, and Ma, “Comprehensive Analysis of the Energy Harvesting Performance of a Fe-Ga Based Cantilever Harvester in Free Excitation and Base Excitation Mode,” *Sensors*, vol. 19, no. 15, p. 3412, Aug. 2019, doi: 10.3390/s19153412.

[156] T. Lafont *et al.*, “Magnetostrictive–piezoelectric composite structures for energy harvesting,” *J. Micromech. Microeng.*, vol. 22, no. 9, p. 094009, Sep. 2012, doi: 10.1088/0960-1317/22/9/094009.

[157] A. Clark, M. Wun-Fogle, J. B. Restorff, and T. A. Lograsso, “Magnetostrictive Properties of Galfenol Alloys Under Compressive Stress,” *Mater. Trans.*, vol. 43, no. 5, pp. 881–886, 2002, doi: 10.2320/matertrans.43.881.

[158] Z. Deng and M. J. Dapino, “Multiphysics modeling and design of Galfenol-based unimorph harvesters,” presented at the SPIE Smart Structures and Materials + Nondestructive Evaluation and Health Monitoring, K. M. Farinholt and S. F. Griffin, Eds., San Diego, California, United States, Apr. 2015, p. 94330B. doi: 10.1117/12.2085550.

[159] L. Daniel and M. Domenjoud, “Anhysteretic Magneto-Elastic Behaviour of Terfenol-D: Experiments, Multiscale Modelling and Analytical Formulas,” *Materials*, vol. 14, no. 18, p. 5165, Sep. 2021, doi: 10.3390/ma14185165.

[160] M. Zucca, A. Hadadian, and O. Bottauscio, “Quantities Affecting the Behavior of Vibrational Magnetostrictive Transducers,” *IEEE Trans. Magn.*, vol. 51, no. 1, pp. 1–4, Jan. 2015, doi: 10.1109/TMAG.2014.2359248.

[161] F. Fausto, in *Magnetic materials for electrical applications: a review*, Istituto Nazionale Di Ricerca Metrologica, 2010, pp. 1–123.

[162] L. Daniel, O. Hubert, and M. Rekik, “A Simplified 3-D Constitutive Law for Magnetomechanical Behavior,” *IEEE Trans. Magn.*, vol. 51, no. 3, pp. 1–4, Mar. 2015, doi: 10.1109/TMAG.2014.2361643.

[163] “Quasi-static Characterization and Modeling of the Bending Behavior of Single Crystal Galfenol for Magnetostrictive Sensors and Actuators.” Accessed: Sep. 08, 2023. [Online]. Available: https://apps.dtic.mil/sti/citations/AD1005542

[164] D. C. Jiles and D. L. Atherton, “Theory of ferromagnetic hysteresis,” *Journal of Magnetism and Magnetic Materials*, vol. 61, no. 1–2, pp. 48–60, Sep. 1986, doi: 10.1016/0304-8853(86)90066-1.

[165] Y. Bernard, E. Mendes, and F. Bouillault, “Dynamic hysteresis modeling based on Preisach model,” *IEEE Trans. Magn.*, vol. 38, no. 2, pp. 885–888, Mar. 2002, doi: 10.1109/20.996228.

[166] L. Daniel and O. Hubert, “An equivalent stress for the influence of multiaxial stress on the magnetic behavior,” *Journal of Applied Physics*, vol. 105, no. 7, p. 07A313, Apr. 2009, doi: 10.1063/1.3068646.

[167] O. Hubert and L. Daniel, “Energetical and multiscale approaches for the definition of an equivalent stress for magneto-elastic couplings,” *Journal of Magnetism and Magnetic Materials*, vol. 323, no. 13, pp. 1766–1781, Jul. 2011, doi: 10.1016/j.jmmm.2011.01.041.

[168] P. Shi, “One-dimensional magneto-mechanical model for anhysteretic magnetization and magnetostriction in ferromagnetic materials,” *Journal of Magnetism and Magnetic Materials*, vol. 537, p. 168212, Nov. 2021, doi: 10.1016/j.jmmm.2021.168212.

[169] A. Adly, D. Davino, A. Giustiniani, and C. Visone, “Experimental tests of a magnetostrictive energy harvesting device toward its modeling,” *Journal of Applied Physics*, vol. 107, no. 9, p. 09A935, May 2010, doi: 10.1063/1.3357403.

[170] Y. Liu, B. Ducharne, G. Sebald, K. Makihara, and M. Lallart, “Investigation of Energy Harvesting Capabilities of Metglas 2605SA1,” *Applied Sciences*, vol. 13, no. 6, p. 3477, Mar. 2023, doi: 10.3390/app13063477.

[171] A. Vakhtang, “Thermodynamic Model of Ideal Magnetostriction,” *Physica Scripta*, Moscow, Russia, pp. 514–521, 1996.

[172] G. Sebald, M. Nakano, M. Lallart, T. Tian, G. Diguet, and J.-Y. Cavaille, “Energy conversion in magneto-rheological elastomers,” *Science and Technology of Advanced Materials*, vol. 18, no. 1, pp. 766–778, Dec. 2017, doi: 10.1080/14686996.2017.1377590.

[173] “Coefficient of Determination: How to Calculate It and Interpret the Result,” Investopedia. Accessed: Oct. 15, 2023. [Online]. Available: https://www.investopedia.com/terms/c/coefficient-of-determination.asp

[174] “Coefficient of Determination,” in *The SAGE Encyclopedia of Social Science Research Methods*, 2455 Teller Road, Thousand Oaks California 91320 United States of America: Sage Publications, Inc., 2004. doi: 10.4135/9781412950589.n132.

[175] E. Hristoforou, A. Ktena, P. Vourna, and K. Argiris, “Dependence of magnetic permeability on residual stresses in alloyed steels,” *AIP Advances*, vol. 8, no. 4, p. 047201, Apr. 2018, doi: 10.1063/1.4994202.

[176] M. Lallart, P.-J. Cottinet, D. Guyomar, and L. Lebrun, “Electrostrictive polymers for mechanical energy harvesting,” *J. Polym. Sci. B Polym. Phys.*, vol. 50, no. 8, pp. 523–535, Apr. 2012, doi: 10.1002/polb.23045.

[177] G. Sebald, S. Pruvost, and D. Guyomar, “Energy harvesting based on Ericsson pyroelectric cycles in a relaxor ferroelectric ceramic,” *Smart Mater. Struct.*, vol. 17, no. 1, p. 015012, Feb. 2008, doi: 10.1088/0964-1726/17/01/015012.

[178] B. Zhang, B. Ducharne, B. Gupta, G. Sebald, D. Guyomar, and J. Gao, “Experimental sea wave energy extractor based on piezoelectric Ericsson cycles,”

Journal of Intelligent Material Systems and Structures, vol. 29, no. 6, pp. 1102–1112, Apr. 2018, doi: 10.1177/1045389X17730917.

[179] M. Unruan, S. Unruan, Y. Inkong, and R. Yimnirun, "Estimation of energy density of PMN-PT ceramics utilizing mechanical stress," *Integrated Ferroelectrics*, vol. 195, no. 1, pp. 39–45, Jan. 2019, doi: 10.1080/10584587.2019.1570042.

[180] S. Patel, A. Chauhan, and R. Vaish, "Enhanced energy harvesting in commercial ferroelectric materials," *Mater. Res. Express*, vol. 1, no. 2, p. 025504, May 2014, doi: 10.1088/2053-1591/1/2/025504.

[181] Y. Goh and S. Jeon, "First-order reversal curve diagrams for characterizing ferroelectricity of $Hf_{0.5}Zr_{0.5}O_2$ films grown at different rates," *Journal of Vacuum Science & Technology B*, vol. 36, no. 5, p. 052204, Sep. 2018, doi: 10.1116/1.5046762.

[182] J. Leon-Gil *et al.*, "Medium and Short Wave RF Energy Harvester for Powering Wireless Sensor Networks," *Sensors*, vol. 18, no. 3, p. 768, Mar. 2018, doi: 10.3390/s18030768.

[183] P. Loreti, A. Catini, M. De Luca, L. Bracciale, G. Gentile, and C. Di Natale, "The Design of an Energy Harvesting Wireless Sensor Node for Tracking Pink Iguanas," *Sensors*, vol. 19, no. 5, p. 985, Feb. 2019, doi: 10.3390/s19050985.

[184] F. Ait Aoudia, M. Gautier, M. Magno, O. Berder, and L. Benini, "Leveraging Energy Harvesting and Wake-Up Receivers for Long-Term Wireless Sensor Networks," *Sensors*, vol. 18, no. 5, p. 1578, May 2018, doi: 10.3390/s18051578.

[185] S. Shi *et al.*, "A Self-Powered Engine Health Monitoring System Based on L-Shaped Wideband Piezoelectric Energy Harvester," *Micromachines*, vol. 9, no. 12, p. 629, Nov. 2018, doi: 10.3390/mi9120629.

[186] G. M. Rani, C.-M. Wu, K. G. Motora, R. Umapathi, and C. R. M. Jose, "Acoustic-electric conversion and triboelectric properties of nature-driven CF-CNT based triboelectric nanogenerator for mechanical and sound energy harvesting," *Nano Energy*, vol. 108, p. 108211, Apr. 2023, doi: 10.1016/j.nanoen.2023.108211.

[187] L. Wang and F. G. Yuan, "Vibration energy harvesting by magnetostrictive material," *Smart Mater. Struct.*, vol. 17, no. 4, p. 045009, Aug. 2008, doi: 10.1088/0964-1726/17/4/045009.

[188] S. Zhou, M. Lallart, and A. Erturk, "Multistable vibration energy harvesters: Principle, progress, and perspectives," *Journal of Sound and Vibration*, vol. 528, p. 116886, Jun. 2022, doi: 10.1016/j.jsv.2022.116886.

[189] T. Yang, S. Zhou, S. Fang, W. Qin, and D. J. Inman, "Nonlinear vibration energy harvesting and vibration suppression technologies: Designs, analysis, and applications," *Applied Physics Reviews*, vol. 8, no. 3, p. 031317, Sep. 2021, doi: 10.1063/5.0051432.

[190] Z.-Q. Lu, D. Shao, Z.-W. Fang, H. Ding, and L.-Q. Chen, "Integrated vibration isolation and energy harvesting via a bistable piezo-composite plate," *Journal of Vibration and Control*, vol. 26, no. 9–10, pp. 779–789, May 2020, doi: 10.1177/1077546319889815.

[191] M. Xie, Y. Zhang, M. J. Kraśny, C. Bowen, H. Khanbareh, and N. Gathercole, "Flexible and active self-powered pressure, shear sensors based on freeze casting ceramic–polymer composites," *Energy Environ. Sci.*, vol. 11, no. 10, pp. 2919–2927, 2018, doi: 10.1039/C8EE01551A.

[192] H. Fu *et al.*, “Rotational energy harvesting for self-powered sensing,” *Joule*, vol. 5, no. 5, pp. 1074–1118, May 2021, doi: 10.1016/j.joule.2021.03.006.

[193] S. P. Beeby *et al.*, “A micro electromagnetic generator for vibration energy harvesting,” *J. Micromech. Microeng.*, vol. 17, no. 7, pp. 1257–1265, Jul. 2007, doi: 10.1088/0960-1317/17/7/007.

[194] A. Khaligh, Peng Zeng, and Cong Zheng, “Kinetic Energy Harvesting Using Piezoelectric and Electromagnetic Technologies—State of the Art,” *IEEE Trans. Ind. Electron.*, vol. 57, no. 3, pp. 850–860, Mar. 2010, doi: 10.1109/TIE.2009.2024652.

[195] B. C. Yen and J. H. Lang, “A variable-capacitance vibration-to-electric energy harvester,” *IEEE Trans. Circuits Syst. I*, vol. 53, no. 2, pp. 288–295, Feb. 2006, doi: 10.1109/TCSI.2005.856043.

[196] M. E. Kiziroglou, C. He, and E. M. Yeatman, “Rolling Rod Electrostatic Microgenerator,” *IEEE Trans. Ind. Electron.*, vol. 56, no. 4, pp. 1101–1108, Apr. 2009, doi: 10.1109/TIE.2008.2004381.

[197] S. Yamaura, T. Nakajima, Y. Kamata, T. Sasaki, and T. Sekiguchi, “Production of vibration energy harvester with impact-sliding structure using magnetostrictive Fe-Co-V alloy rod,” *Journal of Magnetism and Magnetic Materials*, vol. 514, p. 167260, Nov. 2020, doi: 10.1016/j.jmmm.2020.167260.

[198] T. Ueno and S. Yamada, “Performance of Energy Harvester Using Iron–Gallium Alloy in Free Vibration,” *IEEE Trans. Magn.*, vol. 47, no. 10, pp. 2407–2409, Oct. 2011, doi: 10.1109/TMAG.2011.2158303.

[199] A. Adly, D. Davino, A. Giustiniani, and C. Visone, “Experimental tests of a magnetostrictive energy harvesting device toward its modeling,” *Journal of Applied Physics*, vol. 107, no. 9, p. 09A935, May 2010, doi: 10.1063/1.3357403.

[200] S. Kita, T. Ueno, and S. Yamada, “Improvement of force factor of magnetostrictive vibration power generator for high efficiency,” *Journal of Applied Physics*, vol. 117, no. 17, p. 17B508, May 2015, doi: 10.1063/1.4907237.

[201] H. Liu, S. Wang, Y. Zhang, and W. Wang, “Study on the giant magnetostrictive vibration-power generation method for battery-less tire pressure monitoring system,” *Proceedings of the Institution of Mechanical Engineers, Part C: Journal of Mechanical Engineering Science*, vol. 229, no. 9, pp. 1639–1651, Jun. 2015, doi: 10.1177/0954406214545821.

[202] T. Ueno, “U-shape magnetostrictive vibration based power generator for universal use,” presented at the SPIE Smart Structures and Materials + Nondestructive Evaluation and Health Monitoring, N. G. Meyendorf, T. E. Matikas, and K. J. Peters, Eds., Las Vegas, Nevada, United States, Apr. 2016, p. 98060E. doi: 10.1117/12.2218759.

[203] V. Berbyuk, “Vibration energy harvesting using Galfenol-based transducer,” presented at the SPIE Smart Structures and Materials + Nondestructive Evaluation and Health Monitoring, H. Sodano, Ed., San Diego, California, USA, Apr. 2013, p. 86881F. doi: 10.1117/12.2009812.

[204] K. Mori, T. Horibe, S. Ishikawa, Y. Shindo, and F. Narita, “Characteristics of vibration energy harvesting using giant magnetostrictive cantilevers with resonant tuning,” *Smart Mater. Struct.*, vol. 24, no. 12, p. 125032, Dec. 2015, doi: 10.1088/0964-1726/24/12/125032.

[205] T. Sourmail, “Near equiatomic FeCo alloys: Constitution, mechanical and magnetic properties,” *Progress in Materials Science*, vol. 50, no. 7, pp. 816–880, Sep. 2005, doi: 10.1016/j.pmatsci.2005.04.001.

[206] S. M. Al-Jaber, “Path Integral Approach to Faraday’s Law of Induction,” *JEMAA*, vol. 03, no. 06, pp. 184–186, 2011, doi: 10.4236/jemaa.2011.36030.

[207] A. Erturk and D. J. Inman, “Issues in mathematical modeling of piezoelectric energy harvesters,” *Smart Mater. Struct.*, vol. 17, no. 6, p. 065016, Dec. 2008, doi: 10.1088/0964-1726/17/6/065016.

[208] S. Mohammadi and A. Esfandiari, “Magnetostrictive vibration energy harvesting using strain energy method,” *Energy*, vol. 81, pp. 519–525, Mar. 2015, doi: 10.1016/j.energy.2014.12.065.

[209] A. Kefal, C. Maruccio, G. Quaranta, and E. Oterkus, “Modelling and parameter identification of electromechanical systems for energy harvesting and sensing,” *Mechanical Systems and Signal Processing*, vol. 121, pp. 890–912, Apr. 2019, doi: 10.1016/j.ymssp.2018.10.042.

[210] D. Davino, A. Giustiniani, C. Visone, and W. Zamboni, “Stress-Induced Eddy Currents in Magnetostrictive Energy Harvesting Devices,” *IEEE Trans. Magn.*, vol. 48, no. 1, pp. 18–25, Jan. 2012, doi: 10.1109/TMAG.2011.2162744.

[211] J. D. Hobeck and D. J. Inman, “A distributed parameter electromechanical and statistical model for energy harvesting from turbulence-induced vibration,” *Smart Mater. Struct.*, vol. 23, no. 11, p. 115003, Nov. 2014, doi: 10.1088/0964-1726/23/11/115003.

[212] Supermagnete, “Fiche de données article CSR-20-20-04-N.” www.supermagnete.fr.

[213] A. Badel, F. Formosa, and M. Lallart, “Electromechanical Transducers,” in *Advanced Micro and Nanosystems*, 1st ed., D. Briand, E. Yeatman, and S. Roundy, Eds., Wiley, 2015, pp. 27–60. doi: 10.1002/9783527672943.ch3.

[214] H. Zhang, “Power generation transducer from magnetostrictive materials,” *Appl. Phys. Lett.*, vol. 98, no. 23, p. 232505, Jun. 2011, doi: 10.1063/1.3597222.

[215] P. Fagan, B. Ducharne, L. Daniel, A. Skarlatos, M. Domenjoud, and C. Reboud, “Effect of stress on the magnetic Barkhausen noise energy cycles: A route for stress evaluation in ferromagnetic materials,” *Materials Science and Engineering: B*, vol. 278, p. 115650, Apr. 2022, doi: 10.1016/j.mseb.2022.115650.

PUBLICATIONS

- An article has been published with the results of his thematic: Toutsop, B.; Ducharne, B.; Lallart, M.; Morel, L.; Tsafack, P. Characterization of Tensile Stress-Dependent Directional Magnetic Incremental Permeability in Iron-Cobalt Magnetic Sheet: Towards Internal Stress Estimation through Non-Destructive Testing. *Sensors* **2022**, *22*, 6296. https://doi.org/10.3390/s22166296

- Toutsop et al., “Magnetostrictive energy conversion ability of Iron Cobalt Vanadium alloy sheet: Experimental and theoretical evaluation,” *Journal of Intelligent Material Systems and Structures*, p. 1045389X231225502, Jan. 2024, doi: 10.1177/1045389X231225502.I have also been cited as Co-Author:

- Kouakeuo, Sorelle Hilary Nguedjang, Aurélie Solignac, Ruth V. Sabariego, Laurent Morel, Marie-Ange Raulet, **Borel Toutsop**, Pierre Tsafack, and Benjamin Ducharne. "Internal characterization of magnetic cores, comparison to finite element simulations: A route for dimensioning and condition monitoring." *IEEE Transactions on Instrumentation and Measurement* (2022): 1-10., doi: 10.1109/TIM.2022.3194905.

- S.H. Nguedjang Kouakeuo, B. Ducharne, A. Solignac, L. Morel, M.A. Raulet, **B. Toutsop**, Y.A. Tene Deffo, P. Tsafack, Non-invasive local magnetic hysteresis characterization of a ferromagnetic laminated core, Journal of Magnetism and Magnetic Materials, Volume 527, 2021, 167783, ISSN 0304-8853, https://doi.org/10.1016/j.jmmm.2021.167783.